



University of Strathclyde
Department of Mechanical & Aerospace Engineering

Mechanical failure assessment of Lithium ion battery electrode under electrochemical-mechanical condition

Xuanchen Zhu

A thesis presented in fulfilment of the requirements
for the degree of Doctor of Philosophy

2021

Declaration of author's rights

This thesis is the result of the author's original research. It has been composed by the author and has not been previously submitted for examination which has led to the award of a degree.

The copyright of this thesis belongs to the author under the terms of the United Kingdom Copyright Acts as qualified by University of Strathclyde Regulation 3.50. Due acknowledgement must always be made of the use of any material contained in, or derived from, this thesis.

Acknowledgements

I would like to thank the support from my supervisor Dr Haofeng Chen. In the past few years, I have learned a lot of knowledge and thinking methods from Dr Chen. His continuous guidance made the completion of this thesis possible.

Massive thanks go to colleagues in Structure Integrity and Lifetime Assessment research group and in Mechanical and Aerospace Engineering department. The discussions I have had with them has helped me learn not only professional knowledge, new research ideas but also attitude of doing things.

I would also like to thank my friends in Glasgow. Your friendship and the happy time with you made my PhD time enjoyable. I hope to maintain this friendship and wish you the luck in the future.

I would like to express my gratitude towards my family. Their unconditional support always accompanied with me, and encouraged me to continue my study.

Abstract

Lithium ion battery appears to be the dominant energy source of electric vehicles and most portable electronic devices, due to its high energy density, low self-discharge rate as well as wide temperature range. However, its inherent operation mechanism that, Li-ion reversibly inserts into/extracts from battery electrode, would lead to the repeated swelling and shrinking of the host electrode material and the generation of diffusion-induced stress (DIS). The mechanical failure behaviours under diffusion-induced stress could influence the cyclic performance of electrode and battery. Hence, the structural integrity assessment of battery electrode upon electrochemical condition is vital for the development of this new energy source.

This thesis presents the studies of diffusion-induced stress related mechanical failure analyses of Li-ion battery electrode. Firstly, the diffusion driven method and chemical potential driven method are developed and implemented by writing finite element subroutines. These methods make it available to use ABAQUS platform to effectively and efficiently conduct coupled diffusion-stress analysis. Secondly, with using the extended Finite Element Method (XFEM), the complete crack initiation, propagation and fracture process of electrode particle can be investigated, and the critical cracking failure boundaries are innovatively proposed for assessing the different crack status. Thirdly, with using the Linear Matching Method Framework (LMMF), knowledge has been extended on shakedown, reverse plasticity and ratcheting behaviours of battery electrode under electrochemical conditions. Furthermore, a fatigue damage evaluation method is innovatively proposed, which makes it available to assess the continuous mechanical degradation of oxide electrode material. With the proposed assessment method, the fatigue degradation trends of battery electrode configurations under different material levels are modeled. The research works in this thesis offer valuable insights into mechanical failure mechanisms of lithium ion battery electrode under electrochemical loads and provide theoretical information on the optimization of electrode material.

Peer Reviewed Publications

X.C. Zhu, H.F. Chen, W.L. Luan. On the study of cyclic plasticity behaviour of primary electrode particle for lithium-ion battery. *European Journal of Mechanics - A/Solids*, 2021, 86: 104175

X.C. Zhu, Y. Xie, H.F. Chen, W.L. Luan. Numerical analysis of the cyclic mechanical damage of Li-ion battery electrode and experimental validation. *International Journal of Fatigue*, 2021, 142: 105915

X.C. Zhu, H.F. Chen, W.L. Luan. The diffusion induced stress and cracking behaviour of primary particle for Li-ion battery electrode. *International Journal of Mechanical Sciences*, 2020, 178: 105608

X.C. Zhu, H.F. Chen, F.Z. Xuan, X.H. Chen. On the creep fatigue and creep rupture behaviours of 9–12% Cr steam turbine rotor. *European Journal of Mechanics-A/Solids*, 2019, 76: 263-278.

X.H. Chen, K.C. Huang, **X.C. Zhu**, H.F. Chen, M.C. li. Ratcheting behavior of pressurized lateral nozzle of cylinder with local wall thinning under different loading paths. *Engineering Failure Analysis*, 2020, 117: 104947.

X.H. Chen, K.M. Zhuang, **X.C. Zhu**, H.F. Chen. Limit load, shakedown and ratchet analysis of pressurized lateral nozzle. *Smart Structures and Systems, An International Journal*. 2021, 27(3): 421-434.

X.C. Zhu, H.F. Chen. Non-linear fatigue damage accumulation of lithium-ion battery electrode at different material levels. under writing

Contents

Declaration of author’s rights.....	II
Acknowledgements.....	III
Abstract.....	IV
Peer Reviewed Publications.....	II
Contents.....	III
List of figures.....	VI
List of tables.....	XIII
Nomenclatures.....	XIV
Acronyms.....	XVI
Chapter 1 Introduction.....	1
1.1 Research background.....	1
1.2 Objectives of the thesis.....	4
1.3 Methodology.....	4
1.4 Outline of the thesis.....	5
1.5 References.....	6
Chapter 2 Mechanical integrity of Li-ion battery electrode upon electrochemical condition.....	8
2.1 Introduction.....	8
2.2 Diffusion induced stress.....	10
2.2.1 Formation mechanism of DIS.....	10
2.2.2 DIS at different scales.....	12
2.3 Cracking behaviour.....	20
2.4 Cyclic plasticity behaviour.....	27
2.5 Other failure mechanisms.....	30
2.6 Conclusions.....	33
2.7 References.....	33
Chapter 3 Coupled diffusion-stress analysis and study of cracking behaviour.....	40
3.1 Introduction.....	40
3.2 Computational methods.....	41
3.2.1 The first boundary value problem – diffusion equation.....	41
3.2.2 The second boundary value problem– mechanics equation.....	44
3.2.3 Fracture assessment approach.....	45
3.3 Validation of the coupled diffusion-stress methods.....	48
3.4 Diffusion induced stress of primary electrode particle.....	51
3.4.1 Finite element model and material properties.....	51
3.4.2 Stress inside primary electrode particle.....	53
3.5 Fracture evaluation.....	58
3.5.1 Crack initiation.....	58
3.5.2 Crack propagation.....	62
3.6 Conclusions.....	66

3.7 References.....	66
Chapter 4 Cyclic plasticity behaviour of battery electrode.....	68
4.1 Introduction.....	68
4.2 The framework of Linear Matching Method.....	69
4.2.1 Evaluation of the shakedown limit.....	70
4.2.2 Evaluation of the ratchet limit.....	70
4.3 Problem Description.....	71
4.3.1 Finite element model and material property.....	71
4.3.2 Linear Elastic Solutions.....	72
4.4 Shakedown Assessment.....	75
4.4.1 Shakedown limits of electrode particle.....	75
4.4.2 ABAQUS step-by-step analysis.....	77
4.4.3 Shakedown boundaries with the changing of particle diameter.....	77
4.5 Steady state cycle and ratchet limit analysis.....	79
4.5.1 Steady state cycle analysis.....	79
4.5.2 Ratcheting assessment.....	82
4.6 Conclusions.....	84
4.7 References.....	85
Chapter 5 Progressive fatigue damage assessment of battery electrode using strain based fatigue damage model.....	88
5.1 Introduction.....	88
5.2 Mechanics and experiment represented damage models.....	89
5.2.1. Continuum damage mechanics.....	89
5.2.2. Fatigue damage model.....	90
5.2.3. Subroutine development.....	91
5.2.4. The effect of nonlinearity index on damage evolution.....	92
5.2.5. Capacity fading represented damage rule.....	93
5.3 Finite element model.....	93
5.4 Experimental test.....	96
5.4.1 Electrode preparation.....	96
5.4.2 Cell assembling.....	97
5.4.3 Electrochemical performance measurement.....	97
5.5 Model establishment and validation under various C-rate.....	98
5.6 Damage affected stress-strain response.....	102
5.7 Conclusions.....	108
5.8 References.....	108
Chapter 6 Progressive fatigue damage assessment of battery electrode using energy based fatigue damage model under different material scales.....	110
6.1 Introduction.....	110
6.2 Fatigue damage model.....	110
6.2.1 Stress based fatigue life model.....	111
6.2.2 Strain based fatigue life model.....	111
6.2.3 Energy based fatigue life model.....	112
6.3 Various damage accumulation trends of battery electrode.....	114

6.3.1	Moderative damage accumulation.....	115
6.3.2	Accelerated damage accumulation.....	118
6.3.3	Quasi-linear damage accumulation.....	120
6.4	Non-linear fatigue damage simulation of layered electrode.....	122
6.5	Fatigue damage simulation of microscopic multi-particle electrode.....	129
6.5.1	Model description.....	129
6.5.2	Results and discussions.....	133
6.6	Conclusions.....	3
6.7	References.....	4
Chapter 7	Conclusions and Future Work.....	5
7.1	Conclusions.....	5
7.2	Future work.....	6
Appendix 1	8
Appendix 2	11
Appendix 3	22

List of figures

Fig 1. 1 The schematic illustration of charging/discharging principle for Li-ion battery. [1-6].....	2
Fig 1. 2 The schematic diagram of lithiation caused DIS and mechanical fracture.	3
Fig 2. 1 Dendrite growth results in puncturation and short connections [2-3].....	8
Fig 2. 2 Schematic illustration of the position of SEI, where d represents the formed SEI layer between electrolyte c and active material e [2-4].....	9
Fig 2. 3 Schematic diagrams of (a) constraints caused by neighboring electrode particles and current collector during the expansion process, (b) curvature deformation caused by constraint effect of current collector to active film, (c) contact stress between neighboring particles within lithiation phase, (d) mismatch induced stress and strain under phase transformation effect [1-7].....	11
Fig 2. 4 Schematic illustrations of electrode in different scales. The individual particle represents a structural configuration on microscale. Representative volume element is in mesoscale and consists of particles and electrolyte. Electrode plate is the intuitionistic structure in macroscale [2-9].....	12
Fig 2. 5 Schematic illustrations of (a) a spherical particle [2-11], (b) nanowire electrode [2-23], (c) a hollow core-shell electrode [2-28].....	15
Fig 2. 6 Three-dimensional reconstructed mecoscale electrode model [2-32], where red color represents active electrode particle and blue color represents electrolyte.....	17
Fig 2. 7 Schematic illustrations of (a) layered active plate-current collector [2-35], (b) island electrode [2-40].....	18
Fig 2. 8 (a) SEM images of the patterned island electrodes with disparate shapes of void defects, (b) the evolution of DIS at the disparate defect tips [2-44].....	19
Fig 2. 9 SEM images [1-9] of LiFePO ₄ electrode particles (a) prepared sample, (b) electrode before cyclic charging and discharging, (c) electrode after 10 cycles, (d) electrode after 30 cycles, (e) electrode after 60 cycles, (f) particle 1 in (e), (g) particle 2 in (e).....	20
Fig 2. 10 (a) “Electrochemical shock” map for Li _x Mn ₂ O ₄ under galvanostatic condition with logarithmic axes [2-47], (b) a general fracture boundary [2-48].....	22
Fig 2. 11 (a) Bilinear traction-separation law [2-49], (b) A failure map considering orientation angle and location of initial defect.....	23
Fig 2. 12 (a) Disintegration of meatball electrode structure, (b) applying cohesive zone elements to model the fracture between the primary particles[2-58], microcracks within meatball electrode under (c) 0.5C, (d) 2C.....	25
Fig 2. 13 Experimental observation of the crack caused partition of thin film electrode [2-61], (a)	

silicon film with 500nm thickness before cycling, (b) film with 1000nm thickness after 5 cycles, (c) film with 500nm thickness after 5 cycles, (d) film with 200nm thickness after 10 cycles.....	26
Fig 2. 14 Classic Bree’s diagram under cyclic loading conditions.....	28
Fig 2. 15 The boundaries of different cyclic behaviours with the changing of yield strength and injection rate [2-66].....	29
Fig 2. 16 Schematic diagram of the cross section of a hollow re-entrant honeycomb electrode, showing the mechanism of negative Poisson’s ratio [2-58].....	30
Fig 2. 17 Schematic diagram of two modes of decohesion: Mode I (opening) and Mode II (slip) [2-75].....	30
Fig 2. 18 (a) Experimental observations of the morphological evolution of silicon nanowire electrode [2-79], (b) TEM image showing the buckling caused fracture of the silicon core (scale, 50nm) [2-80].....	32
Fig 3. 1 Schematic flowchart showing the finite element implementation for (a) diffusion driven method, (b) chemical potential driven method.....	44
Fig 3. 2 Schematic diagram of crack penetrating element with XFEM [3-8].....	46
Fig 3. 3 Traction-separation law.....	47
Fig 3. 4 Schematic of (a) an ellipsoidal particle [2-13], (b) mesh distribution.....	49
Fig 3. 5 The comparison between Ref [2-13] and the diffusion driven approach (a) concentration of Li at the end of discharge from reference, (b) concentration of Li at the end of discharge from the diffusion driven approach, (c) von Mises stress at the end of discharge from reference. (d) von Mises stress at the end of discharge from the diffusion driven approach.....	50
Fig 3. 6 The comparison between Ref [2-13] and the chemical potential driven approach (a) concentration of Li at the end of discharge from reference, (b) concentration of Li at the end of discharge from the chemical potential driven approach, (c) von Mises stress at the end of discharge from reference. (d) von Mises stress at the end of discharge from the chemical potential driven approach.....	50
Fig 3. 7 The comparison of diffusion induced stress between reference and the developed two methods with varying mesh density (subroutine 1 is the diffusion driven approach, subroutine 2 is the chemical potential driven approach).....	51
Fig 3. 8 Schematic illustrations of (a) primary electrode particle, (b) mesh distribution,	52
Fig 3. 9 The evolution of von Mises stress produced by diffusion driven method for 3 μ m diameter particle, stress distribution along radius during (a) lithiation process (b) delithiation process under 0.3A/m ² ,1A/m ² (c) contours of Li-ion concentration under 1A/m ² at different moment (d) contours of von Mises stress under 1A/m ² at different moments.....	54
Fig 3. 10 The evolution of maximum principal stress produced by diffusion driven method for 3 μ m diameter particle, stress distribution along radius during (a) lithiation process (b)	

delithiation process under $0.3A/m^2, 1A/m^2$, (c) contours of maximum principal stress under $1A/m^2$ at different moments.....	55
Fig 3. 11 Comparison of diffusion induced stress profile generated by diffusion driven method and chemical potential driven method for $3\mu m$ diameter particle with 125GPa constant average Young's modulus (a) under $0.3A/m^2$ current density (b) under $1A/m^2$ current density.....	56
Fig 3. 12 The effect of varying Young's modulus on maximum principal stress (a) the variation of Young's modulus with Li concentration (b) comparison of maximum principal stress with varying Young's modulus and constant Young's modulus of particle under $0.3A/m^2$ during lithiation-delithiation phases (c) comparison of maximum principal stress with varying Young's modulus and constant Young's modulus of particle under $1A/m^2$ during lithiation-delithiation phases.....	57
Fig 3. 13 (a) Damage distribution of $3\mu m$ particle under $0.2875A/m^2$ with spherically symmetric stress field, (b) TXM tomogram of individual NCM particle after charging at C/3 rate to 4.5V [3-13].....	59
Fig 3. 14 (a) Particle model with a tiny stress disturbance acting on one arbitrary point of the surface, (b) The maximum principal stress distribution for $3\mu m$ particle under $0.2875A/m^2$ considering stress disturbance.....	60
Fig 3. 15 The critical current density of crack initiation for $3\mu m$ particle under different mesh densities.....	60
Fig 3. 16 (a) Crack initiation boundary for $3\mu m$ diameter NCM primary particle considering concentration-dependent Young's modulus and constant average Young's modulus, crack and damage distribution with concentration-dependent Young's modulus under (b) $0.225A/m^2$ (c) $0.2875A/m^2$	62
Fig 3. 17 (a) The fracture criteria diagram for NCM primary particle (b) the variation of maximum principal stress with current density for various particle dimensions.....	63
Fig 3. 18 (a) Scanning electron microscopy (SEM) image for a randomly selected area on NCM electrode before charging-discharging test, (b) size distribution of NCM particles from SEM image.....	64
Fig 3. 19 The continuous process of crack initiation and propagation under $0.37A/m^2$ current density at lithiation phase.....	65
Fig 3. 20 The continuous process of crack initiation and propagation for $3\mu m$ diameter crystal under $0.37A/m^2$ current density at delithiation phase.....	65
Fig 4. 1 The history of diffusion-induced stress under $0.3 A/m^2$ and mechanical reference stress for $3\mu m$ diameter electrode particle within one cycle (DOD - depth of discharge, SOC - state of charge).....	74
Fig 4. 2 (a) The contours of elastic von Mises effective stress of four selected instants, (b) the	

contours of concentration fields of four selected instants, (c) the schematic diagram of lithiation caused extrusion between adjacent particles, (d) the contour of mechanical reference stress at instant 3.....	74
Fig 4. 3 (a) Shakedown boundaries of 3um diameter particle under cyclic current density and mechanical load considering different particle arrangements, the schematic diagrams of different particle arrangements, (b) one central particle with two neighbouring particles, (c) one central particle with four neighbouring particles.....	76
Fig 4. 4 The distribution of von Mises stress for 3um diameter particle under (a) two, and (b) four mechanical reference loads.....	76
Fig 4. 5 Plastic strain history (PEMAG) obtained from ABAQUS step-by-step analyses for cyclic loading (a) load point A, (b) load point B.....	77
Fig 4. 6 The shakedown limit curves of the electrode particle with various dimensions subjected to cyclic current density and mechanical load.....	78
Fig 4. 7 The maximum von Mises stress under 0.15A/m ² (a) particle with diameter 2um, (b) particle with diameter 4um, the maximum von Mises stress under mechanical reference load (c) particle with diameter 2um, (d) particle diameter 4um.....	79
Fig 4. 8 (a) shakedown boundary of 3um particle with selected loading points, the contours of plastic strain range of 3um particle under (b) loading point 1, (c) loading point 2, (d) loading point 3, the contours of ratcheting strain of 3um particle under (e) loading point 1, (f) loading point 2, (g) loading point 3.....	80
Fig 4. 9 Hysteresis loops at the most dangerous location of electrode particle under three loading conditions.....	83
Fig 4. 10 Ratcheting and shakedown limit curves for electrode particle with various dimensions under cyclic current density and constant mechanical load.....	83
Fig 4. 11 Ratcheting and shakedown limit curves for electrode particle with various dimensions under coupled cyclic mechanical load - current density and constant mechanical load.....	84
Fig 5. 1 Schematic flowchart showing the finite element implementation of the UMAT and the communications between UMAT and ABAQUS.....	92
Fig 5. 2 The modeled three categories of damage evolution trends with respect to different values of nonlinearity index	93
Fig 5. 3 (a) Schematic diagram of the experimentally tested layered electrode and current collector, (b) mesh of the cathode active layer, (c) mesh of cathode active layer and current collector.....	95
Fig 5. 4 The stress distribution within active layer along the thickness direction (a) considering current collector, (b) considering current collector as a rigid surface.....	95
Fig 5. 5 Schematic diagram of electrochemical performance measurement and experimental output.....	98

Fig 5. 6 The variation of capacity and capacity fading represented damage with respect to the number of cycles for coin cell under 1C.....	99
Fig 5. 7 (a) Contour plot of damage distribution on the layered electrode at 1C, (b) fatigue damage distribution along the direction of thickness.....	100
Fig 5. 8 Capacity fading represented damage, calculated fatigue damage on integration point 1 and 2 against the number of cycles under 1C.....	100
Fig 5. 9 The variation of capacity and capacity fading represented damage with respect to the number of cycles for coin cell under (a) 0.5C, (b) 2C.....	101
Fig 5. 10 Capacity fading based damage, calculated damage on integration point 1 and 2 against the number of cycles under (a) 0.5C, (b) 2C.....	101
Fig 5. 11 (a) The corresponding damage affected Young's modulus and yield strength on two integration points versus the number of cycles, (b) the cross-sectional view of deformed active layer after 150 cycles, (c) the cross-sectional view of concentration distribution within active layer after 150 cycles.....	103
Fig 5. 12 (a) The distribution of in-plane stress component and von Mises stress on the thickness section at the end of lithiation phase of 50 th cycle, (b) the distribution of in-plane stress component and von Mises stress on the thickness section at the end of lithiation phase of 150 th cycle.....	103
Fig 5. 13 The stress-strain hysteresis loops for 50 th , 100 th , 150 th cycle at 1C on (a) integration point 1, (b) integration point 2, (c) the calculated plastic strain range on two integration points versus the number of cycles under 1C.....	105
Fig 5. 14 Three continuous stress-strain hysteresis loops at 1C for (a) integration point 1, (b) integration point 2.....	106
Fig 5. 15 (a) The variation of hydrostatic stress for two integration points within three continuous cycles, (b) the transient changed diffusivity affected by diffusion induced stress within three continuous cycles.....	106
Fig 5. 16 The variation of plastic strain within one cycle under different electrochemical loads (0.5C, 1C, 2C) for (a) integration point 1(top surface), (b) integration point 2 (bottom surface).....	107
Fig 5. 17 The stress-strain hysteresis loops at 100 th cycle under 0.5C, 1C and 2C for (a) integration point 1(top surface), (b) integration point 2(bottom surface).....	107
Fig 6.1 Stress-fatigue life curve.....	111
Fig 6. 2 Schematic diagram of hysteresis loop.....	114
Fig 6. 3 (a) Moderative damage accumulation trend of the top surface of thin film electrode plate, (b) the evolution of the ratio between plastic hysteresis energy and fatigue toughness for moderative accumulation.....	115
Fig 6. 4 The evolution of (a) stress amplitude, (b) plastic strain amplitude with moderative	

damage accumulation trend.....	116
Fig 6. 5 The variation of (a) yield stress, (b) Young's modulus of the top surface of electrode plate affected by moderative fatigue damage accumulation.....	116
Fig 6. 6 The stress-strain hysteresis loops of the top surface of electrode plate at 30 th , 65 th , 100 th , 135 th cycle with moderative damage accumulation trend.....	117
Fig 6. 7 (a) Accelerated damage accumulation trend of the top surface of thin film electrode plate, (b) the evolution of the ratio between plastic hysteresis energy and fatigue toughness for accelerated accumulation.....	118
Fig 6. 8 The evolution of (a) stress amplitude, (b) plastic strain amplitude with accelerated damage accumulation trend.....	119
Fig 6. 9 The variation of (a) yield stress, (b) Young's modulus of the top surface of electrode plate affected by accelerated fatigue damage accumulation.....	119
Fig 6. 10 The stress-strain hysteresis loops of the top surface of electrode plate at 30 th , 65 th , 100 th , 135 th cycle with accelerated damage accumulation trend.....	120
Fig 6. 11 (a) Quasi-linear damage accumulation trend of the top surface of thin film electrode plate, (b) the evolution of the ratio between plastic hysteresis energy and fatigue toughness for quasi-linear accumulation.....	121
Fig 6. 12 The evolution of (a) stress amplitude, (b) plastic strain amplitude with quasi-linear damage accumulation trend.....	121
Fig 6. 13 The stress-strain hysteresis loops of electrode top surface at 50 th , 100 th , 150 th cycle with quasi-linear damage accumulation trend.....	122
Fig 6. 14 The variation of capacity and capacity fading represented damage with respect to the number of cycles under 1C [6-7].....	123
Fig 6. 15 Experiment indicated damage and calculated fatigue damage on plate top surface under 1C.....	124
Fig 6. 16 The variation of Li-ion concentration on the thickness of the section at (a) 200 th cycle, (b) 400 th cycle.....	125
Fig 6. 17 The damage evolution trends of electrode plate under different C-rate conditions (0.5C, 1C and 2C).....	126
Fig 6. 18 The variation of (a) yield stress, (b) Young's modulus of electrode plate under under different C-rate conditions (0.5C, 1C and 2C).....	127
Fig 6. 19 The variation of (a) stress amplitude, (b) plastic strain amplitude of electrode plate under under different C-rate conditions (0.5C, 1C and 2C).....	127
Fig 6. 20 Hysteresis loops of top surface of electrode plate under 0.5C, 1C and 2C at (a) 50 th cycle, (b) 200 th cycle.....	128
Fig 6. 21 (a) A representative volume element of micro multi-particle electrode model, in which the particles represent active material and the rest area is occupied by electrolyte, (b) mesh	

distribution of the representative volume element.....	130
Fig 6. 22 (a) Loading condition in a lithiation-delithiation cycle, (b) schematic diagram showing the area of loading.....	132
Fig 6. 23 The contour plots of displacements of the deformed RVE model	132
Fig 6. 24 The Li-ion concentration distribution of active particles inside RVE model after 10th lithiation, the contour plots of the corresponding von Mises stress of (b) active particles, (c) electrolyte.....	134
Fig 6. 25 The accumulated fatigue damage of RVE model after (a) 25, (b) 50 lithiation-delithiation cycles.....	135
Fig 6. 26 Schematic diagram showing the representative positions on the RVE model.....	136
Fig 6. 27 The stress amplitude, (b) the plastic strain amplitude of the representative positions against the number of cycles, (c) the Li-ion concentration of the representative positions at the end of lithiation phase against the number of cycles.....	137
Fig 6. 28 The stress-strain loops of the representative positions at (a) 25 th , (b) 50 th lithiation-delithiation cycle.....	137
Fig 6. 29 The yield strength of RVE model after (a) 25, (b) 50 lithiation-delithiation cycles.....	138
Fig 6. 30 The Young's modulus of RVE model after (a) 25, (b) 50 cycles.....	139

List of tables

Table 3.1 Material parameters of Mn ₂ O ₄ used in calculation for verifying the proposed methods ...	49
Table 3.2 Material properties for NCM electrode material.....	52
Table 4.1 Material properties of NCM electrode particle	72
Table 4.2 Fitted parameters in the fatigue damage model	82
Table 4.3 Fatigue damage and number of cycles to fatigue failure	82
Table 5.1 Material properties of NCM electrode layer.....	96
Table 5.2 The composition of active layer	97
Table 5.3 Fitted parameters in the fatigue damage model.....	99
Table 6.1 Expressions of S-N curve.....	111
Table 6.2 Expressions of strain-life models	112
Table 6.3 Fitted parameters in the energy based fatigue damage model	124
Table 6.4 Material properties of RVE model	131
Table 6.5 The damage of the representative positions on the RVE model	136
Table 6.6 The yield strength of the representative positions on the RVE model	138
Table 6.7 The Young's modulus of the representative positions on the RVE model	139

Nomenclatures

ρ	Density
c	Concentration
c_s	Specific heat
T	Temperature
ΔT	Temperature increment
Φ	Internal heat source
t	Time
q	Heat flux
J	Diffusion flux
D_f	Diffusivity
D_{f0}	Diffusivity at stress-free condition
Ω	Partial molar volume
σ_h	Hydrostatic stress
μ	Chemical potential
$\nabla\mu$	Chemical potential gradient
F	Driven force in chemical potential driven method
X	Molar fraction of lithium ion
v_a	Average diffusion velocity of electrode particle
M	Mobility of solute
i_n	Current density
ε_{ij}	Strain tensor
σ_{ij}	Stress tensor
E	Elasticity modulus
$E(D)$	Young's modulus of damaged material
ν	Poisson's ratio
δ_{ij}	Kronecher symbol
α	Thermal expansion coefficient
$D(x,t)$	Diffusion induced stress
$P(x,t)$	Surface load
$\bar{\sigma}_{ij}^d(x,t)$	Linear-elastic solution of diffusion induced stress
$\bar{\sigma}_{ij}^p(x,t)$	Linear-elastic solution of surface load
$\bar{\rho}_{ij}$	Constant residual stress field
ρ_{ij}^r	Variation of residual stress
λ_{UB}^S	Multiplier of upper bound shakedown limit
λ_{LB}^S	Multiplier of lower bound shakedown limit
σ_{y0}	Yield strength of undamaged material
$\sigma_y(D)$	Yield strength of damaged material
$\bar{\varepsilon}$	Effective strain rate
$\dot{\varepsilon}_{ij}$	Kinematically admissible strain rate

D	Generalized damage
D_m	Mechanical damage
D_e	Cyclic charge-discharge experiment indicated damage
$\Delta\varepsilon_p$	Plastic strain range
σ_a	Stress amplitude
ε_{pa}	Plastic strain amplitude
n'	Strain hardening exponent
$\dot{\varepsilon}_f$	Fatigue ductility coefficient
c'	Fatigue ductility exponent
C_{e0}	Battery capacity before cycling
C_e	Damage affected battery capacity
W_p	Plastic hysteresis energy
W_s	Fatigue toughness

Acronyms

LIB	Lithium ion battery
DIS	Diffusion induced stress
SEI	Solid electrolyte interface
EPP	Elastic perfect plastic
LMM	Linear matching method
DSCA	Direct steady cycle analysis
SBS	Step-by-step analysis
XFEM	Extended finite element method
CDM	Continuum damage mechanics
RVE	Representative volume element
SOC	State of charge
DOC	Depth of discharge
SEM	Scanning electron microscopy
LEFM	Linear elastic fracture mechanics

This page intentionally left blank

Chapter 1

Introduction

1.1 Research background

The development of human society is inseparable from a variety of energy materials and technologies. With the rapid development of global industrialization, traditional energy sources such as oil, natural gas and other fossil fuels are not only non-renewable, but also cause great harm to the environment. Energy crisis and environmental pollution gradually become the great challenges that humanity needs to face and solve. Therefore, energy conservation, pollution reduction and the development of clean energy have become the focus of attention in recent years. The energy structure should be changed to the form of "clean energy mainly, fossil energy as supplement", and the use of renewable clean energy gradually replaces the traditional fossil fuel.

More than 60% of the air pollution problem is caused by the exhaust emissions of traditional fuel vehicles. While new energy vehicles have the advantages of low carbon emission and low operating cost. It has become the focus of research objects in the world, and has received unprecedented policy support from governments of various countries. Lithium-ion battery (LIB) is the most promising candidate for power supply of new energy vehicles at the present stage [1-1]. Large car companies in the world, such as Tesla, Mercedes-Benz, General Motors, Toyota, Volkswagen and so on, have joined the development teams of high-performance power lithium ion batteries. In 1958, Harris [1-2] firstly proposed the use of a lithium battery. However, as lithium metal is used as the negative electrode, lithium ion deposition in the process of lithium ion deintercalation makes it easy to generate lithium dendrite, which leads to internal short circuiting, thermal runaway and other safety risks. Hence, the development of lithium ion batteries was slow in the early stage. Hereafter, Murphy et al. [1-3] presented that the lithium metal used as the negative electrode could be replaced by an embedded material, so that the lithium ions in the whole system could be cyclically embedded and released. In 1980, Goodenough [1-4] first reported the application of lithium cobaltate with layered structure as positive electrode material in lithium ion batteries. In 1990, Japan's Sony company successfully developed a lithium battery system with lithium cobaltate as the positive electrode and graphite as the negative electrode [1-5]. Introducing this product to the market opened the curtain of commercialization of lithium ion batteries.

Lithium-ion batteries mainly consist of positive and negative materials that can be embedded in lithium ions, electrolytes that have a good ability to transport lithium ions, and membranes that block electrons and only allow lithium ions to pass through. The principle of charging and discharging is

shown in Fig 1.1 [1-6]. For the charging process, oxidation reaction first occurs at the positive electrode and the lithium ions are removed from the inside of the material. The crystal lattice shrinks to a certain extent, but the overall structure of the material remains stable. An electron is lost and the lithium ions move to the electrolyte. Then, under the action of an external circuit, the lithium ions move to the negative electrode material through the electrolyte. The lithium ions embed into the negative electrode and reduction reaction then happens. The lost electron from the positive electrode is transported through an external circuit to the negative electrode to keep charge balance. During the discharging process, the lithium ions leave the negative electrode and are transferred back to the lattice of the positive electrode through the electrolyte, so that the material structure is restored. Meanwhile, the transition metal ions in the positive electrode are reduced and an electron is obtained from the external circuit.

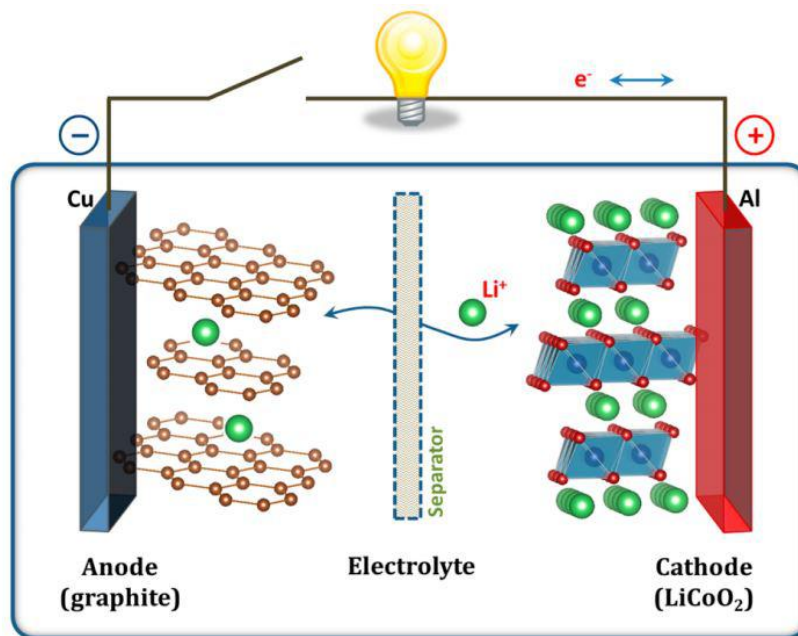


Fig 1. 1 The schematic illustration of charging/discharging principle for Li-ion battery. [1-6]

During the process of Li-ion intercalation into and deintercalation from electrode material, the inhomogeneous distribution of Li-ion concentration from kinetic limitation, together with solid state diffusion of Li-ions will generate evident diffusion induced stress (DIS) [1-7, 1-8] inside electrode material, which is an inherent phenomenon accompanying with lithiation/delithiation process, as shown in Fig 1.2. The stress would further trigger various types of mechanical failure behaviours such as cracking inside active material [1-9, 1-10], debonding behaviour between active layer and current collector [1-11, 1-12], cyclic plasticity behaviour [1-13, 1-14], creep and aging of porous polymer diaphragm [1-15, 1-16], and so on. Such mechanical instabilities work as intrinsic drawbacks and have been demonstrated to cyclically cut down the electrochemical capacity, which gradually renders the electrode unsuitable for subsequent cycling [1-7]. Therefore, the stress generation and the

corresponding mechanical-failure behaviours come into being the hot research issues in developing stable Li-ion batteries.

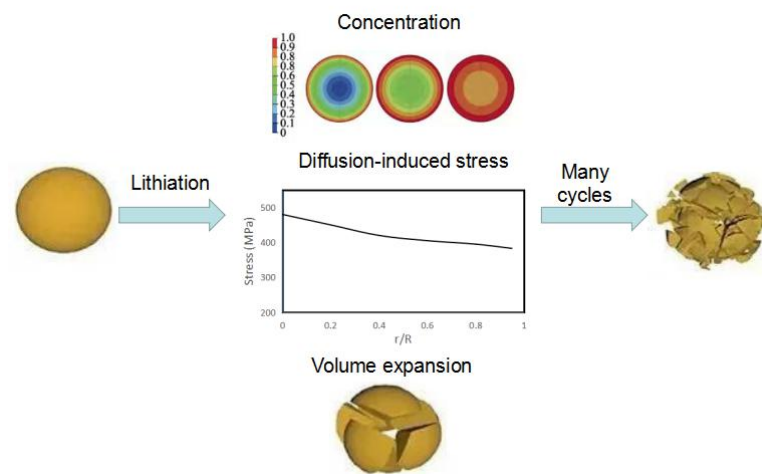


Fig 1. 2 The schematic diagram of lithiation caused DIS and mechanical fracture

It is also reported that, the stress evolution is more significant under high electrochemical cycling rates [1-9, 1-17], which would eventually limit the rate capability of batteries [1-7]. Global efforts have indicated that stress and deformation are bottleneck issues restraining the boosting of capacity for both cathode and anode. For the common cathode materials, phase transformation, lattice change related stress and lattice instability will reduce the practical capacity to only half of the theoretical capacity [1-7, 1-18, 1-19]. For the common anode materials, such like Si, Al and Sn, it is evident that the lithiation/delithiation caused swelling/shrinking reduce the capacity and make the cyclability weakened almost from the initial cycles [1-20, 1-21]. In addition, mechanical disintegrity also hinders electronic conduction and rises ohmic resistance, which may lead to major safety accidents [1-22].

Recently, the development and application of solid state electrolyte batteries have been widely sought after, as the solid state electrolyte is assumed to be able to solve the inflammability issue of traditional liquid electrolyte and also enhance the energy density. While, mechanical degradation comes into being a more problematic issue for this promising energy storage device [1-23]. It is predictable that the usage of unpliant solid state electrolyte would impose more significant mechanical constraints during the lithiation/delithiation deformation, comparing with that of compliant liquid electrolyte [1-24]. Hence, more significant stress generation and fracture behaviour tend to appear at the electrode, electrode/electrolyte interface and even solid electrolyte.

All in all, maintaining mechanical stability appears to be a key topic in the development of high-performance battery electrode and the mechanics perspective is accessible to provide solid theoretical support for a comprehensive understanding of electrode failure.

1.2 Objectives of the thesis

Serving as the promising energy source system, the inherent operation mechanism caused diffusion-induced stress is inevitable for the lithium-ion battery electrode, and the mechanical instability during the lithiation/delithiation is thought to result in irreversible capacity loss and unacceptable cyclability.

Upon electrochemical condition, the first issue required to be figured out is the interaction between diffusion behaviour and stress generation. In addition, the obtained stress field should also be easily accessible to engage the subsequent mechanical integrity assessment. With the consideration of cyclic operation condition, the second is about evaluating the cyclic plasticity failure of battery electrode under the action of electrochemical loads. Furthermore, the failure of battery electrode appears to be a continuous process with the proceeding of cycles. Describing this process as a fatigue damage behaviour makes it available to provide failure details. However, the oxide electrode material is made from slurry by the drying process, and its physical characterization makes the fatigue evaluation method based on metallic material no longer applicable. Besides, how to construct the relationship between electrochemical performance degradation and mechanical failure, and how to obtain the robust fatigue models which can simulate typical electrode degradation trends are required to be clarified.

By taking into account the above issues, this thesis focuses on the listed topics:

1. Developing and testing user subroutines to implement the coupled diffusion-stress analysis, based on the commercial finite element platform ABAQUS. Such approaches could increase the feasibility of mechanical evaluation for battery electrode under electrochemical circumstances.

2. Delivering cyclic plasticity assessment of electrode experiencing electrochemical loads with employing the Linear Matching Method (LMM). New insights into the understanding of cyclic failure mechanisms of battery electrode will be presented.

3. Proposing fatigue damage models being appropriate for battery electrode. Establishing the correlation between electrochemical performance degradation and fatigue damage accumulation. Conducting fatigue damage modeling of battery electrode under different material levels.

1.3 Methodology

The methodologies used in this thesis for different analysis problems are summarized as following:

1. For coupled diffusion-stress analysis, the diffusion driven method and chemical potential

driven method are respectively used as the methodologies.

2. For cracking analysis, the ABAQUS extended finite element method (XFEM) is employed.

3. For cyclic plasticity assessment, the Linear Matching Method (LMM) and step by step analysis are used.

4. For fatigue damage analysis, the Manson-coffin strain based fatigue model and energy based fatigue model are respectively employed as damage models.

1.4 Outline of the thesis

The main contents of each chapter are listed as following:

Chapter 2 presents the theoretical background of diffusion-induced stress (DIS) and the different mechanical failure behaviours of battery electrode under DIS. The mechanical related failures of battery electrode under the micro-meso-macro scales are summarized in step by step order.

Chapter 3 provides the implementation method of diffusion driven approach and chemical potential driven approach for conducting coupled diffusion-stress analysis based on the commercial finite element software ABAQUS. The diffusion-induced stress of primary electrode particle is evaluated. Based on the stress field, the crack initiation, propagation and fracture analyses are performed with employing the ABAQUS extended finite element method (XFEM).

Chapter 4 conducts the shakedown, reverse plasticity and ratcheting assessments of primary electrode particle under electrochemical loads by using the Linear Matching Method (LMM). The essential numerical procedure of the LMM are provided and the cyclic plasticity failure boundaries are established for preventing electrode particle from plastic collapse.

Chapter 5 proposes a fatigue damage assessment strategy to evaluate the continuous mechanical degradation of battery electrode. The numerical procedure is built on the theory of continuum damage mechanics and takes the coupling effect between ion diffusion, stress formation as well as fatigue damage affected stress-strain response into account. With proposing the relevance assumption between electrochemical degradation and mechanical fatigue damage, the charging-discharging experiments at different C-rate conditions are conducted to parameterize and verify the fatigue damage model .

Chapter 6 uses an energy based fatigue damage model to simulate different degradation trends of electrode under electrochemical conditions. The non-linear fatigue damage of the macroscopic electrode plate is evaluated by using the presented model. Besides, the fatigue degradation of the

microscopic representative volume element (RVE) model, considering different particle shapes and relative locations, is also investigated.

Chapter 7 provides the conclusions of main research works of the thesis and the recommendations for future work.

1.5 References

- [1-1] M. Armand, J.M. Tarascon. Building better batteries. *Nature*, 2008, 451 (7179): 652-657.
- [1-2] W.V. Schalkwijk, B. Scrosati. *Advances in Lithium—Ion Batteries*. New York: Kluwer Academic, 2002: 1-5.
- [1-3] B. Murphy. *Materials for advanced batteries*. NATO Conference Series. US: Springer, 1980: 361-374.
- [1-4] K. Mizushima, P. Jones, P. Wiseman. Li_xCoO_2 ($0 < x < 1$): A new cathode material for batteries of high energy density[J]. *Materials Research Bulletin*, 1980, 15(6): 783-789.
- [1-5] T. Nagaura, K. Tazawa. Lithium ion rechargeable battery. *Progress in Batteries and Solar Cells*, 1990, 9(3): 12-20.
- [1-6] J. B. Goodenough, K. S. Park. The Li-ion rechargeable battery: a perspective. *Journal of the American Chemical Society*, 2013, 135(4): 1167-1176.
- [1-7] A. Mukhopadhyay, B.W. Sheldon. Deformation and stress in electrode materials for Li-ion batteries. *Progress in Materials Science*, 2014, 63, 58-116.
- [1-8] L. Weng, J. Zhou, R. Cai. Analytical model of Li-ion diffusion-induced stress in nanowire and negative Poisson's ratio electrode under different operations. *International Journal of Mechanical Sciences*, 2018, 141:245-261.
- [1-9] D. Wang, X. Wu, Z. Wang, L. Chen. Cracking causing cyclic instability of LiFePO_4 cathode material. *Journal of Power Sources*, 2005, 140: 125-128.
- [1-10] P. Yan, J. Zheng, M. Gu, J. Xiao, J. Zhang, C. Wang. Intragranular cracking as a critical barrier for high-voltage usage of layer-structured cathode for lithium-ion batteries. *Nature Communications*, 2017, 8: 14101.
- [1-11] M. Liu. Finite element analysis of lithiation-induced decohesion of a silicon thin film adhesively bonded to a rigid substrate under potentiostatic operation. *International Journal of Solids and Structures*, 2015, 67: 263-271.
- [1-12] M. Liu. Finite element analysis of lithium insertion-induced expansion of a silicon thin film on a rigid substrate under potentiostatic operation. *Journal of Power Sources*, 2015, 275: 760-768.

- [1-13] H. Haftbaradaran. Ratcheting of silicon island electrodes on substrate due to cyclic intercalation. *Applied Physics Letters*, 2012, 100 (12): 121907.
- [1-14] Y. Song. Reducing diffusion induced stress in planar electrodes by plastic shakedown and cyclic plasticity of current collector. *Journal of Power Sources*, 2014, 263: 22-28.
- [1-15] C.T. Love. Thermomechanical analysis and durability of commercial micro-porous polymer Li-ion battery separators. *Journal of Power Sources*, 2011, 196 (5): 2905-2912
- [1-16] C. Peabody, C.B. Arnold. The role of mechanically induced separator creep in lithium-ion battery capacity fade. *Journal of Power Sources*, 2011, 196 (19): 8147-8153
- [1-17] J. Christensen, J. Newman. Stress generation and fracture in lithium insertion materials. *Journal of Solid State Electrochemistry*, 2006, 10, 293.
- [1-18] S. Venkatraman, V. Subramanian, S. Gopu Kumar, N.G. Renganathan, N. Muniyandi. Capacity of layered cathode materials for lithium-ion batteries – a theoretical study and experimental evaluation. *Electrochemistry Communication*, 2000, 2:18.
- [1-19] Y.J. Park, J.G. Kim, M.K. Kim, H.G. Kim, H.T. Chung, Y. Park. Electrochemical properties of LiMn₂O₄ thin films: suggestion of factors for excellent rechargeability. *Journal of Power Sources*, 2000, 87:69
- [1-20] J. Besenhard, M. Winter. Advances in battery technology: rechargeable magnesium batteries and novel negative-electrode materials for lithium ion batteries. *ChemPhysChem*, 2002, 3:155.
- [1-21] W.J. Zhang. A review of the electrochemical performance of alloy anodes for lithium-ion batteries. *Journal of Power Sources*, 2011, 196:13.
- [1-22] J. Cannarella, C.B. Arnold. Stress Evolution and Capacity Fade in Constrained Lithium-Ion Pouch Cells. *Journal of Power Sources*, 2014, 245: 745–751.
- [1-23] J. A. Lewis, J. Tippens, F. J. Q. Cortes, M. T. McDowell. Chemo-mechanical challenges in solid-state batteries. *Trends in Chemistry*, 2019, 1(9): 845-857.
- [1-24] H. Tian, A. Chakraborty, A. Talin, P. Eisenlohr, Y. Qi. Evaluation of The Electrochemo-Mechanically Induced Stress in All-Solid-State Li-Ion Batteries. *Journal of The Electrochemical Society*, 2020, 167: 090541.

Chapter 2

Mechanical integrity of Li-ion battery electrode upon electrochemical condition

2.1 Introduction

The safety, reliability and cyclic life have always been the crucial topics for the application of Li-ion battery as the energy storage device. With the proceeding of cycles, the aging phenomenon of lithium-ion battery, i.e. capacity attenuation and impedance change, has been one of the key issues faced by industrial community and academia. Identifying and detecting the underlying failure mechanisms will be conducive to provide instructive information and prolong cyclic life of lithium-ion battery.

The reasons for the aging of lithium-ion batteries are complex. The following includes the primary mechanisms responsible for the reported aging failures.

- The formation of lithium dendrites:

Lithium dendrite metal is formed when lithium ions are reduced during charging. The dendrite growth of lithium is a fundamental problem affecting the safety and stability of lithium ion batteries [2-1, 2-2]. It could introduce the instability factor to the interface between electrode and electrolyte during the cycling of lithium ion battery, which will destroy the solid electrolyte interface (SEI) film. The growth of lithium dendrites will continue to consume electrolyte and result in the irreversible deposition of lithium metal, leading to low coulomb efficiency. In addition, the formation of lithium dendrites can even puncture the membrane and induce short connections inside the lithium ion battery as shown in Fig 2.1, which could result in the thermal runaway and explosion of the battery.

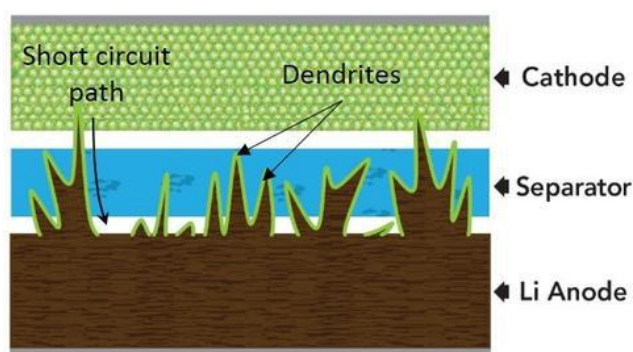


Fig 2. 1 Dendrite growth results in puncturation and short connections [2-3]

- The formation and growth of solid electrolyte interphase (SEI)

For the first charging-discharging cycle, a small amount of polar aprotic solvent in the electrolyte will undergo a reduction reaction after obtaining some electrons, and react with lithium ions to form an interface film [2-4]. SEI is normally formed at the interface between the electrolyte and electrode, as shown in Fig 2.2. The continuous growth of SEI would consume partial lithium ions, which leads to irreversible capacity loss and a decrease in charging-discharging efficiency.

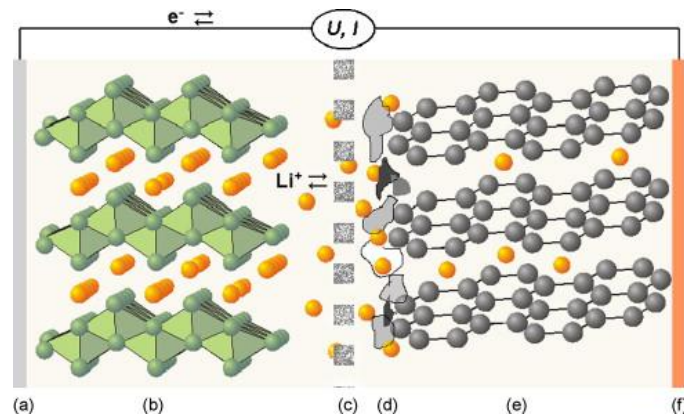


Fig 2. 2 Schematic illustration of the position of SEI, where d represents the formed SEI layer between electrolyte c and active material e [2-4]

- Dissolution of active substances

The inherent solubility of electrode material in electrolyte, the erosion of active substances due to the formation of acidic substances in the electrolyte, the conversion of some metal ions into soluble salts and dissolution into electrolyte during the electrochemical process, would all result in the dissolution of active substances [2-5].

- Collector corrosion

The oxidation decomposition of electrolyte on the surface of electrode and organic electrolyte would lead to collector corrosion. Once the corrosion of the collector occurs, the electronic conductivity between the collector and the electrode active material will be weakened. The contact resistance between the collector and the electrode will aggrandize significantly, which inevitably influence the cycle efficiency, specific capacity and life of the battery [2-6].

- Thermal runaway

Thermal runaway of a battery refers to the accumulative enhancement of temperature and battery current when the battery is charged at constant pressure. The rising of temperature and exothermic reaction rate is mutually boosted, which would further trigger the explosion and fire [2-7, 2-8]. Besides, the discontinuity of configuration and material may cause thermal gradient and further thermal stress within the battery, which would contribute mechanical damage to the structure.

- Mechanical failure

During the electrochemical cycle, the lithium ions insert into or extract from cathode/anode material, and lead to the deformation as well as the generation of a sort of diffusion induced stress (DIS). Various mechanical damages at different scales would be produced under this stress caused by lithium ion reaction and solid phase diffusion.

Although, mechanical factors are not the only reasons leading to lithium ion battery aging, its influence is pronounced and inevitable. Finally, it would pose a threat to the safety and stability of the whole battery and battery pack. Evidence has demonstrated that these mechanical damages will cause the electrochemical performance of lithium ion batteries to degrade to varying degrees. Hence, the mechanical integrity of electrode comes into being a non trivial issue in the development of lithium ion batteries.

The fundamentals of diffusion induced stress and the corresponding mechanical failure behaviours of electrode have attracted global research efforts conducted to date. However, the diversity of researches makes it not easy to have a logic impression of the features of DIS and potential failure mechanisms under different configuration scales. This chapter presents an essential insight into concepts and mechanisms on the mechanical integrity of battery electrode upon electrochemical condition. The formation mechanisms, features, calculation methods and mitigation strategies of diffusion induced stress of electrode at macro-meco-micro scale are provided. The primary DIS caused mechanical failure behaviours such as cracking, cyclic plasticity behaviours, debonding and buckling are described for different electrode configurations under different scales. The fundamental aim of this chapter is to provide a comprehensive understanding of mechanical disintegrity of electrode subjected to electrochemical loads.

2.2 Diffusion induced stress

2.2.1 Formation mechanism of DIS

In general, the major reasons of the production of DIS during lithiation-delithiation process can be concluded as three mechanisms [1-7]. The first mechanism is the physical constraint on the dimensional changes in active materials. The intercalation and deintercalation of Li-ion to host lattices of the active electrode material will cause the variation of lattice parameters or the formation of new crystalline/amorphous phases. The primary consequence of this phenomenon is morphological change. On different scales, the neighboring micro-structures, the current collector and the geometry of the cell will restrain the dimensional change, as shown in Fig 2.3 (a) and (b). Hence, the stress will be generated with the physical constraint during the lithiation-delithiation process.

The second mechanism is the contact action between micro-structures inside the active electrode material. Within the lithiation process, the micro-structures of active electrode material will expand due to the insertion of Li-ion. It makes the structure contact and causes the pronounced contact stress, as presented in Fig 2.3 (c).

The third mechanism is the mismatch between crystalline phases and Li-concentration gradient. The insertion and removal of Li-ion may cause the phase transformation of the host material. The Li-ion concentration may vary at different positions of the host material due to the diffusion limitations such as diffusivity, structural feature and electrochemical condition. Hence, the neighboring areas in the host material may share different crystal phases and molar volumes. The contact of these areas during the intercalation/deintercalation process will prompt the development of mismatch induced stress.

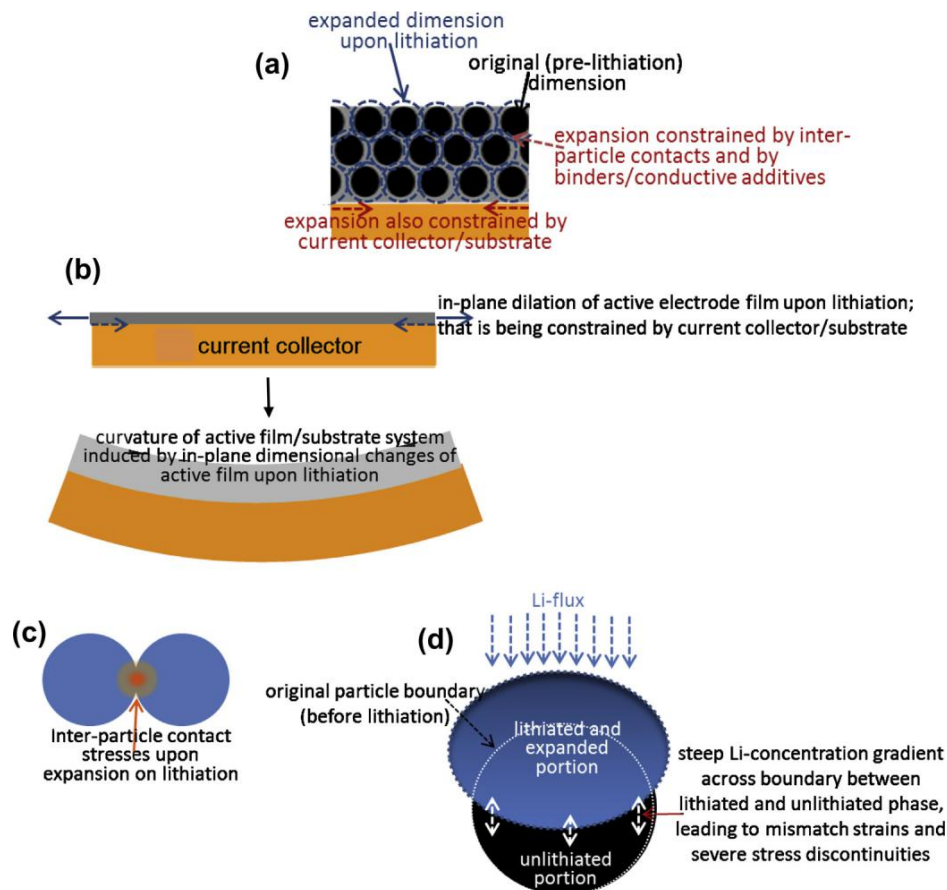


Fig 2. 3 Schematic diagrams of (a) constraints caused by neighboring electrode particles and current collector during the expansion process, (b) curvature deformation caused by constraint effect of current collector to active film, (c) contact stress between neighboring particles within lithiation phase, (d) mismatch induced stress and strain under phase transformation effect [1-7].

2.2.2 DIS at different scales

The battery electrode appears to be a continuum and the representative configurations under different scales have their own characteristics, as shown in Fig 2.4 [2-9]. On the microscopic scale, the individual particle works as the most common configuration and undertakes the basic ion interaction task. Moving forward to meco scale, many particles and electrolyte occupied porous volume form a representative volume element (RVE), which makes it available to investigate the discrete distribution feature of the composite structure and material. In macroscopic scale, the intuitionistic electrode structure is always produced to be a thin film, which is not only able to ensure stable and fast electrochemical response during charging-discharging process, but also can be applied for miniaturized or portable electronic devices [2-10]. For different electrode configurations at different scales, the features, calculation methods and mitigation strategies of diffusion induced stress vary a lot. To shed light on these questions, global efforts have been dedicated to study it over the last few decades.

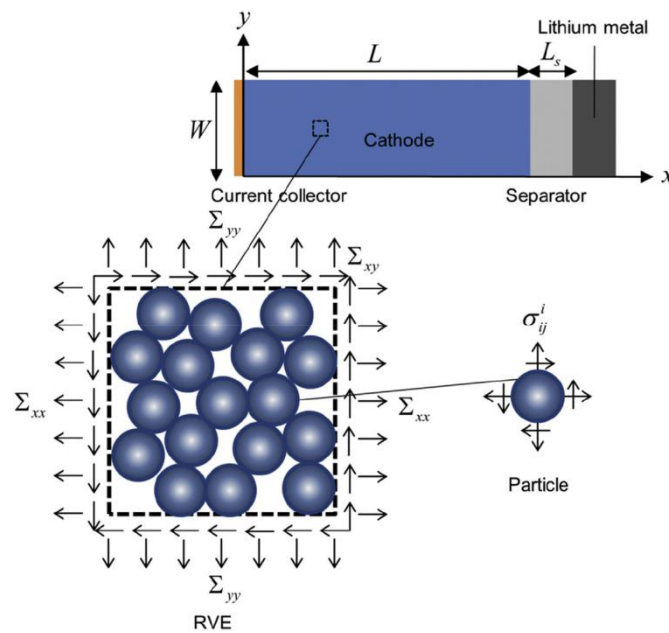


Fig 2. 4 Schematic illustrations of electrode in different scales. The individual particle represents a structural configuration on microscale. Representative volume element is in mesoscale and consists of particles and electrolyte. Electrode plate is the intuitionistic structure in macroscale [2-9].

- Microscale

Particle, as shown in Fig 2.5 (a) [2-11], is the most common nano-architecture for prevalent electrode materials in microscopic scale. Considerable efforts have focused on the optimization of the shape and size of electrode structure, and it is reported that the particle configuration is not vulnerable to fail to compare with other micro configurations. It is believed that batteries with micro particle

configuration will hold better cyclability [2-12]. Global efforts have been dedicated to investigate the evolution features of DIS within particle structure and how to mitigate this stress for maintaining mechanical integrity.

Zhang and co-workers [2-13] systematically researched the intercalation-induced stress of LiMn_2O_4 ellipsoidal electrode particles by using the finite element method, and further verified the results via the finite difference method. It is suggested that, particle size, current density and ellipsoid aspect ratio are three primary ingredients affecting the intercalation induced stress. Reducing the applied current density, synthesizing particles with smaller sizes and larger aspect ratios are conducive to alleviate the stress. Korsunsky and co-workers [2-14] have established an expression of Li-ion concentration in a function of time τ and coordinate r , and derived a closed form formulae of DIS for spherical particle, as shown in Eq. 2.1-2.4. m is a power law parameter and γ is a material inherent parameter as strain value. The diffusion behaviour and stress generation are considered based on the sequentially coupled treatment. This work makes it efficient and effective to obtain the concentration and DIS of one point within a spherical particle only by importing time and distance from the particle center. These expressions provide a robust basis in the evaluation of stress caused damage to battery electrode.

$$m = 0.655\tau^{-0.546} \quad (2.1)$$

$$c(r, t) = \left(\frac{r}{a}\right)^m \quad (2.2)$$

$$\sigma_\theta(r) = \frac{(2 - (m + 2)\left(\frac{r}{a}\right)^m)}{(m + 3)} \frac{E\gamma}{(1 - \nu)} \quad (2.3)$$

$$\sigma_r(r) = -\frac{2\left(\left(\frac{r}{a}\right)^m - 1\right)}{(m + 3)} \frac{E\gamma}{(1 - \nu)} \quad (2.4)$$

Christensen and Newman [1-17] rose up a fully coupled mathematical model to calculate concentration and stress for the spherical electrode particle within the lithiation and delithiation process. With the fully coupled model, the time at which the maximum stress occurs is influenced not only by the imposed electrochemical potential but also by the diffusion behaviour of the host material. The model is defended to be able to obtain high precision solutions, but it includes 11 governing equations and 11 variables, which may influence the applicability and robustness of the model.

According to some experimental observations [2-15, 2-16], the transition within the host material possessing inhomogeneous concentration may be discontinued and a sharp reaction front would be formed at the interface. This partially lithiated/delithiated process is considered to be the two-phase electrochemical reaction lithiation/delithiation. Unlike the single-phase lithiation/delithiation process

[2-17], the sharp change of Li concentration at the interface introduces considerable volume strain inhomogeneity as well as stress discontinuity. Ma's research team [2-17] defined a transition layer inserted between the inner crystalline Si and outer amorphous Li_xSi . The relation between diffusion induced stress and radius of the transition layer was analytically derived. It is suggested that, for the thinner transition layer, the evolution of DIS presents a two-phase feature as the hoop stress transfers from compressive state to tensile state in the surface layer. On the contrary, for the dense transition layer, the hoop stress keeps compressive of a single-phase. It can be expected that, the stress discontinuity at the interface is affected by the ratio of the concentrations on the two phases and the rising of this ratio promotes the stress discontinuity [2-18]. Phase transformation caused by the variation of Li-ion concentration may also contribute to the change of material properties, and the difference of two-phase material properties also facilitates the interfacial stress discontinuity. In conclusion, the concentration difference in different material phases and phase transformation caused change of material properties can both lead to stress discontinuity at phase interface. For reducing this stress discontinuity, it can be greatly alleviated when the products of partial molar volume and concentration of two-phase materials are equal, which indicates that the swelling of two phases shares the same tendency. Besides, for a given Young's modulus ratio, there exists a certain partial molar volume ratio, which could mitigate the discontinuity effect to the minimum [2-18]. Undoubtedly, phase transformation caused sharp concentration change at phase interface will further result in stress discontinuity, which should be considered to avoid electrode degradation.

Generally, there exist two modes of electrochemical boundary conditions, known as potentiostatic condition and galvanostatic condition. Potentiostatic control refers to a charging-discharging operation whereby the electrode is maintained at a constant voltage and the electrode surface concentration is also assumed to be constant. While for the galvanostatic control, the applied current and diffusion flux at the surface are set to be constant. Cheng and Verbrugge [2-19] have studied the development of diffusion-induced stress in spherical particles under potentiostatic and galvanostatic conditions by deriving analytical expressions. It is concluded that, under potentiostatic condition, both of the radial and tangential stresses follow an increasing-decreasing trend against time. On the contrary, for the galvanostatic condition, the radial and tangential stresses would rise to a steady value, which is then independent of time. A phase field model [2-20] is developed to investigate the DIS of two-phase lithiation process under potentiostatic and galvanostatic controls. The lithiation rate of potentiostatic operation gradually declines with the proceeding of cycles, whereas that of galvanostatic control approximately maintains stability. While, different charging modes rarely affect tangential stress on particle surface within the two-phase lithiation process.

The Li-ion diffusion caused dislocation is an interesting mechanism, which has been proved to influence the diffusion induced stress in spherical electrode particle [2-21, 2-22]. The research work

shows that [2-21], comparing with the situation without considering dislocation, the tangential tensile stress and radial tensile stress inside electrode particle are relatively small when the dislocation is considered. It is also claimed that the dislocation can reduce tensile stress and change the stress state from tensile to compressive, which is regarded as a novel way of the inhibition of crack initiation [2-22].

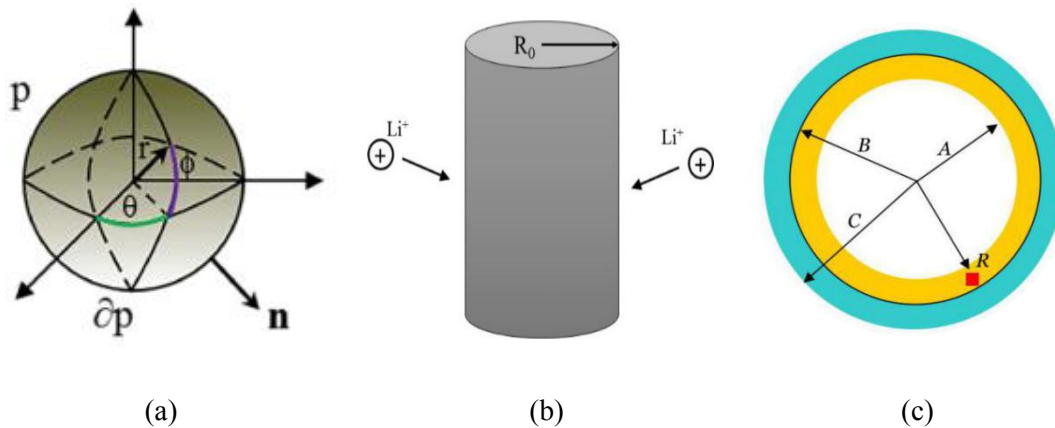


Fig 2. 5 Schematic illustrations of (a) a spherical particle [2-11], (b) nanowire electrode [2-23], (c) a hollow core-shell electrode [2-28]

Another common structure in microscopic scale is nanowire electrode shown in Fig 2.5 (b) [2-23], which is believed to be able to endure large strain without pulverization and better at electronic conduction. Chen [2-24] presented that the polycrystalline CuO nanowire has a high reversible capacity and satisfactory electrochemical performance, which makes it available to be used as the anode of lithium ion batteries. It is also accessible to obtain the structure, morphology and electrochemical performance of the nanowire by using a series of XRD, SEM, TEM, HRTEM, CV and galvanostatic methods.

The surface effect is supposed to influence the electrochemical performance of nanowire-based electrode. Deshpande and co-workers [2-25] established a mathematical model to consider the surface energy with the development of diffusion induced stress of nanowire electrode. It is founded that the tensile stress will be decreased with the consideration of surface effects. Besides, the research also showed that reducing the nanowire radius is able to decrease the diffusion induced stress. Li [2-26] also presented the same conclusion that considering the surface effect is conducive to avoid the mechanical damage for the nanowire electrode. In this research, the electrode is able to possess negative Poisson's ratio by changing the morphology of the nanowire electrode and manufacturing the re-entrant honeycomb podetium electrode. This work has also established the analytical model for calculating the diffusion induced stress of both nanowire electrode and negative Poisson's ratio electrode under galvanostatic condition and potentiostatic condition.

The effect of dislocation mechanic on diffusion-induced stress is also investigated in cylindrical

wire electrode configuration [2-27]. An analytical model has been developed in this work for explaining dislocation mechanic and the results are consistent with the conclusions for spherical particle that the dislocation mechanic is beneficial to decrease tensile stress and prevent crack nucleation.

A hollow core-shell nanostructure is recently developed for battery electrode, as illustrated in Fig 2.5 (c) [2-28]. This design makes the stiff shell separate the inner core electrode and outer electrolyte. In this way, the core can only swell inward and the outward expanding is constrained, which efficiently suppress the repeated SEI formation and shedding. The nanostructure is beneficial to maintain the electrochemical stability as well as electric contact between electrolyte and electrode.

It is founded that [2-28], during lithiation process, the core electrode is in the compressive state in the radial direction and the compressive stress in the core leads to a considerable tensile hoop stress in the stiff shell. While in the delithiation phase, the interface between the core and the stiff shell is in a tensile state, which may lead to the interfacial debonding behaviour. Ref [2-29] presents the analytical solutions for stress components of both electrode core and stiff shell in the cylindrical coordinate system, (r, θ, z) . It indicates that the stress of an arbitrary point in core-shell structure is decided by state of charge (SOC) and the charging rate (N). Yang [2-30] derived the analytical solutions for an elastic hollow cylinder considering both traction free boundary and built-in boundary at one end of the cylinder. The stress state at the end face of the cylinder was detailedly studied within lithiation process, and it was observed that the end face always experiences compressive hoop stress under both traction free boundary and built-in boundary. Li and co-workers [2-31] analytically studied the evolution of concentration and stress of hollow spherical-electrode with the consideration of plastic yielding. Their work concluded that continual plastic yielding is beneficial to ease lithiation caused expansion and also suppress cracking behaviour.

- Mecoscale

For mass-produced electrode, the fabrication process is not easy to guarantee the generation of uniform electrode material. Variations in the local microstructure are expected over the mesoscale, and mesocale variations may affect the macroscopical electrochemical-performance. A few studies have been conducted to investigate the mechanical response of battery electrode in mesoscale.

Wu et al. [2-32] have employed the finite element method to analyse the lithiation and phase transition caused stress of the 3D reconstructed model shown in Fig 2.6. It was founded that only particles in the conductive environment could be lithiated and some isolated particles would not accommodate Li-ion, which may lead to capacity loss. The concave and convex regions would experience the highest DIS. Chen's research team [2-33] employed synchrotron transmission X-ray microscopy tomography to reconstruct the three-dimensional morphologies of the electrode. It showed that the interface between solid electrode and active material tends to experience the

maximum DIS. Besides, saving the space between solid electrode and active material is conducive to adopt the expansion of active material, which can reduce the DIS during lithiation process. It is also available to measure the electrochemical performance of electrode by using the coupled macroscale charging-discharging experiment of coin cell with microscale three-dimensional reconstructed morphology based on the nano-scale X-ray computed tomography data [2-34]. In addition, inhomogeneous structure distribution makes the electrochemical properties of material vary greater, which is also assumed to influence the evolution of diffusion-induced stress.

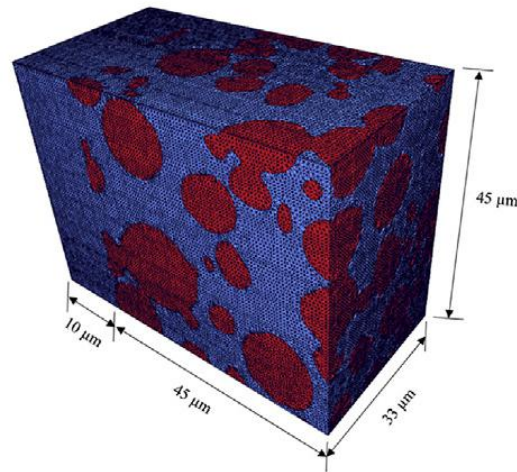


Fig 2. 6 Three-dimensional reconstructed macroscale electrode model [2-32], where red color represents active electrode particle and blue color represents electrolyte

- Macroscale

The diffusion-induced stress in intuitionistic electrode model has also been widely studied. A layered electrode plate, as shown in Fig 2.7 (a) [2-35], is the most common configuration of macroscale lithium-ion battery electrode. Zhang and co-workers [2-35] have established the analytical formulations to calculate the diffusion induced stress of both symmetric electrode and asymmetric active plate-current collector configuration. Their research work has concluded that using a current collector with a smaller elastic modulus and decreasing the thickness of the current collector are conducive for reducing the DIS in active plate. In another work of this research group [2-36], the effects of concentration-dependent Young's modulus on the diffusion behaviour and DIS were systematically studied for the layered electrode model. It was founded that, for more flexible active material, DIS promotes the diffusion behaviour less obvious and the DIS can then be decreased with a less pronounced concentration gradient.

Liu [1-12] has employed the finite element model to investigate the DIS of a Si thin film bonded to a rigid substrate, where the model incorporates plasticity, the interaction between solute diffusion and stress formation, diffusion from the edge surface, and concentration affected material parameters. The diffusion-induced stress within the active plate-current collector electrode can also be reduced by

applying a pre-strain to the structure, according to Ref [2-37]. The stresses at the interface of the active plate-current collector and the upper surface of the active plate are reported to be significantly decreased by using this method. Kang's research team [2-38] recently presented a theoretical model associated with the experimental method to quantitatively measure the diffusion induced stress in the layered electrode. The theoretical model was constructed considering the variation of Young's modulus. Combining with the in situ bending deformation experiment, the diffusion induced stress in Si electrode material was obtained and the maximum compressive stress reached 8.53MPa in their case. The influences of material properties and mechanical constraints on the coupled diffusion-stress process for layered electrode plate are systematically analyzed by Song and co-workers [2-39]. Depending on the material and structure characteristics, this research provides insight into the significance of introducing the stress effect on diffusion behaviour in numerical simulation for electrode material.

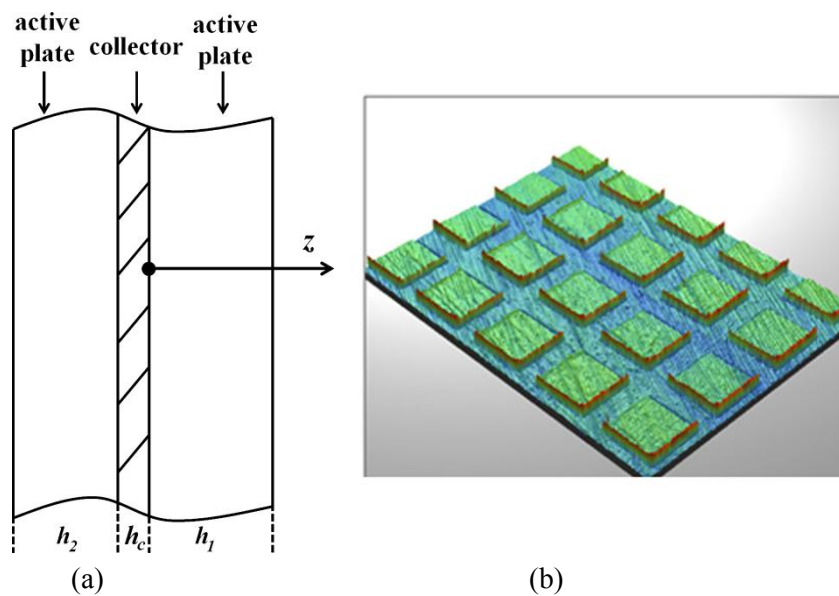


Fig 2. 7 Schematic illustrations of (a) layered active plate-current collector [2-35], (b) island electrode [2-40]

During the charging-discharging cycles, thin film electrode may experience serious in-plane cracking, which poses a major threat to battery performance. To avoid this, the island electrode shown in Fig 2.7 (b) [2-40] is presented, where the electrode thin film is prefabricated into small pieces. The reserved space between electrode pieces makes it available to accommodate the expansion and deformation during lithiation process. The stress can therefore be reduced and cracking can be effectively avoided.

It is reported [2-41] that the in situ measurement of DIS in the patterned electrode can be implemented with the help of multi beam optical stress sensor monitoring the real-time bending. The nominal stress σ_{nom} , average stress σ and measure curvature κ have the following relation:

$$\sigma_{nom} = \frac{B_s h_s^2}{6h_0} \kappa \quad (2.5)$$

$$\sigma = \sigma_{nom} \frac{h_0}{h} \quad (2.6)$$

where B_s and h_s respectively indicate the biaxial modulus and thickness of the current collector. h_0 and h represent the initial thickness and real-time thickness of active material. In this approach, this research work detected the DIS evolution of unpatterned and patterned to different sized silicon electrode. Striking stress difference is experimentally measured for these cases. On the whole, patterning the electrode alleviates the maximum stress to be less than the critical yielding stress.

During the fabrication and synthesis process of the battery electrode, the initial defects appear to be an inescapable issue weakening the mechanical stability [2-42, 2-43]. Based on the finite element method, Chen and Fang' research team [2-44] simulated the development of DIS of several patterned silicon island electrodes with disparate shapes of void defects, shown in Fig 2.8 (a). It was suggested that, the surge slopes of stress are in positive correlation with the higher curvature of void defects, which reveals that patterned island electrode with higher curvature defect is vulnerable to mechanical failure.

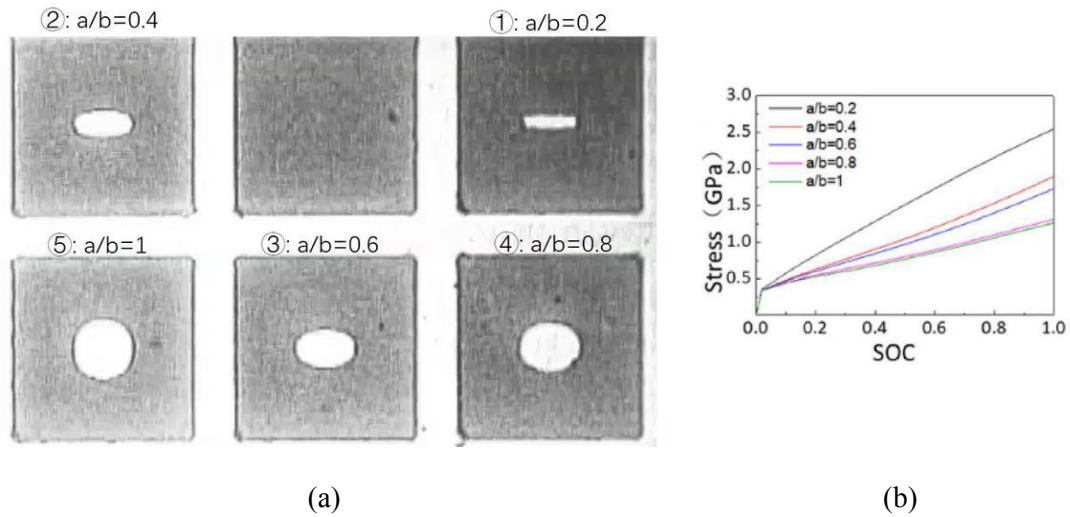


Fig 2. 8 (a) SEM images of the patterned island electrodes with disparate shapes of void defects, (b) the evolution of DIS at the disparate defect tips [2-44]

For the type of material that may produce DIS, it has been proved that the DIS can be generated in both cathode material and anode material. The DIS of common cathode material, such as LiMn_2O_4 [2-13], LiCoO_2 [2-14], NCM [2-32] has been studied by many scholars. Besides, it is also founded that the diffusion-induced stress limits the capacity performance and stability of anode material like Si [2-23, 2-29, 2-40], which is regarded as the next generation anode material due to its high energy

density and huge reserves. Hence, the DIS inside electrode material is an important and common issue in considering the electrode stability.

2.3 Cracking behaviour

Evidences show that the diffusion induced stress generated in the process of lithium intercalation/deintercalation would lead to the formation of tiny cracks in battery electrode, as shown in Fig. 2.9 [1-9], which will further develop and influence the performance of the electrode. From Fig 2.9, it is available to observe that the surface of particles is relatively smooth before electrochemical cycles. With the proceeding of cycles, cracks gradually initiate, propagate and divide the individual particle into small pieces. The newly exposed surface of active material comes into contact with electrolyte, which leads to the degradation of electrochemical performance and stability of electrode. Hence, tremendous research efforts have been taken to understand the cracking behaviour of battery electrode upon electrochemical condition.

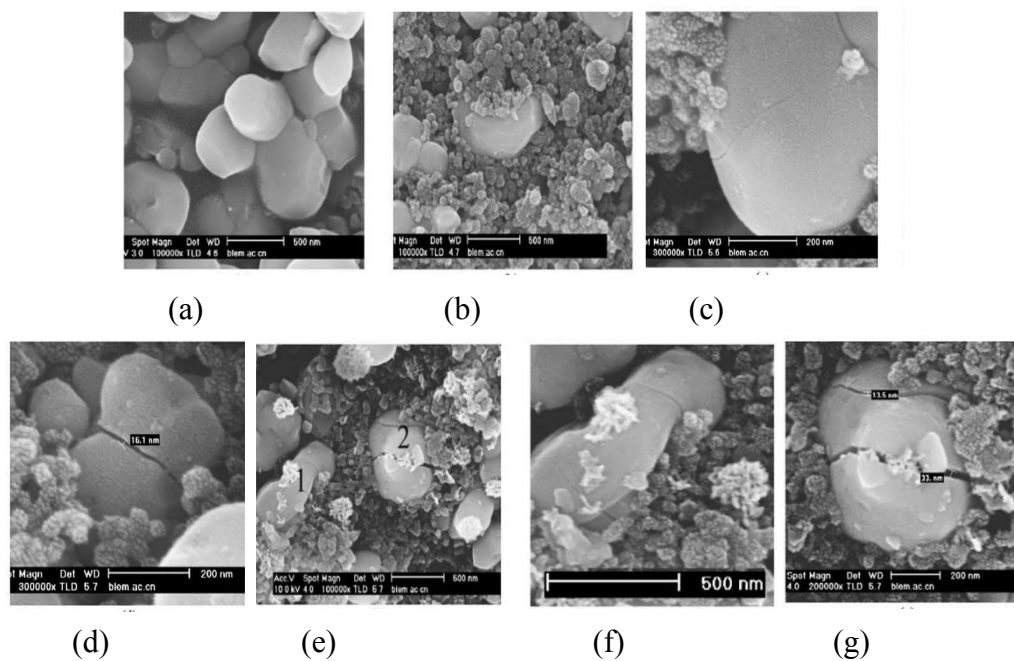


Fig 2. 9 SEM images [1-9] of LiFePO_4 electrode particles (a) prepared sample, (b) electrode before cyclic charging and discharging, (c) electrode after 10 cycles, (d) electrode after 30 cycles, (e) electrode after 60 cycles, (f) particle 1 in (e), (g) particle 2 in (e)

- Microscale

In microscale, Wolfenstine took the lead in concluding that the decreasing of particle size is beneficial for avoiding the occurrence of microcracks in electrode particle from the point of view of energy [2-45]. A critical grain size d_{crit} could be deduced as following Eq (2.7), below which microcrack would not develop.

$$d_{crit} = 32.2\gamma(1-2\nu)^2 V_0^2 E \Delta V^2 \quad (2.7)$$

where V_0 and ΔV respectively represent the initial volume and volume change. γ appears to be surface energy. As a similar job, with using the linear elastic fracture mechanics, Hu and co-workers [2-46] employed a critical energy release rate to ascertain the critical size of particle containing initial cracklike flaws so as to avert further cracking. In this work, the critical size is expressed by

$$d_{crit} = \frac{2\gamma}{Z_{max} E \varepsilon_m^2} \quad (2.8)$$

where Z_{max} and ε_m are dimensionless ratio and mismatch strain, which respectively reflect structural feature and material characteristic.

With the investigation of the growth of a pre-existing dominant flaw in single-particle electrode, Woodford [2-47] came up with the “electrochemical shock” map also based on the linear elastic fracture mechanics, as shown in Fig 2.10 (a). The solid lines from a to e represent the boundaries considering variational fracture toughness, which is anticipated to fluctuate within a reasonable range. This map was plotted to relate the imposing C-rate condition with the critical onset fracture size of electrode particle under galvanostatic charging condition, and it was apparent that the rising of C-rate would decline the admissible grain size. The research output was defended as a material selection tool, that for the given usage condition, the electrode particle could be fabricated and synthesized to be less than a safe size. A more general fracture boundary was presented by Ref [2-48], as shown in Fig 2.10 (b). It is assumed that the DIS is chiefly caused by lithium inhomogeneity, which is ascertained by competition behaviour between diffusion rate and external importing rate. The parameter \mathcal{X} on the X-axis represents this relative rate decided by particle characteristic size L , diffusivity D and diffusion time τ . The parameter Λ on the Y-axis is a relative rate between energy release rate and fracture energy Γ . A small Λ indicates that the elastic energy is less than the required energy to trigger fracture. As a comprehensive parameter, it is available to see that the descent of material stiffness, structural size and a larger fracture energy are conducive to guard against fracture. The above research works are mainly based on the fracture mechanics theory to derive the critical size of crack fracture, which provide an effective and efficient method to quickly judge fracture state. While, considering the cracking development process, it includes initiation, growth, growth arrest, regrowth and fracture phases. A critical fracture size does not reflect the complete development process.

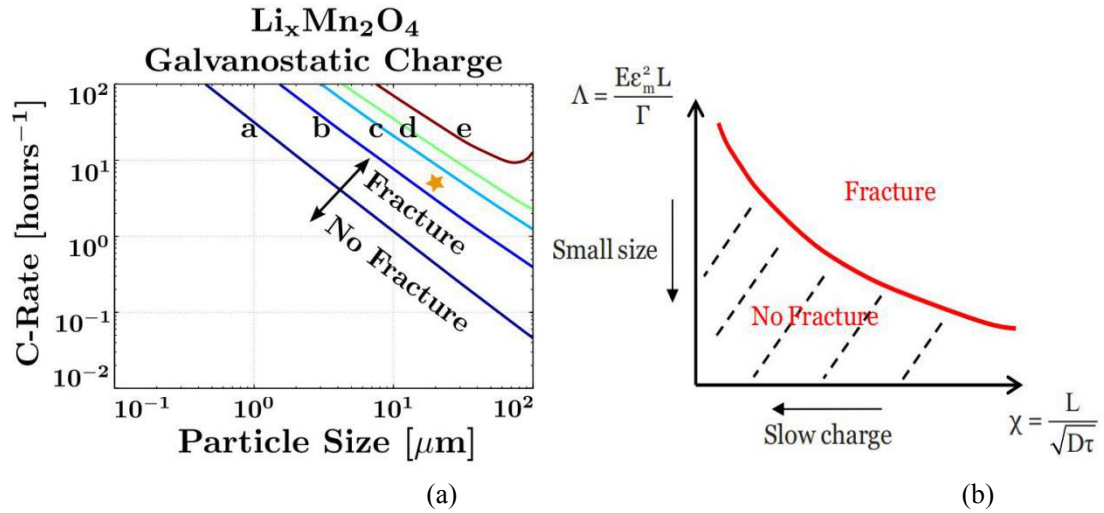


Fig 2. 10 (a) “Electrochemical shock” map for $\text{Li}_x\text{Mn}_2\text{O}_4$ under galvanostatic condition with logarithmic axes [2-47], (b) a general fracture boundary [2-48]

It is also accessible to investigate the crack propagation by using the cohesive zone element [2-49]. Cohesive zone element, characterizing as zero-thickness, is applied on the potential cracking zone and works as traction to neighbouring material with traction-separation law. The most commonly used law is the bilinear traction-separation law, as shown in Fig 2.11(a). Before reaching the damage initiation stress σ_i , the material obeys the linear elastic relation. Once the stress approaches σ_i , degradation begins accompanying by crack initiation. The subsequent damage accumulation and crack propagation simultaneously happen. The element will be completely unloadable as the enclosed energy area reaches the critical failure energy of the material. This method is a more robust tool to study the complete crack development process, and is worth focusing on. By applying the cohesive zone model in finite element analysis, Grantab [2-49] investigated the effects of location and orientation on crack growth in two-dimensional graphite particle model with pre-existing defects. A failure map was summarized with the consideration of the orientation and location of the initial defect, shown in Fig 2.11 (b), where red and blue zones respectively represent safe and unsafe regions. It is suggested that all defects mis-align from radial direction by more than 26° would always be in a stable state and no more propagate. For defects excused less than 26° , it would not grow if the defects are located within 88% of the particle’s radius from the center. As the driving force of crack propagation, high tensile hoop stress is generated at the outer particle.

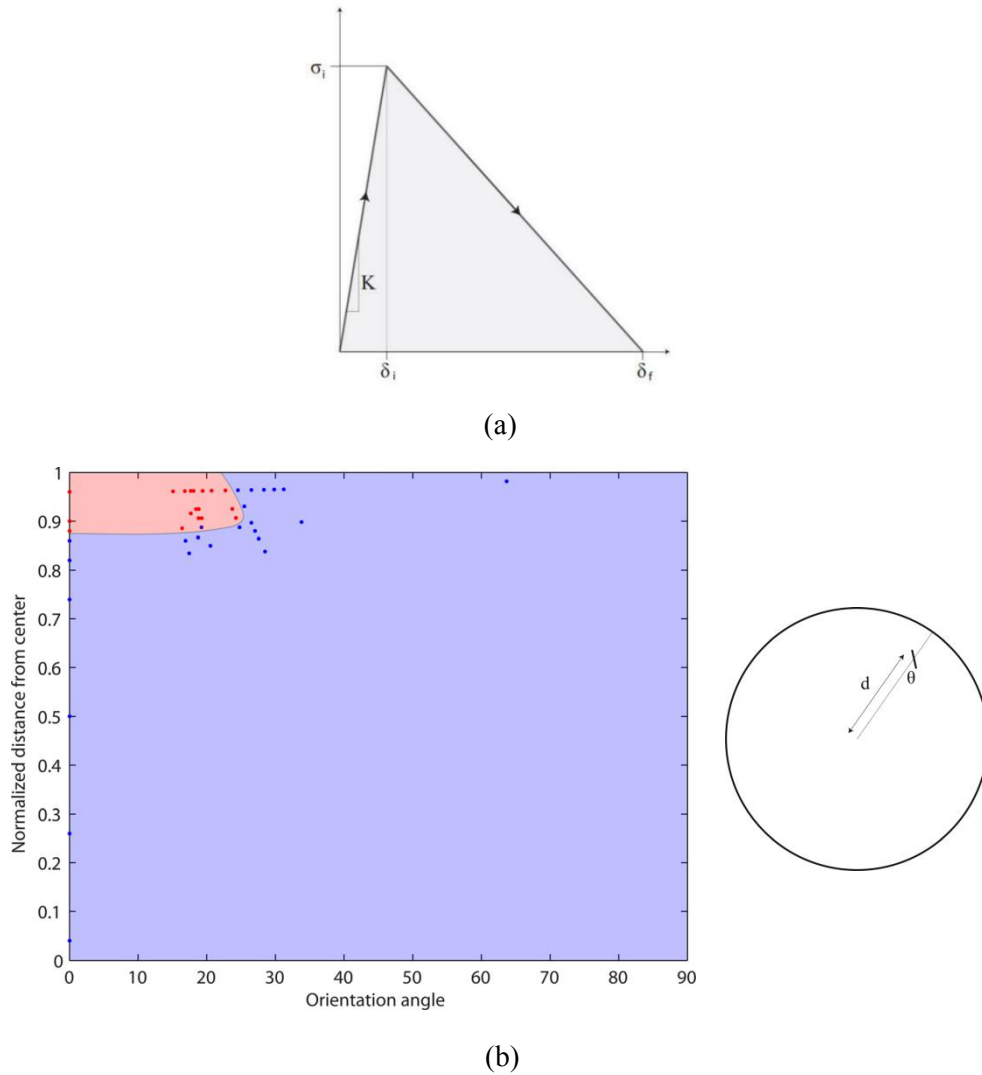


Fig 2. 11 (a) Bilinear traction-separation law [2-49], (b) A failure map considering orientation angle and location of initial defect.

Another common assessment method for modeling crack development is phase field method. The phase field model is a powerful tool for predicting the microstructure evolution during the solid phase transition process based on the thermodynamics and dynamics. The phase field model can simulate crystal growth, solid phase transition, crack evolution, thin film phase transition, ion migration at the interface, etc., but the simulation results lack quantitative comparison with time observations. Klinsmann and co-workers [2-50, 2-51] developed a coupled model considering Li-ion diffusion, diffusion-induced stress and crack growth with the help of phase field method. The established model was applied to research the intragranular crack propagation and fracture of particles during lithiation-delithiation process.

Cheng and Verbrugge [2-52] worked out the analytical solution for total elastic energy in spherical particle caused by diffusion-induced stress. By further combining with the Hasselman crack propagation model, they defined crack propagation criteria for the spherical electrode. Yang [2-53]

regarded the fracture as a pseudoreversible procedure and calculated the average size of fragments generated within lithiation process of spherical particle from an energy viewpoint. Aifantis [2-54] employed fracture mechanics to establish the stability diagrams considering crack growth of various microstructures of electrode material so as to seek for the most effective material configurations.

For the nanowire electrode, Ryu and co-workers [2-55] presented that 300nm is the critical size for silicon nanowire electrode, below which the structure could not fracture even with pre-existing cracks. They also experimentally found a range of critical size avoiding the pulverization of nanowire electrode and compared in good agreement with numerical results based on the fracture mechanics method. It is due to the fact that, with the descent of nanowire size, the lithium could diffuse into the configuration more rapidly and generate a relatively low stress field even large deformation happens. Grantab also employed the cohesive zone element to investigate the propagation behaviour of the pre-existing crack [2-56]. In this work, the effects of pressure gradient caused by enormous volumetric expansion on diffusion flux were given particular attention. In their case, almost the entire stress field of the nanowire was considerably reduced by introducing the pressure gradient effect and the admissible electrochemical load was also broadened. As pressure gradient promotes more regions to reach a high diffusion flux level, which is thought to result in a more constant lithium concentration distribution and lower stress field. Besides, a localized high diffusion flux appears at the crack tip under pressure gradient, which is accessible to lower the tensile stress at the crack tip and alleviate crack propagation.

Cai's [2-57] research team applied the stress integrity factor to detailedly investigate the fracture mechanism of the hollow cylindrical electrode. For hollow cylinder structure, the stress integrity factor K can be written as following.

$$K = \frac{1}{\sqrt{2\pi a}} \sqrt{W} \int_0^a \sigma(x) \sum_{i=1}^J \beta_i(a) \left(1 - \frac{x}{a}\right)^{i-\frac{3}{2}} dx \quad (2.9)$$

where a and W respectively represent the crack length and cylindrical wall thickness. For four types of crack (radial crack and circumferential crack in lithiation and delithiation process), the model is able to calculate the critical cracking length with given electrode size or in contrast to determining. Suo and co-worker [2-28] employed the energy release rate to study the fracture of the outer shell, as shown below. It can be seen that the fracture is co-determined by the yield strength of active material core σ_Y , Young' modulus of outer shell E_s , size of core-shell structure B , C and a shown in Eq 2.10,

$$G_f = 2 \frac{\sigma_Y^2}{E_s} \left(\log \frac{B}{a}\right) \frac{B^2}{C - B} \quad (2.10)$$

- Mecoscale

There is a kind of hierarchical meatball electrode structure or secondary particle electrode structure, which consists of densely packed primary particles holding together by weak Van der Waals interactions [2-58]. For this configuration, the intergranular decohesion and fracture phenomenon between grains, shown in Fig 2.12 (a), will result in serious mechanical degradation of secondary particle structure upon electrochemical operation condition. The cohesive zone element method is commonly applied in modeling this cracking behaviour. Xu et al. [2-58] applied the cohesive zone element to model the fracture phenomenon between grains and concluded that the microcracks are more prone to initiate and propagate under lower C-rate, as shown in Fig 2.12 From which, it is available to see that fewer cracks are grown at 2C than that of 0.5C. With the initiated cracks, Zhang and co-workers [2-59] performed a systematically parametric study of crack propagation considering the variations of C-rate and fracture energy. This research work presented that, under low fracture energy, it is more likely to generate long crack and crack branching which leads to a higher crack density. In the work of Sun et al. [2-60], the effects of anisotropic lithiation expansion on the fragmentation of secondary particle were investigated using cohesive crack model. The 2D model presented that swelling in one direction and shrink in the other direction turn out to intrigue more cracks than that of unipolar expansion. It is because of that the shrinking would produce tensile stress at grain boundaries, which will tear the interfaces.

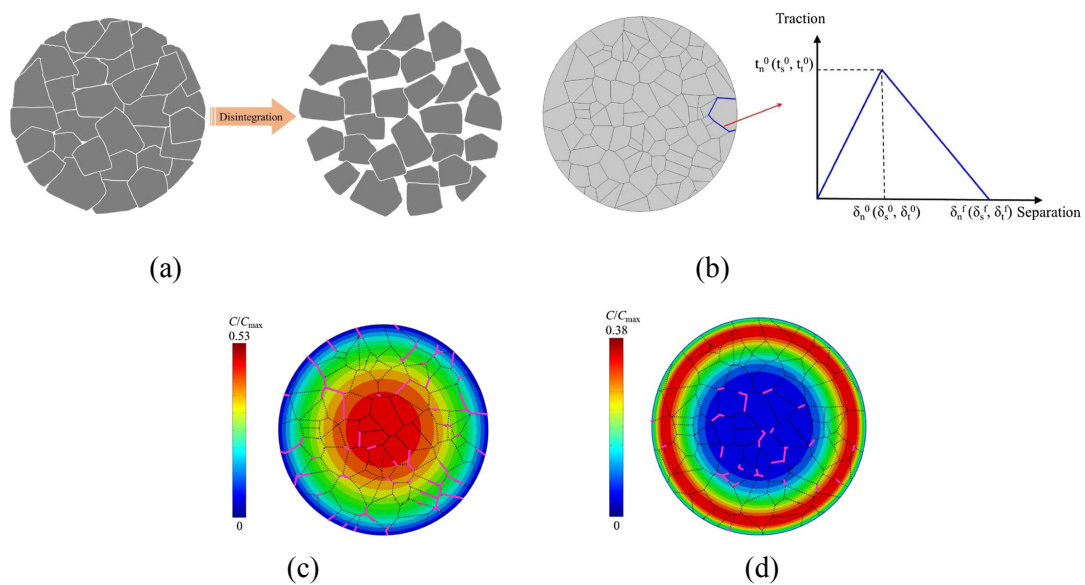


Fig 2. 12 (a) Disintegration of meatball electrode structure, (b) applying cohesive zone elements to model the fracture between the primary particles[2-58], microcracks within meatball electrode under (c) 0.5C, (d) 2C

- Macroscale

Note that repetitive swelling and shrinking upon electrochemical cycles are also recognized to intrigue the in-plane cracking of layered electrode plate. Fig 2.13 (a) is the scanning electron microscopy image of thin film before cycling [2-61]. Fig 2.13 (b), (c) and (d) show the sceneries after

certain cycles with different plate thickness. It is apparent that the crackings partition the entire electrode plate to massive isolated pieces, which result in the loss of electrochemical conductivity and capacity fading.

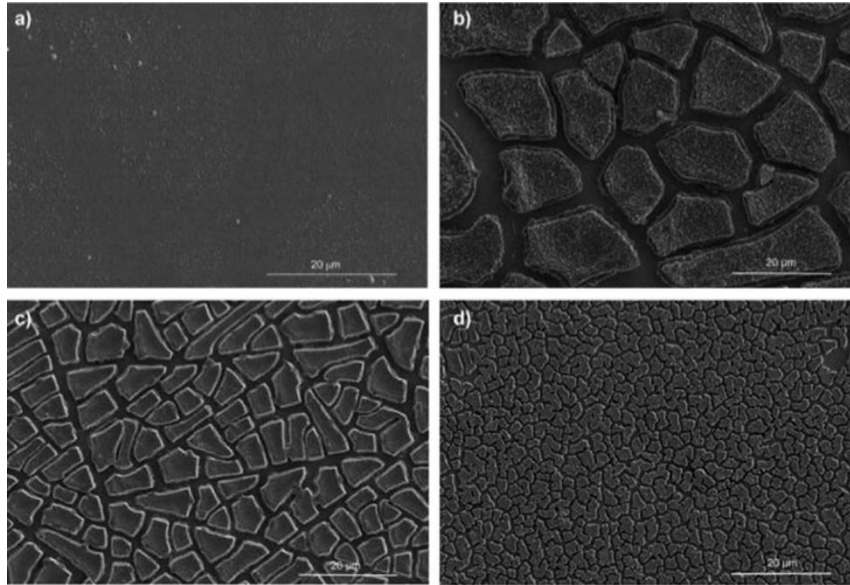


Fig 2. 13 Experimental observation of the crack caused partition of thin film electrode [2-61], (a) silicon film with 500nm thickness before cycling, (b) film with 1000nm thickness after 5 cycles, (c) film with 500nm thickness after 5 cycles, (d) film with 200nm thickness after 10 cycles

Chew [2-61] applied the finite element method with programming UMATHT subroutine to simulate the stress field within silicon thin film during intercalation process, and J-integral was set as the driving force of fracture. It is concluded that, the swelling of silicon surface accepting Li flux makes the film near the edges bending and produces a high tensile stress zone at a fixed distance away from the non-lithiated silicon at the beginning of lithiation process, which would initiate micro cracks. These micro cracks could let the inner film bend and sequentially produce uniform cracks from the film edge to the interior of the silicon plate upon cycles. Li and co-workers [2-62] applied the spring-block model to investigate the cracking behaviour of silicon thin film electrode, and proposed two strategies to avoid crack happening. The first one is to reduce the size of the patterned electrode to be less than a critical crack initiation size a_{cr} with specific film thickness shown in Eq 2.1, where σ_Y , τ_{cr}^{int} and h respectively indicate yield strength of active material, interfacial force and film thickness. The second method is to constrain the film thickness to be smaller than a critical value shown in Eq 2.12, where σ and G_c represent stress in electrode film and crack resistance force.

$$a_{cr} = 2 \frac{\sigma_y}{\tau_{cr}^{int}} h \quad (2.11)$$

$$h_c = 4\sqrt{2} \frac{G_c E}{\sigma^2 (1 - \gamma^2)} \quad (2.12)$$

Zhang et al. [2-63] analytically proposed the expressions of stress integrity factor at the crack tip for the layered electrode. It is founded that, with the rising of cracking length, the calculated stress integrity factor would decline. Hence, when the cracking propagates to a certain length and stress integrity decreases to a critical value, the cracking growth could be suppressed. Bhandakkar [2-64] adopted the cohesive model with bilinear traction-separation law to investigate the crack initiation for electrode plate. The most primary contribution of this work is to give the analytical solution of a critical length shown as following, where the Γ , ν , D , E and Ω are material properties of active material. I represents the surface current density as input condition. For electrode size less than this critical value, crack initiation will not occur.

$$l_{ft} = \left\{ \frac{\Gamma(1-\nu)F^2 D^2}{E(1+\nu)\Omega^2 I^2} \right\}^{1/3} \quad (2.13)$$

2.4 Cyclic plasticity behaviour

With the consideration of the practical cyclic operation condition of battery electrode, some scholars presented that the failure in electrode material is a fatigue process instead of the commonly assumed brittle fracture [2-65]. It has also been proved that the lithiation/delithiation of electrode material always accompanies plastic flow and the electrode configuration does not recover its original shape after cyclic lithiation [2-66]. Besides, many other research works have also presented the effect of fatigue behaviour on Li-ion batteries in recent years. In reference [2-67], the fatigue induced spatial lithium inhomogeneities along the radial direction of a cylinder-type Li-ion cell was investigated. Schweidler et al. [2-68] presented work on the long-term cycling performance of graphite/NCM851005 cell. They specifically associated the electrochemical results with (micro)structural data from operando X-ray diffraction and electron microscopy to study the fatigue behaviour. By employing in situ neutron powder diffraction and electrochemical impedance spectroscopy [2-69], the fatigue process was investigated as a function of cycling temperature for different types of Li-ion batteries. Hence, considering the cyclic electrochemical conditions, it is also important to study the cyclic ductile failure behaviour of battery electrode.

One severe consequence from diffusion induced stress is the occurrence of cyclic plasticity behaviour, which is thought to be a major factor affecting the mechanical stability and

electrochemical performance of batteries [2-70, 2-66]. A structure may fail under a low cyclic loading condition, which could be much less than the limit load. As the cycling caused residual stress field and plastic strain in one cycle would influence the structural response of the subsequent cycles. The structure responses under cyclic loading conditions could be categorized into four types: purely elastic behaviour, elastic shakedown (strict shakedown), plastic shakedown (global shakedown) and ratcheting. Fig 2.14 illustrates the classic Bree diagram showing the above four cyclic plasticity behaviours.

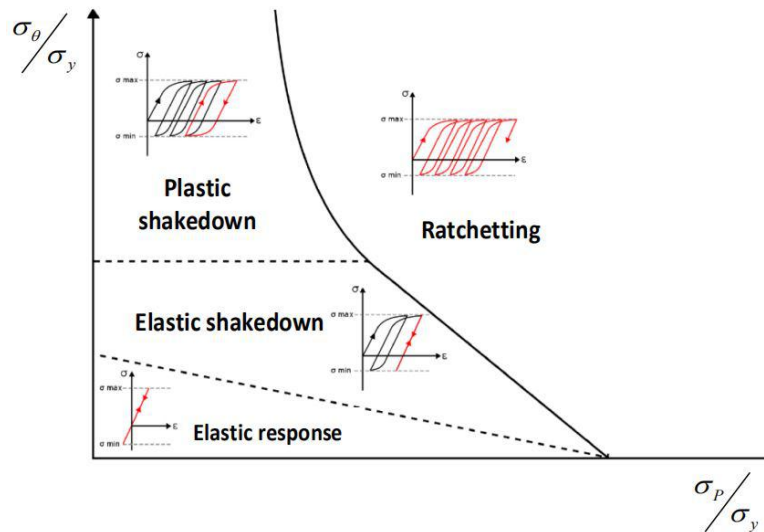


Fig 2. 14 Classic Bree's diagram under cyclic loading conditions

- Purely elastic behaviour: The loading condition is quite small such that the structure response would be overall elastic and no plastic yielding happens
- Elastic shakedown (strict shakedown): Plastic yielding only occurs at the first few cycles and the subsequent cycles remain elastic response
- Plastic shakedown (global shakedown): The generated plastic strain at loading phase is equal to that of the unloading phase, and no incremental strain would be accumulated.
- Ratcheting: Plastic strain accumulates with the proceeding of cycles, leading to plastic collapse.

Brassart and cooperators [2-66] have applied a coupled diffusion and finite-strain plasticity theory to study the intercalation-deintercalation cycles of electrode particle and presented the effects of elastic behaviour, elastic shakedown and plastic shakedown on the electrochemical performance of electrode. The different material responses during lithiation/delithiation cycles with the variations of charging rate and yield stress were identified, as shown in Fig 2.15. As expected, the higher yield strength and lower injection rate make it easily accessible for electrode to enter the elastic zone. Haftbaradaran [1-13] have investigated the ratcheting behaviour in patterned island electrode under cyclic lithiation-delithiation by performing theoretical and numerical calculations. A critical length

l_{cr} is simply defined to avoid the plastic deformation and ratcheting, that plastic yielding would not happen for electrode size less than this characteristic value. h appears to be the thickness of the patterned electrode. σ_y and τ_0 represent yield strength and effective interfacial shear strength at lithiation phase. The symbol (‘) indicates the value for the delithiation process.

$$l_{cr} = \min\left(\frac{\sigma_y h}{\tau_0}, \frac{\sigma'_y h}{\tau'_0}\right) \quad (2.14)$$

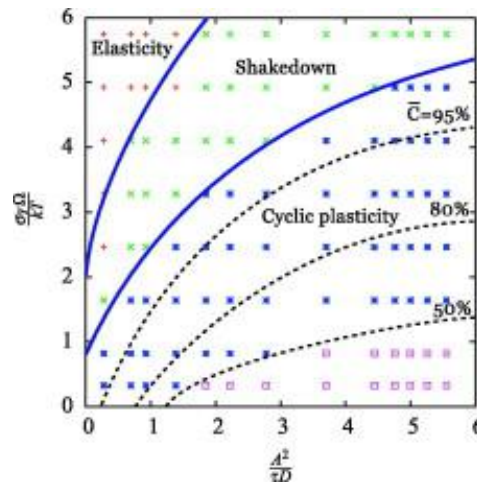


Fig 2. 15 The boundaries of different cyclic behaviours with the changing of yield strength and injection rate [2-66]

Xu et al. [2-71] analytically investigated the ratcheting of flexible electrode considering the bending behaviour. It is concluded that a tiny bending stress would contribute to the accumulation of plastic strain for the flexible electrode. Considering the ratcheting mechanism, if the Li-ion diffusion could boost the yield strength of electrode material, this strain hardening effect is conducive to maintain mechanical integrity for the electrode. In another work of this research group [2-72], the manufacturing of negative Poisson's ratio structure was reported to suppress the ratcheting behaviour of electrode. Fig 2.16 presents the cross section of a hollow re-entrant honeycomb electrode for showing the mechanism of the negative Poisson's ratio. For normal rectangle plane, the vertical and horizontal direction would be in a dissimilar swelling/shrinking state when the structure experiences uniaxial tension or compression. While for this hollow re-entrant honeycomb structure, it is available to expand or contract in all directions under unidirectional action and exhibit negative Poisson's ratio behaviour. The comparison between traditional thin film electrode and negative Poisson's ratio electrode suggests that this optimization design is accessible to suppress the ratcheting phenomenon and boost cyclic life by 8.1%.

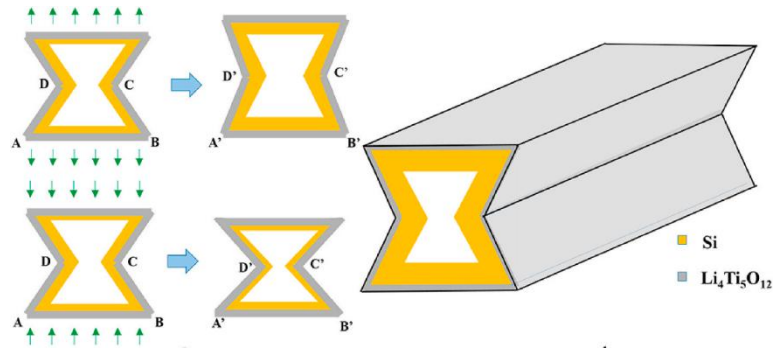


Fig 2. 16 Schematic diagram of the cross section of a hollow re-entrant honeycomb electrode, showing the mechanism of negative Poisson's ratio [2-58]

The above research works use a series of rigorous numerical derivation to study the cyclic plasticity behaviour and critical condition, which are of great value to understand the structural integrity of battery electrode. While, the calculation of cyclic plasticity boundaries is a systematic and complex work. How to obtain the accurate limit condition for different electrode configurations with the changing structural dimensions is still a topic worthy of attention.

2.5 Other failure mechanisms

In addition to the above mentioned mechanisms, several efforts have been made to investigate other failure mechanisms for electrode under electrochemical condition. The debonding between active material layer and current collector is generally considered to change the electric current and cause the peeling of the whole active material [2-73, 2-74], which would present a serious impact on the cyclic life of battery. Normally, there exists two modes of delamination, as Mode I (opening) and Mode II (slip), shown in Fig 2.17 [2-75]. The evolution to which kind of decohesion is decided by competition mechanisms as radical swelling-shrinking and bending deformation.

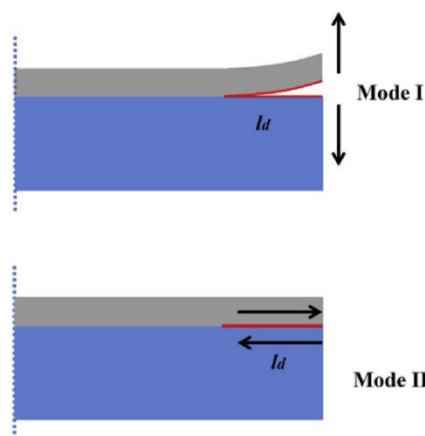


Fig 2. 17 Schematic diagram of two modes of decohesion: Mode I (opening) and Mode II (slip) [2-75]

Based on the principle of delamination, researchers have proposed two categories of approaches to prevent the layered electrode from debonding. The first one is to reduce the size of electrode. Xiao [2-74] experimentally suggested that, the cyclic life of battery could be enhanced if the continuous thin film could be patterned into small pieces with characteristic size. Haftbaradaran [2-76] analytically predicted the characteristic size of thin film electrode delamination by applying a shear hysteresis model. While, the boundedness of the model makes it inaccessible to simulate the crack propagation behaviour and relate the mechanical damage status with the charging rate. Liu [1-11] applied the finite element method to investigate the delamination of thin film - rigid substrate structure, and a layer of cohesive zone element was inserted at the interface. It is suggested that the corner of the interface turns out to be the decohesion initiation location and the decohesion would gradually develop toward the interface center. While, considering the adverse effects, manufacturing patterned electrode not only acquires higher fabricating skills, but also generates more surfaces which would consume large amounts of Li ions to overproduce SEI. Hence, this approach is questionable for being used to avoid thin film delamination.

Lu [2-75] proposed the second approach that, the decohesion behaviour could be mitigated by manipulating the state of charge (SOC) and depth of discharge (DOC) at the same time using relatively large electrode. In his work, a theoretical model is deduced to investigate the critical SOC (DOC) and time for decohesion initiation. Aiming at charging/discharging state and cathode/anode material, avoiding the SOC (DOC) and time to reach the critical value. Although, it is claimed that the anode material can not be fully unlocked in this way. It defends that the capacity of the battery is mainly determined by the capacity of cathode material, and the enhancement of anode efficiency boosts battery capacity to a limited extent. Hence, this approach is adaptable to predict thin film delamination.

For wire-like electrode, the buckling behaviour may be a primary factor leading to the mechanical degeneration [2-77], as well as capacity fading [2-78]. Liu et. al. [2-79] experimentally detected the buckling behaviour of two-end fixed silicon nanowire electrode during the Li-ion insertion process, as shown in Fig 2.18. The lithiation caused buckling may also lead to the occurrence of brittle fracture [2-80], as shown in Fig 2.18 (b). The intercalation caused swelling let nanowire buckle and further bend. In the experiment, the silicon nanowire was partially lithiated, where the outer surface was lithiated to be $\text{Li}_{3.75}\text{Si}$ shell and the core still remained as pristine silicon. It is apparent that the brittle silicon core was fractured and the outer lithiation caused $\text{Li}_{3.75}\text{Si}$ shell displayed a high damage tolerance with undergoing a considerable tensile deformation. There is no doubt that this buckling caused fracture results in the loss of electronic contact and battery capacity.

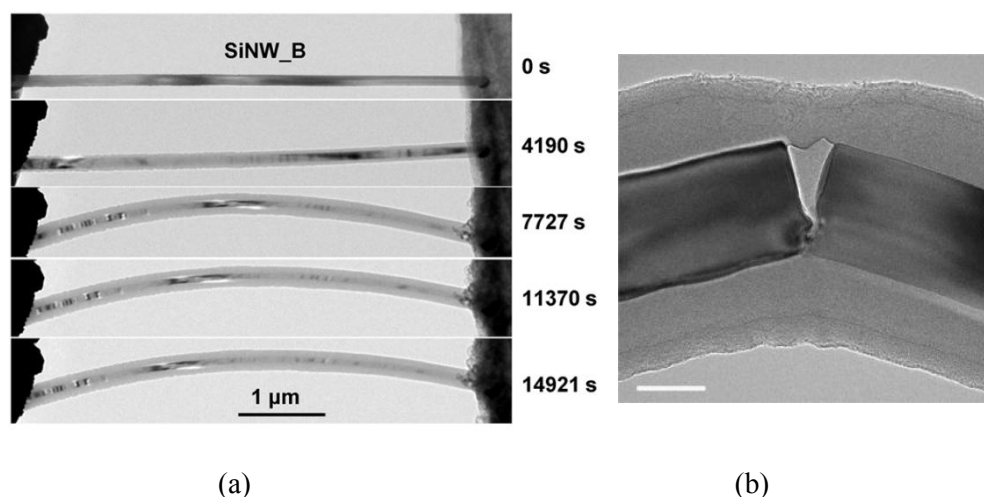


Fig 2. 18 (a) Experimental observations of the morphological evolution of silicon nanowire electrode [2-79], (b) TEM image showing the buckling caused fracture of the silicon core (scale, 50nm) [2-80]

As expected, investigators have shown that [2-77], the rising of C-rate always results in the fast arrival of electrode buckling, as higher C-rate intrigues a faster increase of the axial force. Besides, the increasing of the ratio between length and radius also boosts the occurrence of buckling in general. Concentration-dependent elastic modulus is assumed to be an important variable and is studied in their work with the comparison of constant elastic modulus. The critical buckling time is not modified by the variation of Young's modulus under all C-rate conditions when the ratio between length and radius exceeds 75. As the phase separation will not appear when the buckling initiates. Considering the low ratio of the length to the radius, the concentration modified Young's modulus is beneficial to mitigate the buckling behaviour due to the decline of Euler force and axial force. Hence, for the small length-radius ratio electrode, the concentration modified Young's modulus has a remarkable impact on the stress evolution.

Zhang and co-workers [2-78] discussed the effect of constraint conditions at two electrode ends on the critical buckling initiation time, by adopting the developed Cahn–Hilliard-type phase-field model. It suggests that, the intense constraint (fixed at two ends) is conducive to suspend the buckling time, than that of a relatively weak constraint (one fixed end, one pinned end). They defended this result with the explanation that, for a given length wire, it is accessible to bear a larger axial force under a stronger constraint. In this work, the critical buckling time of different phase reaction materials was also investigated. Generally, the host materials with/without sharp front reaction can be categorized into two-phase reaction material or one-phase reaction material. The research work reveals that the critical buckling initiation time is independent of the material category, i.e. buckling onset time is identical for two material cases with the same configuration and input load.

2.6 Conclusions

This chapter gives a detailed review of the diffusion-induced stress and corresponding mechanical failure behaviours of Li-ion battery electrode at different material levels. The key conclusions are:

- (1) The research works on the diffusion-induced stress of electrode configurations at different material levels, as particle, nanowire and hollow core-shell in microscale, representative volume element in mesoscale and layered electrode plate, island electrode in macroscale, are reviewed. For calculating the stress field, a series of numerical methods, as analytical solution, finite element method, finite difference method, phase field model, are developed, which are valuable in understanding the characteristic of DIS. However, some methods are based on the sequentially coupled treatment or some methods include too many equations or material variables. Besides, considering the subsequent complex structural integrity assessment, there needs to be a convenient stress field as input condition and the method is required to be applicable for electrode configurations at different material levels.
- (2) Electrode cracking fracture upon electrochemical condition have been reviewed. Aiming at each electrode scale, the different cracking development trends and strategies to prevent battery electrode from cracking fracture are reviewed. Massive cracking research works focus on studying the electrode configuration with initial defect. However, the entire crack development should include initiation, growth and fracture phases, and different phases correspond to different critical electrochemical conditions. There is a need to study the entire crack evolution process and clarify failure conditions at different phases.
- (3) Considering the cyclic operation conditions, the potential cyclic plasticity behaviours, such as elastic shakedown, reverse plasticity and ratcheting, of electrode have also been introduced. Structure optimization, material selection and determination of critical electrochemical condition have been reviewed for avoiding the strain accumulation caused collapse. Besides, exclusive mechanical failure behaviours of specific configurations, such as delamination between active material and current collector, buckling of nanowire electrode, are also concluded.

2.7 References

[2-1] X. Xu, S. Wang, H. Wang, C. Hu, Y. Jin, J. Liu, H. Yan. Recent progresses in the suppression method based on the growth mechanism of lithium dendrite. *Journal of Energy Chemistry*, 2018, 27(2): 513-527.

- [2-2] A. Jana, S. Woo, K. Vikrant, R. Garcia. Electrochemomechanics of lithium dendrite growth. *Energy Environmental Science*, 2019, 12: 3595.
- [2-3] SLAC National Laboratory, Stanford University.
- [2-4] P. Verma, P. Maire, P. Novak. A review of the features and analyses of the solid electrolyte interphase in Li-ion batteries. *Electrochimica Acta*, 2010, 55(22): 6332-6341
- [2-5] Y. Lee, J. Park, W. Liu. A comprehensive experimental and modeling study on dissolution in Li-ion batteries. *Journal of The Electrochemical Society*, 2019, 166: A1340
- [2-6] T. Ma, G. Xu, Y. Li, L. Wang, X. He, J. Zheng, J. Liu, M. Engelhard, P. Zapol, L. Curtiss, J. Jorne, K. Amine, Z. Chen. Revisiting the corrosion of the aluminum current collector in Lithium-ion batteries. *The Journal of Physical Chemistry Letters*, 2017, 8: 1072-1077
- [2-7] Q. Wang, P. Ping, X. Zhao, G. Chu, J. Sun, C. Chen. Thermal runaway caused fire and explosion of lithium ion battery. *Journal of Power Sources*, 2012, 208: 210-224.
- [2-8] X. Feng, M. Ouang, X. Liu, L. Lu, Y. Xia, X. He. Thermal runaway mechanism of lithium ion battery for electric vehicles: a review. *Energy Storage Materials*, 2018, 10: 246-267.
- [2-9] B. Wu, W. Lu. A battery model that fully couples mechanics and electrochemistry at both particle and electrode levels by incorporation of particle interaction. *Journal of Power Sources*, 2017, 360, 360-372
- [2-10] M. Yu, X. Feng. Thin-Film Electrode-Based Supercapacitors. *Joule*, 2019, 3(2): 338-360
- [2-11] A. Bagheri, J. Arghavani, R. Naghdabadi. On the effects of hydrostatic stress on Li diffusion kinetics and stresses in spherical active particles of Li-ion battery electrodes. *Mechanics of Materials*, 2019, 137: 103134
- [2-12] Y. Liu, H. Duan. Stress analysis of electrode particles in lithium-ion battery. *Alkali-ion Batteries*, 2016.
- [2-13] X.C. Zhang, W. Shyy, A.M. Sastry. Numerical simulation of intercalation-induced stress in Li-ion battery electrode particles. *Journal of The Electrochemical Society*, 2007, 154(10), A910-A916.
- [2-14] A.M. Korsunsky, T. Sui, B. Song. Explicit formulae for the internal stress in spherical particles of active material within lithium ion battery cathodes during charging and discharging. *Materials and Design*, 2015, 69: 247-252.
- [2-15] M.T. McDowell, S.W. Lee, C. Wang, W.D. Nix, Y. Cui. Studying the kinetics of crystalline silicon nanoparticle lithiation with in situ transmission electron microscopy. *Advanced Materials*, 2021, 24: 6034-6041
- [2-16] M.T. McDowell, S.W. Lee, J.T. Harris, B.A. Korgel, C. Wang, W.D. Nix, Y. Cui. In situ TEM of two-phase lithiation of amorphous silicon nanospheres. *Nano Letters*, 2013, 13: 758-764

- [2-17] H. Wu, Z. Xie, Y. Wang, C. Lu, Z. Ma. Modeling diffusion-induced stress on two-phase lithiation in lithium-ion batteries. *European Journal of Mechanics - A/Solids*, 2018, 71: 320-325
- [2-18] R. Deshpande, Y. Cheng, M.W. Verbrugge, A. Timmons. Diffusion Induced Stresses and Strain Energy in a Phase-Transforming Spherical Electrode Particle. *Journal of The Electrochemical Society*, 2011, 158 (6) A718-A724
- [2-19] Y.T. Cheng, M.W. Verbrugge. Evolution of stress within a spherical insertion electrode particle under potentiostatic and galvanostatic operation. *Journal of Power Sources*, 2009, 190, 2: 453-460.
- [2-20] L. Chang, Y. Lu, L. He, Y. Ni. Phase field model for two-phase lithiation in an arbitrarily shaped elastoplastic electrode particle under galvanostatic and potentiostatic operations. *International Journal of Solids and Structures*, 2018, 143: 73-83.
- [2-21] Z. Liu, J. Zhou, B. Chen, J. Zhu. Interaction between dislocation mechanics on diffusion induced stress and electrochemical reaction in a spherical lithium ion battery electrode. *RSC Adv.*, 2015, 5(91): 74835–74843.
- [2-22] P. Wei, J. Zhou, X. Pang, H. Liu, K. Deng, G. Wang, Y. Wu, B. Chen. Effects of dislocation mechanics on diffusion-induced stresses within a spherical insertion particle electrode. *Journal of Materials Chemistry A*, 2014, 2, 4: 1128-1136.
- [2-23] K. Zhang, Y. Li, B. Zheng, G. Wu, J. Wu, F. Yang. Large deformation analysis of diffusion-induced buckling of nanowires in lithium-ion batteries. *International Journal of Solids and Structures*, 2017, 108: 230-243.
- [2-24] L. Chen, N. Lu, C. Xu, H. Yu, T. Wang. Electrochemical performance of polycrystalline CuO nanowires as anode material for Li ion batteries. *Electrochimica Acta*, 2009, 54 (17): 4198-4201.
- [2-25] R. Deshpande, Y. Cheng, M. Verbrugge. Modeling diffusion-induced stress in nanowire electrode structures. *Journal of Power Sources*, 2010, 195 (15): 5081-5088.
- [2-26] L. Weng, J. Zhou, R. Cai. Analytical model of Li-ion diffusion-induced stress in nanowire and negative Poisson's ratio electrode under different operations. *International Journal of Mechanical Sciences*, 2018, 141: 245-261.
- [2-27] J. Li, Q. Fang, F. Liu, Y. Liu. Analytical modeling of dislocation effect on diffusion induced stress in a cylindrical lithium ion battery electrode. *Journal of Power Sources*, 2014 272: 121-127
- [2-28] K. Zhao, M. Pharr, L. Hartle, J.J. Vlassak, Z. Suo. Fracture and debonding in lithium-ion batteries with electrodes of hollow core-shell nanostructures. *Journal of Power Sources*, 2012, 218: 6-14.
- [2-29] K. Zhang, J. Chen, Y. Li, D. Liu, B. Zheng, Y. Kai. Rate-dependent lithiation-induced failure modes of a cylindrical core-shell electrode. *Results in Physics*, 2020, 16: 103018

- [2-30] F. Yang. Effect of diffusion-induced bending on diffusion-induced stress near the end faces of an elastic hollow cylinder. *Mechanics Research Communications*, 2013, 51: 72-77
- [2-31] J. Li, Q. Fang, H. Wu, Y. Liu, P. Wen. Investigation into diffusion induced plastic deformation behavior in hollow lithium ion battery electrode revealed by analytical model and atomistic simulation. *Electrochimica Acta*, 2015, 178: 597-607
- [2-32] L.M. Wu, X.H. Xiao, Y.H. Wen, J. Zhang. Three-dimensional finite element study on stress generation in synchrotron X-ray tomography reconstructed nickel-manganese-cobalt based half cell. *Journal of Power Sources*, 2016, 336, 8-18.
- [2-33] H. Fathiannasab, L. Zhu, Z. Chen. Chemo-mechanical modeling of stress evolution in all-solid-state lithium-ion batteries using synchrotron transmission X-ray microscopy tomography. *Journal of Power Sources*, 2021, 483: 229028
- [2-34] A. Kashkooli, S. Farhad, D. Lee, K. Feng, S. Litster, S. Babu, L. Zhu, Z. Chen. Multiscale modeling of lithium-ion battery electrodes based on nano-scale X-ray computed tomography. *Journal of Power Sources*, 2016, 307: 496-509
- [2-35] J. Zhang, B. Lu, Y. Song, X. Ji. Diffusion induced stress in layered Li-ion battery electrode plates. *Journal of Power Sources*, 2012, 209: 220-227.
- [2-36] Y. He, H. Hu, Y. Song, Z. Guo, C. Liu, J. Zhang. Effects of concentration-dependent elastic modulus on the diffusion of lithium ions and diffusion induced stress in layered battery electrodes. *Journal of Power Sources*, 2014, 248: 517-523.
- [2-37] F. Hao, D. Fang. Reducing diffusion-induced stresses of electrode–collector bilayer in lithium-ion battery by pre-strain. *Journal of Power Sources*, 2013, 242: 415-420.
- [2-38] H. Xie, Q. Zhang, H. Song, B. Shi, Y. Kang. Modeling and in situ characterization of lithiation-induced stress in electrodes during the coupled mechano-electro-chemical process. *Journal of Power Sources*, 2017, 342: 896-903.
- [2-39] Y. Song, X. Shao, Z. Guo, J. Zhang. Role of material properties and mechanical constraint on stress-assisted diffusion in plate electrodes of lithium ion batteries. *Journal of Physics D: Applied Physics*, 2013, 46: 105307.
- [2-40] X. Xiao, P. Liu, M.W. Verbrugge, H. Haftbaradaran. Improved cycling stability of silicon thin film electrodes through patterning for high energy density lithium batteries. *Journal of Power Sources*, 2011, 196 (3): 1409-1416.
- [2-41] S. Soni, B. Sheldon, X. Xiao, M. Verbrugge, D. Ahn, H. Haftbaradaran. Stress Mitigation during the Lithiation of Patterned Amorphous Si Islands. *Journal of The Electrochemical Society*, 2012, 159 (1) A38-A43
- [2-42] M.R. Palacin, A. de Guibert. Why do batteries fail? *Science*, 2016, 351: 1253292

- [2-43] D. Mohanty, E. Hockaday, J. Li, D.K. Hensley, C. Daniel, D.L.I. Wood. Effect of electrode manufacturing defects on electrochemical performance of lithium-ion batteries: cognizance of the battery failure sources. *Journal of Power Sources*, 2016, 312: 70-79
- [2-44] L. Yang, H. Chen, W. Song, D. Fang. In situ optical observations and simulations on defect induced failure of silicon island anodes. *Journal of Power Sources*, 2018, 405: 101-105.
- [2-45] J. Wolfenstine. Critical grain size for microcracking during lithium insertion. *Journal of Power Sources*, 1999, 79(1):111-113
- [2-46] Y Hu, X Zhao, Z Suo. Averting cracks caused by insertion reaction in lithium-ion batteries. *Journal of Materials Research*, 2010, 25(06): 1007-1010.
- [2-47] W. Woodford, Y. Chiang, W. Carter. “Electrochemical Shock” of intercalation electrodes: A Fracture Mechanics Analysis. *Journal of The Electrochemical Society*, 2010, 157(10): A1052-A1059.
- [2-48] K. Zhao, M. Pharr, J.J. Vlassak, Z. Suo. Fracture of electrodes in lithium-ion batteries caused by fast charging. *Journal of Applied Physics*, 2010, 108(073517): 1-6.
- [2-49] R. Grantab, V.B. Shenoy. Location- and orientation-dependent progressive crack propagation in cylindrical graphite electrode particles. *Journal of The Electrochemical Society*, 2011, 158(8):A948
- [2-50] M. Klinsmann, D. Rosato, M. Kamlah, R.M. McMeeking. Modeling crack growth during Li insertion in storage particles using a fracture phase field approach. *Journal of the Mechanics and Physics of Solids*, 2016, 92:313-344.
- [2-51] M. Klinsmann, D. Rosato, M. Kamlah, R.M. McMeeking. Modeling crack growth during Li extraction in storage particles using a fracture phase field approach. *Journal of the Electrochemical Society*, 2016, 163:102-118.
- [2-52] Y.-T. Cheng, M.W. Verbrugge. Application of Hasselman’s crack propagation model to insertion electrodes. *Electrochemical and Solid State Letters*, 2010, 13: A128-A131
- [2-53] F. Yang. Insertion-induced breakage of materials. *Journal of Applied Physics*, 2010, 108: 1-5
- [2-54] K.E. Aifantis, J.P. Dempsey. Stable crack growth in nanostructured Li-batteries. *Journal of Power Sources*, 2005, 143:203-211.
- [2-55] I. Ryu, J. Choi, Y. Cui, W. Nix. Size-dependent fracture of Si nanowire battery anodes. *Journal of the Mechanics and Physics of Solids*, 2011, 59(9): 1717-1730.
- [2-56] R. Grantab, V. Shenoy. Pressure-Gradient Dependent Diffusion and Crack Propagation in Lithiated Silicon Nanowires. *Journal of The Electrochemical Society*, 2012, 159(5): A584-A591
- [2-57] C. Xu, L. Weng, B. Chen, J. Zhou, R. Cai. An analytical model for the fracture behavior in hollow cylindrical anodes. *International Journal of Mechanical Sciences*, 2019, 157-158: 87-97.
- [2-58] R. Xu, L.S. de Vasconcelos, J. Shi, J. Li, K. Zhao. Disintegration of meatball electrodes for LiNi_xMn_yCo_zO₂ cathode materials. *Experimental Mechanics*, 2018, 58, 549-559.

- [2-59] Y. Zhang, C. Zhao, Z. Guo. Simulation of crack behavior of secondary particles in Li-ion battery electrodes during lithiation/ delithiation cycles. *International Journal of Mechanical Sciences*, 2019, 155:178-186
- [2-60] G. Sun, T. Sui, B. Song, H. Zheng, L. Liu, A. Korsunsky. On the fragmentation of active material secondary particles in lithium ion battery cathodes induced by charge. *Extreme Mechanics Letters*, 2016, 9: 449-458.
- [2-61] H. Chew, B. Hou, X. Wang, S. Xia. Cracking mechanisms in lithiated silicon thin film electrodes. *International Journal of Solids and Structures*, 2014, 51: 4176-4187.
- [2-62] J. Li, A. Dozier, Y. Li, F. Yang, Y. Cheng. Crack Pattern Formation in Thin Film Lithium-Ion Battery Electrodes. *Journal of The Electrochemical Society*, 2011, 158 (6) A689-A694
- [2-63] A. Zhang, B. Wang, G. Li, J. Wang, J. Du. Fracture analysis of bi-layer electrode in lithium-ion battery caused by diffusion-induced stress. *Engineering Fracture Mechanics*, 2020, 235: 107189.
- [2-64] T. Bhandakkar. Cohesive modeling of crack nucleation under diffusion induced stresses in a thin strip: Implications on the critical size for flaw tolerant battery electrodes. *International Journal of Solids Structure*, 2010, 47:1424-34.
- [2-65] D. Chen, D. Kramer, R. Mönig. Chemomechanical fatigue of $\text{LiMn}_{1.95}\text{Al}_{0.05}\text{O}_4$ electrodes for lithium-ion batteries. *Electrochimica Acta*, 2018, 259: 939-948
- [2-66] L. Brassart, K. Zhao, Z. Suo. Cyclic plasticity and shakedown in high-capacity electrodes of lithium-ion batteries. *International Journal of Solids and Structures*, 2013, 50: 1120-1129.
- [2-67] M.J. Mühlbauer, O. Dolotko, M. Hofmann, H. Ehrenberg, A. Senyshyn. Effect of fatigue/ageing on the lithium distribution in cylinder-type Li-ion batteries. *Journal of Power Sources*, 2017, 348: 145-149.
- [2-68] S. Schweidler, L. de Biasi, G. Garcia, A. Mazilkin, P. Hartmann, T. Brezesinski, J. Janek. Investigation into mechanical degradation and fatigue of High-Ni NCM cathode material: a long-term cycling study of full cells. *Applied Energy Materials*, 2019, 2: 7375-7384.
- [2-69] D. Sørensen, M. Heere, J. Zhu, M. Darma, S. Zimnik, M. Mühlbauer, L. Mereacre, V. Baran, A. Senyshyn, M. Knapp, H. Ehrenberg. Fatigue in high-energy commercial Li batteries while cycling at standard conditions: an in situ neutron powder diffraction study. *Applied Energy Materials*, 2020, 3: 6611-6622.
- [2-70] K.J. Zhao, W.L. Wang, J. Gregoire, M. Pharr, Z.G. Suo, J.J. Vlassak, E. Kaxiras. Lithium-assisted plastic deformation of silicon electrodes in lithium-ion batteries: a first-principles theoretical study. *Nano Letters*, 2011, 11: 2962-2967.
- [2-71] C. Xu, L. Weng, B. Chen, L. Ji, J. Zhou, R. Cai, S. Lu. Modeling of the ratcheting behavior in flexible electrodes during cyclic deformation. *Journal of Power Sources*, 2020, 446, 227353

- [2-72] L. Weng, C. Xu, B. Chen, J. Zhou, R. Cai, Y. Shi. A comparative study on ratcheting deformation between negative Poisson's ratio electrode and thin film electrode in Li-ion battery cyclic operation. *Mechanics of Materials*, 2020, 150: 103567.
- [2-73] L.Y. Beaulieu, K.W. Eberman, R.L. Turner, L.J. Krause, J.R. Dahn. Colossal reversible volume changes in lithium alloys . *Electrochemical and Solid-State Letters*, 2001, 4(9): A137-A140
- [2-74] X. Xiao, P. Liu, M.W. Verbrugge, H. Haftbaradaran. Improved cycling stability of silicon thin film electrodes through patterning for high energy density lithium batteries. *Journal of Power Sources*, 2011, 196(3): 1409-1416.
- [2-75] B. Lu , Y. Song, J. Zhang. Time to delamination onset and critical size of patterned thin film electrodes of lithium ion batteries. *Journal of Power Sources*, 2015, 289: 168-183
- [2-76] H. Haftbaradaran, X. Xiao, M.W. Verbrugge. Method to deduce the critical size for interfacial delamination of patterned electrode structures and application to lithiation of thin-film silicon islands. *Journal of Power Sources*, 2012, 206: 357-366
- [2-77] Y. Zhang, S. Zhan, K. Zhang, B. Zheng, L. Lyu. Buckling behavior of a wire-like electrode with a concentration-dependent elastic modulus based on a deformed configuration. *European Journal of Mechanics / A Solids*, 2021, 85: 104111.
- [2-78] K. Zhang, Y. Li, J. Wu, B. Zheng, F. Yang. Lithiation-induced buckling of wire based electrodes in lithium-ion batteries: a phase-field model coupled with large deformation. *International Journal of Solid Structure*, 2018, 144: 289–300.
- [2-79] X. Liu, F. Fan, H. Yang, S. Zhang, J. Huang, T. Zhu. Self-limiting lithiation in silicon nanowires. *ACS Nano*, 2013, 7:1495–1503.
- [2-80] X. Wang, F. Fan, J. Wang, H. Wang, S. Tao, A. Yang, Y. Liu, H.B. Chew, S.X. Mao, T. Zhu. High damage tolerance of electrochemically lithiated silicon, *Nature Communications*, 2015, 6: 1–7.

Chapter 3

Coupled diffusion-stress analysis and study of cracking behaviour

3.1 Introduction

As described in chapter 2, scholars have proposed various methods including analytical method, finite element method, finite difference method, etc. to model the diffusion-induced stress within Li-ion battery electrode. These methods provide different perspectives on studying the problem and contribute to understanding the mechanism affecting the structural integrity of battery electrode. Due to the complexity of the subsequent structural integrity assessment, an effective and efficient method is required to provide an accurate and robust diffusion-induced stress field.

As the most basic electrode configuration, tremendous investigations have used different principles to study and avoid the fracture behaviour of electrode particle with pre-existing crack. While for pristinely primary electrode particle, the fracture process includes crack initiation, propagation and final fracture phases. Electrode in different cracking status affects the electrochemical performance of the battery to varying degrees. In addition, crack initiation and fracture generally corresponds to different critical electrochemical conditions. Therefore, it is significant that the fracture analysis of electrode particle is ought to evaluate the crack initiation, evolution and fracture processes. And the critical failure boundary is required to be established so as to estimate the particle cracking status under certain electrochemical load. In addition, the non-uniform particle size distribution in micrometer scale decides the fact that the particle dimensions greater than the critical size will fracture under certain electrochemical load, while the rest of the particles with smaller size remain stable. Hence, there is a need to associate the calculated critical particle dimension with the distribution of particle size in experimental samples so as to determine the proportion of cracked particles.

Considering the complexity of subsequent cracking assessment, using the analytical solutions of DIS to research the cracking behaviour of primary electrode particle is not easily accessible. Hence, based on the finite element simulation platform ABAQUS, this work implements the diffusion driven approach and chemical potential driven approach to perform the coupled diffusion-stress analysis of NCM cathode particle via developing finite element user subroutines, which are for incorporating the

coevolving process between diffusion behaviour and stress generation under intercalation-deintercalation condition. The accuracy of the implemented approaches is verified and the calculation result difference between these two approaches is discussed. Based on the coupled diffusion-stress analysis, ABAQUS XFEM is applied to study the crack initiation, propagation and fracture of the primary electrode particle. Besides, critical crack initiation and fracture boundaries are established to avert the mechanical collapse of the electrode particle. The equations to calculate critical particle dimension for crack onset and fracture under the applied electrochemical loads are fitted. The fracture proportion is proposed for the battery electrode by associating the critical failure diagram with the size distribution of micro particles.

3.2 Computational methods

Considering the stress induced fracture of cathode particles under electrochemical condition, essentially, the research emphasis can be classified as solving a coupled boundary value problem that is the coupled diffusion-mechanics issue, and conducting subsequent fracture evaluation. In this section, the detailed formulas and methodologies are provided for studying the diffusion process, mechanics simulation, fracture assessment in sequence.

3.2.1 The first boundary value problem – diffusion equation

As for a heat conduction process, it obeys energy conservation law as listed below

$$\rho c_s \frac{\partial T}{\partial t} + \nabla q = \Phi \quad (3.1)$$

where ρ , c_s , T , Φ denote density, specific heat, temperature and internal heat source respectively, and t is defined as time here. The symbol q in the equation represents the heat flux, which describes the flow of energy per unit of area per unit of time.

When it comes to the diffusion problem, Crank has solved basic equations in [3-1] where mass conservation law is satisfied:

$$\frac{\partial c}{\partial t} + \nabla J = 0 \quad (3.2)$$

where c represents the concentration, and J is the diffusion flux which measures the amount of substance that will flow through a unit area during a unit time interval.

It is evident that one can make the following analogy so as to treat mass diffusion process as heat conduction process [2-46]

$$\begin{aligned}
T=c \quad \Phi =0 \\
q=J \quad \rho c_s=1
\end{aligned}
\tag{3.3}$$

There are several approaches to update diffusion flux J so as to incorporate the bidirectional influence between stress and Li distribution. An effective method is the diffusion driven process based on classic Fick diffusion law. An alternative one stems from the chemical potential driven process.

For diffusion driven process [3-2], diffusion flux can be expressed as

$$J = -D_f \nabla c \tag{3.4}$$

$$D_f = D_{f0} \exp\left(\frac{\Omega \sigma_h}{RT_a}\right) \tag{3.5}$$

where D_f is diffusivity, D_{f0} is diffusivity at stress-free condition, Ω represents the partial molar volume. σ_h is hydrostatic stress and can be calculated as $\sigma_h = (\sigma_{11} + \sigma_{22} + \sigma_{33})/3$. The effect of stress on diffusion is incorporated in calculating diffusivity and diffusion flux, which are updated in real time based on the obtained hydrostatic stress at different instants. R is the gas constant, T_a denotes absolute temperature. The above equations can be implemented in ABAQUS by compiling a set of USDFLD-UMATHT subroutine to conduct diffusion driven coupled analysis, as shown in Appendix 1.

For chemical potential driven process [2-13, 3-3], the diffusion process is driven by chemical potential gradient $\nabla \mu$, where the driven force F on particle can be determined by

$$F = -\nabla \mu \tag{3.6}$$

The minus sign in equation (3.6) represents that diffusion proceeds along the direction of decreasing chemical potential, and μ is the chemical potential which can be written as the following formula in ideal solid

$$\mu = \mu_0 + RT_a \ln X - \Omega \sigma_h \tag{3.7}$$

where μ_0 is a constant and X is the molar fraction of lithium ion. The average diffusion velocity v of particle is in direct proportion of driven force F

$$v = MF = M(-\nabla \mu) \tag{3.8}$$

where M is the mobility of solute. The diffusion flux in this method is then expressed as mass concentration of diffusion solute c timing its average velocity

$$J = cv = cM(-\nabla \mu) \tag{3.9}$$

By substituting equation (3.7) into equation (3.9), it is available to obtain another expression of diffusion flux with stress effect [3-3], as shown in equation (3.10). Resorting to the expression of chemical potential, the gradient of hydrostatic stress is embedded into calculating diffusion flux in real time.

$$J = -MRT_a \left(\nabla c - \frac{\Omega c}{RT_a} \nabla \sigma_h \right) \quad (3.10)$$

Through developing another set of USDFLD-UMATHT subroutine shown in Appendix 2, the above formulas are accessible to be embedded in ABAQUS for performing coupled diffusion-stress analysis driven by chemical potential gradient. The main hinderance there is how to calculate the gradient of hydrostatic stress as it is not automatically passed into UMATHT subroutine for information. In order to figure out this issue, a pointwise least squares linear regression method is adopted, which was employed for calculating meaningful strain via obtained displacement in digital image correlation [3-4]. For obtaining the gradient of hydrostatic stress at one integration point, it is available to assume the coordinates and hydrostatic stress obey the following linear relationship within a sphere zone where the targeted integration point acts as the centre point of this sphere.

$$\sigma_h(x_i) = a_0 + a_1 x_{1i} + a_2 x_{2i} + a_3 x_{3i} \quad (i = 1 \dots n) \quad (3.11)$$

where a_0, a_1, a_2, a_3 are assumed polynomial coefficients needed to be fitted, $\sigma_h(x_i)$ represents the fitted value of hydrostatic stress based on the above linear relation. x_{1i}, x_{2i}, x_{3i} are coordinates of one integration and n represents all integration points within the sphere zone. Employing the least squares linear regression to minimize the fitting error.

$$e_i = y_i - \sigma_h(x_i) \quad (3.12-1)$$

$$S_r = \sum_{i=1}^n e_i^2 = \sum_{i=1}^n [y_i - (a_0 + a_1 x_{1i} + a_2 x_{2i} + a_3 x_{3i})]^2 \quad (3.12-2)$$

where y_i is the true value of the hydrostatic stress at each integration point and e_i is the difference between true value and fitted value of hydrostatic stress. If one partially differentiates S_r with each polynomial coefficient and equates it to zero

$$\frac{\partial S_r}{\partial a_0} = 0 = -2 \sum_{i=1}^n [y_i - (a_0 + a_1 x_{1i} + a_2 x_{2i} + a_3 x_{3i})] \quad (3.13-1)$$

$$\frac{\partial S_r}{\partial a_k} = 0 = -2 \sum_{i=1}^n [x_{ki} (y_i - (a_0 + a_1 x_{1i} + a_2 x_{2i} + a_3 x_{3i}))] \quad (k=1, 2, 3) \quad (3.13-2)$$

By reorganizing the equations, it is available to obtain the following relations

$$a_0 n + a_1 \sum_{i=1}^n x_{1i} + a_2 \sum_{i=1}^n x_{2i} + a_3 \sum_{i=1}^n x_{3i} = \sum_{i=1}^n y_i \quad (3.14-1)$$

$$a_0 \sum_{i=1}^n x_{ki} + a_1 \sum_{i=1}^n x_{ki} x_{1i} + a_2 \sum_{i=1}^n x_{ki} x_{2i} + a_3 \sum_{i=1}^n x_{ki} x_{3i} = \sum_{i=1}^n x_{ki} y_i \quad (k=1, 2, 3) \quad (3.14-2)$$

Applying the hydrostatic stress and coordinates of all integration points in sphere zone to fit unknown polynomial coefficients, it is accessible to calculate hydrostatic stress gradient of targeted integration point and further incorporate diffusion induced stress effect onto Li distribution. Fig 3.1 presents the schematic flowchart on the finite element implementation for diffusion driven method and chemical potential driven method.

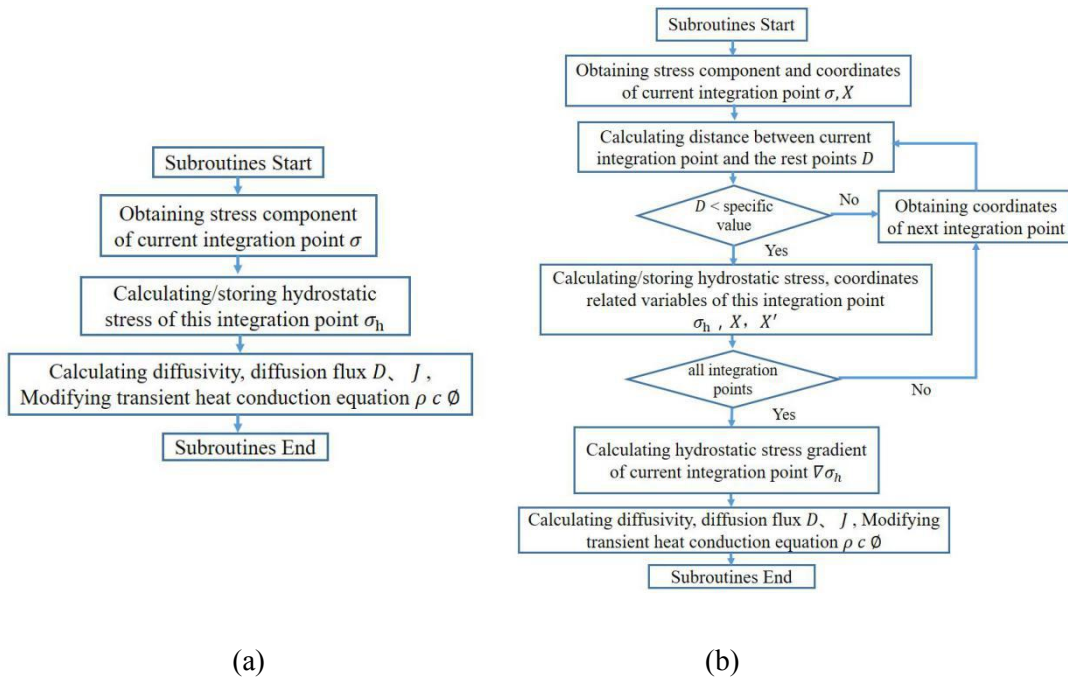


Fig 3. 1 Schematic flowchart showing the finite element implementation for (a) diffusion driven method, (b) chemical potential driven method.

The diffusion boundary condition in this section is given as the Neumann boundary condition

$$J = \frac{i_n}{F_a} \quad (3.15)$$

where i_n is the current density applied on the particles surface, F_a is Faraday constant, which is 96485 C/mol.

3.2.2 The second boundary value problem– mechanics equation

For an elasticity issue, the equilibrium equation ignoring body forces F_{bj} and the geometric equation describing strain-displacement relation in elastomer can be given as equation (3.16) and (3.17) [2-13]

$$\sigma_{ij,i} = 0 \quad (3.16)$$

$$\varepsilon_{ij} = \frac{1}{2}(u_{i,j} + u_{j,i}) \quad (3.17)$$

The stress-strain relation considering thermal effect can be determined as following

$$\varepsilon_{ij} = \left(\frac{1+\nu}{E} \sigma_{ij} - \frac{\nu}{E} \sigma_{kk} \delta_{ij} \right) + \alpha \Delta T \delta_{ij} \quad (3.18)$$

where ε_{ij} , σ_{ij} represent strain tensor and stress tensor respectively, E is elasticity modulus, ν is Poisson's ratio, δ_{ij} is kronecher symbol, α is thermal expansion coefficient, ΔT is temperature increment. While, the constitutive equation under diffusion caused volumetric expansion situation is accessible to be written by

$$\varepsilon_{ij} = \left(\frac{1+\nu}{E} \sigma_{ij} - \frac{\nu}{E} \sigma_{kk} \delta_{ij} \right) + \frac{\Omega \Delta c}{3} \delta_{ij} \quad (3.19)$$

It is evident that one can make an analogy between these two constitutive equations as

$$\alpha \Delta T = \frac{\Omega \Delta c}{3} \quad (3.20)$$

Associating the above analogous term, ABAQUS coupled thermal-stress analysis could be converted to figure out targeted coupled diffusion-stress problem. With the consideration of a free-standing electrode particle surrounding by electrolyte, the rigidity of electrolyte is far less than electrode particle. One can assume that there is no traction at the particle surface. The mechanical boundary condition can then be set as traction-free surface for particle in this study [2-13] and expressed as

$$F_{sx} = \sigma_x l + \tau_{xy} m + \tau_{xz} n = 0 \quad (3.21-1)$$

$$F_{sy} = \tau_{yx} l + \sigma_y m + \tau_{yz} n = 0 \quad (3.21-2)$$

$$F_{sz} = \tau_{zx} l + \tau_{zy} m + \sigma_z n = 0 \quad (3.21-3)$$

where l , m , n are direction cosines between axis and external normal.

3.2.3 Fracture assessment approach

Based on coupled diffusion-stress analysis, it is accessible to employ the Extended Finite Element Method (XFEM) in ABAQUS [3-5] to simulate the crack fracture and material damage of electrode particle. When using the conventional finite element method to simulate the crack, it is required to consider the stress singularity of crack tip and the singular mesh should be employed to

model the crack tip for satisfying the non-continuity of the crack tip. The conventional finite element method uses the continuous function as shape function. For addressing the discontinuous geometry problem such as cracking, it is needed to set the crack plane as the edge of the element and crack tip as the node of the element. It is also required to generate high-density mesh around crack tip and carry out continuous mesh redivision in the simulation of crack propagation, which makes the finite element modelling complicated.

As an extension of conventional finite element method, the conceptual framework of XFEM was presented by Belytschko and Black [3-6]. Comparing with traditional FEM, The biggest convenience of XFEM is that XFEM is able to simulate crack initiation and propagation along an arbitrary path with no need to mesh for matching the geometry of the discontinuities [3-7] and crack can penetrate element to develop, as shown in Fig 3.2 [3-8] . The XFEM is based on the principle of unity partition, the enrichment function reflecting discontinuity feature is added to finite element shape function. It includes asymptotic crack-tip function describing the stress singularity in crack tip area and jump function representing displacement jump crossing crack surfaces. The displacement vector function including enrichment function can be written as following

$$u = \sum_{I=1}^N N_I(x) \left[u_I + H(x)a_I + \sum_{\alpha=1}^4 F_{\alpha}(x)b_I^{\alpha} \right] \quad (3.22)$$

In Eq. 3.32, $N_I(x)$ is nodal shape function. The first item in parentheses represents nodal displacement vector. a_I in second item is nodal enriched degree of freedom vector for node on the crack penetrated element shown as green circle in Fig 3.2. $H(x)$ is jump function. b_I^{α} in third item is nodal enriched degree of freedom vector for node on element where crack tip is located, shown as grey square in Fig 3.2. $F_{\alpha}(x)$ is asymptotic crack-tip function.

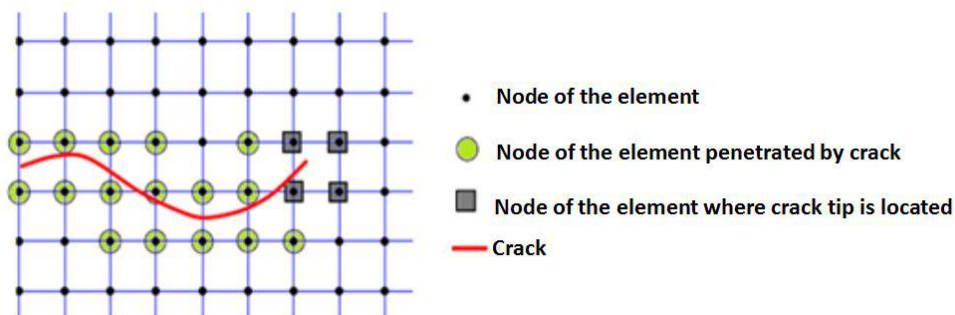


Fig 3. 2 Schematic diagram of crack penetrating element with XFEM [3-8]

In ABAQUS, there are two damage modeling methods within XFEM framework to model propagation crack, which are linear elastic fracture mechanics (LEFM) approach and cohesive segment approach [3-5]. The LEFM based approach uses the virtual crack closure technique (VCCT) to calculate the strain energy release rate at the crack tip and compares with critical value. There are limitations to this approach and it is more appropriate for brittle fracture.

The cohesive segment approach uses the traction-separation law shown in Fig 3.3 to describe the degradation and eventual failure of enriched element, and can be applied for brittle and ductile fracture. In this damage principle, the initial material response is assumed to be linear before damage initiation. When the stress or strain satisfies specific damage initiation criteria, the degradation begins accompanying with crack initiation. The following damage accumulation and crack propagation proceed in a simultaneous way, while the bearing capacity of enriched element declines with the crack growth. The eventual failure occurs when the critical failure condition is achieved and the element is going to be completed cracked.

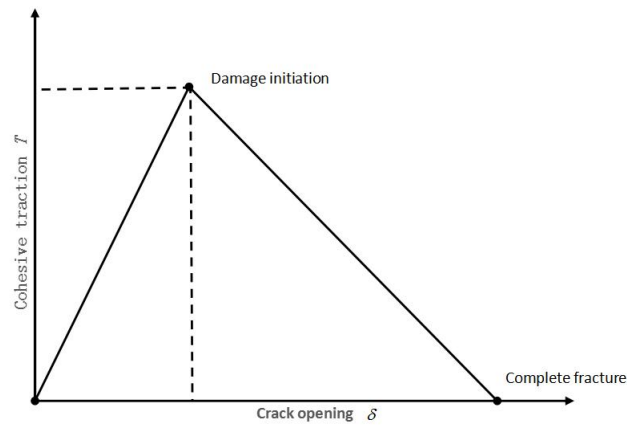


Fig 3. 3 Traction-separation law

For cohesive damage initiation, there are three stress based and three strain based criteria [3-9].

- Maximum principal stress criterion $f = \frac{\langle \sigma_n \rangle}{\sigma_{\max}^0}$ $\langle \sigma_n \rangle = \begin{cases} \sigma_n & \text{for } \sigma_n > 0 \\ 0 & \text{for } \sigma_n < 0 \end{cases}$
- Maximum principal strain criterion $f = \frac{\langle \varepsilon_n \rangle}{\varepsilon_{\max}^0}$ $\langle \varepsilon_n \rangle = \begin{cases} \varepsilon_n & \text{for } \varepsilon_n > 0 \\ 0 & \text{for } \varepsilon_n < 0 \end{cases}$
- Maximum nominal stress criterion $f = MAX \left\{ \frac{\langle \sigma_n \rangle}{N_{\max}}, \frac{\sigma_t}{T_{\max}}, \frac{\sigma_s}{S_{\max}} \right\}$ $\langle \sigma_n \rangle = \begin{cases} \sigma_n & \text{for } \sigma_n > 0 \\ 0 & \text{for } \sigma_n < 0 \end{cases}$
- Maximum nominal strain criterion $f = MAX \left\{ \frac{\langle \varepsilon_n \rangle}{\varepsilon_n^{\max}}, \frac{\varepsilon_t}{\varepsilon_t^{\max}}, \frac{\varepsilon_s}{\varepsilon_s^{\max}} \right\}$ $\langle \varepsilon_n \rangle = \begin{cases} \varepsilon_n & \text{for } \varepsilon_n > 0 \\ 0 & \text{for } \varepsilon_n < 0 \end{cases}$
- Quadratic nominal stress criterion $f = \left(\frac{\langle \sigma_n \rangle}{N_{\max}} \right)^2 + \left(\frac{\sigma_t}{T_{\max}} \right)^2 + \left(\frac{\sigma_s}{S_{\max}} \right)^2$ $\langle \sigma_n \rangle = \begin{cases} \sigma_n & \text{for } \sigma_n > 0 \\ 0 & \text{for } \sigma_n < 0 \end{cases}$

- Quadratic nominal strain criterion $f = \left(\frac{\langle \varepsilon_n \rangle}{\varepsilon_n^{\max}} \right)^2 + \left(\frac{\varepsilon_t}{\varepsilon_t^{\max}} \right)^2 + \left(\frac{\varepsilon_s}{\varepsilon_s^{\max}} \right)^2 \langle \varepsilon_n \rangle = \begin{cases} \varepsilon_n & \text{for } \varepsilon_n > 0 \\ 0 & \text{for } \varepsilon_n < 0 \end{cases}$

Damage appears to occur when the following condition is satisfied, which is also the activation judgement condition of XFEM in ABAQUS

$$1.0 \leq f \leq 1.0 + f_t \quad (3.23)$$

where f_t in the equation is a self-set parameter for adjusting increment to satisfy damage criterion and usually takes 0.05.

For fracture failure, there are two critical criteria by defining the critical equivalent separation displacement and the critical fracture energy. The equivalent separation displacement δ_e can be given as

$$\delta_e = \sqrt{\delta_n^2 + \delta_s^2 + \delta_t^2} \quad (3.24)$$

where δ_n is normal separation displacement. δ_s and δ_t respectively denote two tangential separation displacements. The fracture happens when the equivalent separation displacement reaches the critical value δ_e^c . The fracture energy is the area enclosed by the traction-separation curve.

According to the following relation, it is accessible to use the critical fracture energy G^c instead of the critical equivalent separation displacement, and two failure criteria are theoretically interchangeable.

$$G^c = \frac{\delta_e^c T_e^0}{2} \quad (3.25)$$

In this work, with using cohesive segment approach under ABAQUS XFEM framework, the maximum principal stress criterion is used as the threshold for crack initiation, where damage occurs as the maximum principal stress exceeds material tensile strength. The critical fracture energy is introduced as the judgement condition for complete fracture.

3.3 Validation of the coupled diffusion-stress methods

Before any results can be considered, it is important to ensure that the steps involved in our coupled diffusion-stress methods are correct and give accurate results. One way to do this is to compare the results obtained to those obtained in previous studies. A previous study, by Zhang et al

[2-13], has been used as a reference for the methods employed in this work. Where the concentration and stress fields of an ellipsoid particle under lithiation and delithiation process are analysed.

The coupled diffusion-stress analysis is conducted for the same configuration with same material properties as shown in Fig 3.4 (a) and Table 3.1 by using two developed finite element subroutines (diffusion driven approach and chemical potential driven approach). According to the description in reference, the ellipsoid volume is decided to be $V = 4\pi \times 5^3/3 \text{ um}^3$ and the lengths of three semiaxes a, b, and c are respectively defined as 4um, 4um and 7.81um with aspect ratio 1.953. The boundary condition is consistent with that of reference model and set as traction-free for particle surface. A typical mesh distribution of ellipsoidal particle is shown in Fig 3.4 (b).

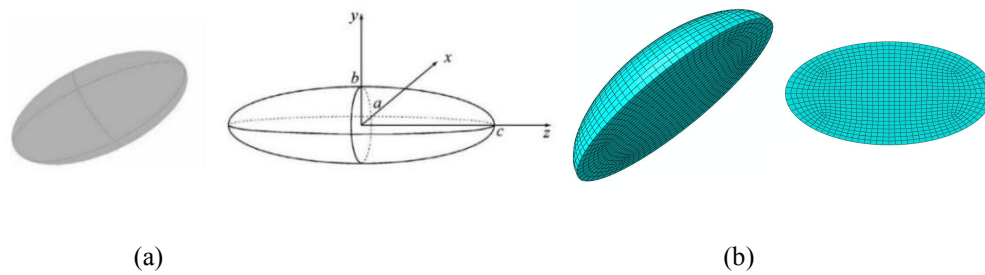


Fig 3. 4 Schematic of (a) an ellipsoidal particle [2-13], (b) mesh distribution

Table 3.1 Material parameters of Mn_2O_4 used in calculation for verifying the proposed methods. [2-13]

Property	Value
Young's modulus (GPa)	10
Poisson's ratio	0.3
Maximum concentration (mol/m^3)	22900
Diffusivity (m^2/s)	7.08E-15
Partial molar volume (m^3/mol)	3.497E-6
Current density (A/m^2)	2

In Fig 3.5, the comparisons of concentration and stress fields from reference results and the diffusion driven method are given. It is observable that, the contours of both concentration and stress from two methods match well. The long axis tip regions gather the most Li ions and the short axis tip regions experience the maximum von Mises stress. With the same maximum Li concentration, the variance of calculation of von Mises is around 5.8%. Fig 3.6 presents the calculation results from Ref [2-13] and the chemical potential driven approach. In this case, the calculation variance of von Mises is about 2.8%. Both of two proposed methods present reliable calculation accuracy of coupled diffusion-stress analysis and the calculation variance with reference results can be further reduced via model mesh adjustment.

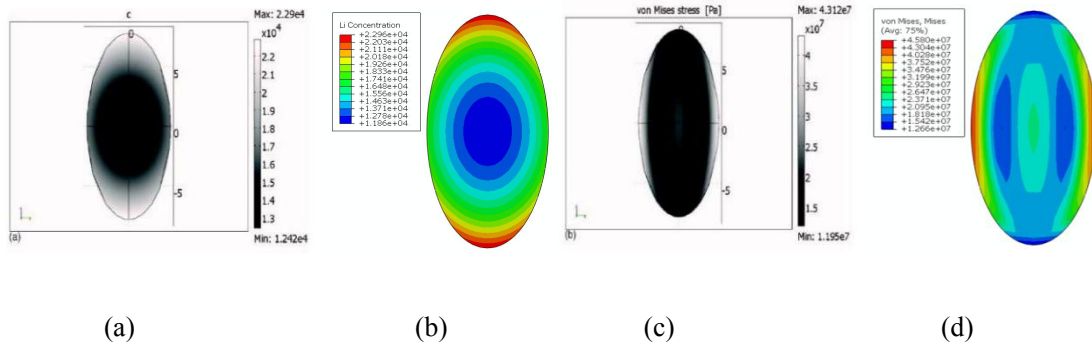


Fig 3. 5 The comparison between Ref [2-13] and the diffusion driven approach (a) concentration of Li at the end of discharge from reference, (b) concentration of Li at the end of discharge from the diffusion driven approach, (c) von Mises stress at the end of discharge from reference. (d) von Mises stress at the end of discharge from the diffusion driven approach

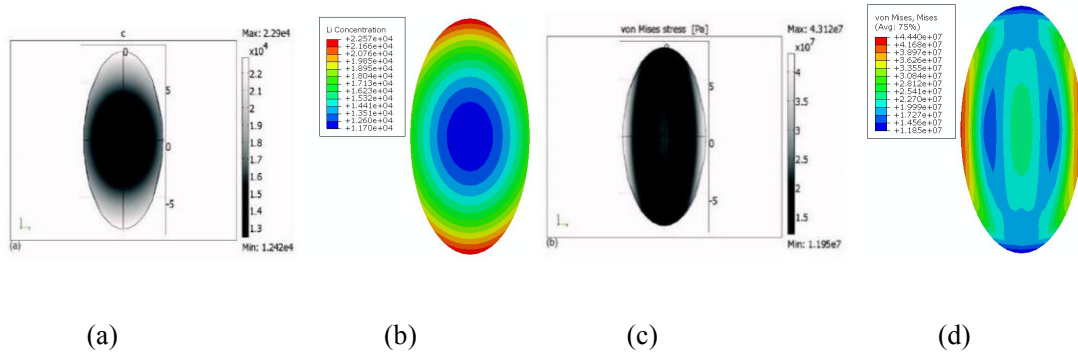


Fig 3. 6 The comparison between Ref [2-13] and the chemical potential driven approach (a) concentration of Li at the end of discharge from reference, (b) concentration of Li at the end of discharge from the chemical potential driven approach, (c) von Mises stress at the end of discharge from reference. (d) von Mises stress at the end of discharge from the chemical potential driven approach

For further considering the mesh sensitivity, it is available to calculate the diffusion-induced stress under different mesh density via using two developed methods, as shown in Fig 3.7. The reference value of maximum von Mises stress is known as 43.12 MPa and the calculated stress values from two proposed methods are in the range of 38 MPa - 45 MPa. The comparison results present that the two proposed couple diffusion-stress analysis method are capable of providing reasonable calculation result and can be applied for subsequent numerical analysis.

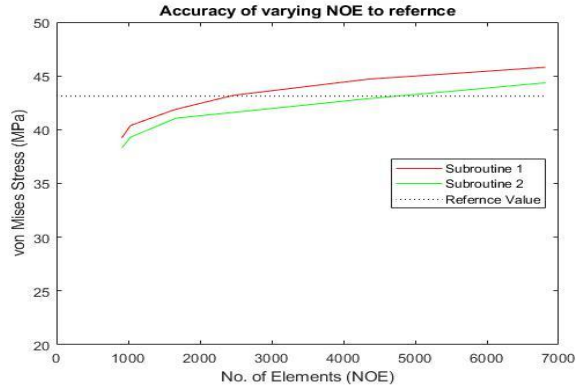


Fig 3. 7 The comparison of diffusion induced stress between reference and the developed two methods with varying mesh density (subroutine 1 is the diffusion driven approach, subroutine 2 is the chemical potential driven approach)

3.4 Diffusion induced stress of primary electrode particle

3.4.1 Finite element model and material properties

As described above, scholars have proposed various methods including analytical method, finite element method, finite difference method, etc. to simulate the diffusion induced stress within particles. These methods provide different perspectives on studying the problem and contribute to understand the mechanism affecting the structural integrity of battery electrode. In this section, the research purpose is the cracking behaviour of the primary particle under lithiation-delithiation condition. Due to the complexity of structure considering cracks, employing the analytical solutions of diffusion-induced stress as the basis to study the cracking behaviour of particle is not easily accessible. Therefore, in this work, the finite element software is employed by developing user subroutines to conduct the coupled diffusion-stress analyses and the following cracking assessment.

The finite element model of primary electrode particle is presented in Fig 3.8 (a) and (b), where the particle surface is traction free for the case of independent particle. C3D20RT element type is used for coupled diffusion-stress analysis. The diffusion flux applied on the particle surface can be calculated based on Eq 3.15 with given current density and the variation rule of diffusion flux in one lithiation-delithiation cycle is shown in Fig 3.8 (c). All material parameters involved in this simulation work are summarized in Table 3.2. The material is assumed as isotropy due to the fact that microcosmic grains are distributed randomly. It is worth noting that the material parameters come from different references. As the simulation involves multiple electrochemical and mechanical parameters, different research teams may just focus on some specific parameters and the workload of measurement on a single parameter is relatively large. Hence, the relevant parameters need to be obtained from different references. As discussed above, an equivalent thermal-stress analysis is

applied for the diffusion-stress analysis with developing user subroutines, and the corresponding thermal properties inputted in the thermal analysis module can be concluded here. The density and specific heat are set as 1. The numerical value of conductivity is equal to the diffusivity and the coefficient of thermal expansion is one third of partial molar volume, as $\alpha = \frac{\Omega}{3}$. Besides, when performing the calculation with using ABAQUS software, it is required to unify the units of variables according to the size characteristic of analysis model. According to the statistical analysis on the size distribution of NCM cathode samples under micrometer scale, seven various particle diameters are simulated under a large range of current densities. The current density can be obtained as C-rate multiplied capacity, then divided by the area of electrode.

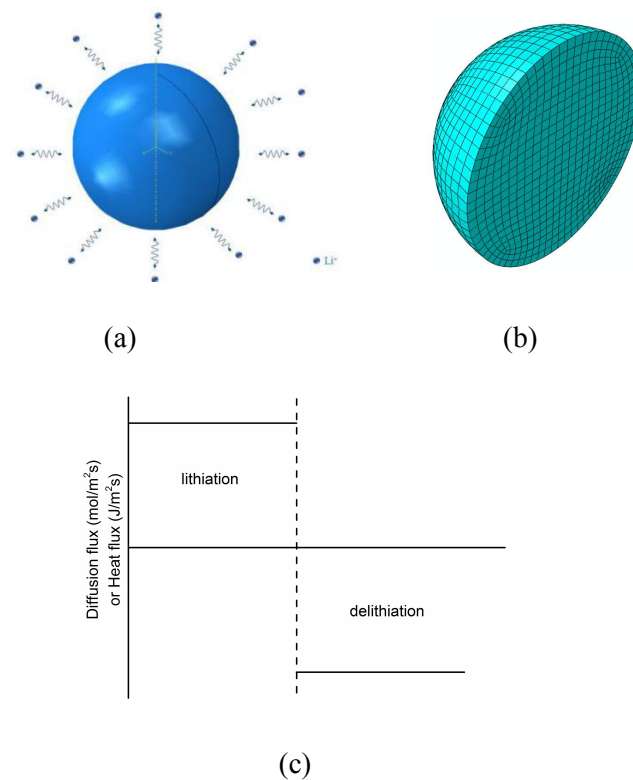


Fig 3. 8 Schematic illustrations of (a) primary electrode particle, (b) mesh distribution, (c) loading condition in a lithiation-delithiation cycle

Table 3.2 Material properties of NCM electrode material

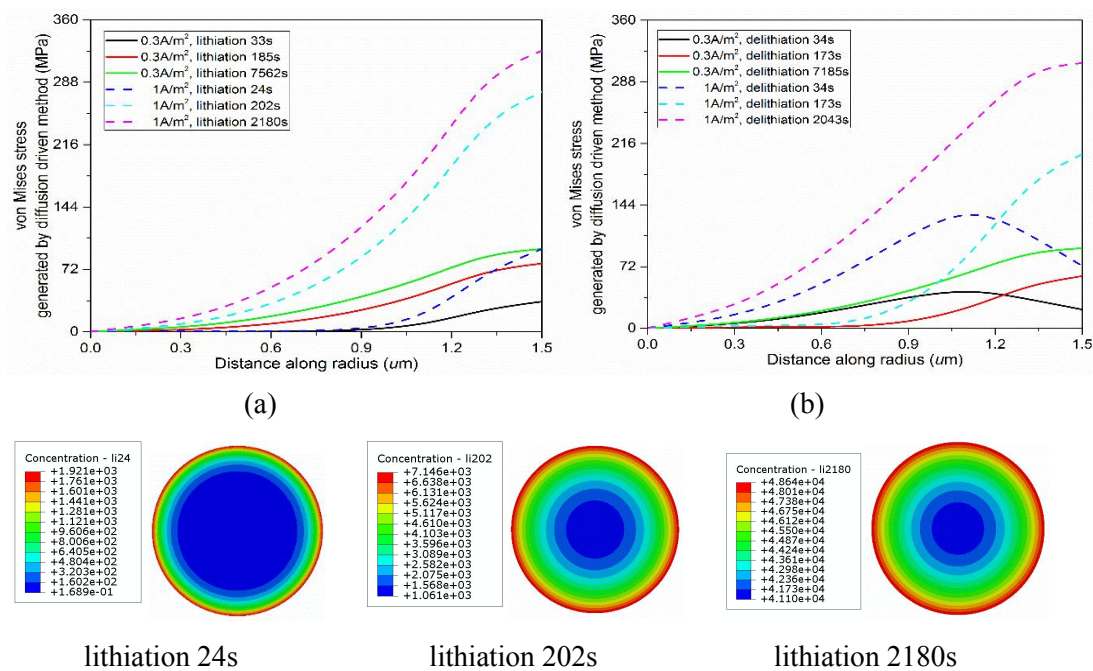
Property	Value
Particle diameter (um)	0.5, 0.7, 1, 2, 3, 4, 5
Constant average Young's modulus (GPa)	125 [3-10]
Poisson's ratio	0.3 [3-10]
Diffusivity (m²/s)	1E-15 [3-11]
Partial molar volume (m³/mol)	2.1E-6 [3-12]
Current density (A/m²)	0.01~4
Damage initiation stress (MPa)	100 [2-55]
Fracture energy (J/m²)	0.11 [2-55]

3.4.2 Stress inside primary electrode particle

The evaluation of diffusion-induced stress works as the basis for failure analysis of electrode material, and this section gives the assessment of diffusion-induced stress of primary electrode particle. The comparison calculations of two coupling methods are performed, and the effects of diffusion on DIS are also discussed.

Fig 3.9 (a) and (b) exhibit the distribution of von Mises stress along the radius of NCM primary particle under current density of 0.3 A/m^2 and 1 A/m^2 with 125 GPa Young's modulus during lithiation and delithiation phases respectively, where the couple effect between Li-ion diffusion and diffusion-induced stress is implemented by diffusion driven method. Fig 3.9 (c) leaves the contours of Li-ion concentration at different moments within lithiation and delithiation phases, and Fig 3.9 (d) gives the corresponding contours of von Mises stress.

During the lithiation and delithiation processes, the magnitude of von Mises stress at one point is positively related to the distance from this point to particle centre at the most moments, where the maximum value always takes place at the surface of primary particle. The exceptional case is at the initial phase of delithiation process, when the maximum von Mises stress happens at the interlayer of particle owing to the geometry configuration and conversion of diffusion direction. Besides, it is obvious to see that higher current density will reduce the charging and discharging time, but generate greater stress profile and stress gradient along radius, which ulteriorly bring more threat to the mechanical stability. Hence, it is significant to assess the critical current density so as to reach the shortest charging-discharging time and maintain the better mechanical stability.



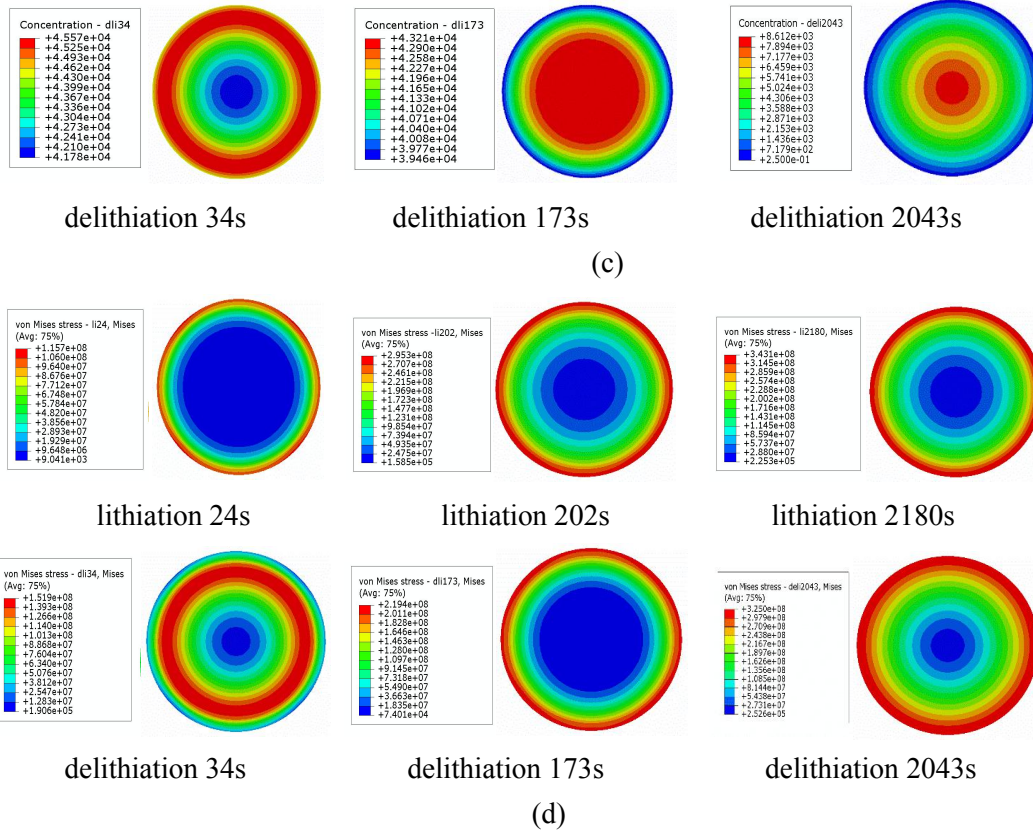


Fig 3. 9 The evolution of von Mises stress produced by diffusion driven method for $3\mu\text{m}$ diameter particle, stress distribution along radius during (a) lithiation process (b) delithiation process under $0.3\text{A}/\text{m}^2, 1\text{A}/\text{m}^2$ (c) contours of Li-ion concentration under $1\text{A}/\text{m}^2$ at different moment (d) contours of von Mises stress under $1\text{A}/\text{m}^2$ at different moments

Fig 3.10 shows the profiles of maximum principal stress under the same simulation conditions with von Mises stress. In comparison to von Mises stress, the maximum principal stress of one point presents a negative correlation with the increase of the distance from the point to particle core at the lithiation phase. The core of particle always experiences the extremum of maximum principal stress, however the corresponding von Mises stress here is zero. It is caused by the fact that the spherical geometry configuration makes the core of particle experience three equivalent principal stress components. For the delithiation process, maximum principal stress at the centre of particle gradually converts from tensile stress to compressive stress owing to the variation of concentration gradient, while particle surface maintains tensile stress status during the overall deintercalation process. Considering the fact that the extremum of maximum principal stress in intercalation phase is greater than that of deintercalation phase and fracture only occurs under tensile stress, it is concluded that the core of primary particle is the most dangerous location under strength fracture condition. Besides, the maximum principal stress field is more worthy of attention when employing the maximum principal stress failure criterion in fracture analysis.

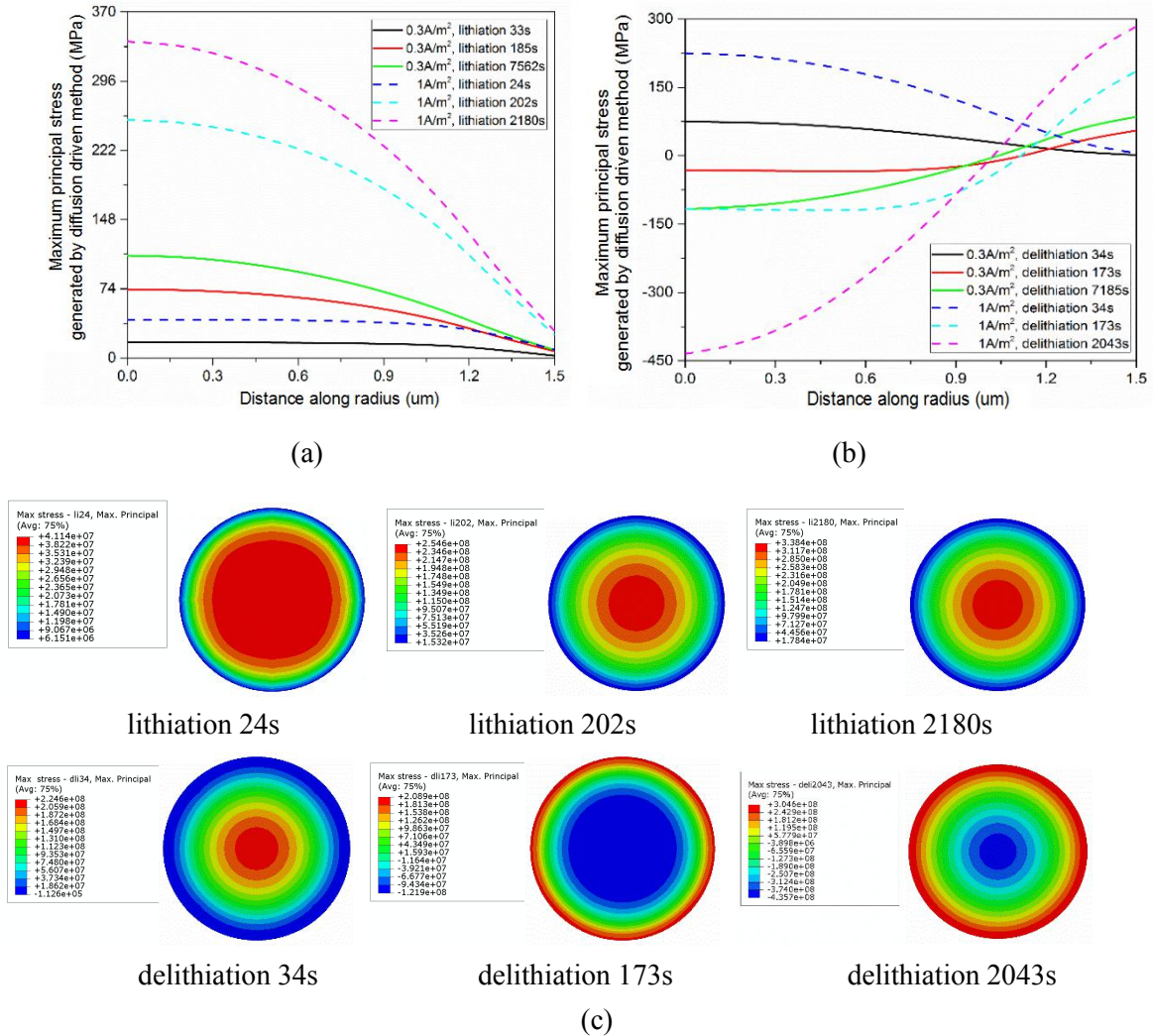


Fig 3. 10 The evolution of maximum principal stress produced by diffusion driven method for $3\mu\text{m}$ diameter particle, stress distribution along radius during (a) lithiation process (b) delithiation process under $0.3\text{A}/\text{m}^2, 1\text{A}/\text{m}^2$, (c) contours of maximum principal stress under $1\text{A}/\text{m}^2$ at different moments

Based on the chemical potential driven approach, it is accessible to develop another set of ABAQUS UMATHT subroutines for simulating the diffusion-induced stress and further make a comparison with the results produced from the diffusion driven approach. Two sets of juxtaposition in Fig 3.11 exhibit the computed maximum principal stress from diffusion driven method and chemical potential driven method. Fig 3.11 (a) shows the stress distribution along the radius of $3\mu\text{m}$ diameter particle with 125GPa Young's modulus under $0.3\text{A}/\text{m}^2$ current density and Fig 3.11 (b) is for the same particle under $1\text{A}/\text{m}^2$. It shows that, under relatively low current density condition ($0.3\text{A}/\text{m}^2$), two coupled diffusion-stress methods produce the proximate results. While under high current density ($1\text{A}/\text{m}^2$), the calculation results show the significant differences on the centre of particle at the end phase of intercalation process and deintercalation process, where the differences reach 11.8% and -13.1% respectively.

The variance of calculation results lies on the different ways to define diffusion flux so as to incorporate the bidirectional effect between Li-ion diffusion and stress generation. For diffusion driven method, the coupling effect is incorporated in updating the diffusivity. While for the chemical potential driven method, the expression of chemical potential in the definition of diffusion flux considers this reciprocal influence. With the consideration of calculation efficiency, the chemical potential driven method costs more computing effort than the diffusion driven approach, due to the requirement of distance judgement between current integration point and every other integration points at each iteration in ABAQUS subroutines. Hence, it is more efficient and also reliable to employ the diffusion driven approach to calculate the diffusion-induced stress under relatively low current density condition.

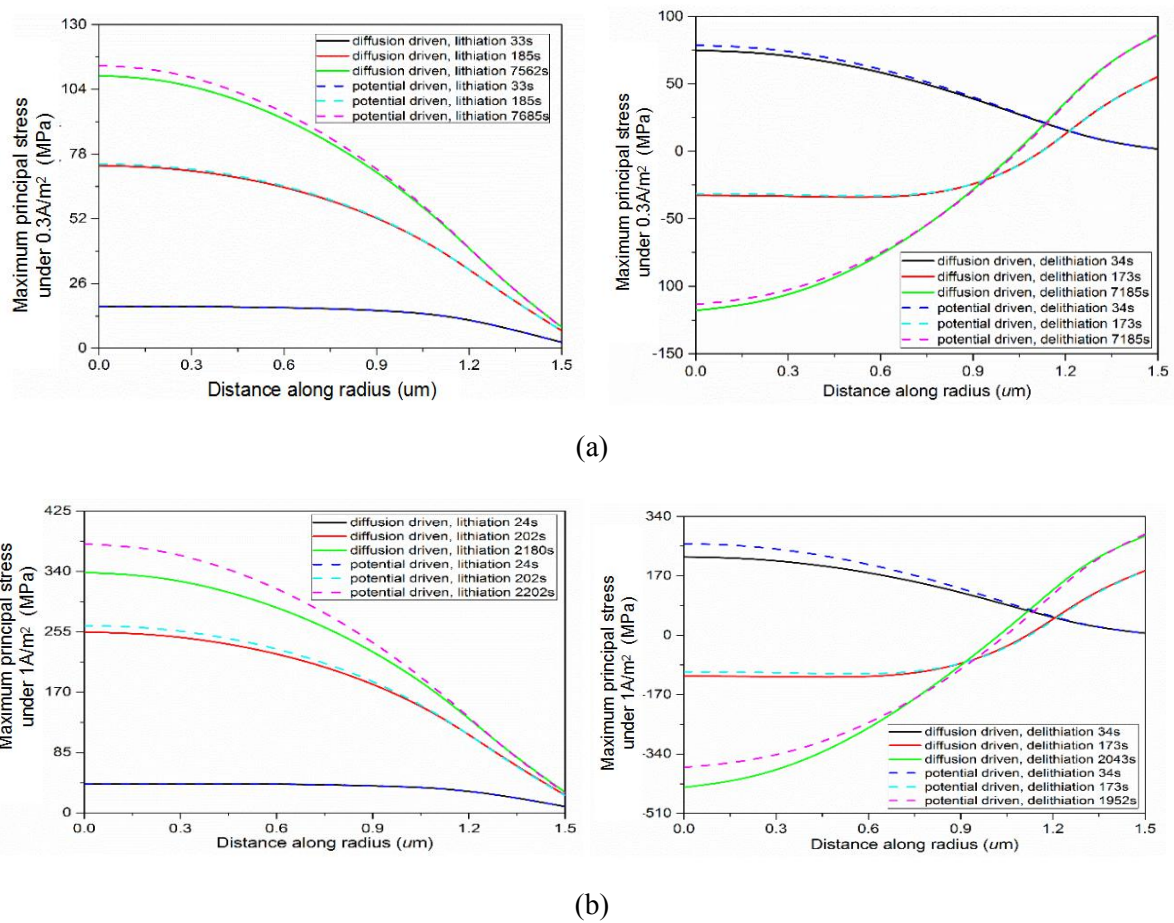


Fig 3. 11 Comparison of diffusion induced stress profile generated by diffusion driven method and chemical potential driven method for 3 μ m diameter particle with 125GPa constant average Young's modulus (a) under 0.3A/m² current density (b) under 1A/m² current density

It is well known that the diffusion behaviour will influence the material properties of active cathode. According to the experimental results [3-7], there exists a significant hardening phenomenon of NCM ternary material. The Young's Modulus of NCM523 cathode material will decline with the Li-ion deintercalation process owing to the decrease of bonding strength between transition metals

ions and oxygen. It is shown that the Young's Modulus monotonically changes from 145GPa of $\text{LiNi}_{0.5}\text{Co}_{0.2}\text{Mn}_{0.3}\text{O}_2$ to 111GPa of $\text{Li}_{0.5}\text{Ni}_{0.5}\text{Co}_{0.2}\text{Mn}_{0.3}\text{O}_2$. Therefore, concentration dependent Young's Modulus should be considered as a key factor affecting the generation of diffusion-induced stress. Fig 3.12 (a) shows the variation of Young's Modulus for NCM523 cathode material with Li-ion concentration based on experimental data. In the figure, 1 on the x-axis represents $\text{LiNi}_{0.5}\text{Co}_{0.2}\text{Mn}_{0.3}\text{O}_2$ and 0.5 on the x-axis denotes $\text{Li}_{0.5}\text{Ni}_{0.5}\text{Co}_{0.2}\text{Mn}_{0.3}\text{O}_2$. The Young's modulus can then be expressed as a function of concentration which is further determined by coordinates and time, as $E = f[c(x,t)]$. For comparison calculation, constant average Young's modulus is still set as 125GPa during intercalation-deintercalation course.

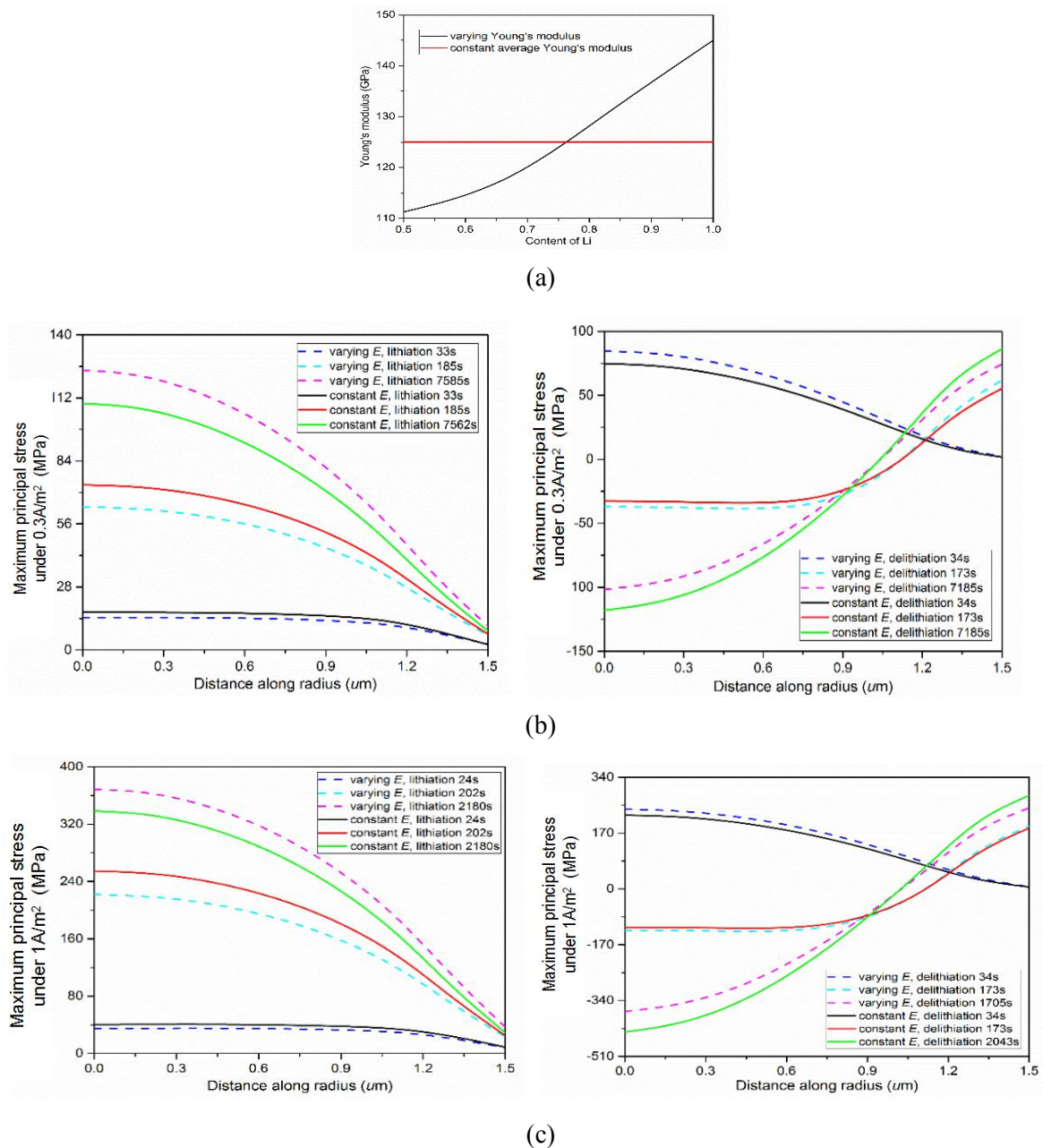


Fig 3. 12 The effect of varying Young's modulus on maximum principal stress (a) the variation of Young's modulus with Li concentration (b) comparison of maximum principal stress with varying

Young's modulus and constant Young's modulus of particle under $0.3A/m^2$ during lithiation-delithiation phases (c) comparison of maximum principal stress with varying Young's modulus and constant Young's modulus of particle under $1A/m^2$ during lithiation-delithiation phases

Fig 3.12 (b) makes a comparison of maximum principal stress respectively considering concentration dependent Young's modulus and constant Young's modulus under $0.3A/m^2$ during lithiation and delithiation phases. Fig 3.12 (c) gives the comparison of maximum principal stress under $1A/m^2$ considering two kinds of change of Young's modulus. It can be seen that concentration dependent Young's modulus has an obvious impact on the evolution of diffusion-induced stress. On the whole, stress evolution trends under $0.3A/m^2$ and $1A/m^2$ are almost analogous. Apparently, at the initial phase of lithiation course and the end phase of delithiation course, the maximum principal stress generated with constant Young's modulus is greater than that of concentration dependent Young's modulus. Conversely, at the relatively deep li-embedding stage including the end phase of lithiation course and the initial phase of delithiation course, maximum principal stress with varying Young's modulus exceeds that of constant average Young's modulus. It is due to the fact that the maximum principal stress is in direct proportion to the magnitude of Young's modulus, which is positively determined by Li-ion concentration. Associating with the fact that cracking fracture is always caused by tensile stress, it can be concluded that the changing Young's modulus caused by Li-ion concentration variation will aggravate the fracture at the particle centre within lithiation phase, but is beneficial for avoiding fracture at particle surface during delithiation stage.

3.5 Fracture evaluation

3.5.1 Crack initiation

The cracking of cathode under DIS will expose fresh surfaces of active material to the electrolyte and influence the stability of the battery. In addition, the cathode material under different electrochemical loads will be in different cracking stages which affect battery performance to varying degrees. Hence, this work conducts the cracking assessment including initiation, propagation and fracture phases for primary electrode particle, and studies the critical triggering conditions for various cracking status. Based on the coupled diffusion-stress analysis, ABAQUS extended Finite Element Method (XFEM) is employed to investigate the mechanical fracture mechanism of NCM primary particle. Where the material degradation and crack initiation happen when the maximum principal stress within enriched element reaches the damage initiation stress.

In the ideal state, the spherically symmetrical geometry model, boundary conditions and uniform material properties will generate spherically symmetrical stress field distributed like the above stress calculation results. Associating the maximum principal stress failure criteria with the maximum principal stress distribution of the particle shown in Fig 3.10, crack and damage will initiate from the particle centre. Nevertheless, the lack of stress concentration point around the particle centre will lead

to the result that crack cannot grow along specific direction after initiation. Fig 3.13 (a) exhibits the damage distribution of 3 μm particle under 0.2875A/m² with spherically symmetric stress field. Where the variable STATUSXFEM presents the status of enriched element, and it varies from 0 (non-damage status) to 1 (completely cracked). It can be seen that the damage initiates at the centre of particle, but there is no existing of crack in the centre zone. Fig 3.13 (b) presents the TXM tomogram of individual NCM particle after charging at C/3 rate [3-13]. Where the relation between C-rate and current density is based on the parameter characteristics of practically tested Li-ion battery. In experiments, the capacity of coin cell is 0.1mAh. Under this case, the corresponding current density for C/3 is 0.294A/m². From TXM tomogram, it can be observed that the practical crack initiates at the centre of particle and gradually propagates outward along specific direction. In reality, this is due to the fact that the practical particles cannot be perfectly spherical, and the material is not absolutely uniform. Therefore, the practical diffusion-induced stress field cannot be spherically symmetrical within the particle.

In the finite element analysis, establishing irregular geometry model, adopting non-uniform material property and applying an additional stress disturbance can all be employed to simulate this non-uniform stress field. In this work, for equivalently studying the crack behaviour under the non-uniform stress field, a tiny stress disturbance is added on the model. A concentrated force, which is far less than the diffusion-induced stress, is applied to an arbitrary point on the particle surface so as to simulate the non-perfectly symmetrical stress in practice, as given in Fig 3.14 (a). Fig 3.14 (b) shows the contour of non-uniform maximum principal stress for 3 μm particle under 0.2875A/m² with considering the stress disturbance. From which it can be seen that the integral stress distribution is spherically symmetrical except the finite area around the point applied the concentrated force. Under this circumstance, the integral stress status is not changed, but the introduction of the tiny stress disturbance applied on the arbitrary direction makes it accessible for crack to propagate.

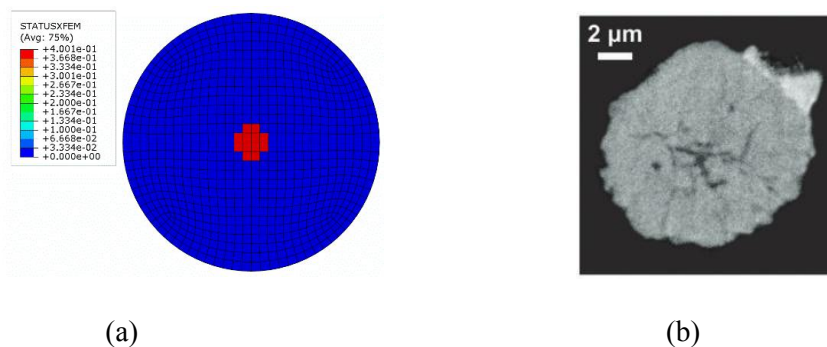


Fig 3. 13 (a) Damage distribution of 3 μm particle under 0.2875A/m² with spherically symmetric stress field, (b) TXM tomogram of individual NCM particle after charging at C/3 rate to 4.5V [3-13]

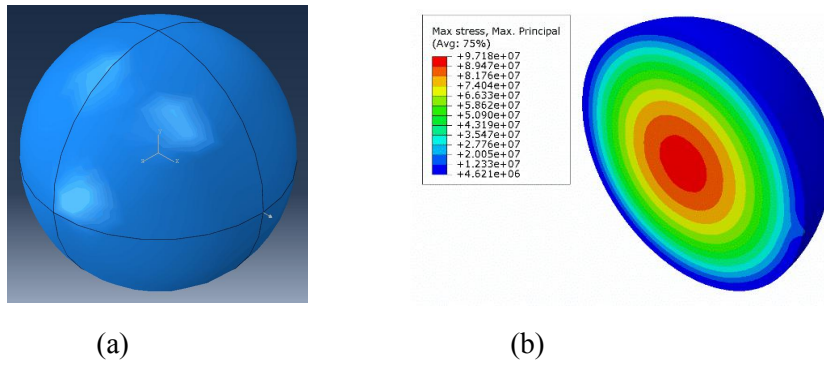


Fig 3. 14 (a) Particle model with a tiny stress disturbance acting on one arbitrary point of the surface, (b) The maximum principal stress distribution for 3μm particle under 0.2875A/m² considering stress disturbance

In addition, the appropriate mesh density is required to be defined in cracking simulations, as the mesh sensitivity is commonly regarded as a significant factor affecting the crack initiation status. Fig 3.15 presents the critical current density on crack initiation under different mesh densities for 3μm diameter particle. Obviously, the decreasing of element size is beneficial to obtain more accurate stress field. But the calculation results show that the critical current density keeps constant when the element size is less than 0.16. From the point of view of computational efficiency, the element size of 0.14 is set for the subsequent cracking analyses.

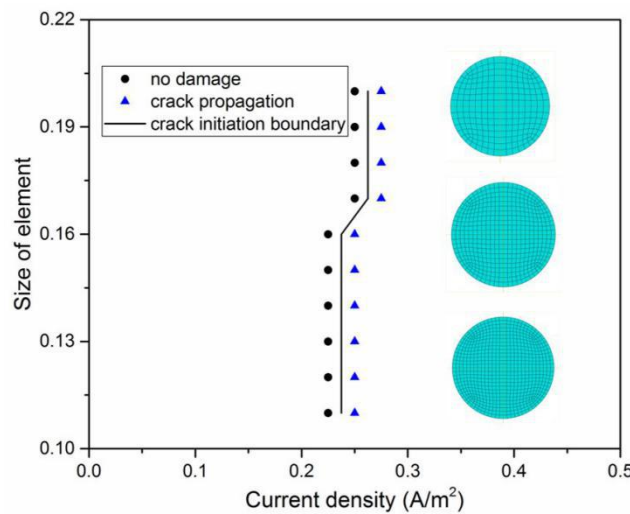
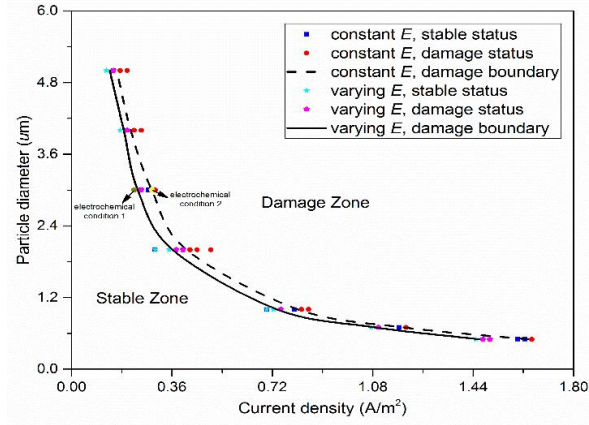


Fig 3. 15 The critical current density of crack initiation for 3μm particle under different mesh densities.

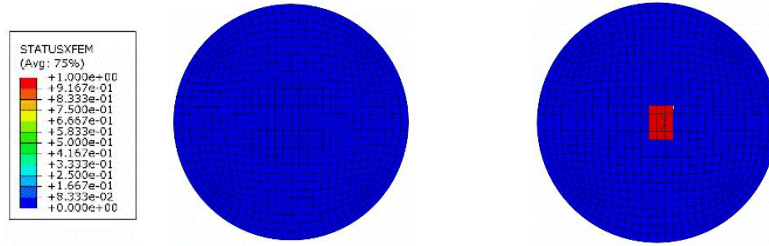
The crack initiation analysis of NCM primary particle is performed under diffusion-induced stress field with a stress disturbance. Fig 3.16 (a) plots the critical current density for crack initiation against varying particle size. Where the diffusion driven approach is applied for conducting coupled diffusion-stress analysis and the effect of diffusion on Young's modulus is also incorporated. In Fig 3.16 (a), blue diamond and light blue five-pointed star represent the permissible current density for corresponding particle size without crack initiation, red dot and magenta pentagram indicate

superfluous current density leading to cracking. Apparently, in both cases, the permissible current density for primary particle increases with the decline of particle size, and reducing the average size of particles is beneficial for improving the mechanical stability for NCM electrode. Fig 3.16 (b), (c) exhibit the distribution of crack and the status of enriched elements for NCM primary particle with concentration-dependent Young's modulus under no-damage current density (0.225A/m^2) and damage current density (0.2875A/m^2). Under no-damage current density, the particle maintains stable status. While for the damage current density, crack initiates at the core of particle which has been verified from TXM tomogram of NCM particle after charging in Fig 3.13 (b) [3-13].

In addition, Fig 3.16 (a) presents that the effect of diffusion on material property will weaken the electrochemical bearing capacity of NCM cathode material. For a specific particle size, the permissible current density with concentration dependent Young's modulus is lower than that with constant average Young's modulus. The result is due to the combined effect of stress generation process and maximum principal stress failure criterion. According to the evaluation of diffusion-induced stress, the extremum of tensile maximum principal stress always occurs at the end phase of lithiation process on the particle core, when the concentration dependent Young's modulus has exceeded the constant average Young's modulus on account of high Li-ion concentration. In this case, particle core with concentration dependent Young's modulus will experience relatively greater tensile maximum principal stress under the same current density comparing with the particle holding constant average Young's modulus. Hence, for NCM ternary cathode material with a specific maximum principal stress failure criterion, the consideration of concentration dependent Young's modulus will produce a relatively conservative crack initiation boundary than employing the assumed constant average Young's modulus, and it is therefore crucial to incorporate this diffusion effect on Young's modulus so as to obtain the accurate critical condition in the following fracture analysis. In view of particle at $3\mu\text{m}$ diameter, degradation and crack will occur under relatively low current density condition. According to comparative stress calculation analysis from the previous section, in this case, diffusion driven approach and chemical potential driven approach produce almost the same stress field. Therefore, for improving calculation efficiency, the diffusion driven approach will be employed to perform the coupled diffusion-stress analysis as the input condition for subsequent fracture evaluation.



(a)



(b)

(c)

Fig 3. 16 (a) Crack initiation boundary for 3 μ m diameter NCM primary particle considering concentration-dependent Young's modulus and constant average Young's modulus, crack and damage distribution with concentration-dependent Young's modulus under (b) 0.225A/m² (c) 0.2875A/m²

3.5.2 Crack propagation

After the maximum principal stress within enriched element exceeds the damage initiation stress, the crack will gradually propagate in the element until the moment when the critical fracture energy is reached and the corresponding element is exposed to fracture completely. With the proceeding of intercalation-deintercalation process, fracture occurs at more cohesive elements, which results in the overall mechanical destruction of the particle. Here, crack propagation analysis is conducted with using 0.11J/m² as critical fracture energy [2-55] and the failure boundary for NCM primary particle is established in Fig 3.17. In Fig 3.17 (a), crack initiation and fracture boundaries divide the entire failure diagram to three zones, which are named as fracture zone, crack propagation zone and stable zone respectively. The following equations are fitted to acquire the corresponding particle dimension with respect to crack initiation (d_i) and fracture (d_f) status under given current density.

$$d_i = 0.7424i_n^{-0.978} \quad (\text{crack initiation}) \quad (3.26-1)$$

$$d_f = 0.8155i_n^{-0.979} \quad (\text{crack fracture}) \quad (3.26-2)$$

where i_n denotes the applied current density.

It is worth noting that, for bulky particle (diameter over 4 μm), the crack initiation boundary and fracture boundary are close together. It presents that the bulky particle has brittle characteristic, and the crystal will be fracturing rapidly once crack initiates within crystal. The underlying reason for this phenomenon is that, the isometrical increment of current density will produce greater increment of stress for bulky particle comparing with small particle. Fig 3.17 (b) exhibits the variation of maximum principal stress against current density for different particle dimensions, where the slopes of curves show that the maximum principal stress increases faster with the increasing of current density for bulky particle. Hence, when the crack initiates in the bulky particle, the increasing of current density will lead to more drastic growth of maximum principal stress, which further accelerates the fracture of bulky particle.

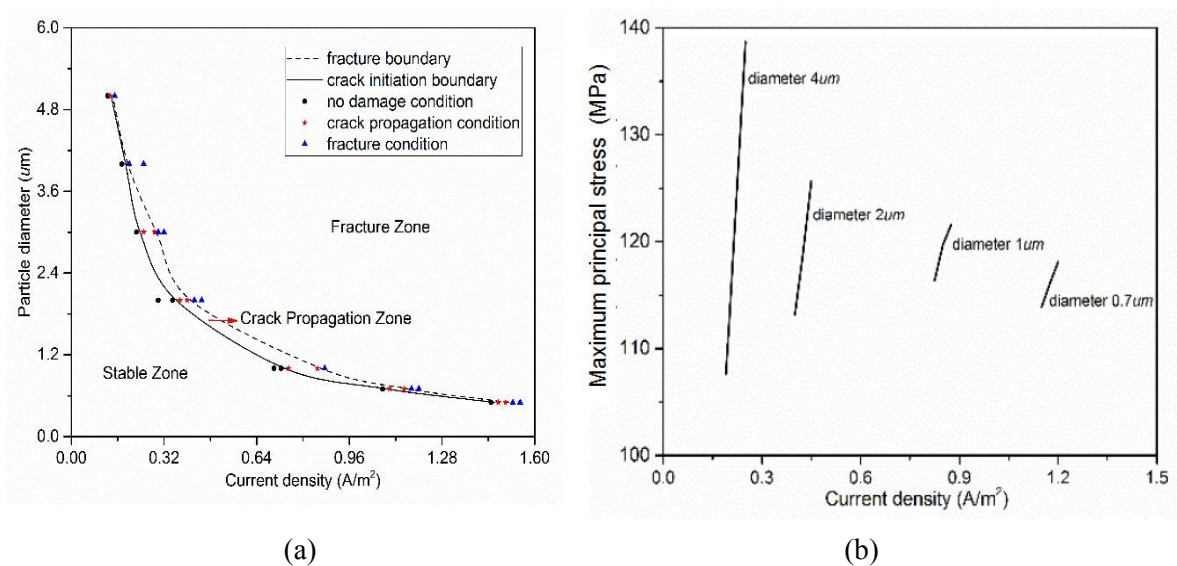


Fig 3. 17 (a) The fracture criteria diagram for NCM primary particle (b) the variation of maximum principal stress with current density for various particle dimensions

As the particle sizes under micrometre scale are not uniform, there is a part of particles that will initiate crack or fracture under a specific current density, while the rest of the particles with relatively smaller dimensions remain stable. Therefore, it is important to understand the relation between the critical particle dimension and the distribution of particle sizes in practical experiment samples. It is accessible to introduce a concept of fracture proportion by associating the critical failure diagram with statistical analysis of microscopic particle size. For the certain electrochemical load, it is available to acquire the critical particle dimension for crack initiation and fracture with using the established Eq. (3.26-1), (3.26-2). Experimentally, the ImageJ software is employed to measure and calculate the size distribution of NCM particles in the scanning electron microscopy (SEM) image as shown in Fig 3.18 (a), which is captured from a randomly selected area on NCM electrode sample before charging-discharging test. Fig 3.18 (b) plots the size distribution of NCM particles from SEM image. One can obtain the fracture proportion that how many percentage of electrode particles initiate crack

or fracture under specific current density. For electrode under 0.5A/m^2 current density, 22.22% particles occur cracking behaviour, among which 20.98% particles are completely fractured.

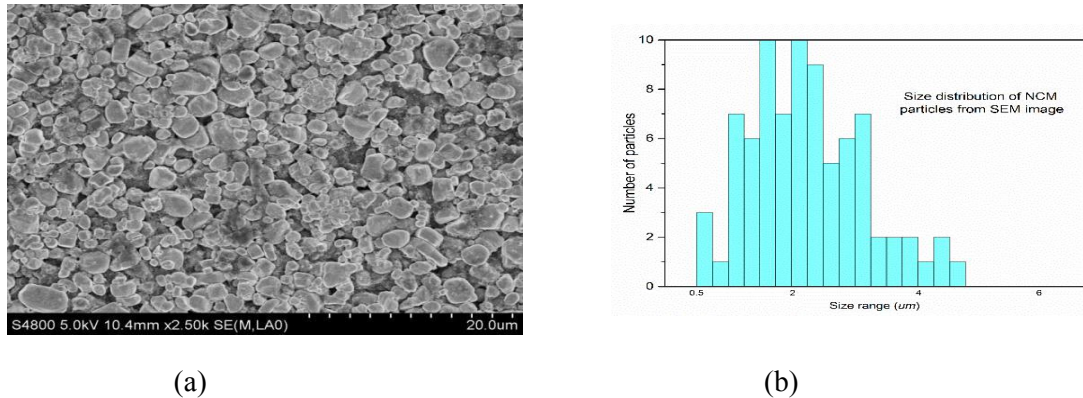


Fig 3. 18 (a) Scanning electron microscopy (SEM) image for a randomly selected area on NCM electrode before charging-discharging test, (b) size distribution of NCM particles from SEM image

Fig 3.19 and Fig 3.20 give the contours of crack initiation and propagation process for $3\mu\text{m}$ particle experiencing 0.37A/m^2 current density during lithiation and delithiation phases respectively. It can be seen that, during the lithiation phase, crack initiates at the core of particle and gradually develops until 370s. At this moment, crack propagates outward rapidly and symmetrically. Whereafter, the crack slowly develops until the end of lithiation phase. This simulation result is in accordance with TXM tomogram [3-13], that microdefect of individual NCM particle initiates from the core of particle and propagates outward. In addition, at this lithiation phase, the crack remains within the particle and has not penetrated the crystal.

In Fig 3.20, the propagation of cracks within the particle and at the particle surface during delithiation phase is collaterally exhibited with two angles. It can be observed that a new crack initiates on the particle surface at 204s, meanwhile the internal crack remains stable. The generation of surface crack can be explained from previous stress analysis that, during delithiation process, the maximum principal stress at outer surface zone keeps growing in tensile stress due to the change of concentration gradient caused by Li-ion flow. Afterwards, this newly formed crack rapidly propagates at the particle surface accompanying with the extension of internal crack. The two cracks ultimately converge, leading to the penetrative fracture of the particle, and the integral crack evolution process is so far given. It is worth noting that the crack growth is unstable within lithiation - delithiation process, where it rapidly develops in a short time and slowly grows in a long time. It is due to the fact that the growth of crack requires enough energy release. With the proceeding of lithiation-delithiation, the driving force of energy release of a region around crack accumulates and crack will rapidly grow when the energy release satisfies the resistance of surface energy. After rapid growth period, the energy relief is insufficient to meet the required resistance of surface energy for crack regrow, and the crack development temporarily halts. Hence, the crack growth shows time discontinuity.

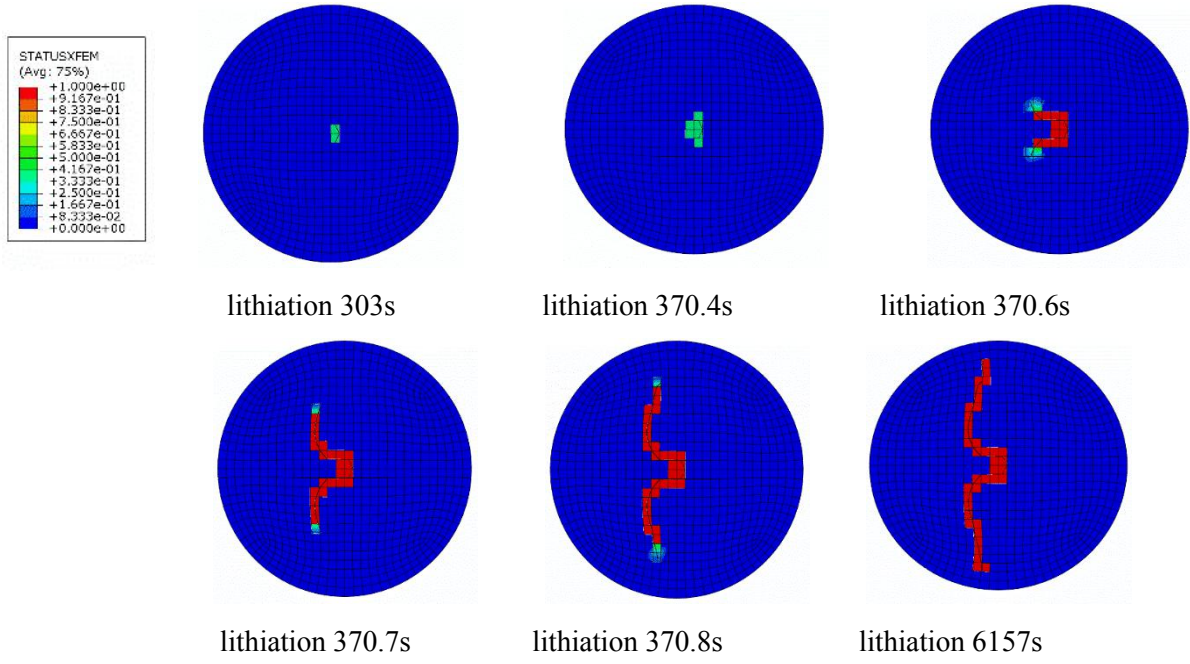


Fig 3. 19 The continuous process of crack initiation and propagation under 0.37A/m^2 current density at lithiation phase

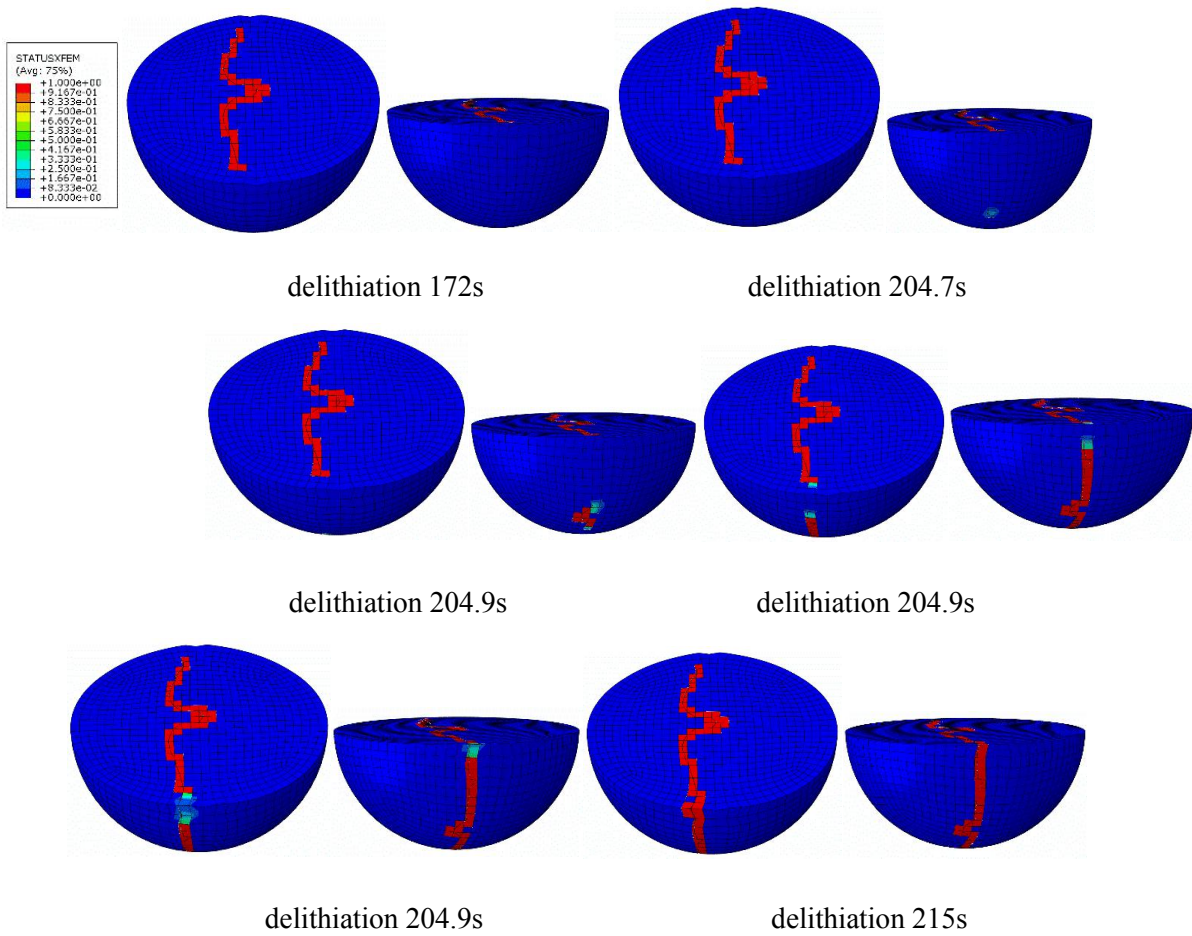


Fig 3. 20 The continuous process of crack initiation and propagation for $3\mu\text{m}$ diameter crystal under 0.37A/m^2 current density at delithiation phase

3.6 Conclusions

In this chapter, the coupled diffusion-stress analyses of NCM primary particle have been performed based on ABAQUS platform with developing user subroutines. Based on the obtained diffusion-induced stress field, the crack initiation, propagation and fracture evaluations of NCM particle have been comprehensively studied by using the ABAQUS extended finite element method (XFEM). The key conclusions are:

- (1) A diffusion driven approach and a chemical potential driven approach have been implemented by developing ABAQUS user subroutines, which make the ABAQUS platform available to conduct coupled diffusion-stress analysis.
- (2) In lithiation process, the extremum of the tensile maximum principal stress always occurs in the core of the particle. And with delithiation process, the extremum of the tensile maximum principal stress insides electrode particle changes from particle center to particle surface.
- (3) The critical failure diagrams and semi-empirical equations for crack initiation and fracture are established for estimating the cracking status of primary particle under certain electrochemical load. It is worth noting that, the bulky particles (diameter over 4 μm) show obvious brittle characteristics that the permissible electrochemical load of crack fracture is almost equal to that of crack initiation.
- (4) From the contour plots of typical crack onset and growth procedure, it is observable that the crack initiates at the core of particle and symmetrically propagates outward during lithiation phase. In delithiation phase, the internal crack gradually penetrates the particle accompanying with the formation of new surface crack.

3.7 References

- [3-1] J. Crank. The Mathematics of Diffusion. Oxford University Press, UK, 1979.
- [3-2] S.L. Zhang. Chemomechanical modeling of lithiation-induced failure in high-volume-change electrode materials for lithium ion batteries. Computational Materials, 2017, 3:7
- [3-3] M. Zhu, J. Park, A.M. Sastry. Fracture analysis of the cathode in Li-ion batteries: a simulation study. Journal of The Electrochemical Society, 2012, 159(4): A492-A498.
- [3-4] B. Pan, A. Asundi, H. Xie, J. Gao. Digital image correlation using iterative least squares and pointwise least squares for displacement field and strain field measurements. Optics and Lasers in Engineering, 2009, 47(7-8):865-874.
- [3-5] H. Hibbitt, B. Karlsson, P. Sorensen. ABAQUS Theory Manual, Version 6.12. Pawtucket, Rhode Island, USA, 2012.

- [3-6] T. Belytschko, T. Black. Elastic crack growth in finite elements with minimal remeshing. *International Journal for Numerical Methods in Engineering*, 1999, 45(5): 601-620.
- [3-7] F. Stuparu, D.M. Constantinescu, D.A. Apostol, M. Sandu. A combined cohesive elements-XFEM approach for analysing crack propagation in bounded joints. *The Journal of Adhesion*, 2016, 92:535-552.
- [3-8] H. Benzaama, M. Mokhtari, G. Sadek. Using XFEM technique to predict the damage of unidirectional CFRP composite notched under tensile load.
- [3-9] Z. Du. eXtended Finite Element Method (XFEM) in Abaqus. SIMULIA.
- [3-10] R. Xu, H. Sun, L. Vasconcelos, K. Zhao. Mechanical and structural degradation of $\text{LiNi}_x\text{Mn}_y\text{Co}_z\text{O}_2$ cathode in Li-ion Batteries: An Experimental study. *Journal of Electrochemical Society*, 2017, 164(13):A3333-A3341
- [3-11] A. Verma, K. Smith, S. Santhanagopalan, D. Abraham. K. Yao, P. Mukherjee. Galvanostatic intermittent titration and performance based analysis of $\text{LiNi}_{0.5}\text{Co}_{0.2}\text{Mn}_{0.3}\text{O}_2$ cathode. *Journal of The Electrochemical Society*, 2017, 164(13):A3380-A3392
- [3-12] O. Dolotko, A. Senyshyn, M.J. Muhlbauer, K. Nikolowski, H. Ehrenberg. Understanding structural changes in NMC Li-ion cells by in situ neutron diffraction. *Journal of Power Sources*, 2014, 255:197-203
- [3-13] P. Tsai, B. Wen, M. Wolfman, M. Choe, M. S. Pan, L. Su, K. Thornton, J. Cabana, Y. Chiang. Single-particle measurements of electrochemical kinetics in NMC and NCA cathodes for Li-ion batteries. *Energy and Environmental Science*, 2018, 11, 860.

Chapter 4

Cyclic plasticity behaviour of battery electrode

4.1 Introduction

As described in chapter 2.4, a low cyclic diffusion-induced stress far less than the limit load may lead to the electrode degradation due to the occurrence of cyclic plasticity failure. Besides, the lithiation caused expansion of electrode material will result in the potential extrusion force between neighbouring electrode configurations. This mechanical load will interact with cyclic diffusion-induced stress, and further lead to more obvious cyclic plasticity failure. The effects of different post yielding behaviours, as elasticity, shakedown and cyclic plasticity, on electrochemical performance of electrode have been discussed in Ref [2-63]. Especially, it has been experimentally demonstrated [4-1, 4-2] and numerically simulated [2-64, 4-3] that, the occurrence of potential ratcheting behaviour greatly influence the cycle ability of battery and electrode. Hence, the systematic study of cyclic plasticity behaviour of electrode is crucial for its safe operation subjected to electrochemical conditions [4-4].

However, the calculation of cyclic plasticity limits is a complex assignment and involves many mechanism issues. For efficiently obtaining boundary diagram to avoid alternating plasticity or incremental plastic collapse, a number of direct methods, including the mathematical programming methods [4-5, 4-6, 4-7], the Uniform Modified Yield (UMY) surface method [4-8], the Generalized Local Stress Strain (GLOSS) r-node method [4-9], the Elastic Compensation Method (ECM) [4-10] and the Linear Matching Method (LMM) [4-11, 4-12], built on the Koiter's [4-13] kinematic and the Melan's [4-14] static theorems have been developed and applied in shakedown and ratcheting analyses. In these methods, the LMM has been demonstrated to be capable of providing accurate evaluations on cyclic plasticity behaviour for complex structures under various loading conditions [4-15, 4-16], and has also been verified by comparing with experimental tests [4-17]. Besides, the LMM ABAQUS user subroutines [4-18] have been consolidated by the R5 Procedure [4-19] research programme of EDF Energy to the commercial standard, and widely used in academic research and industrial community. Therefore, the Linear Matching Method is adopted in this chapter to simulate the post yielding behaviour of electrode particle under cyclic electrochemical conditions.

The objective of this chapter is to investigate and evaluate the cyclic plasticity failure of primary electrode particle under electrochemical condition by using the LMM. The coupled diffusion-stress analysis of electrode particle during lithiation-delithiation process is performed with the developed

finite element subroutines as the groundwork for the subsequent cyclic plasticity assessment. The shakedown boundaries are established for electrode particle considering the variation of particle diameter by means of the LMM. ABAQUS full cyclic incremental analysis is employed to verify the applicability and accuracy of the obtained boundary. Two types of failure mechanisms known as low-cycle fatigue and ratcheting are investigated for particle subjected to loading history out of shakedown boundary. Steady state cycle analysis is conducted to study the generation of plastic strain range of particle under certain electrochemical conditions and the corresponding low-cycle fatigue damage is assessed. Different forms of ratcheting boundaries for electrode particle with various dimensions are created and the influences of cyclic current density and mechanical load on cyclic plasticity limits are clarified. The established critical failure diagrams provide the instructional information regarding the design of electrode material in microscale within designated electrochemical condition.

4.2 The framework of Linear Matching Method

In this chapter, we consider a structure experiencing a cyclic history of diffusion-induced stress $\lambda_d D(x,t)$ throughout its volume V and cyclic surface load $\lambda_p P(x,t)$ acting on portion of the structure surface S_T . λ herein represents a scalar load multiplier and the rest part of structure surface S_u ($S = S_T + S_u$) is fixed. One loading cycle is assumed to be in the time interval $0 \leq t \leq \Delta t$. The material of the structure is set as isotropic, elastic-perfectly plastic and obeys von Mises yielding condition. The linear-elastic solution of the aforementioned loading condition can be given as

$$\hat{\sigma}_{ij}(x,t) = \lambda_d \hat{\sigma}_{ij}^d(x,t) + \lambda_p \hat{\sigma}_{ij}^p(x,t) \quad (4.1)$$

$\hat{\sigma}_{ij}^d(x,t)$ and $\hat{\sigma}_{ij}^p(x,t)$ represent the linear-elastic solutions produced by $D(x,t)$ and $P(x,t)$ respectively.

After plenty of cycles, the stresses and strain rates will approximate to a cyclic state, i.e.,

$$\sigma_{ij}(t) = \sigma_{ij}(t + \Delta t), \quad \dot{\epsilon}_{ij}(t) = \dot{\epsilon}_{ij}(t + \Delta t) \quad (4.2)$$

The cyclic stress history herein consists of three components,

$$\sigma_{ij}(x,t) = \lambda \hat{\sigma}_{ij}(x,t) + \bar{\rho}_{ij}(x) + \rho_{ij}^r(x,t) \quad (4.3)$$

where $\lambda \hat{\sigma}_{ij}$ represents the elastic stress solution, $\bar{\rho}_{ij}$ is a constant residual stress field in equilibrium with no surface traction acting on S_T and corresponds to the residual stress filed at the start and end of the cycle. ρ_{ij}^r denotes the variation of residual stress within the cycle and follows

$$\rho_{ij}^r(x,0) = \rho_{ij}^r(x,\Delta t) \quad (4.4)$$

4.2.1 Evaluation of the shakedown limit

The shakedown analysis in the LMM calculates both the upper and lower bounds of shakedown limit using the Koiter's upper bound theorem and Melan's lower bound theorem respectively. Koiter's theorem presents that the shakedown behaviour will not happen if any kinematically admissible strain rate can be satisfied such that the strain field is compatible with the applied displacements and the plastic dissipation is less than or equal to the applied work. Melan states that the structure will enter shakedown state if there is a constant residual stress field such that, for any combination of residual stress field and elastic stress field caused by the applied load, the yielding criterion is not violated within the whole structure.

The cyclic stress history in shakedown problem can be simplified to the following form, as the variation of residual stress ρ_{ij}^r equals to zero.

$$\sigma_{ij}(x,t) = \lambda \hat{\sigma}_{ij}(x,t) + \bar{\rho}_{ij}(x) \quad (4.5)$$

The upper bound shakedown limit λ_{UB}^S can be obtained through

$$\lambda_{UB}^S = \frac{\int_V \int_0^{\Delta t} \sigma_y \bar{\epsilon}(\dot{\epsilon}_{ij}) dt dV}{\int_V \int_0^{\Delta t} (\hat{\sigma}_{ij} \dot{\epsilon}_{ij}) dt dV} \quad (4.6)$$

where σ_y is the yield strength of the material, $\bar{\epsilon}$ and $\dot{\epsilon}_{ij}$ represent the effective strain rate and kinematically admissible strain rate. In shakedown problem, the combination of the elastic stress fields and constant residual stress field under von Mises yielding condition will not lead to the accumulation of plastic strain. It is thereby to obtain the lower bound of shakedown limit through applying the following equation at all integration points for each loading instances.

$$f(\lambda_{LB}^S \hat{\sigma}_{ij}(x_i,t) + \bar{\rho}_{ij}(x_i)) \leq 0 \quad (4.7)$$

λ_{LB}^S in equation denotes the multiplier of lower bound shakedown limit.

4.2.2 Evaluation of the ratchet limit

The evaluation of ratchet limit can be decomposed to two parts [4-20]. The first part is to solve the varying residual stress field ρ_{ij}^r which is implemented as the Direct Steady Cycle Analysis (DSCA) of LMM framework. The DSCA involves m iterative cycles, where $m=1, 2, \dots, M$. Each iterative cycle consists of n increments, where $n=1, 2, \dots, N$ for N load instances. By employing Eq. (4.8), it is available to calculate the constant residual stress $\bar{\rho}_{ij}^r$.

$$\bar{\rho}_{ij}^r = \sum_{m=1}^M \sum_{n=1}^N \Delta \rho_{ij}^r(x_k, t_n)_m \quad (4.8)$$

where $\Delta \rho_{ij}^r(x_k, t_n)_m$ denotes the changing residual stress corresponding to elastic stress $\sigma_{ij}^\Delta(x_k, t_n)$.

The varying residual stress $\rho_{ij}^r(x, t_n)$ at the steady state cycle can then be given as

$$\rho_{ij}^r(x, t_n) = \bar{\rho}_{ij}^r(x) + \sum_{k=1}^n \Delta \rho_{ij}^r(x, t_k)_M \quad (4.9)$$

The associated converged increment of plastic strain at time t_n is described as

$$\Delta \varepsilon_{ij}^p(x, t_n) = \frac{1}{2\bar{\mu}_n(x, t_n)} \left[\hat{\sigma}_{ij}^\Delta(x, t_n) + \rho_{ij}^r(x, t_n) \right] \quad (4.10)$$

$\bar{\mu}_n$ in equation denotes the iterative shear modulus which can be calculated by linear matching equation [4-20]. $\hat{\sigma}_{ij}^\Delta$ is the linear elastic solution of the predefined cyclic loading and the notation (') represents the deviator component of the stress and strain.

The second part is to apply the shakedown theorem to calculate the ratchet limit, where the linear elastic solution of the predefined cyclic loading is modified by the changing residual stress $\rho_{ij}^r(x, t_n)$.

By using the von Mises yielding criteria, an upper bound multiplier of ratchet limit can be given as

$$\lambda = \frac{\int_V \sum_{n=1}^N (\sigma_y \bar{\varepsilon}(\Delta \varepsilon_{ij}^n(x, t_n))) dV - \int_V \sum_{n=1}^N ((\hat{\sigma}_{ij}^\Delta(x, t_n) + \rho_{ij}^r(x, t_n)) \Delta \varepsilon_{ij}^n(x, t_n)) dV}{\int_V \hat{\sigma}_{ij}^F(x) (\sum_{n=1}^N \Delta \varepsilon_{ij}^n(x, t_n)) dV} \quad (4.11)$$

where $\bar{\varepsilon}(\Delta \varepsilon_{ij}^n) = \sqrt{\frac{2}{3} \Delta \varepsilon_{ij}^n \Delta \varepsilon_{ij}^n}$ and $\Delta \varepsilon_{ij}^n$ denotes a kinematically admissible plastic strain rate. The ratcheting multiplier λ here defines the capacity of the structure subjected to a combination of cyclic loads to accommodate an additional constant load without ratcheting happens. According to the aforementioned framework, the LMM iteratively generates a series of monotonically decreasing upper bounds and converges to the least upper ratchet limit for the selected class of displacement fields. The aforementioned numerical methods are implemented in ABAQUS [3-5] by developing user subroutines and detailedly described in Ref. [4-20].

4.3 Problem Description

4.3.1 Finite element model and material property

The model of primary electrode particle is constructed and meshed by employing the finite element program ABAQUS. In this chapter, the finite element model of primary particle keeps in line with Chapter 3. The geometry and mesh configurations are identical in the coupled diffusion-stress analysis and cyclic plasticity analysis. For mechanical boundary condition, the particle surface is set

as traction free in both coupled diffusion-stress analysis and cyclic plasticity analysis, where no traction is applied on the particle surface. In coupled diffusion-stress analysis, the particle surface experienced diffusion flux J can be obtained by $J = \frac{i_n}{F_a}$, where i_n is the applied current density and F_a is the Faraday constant. For element type, C3D20RT is employed for coupled diffusion-stress analysis and C3D20R is applied in cyclic plasticity analysis.

The adopted properties in numerical work for the NCM material are listed in Table 4.1. The NCM material is assumed as isotropic, elastic-perfectly plastic (EPP) and obeys von Mises yielding condition in this work. According to the section 3.2.2, the diffusion-induced expansion strain can be calculated as $\frac{\Omega}{3} \Delta c$ [2-13, 4-21]. For NCM electrode material, the maximum expansion strain is 3.3761%. Based on the Hooke's law, the maximum elastic strain can be obtained as 0.08%. The total strain is less than 4% for NCM material, which makes it reasonable to consider the material satisfying small deformation assumption.

Table 4.1 Material properties of NCM electrode particle

Property	Value
Young's modulus (GPa)	125 [3-10]
Poisson's ratio	0.3 [3-10]
Diffusivity (m ² /s)	1E-15 [3-11]
Partial molar volume (m ³ /mol)	2.1E-6 [3-12]
Yield strength (MPa)	100

4.3.2 Linear Elastic Solutions

The theoretical foundation of the Linear Matching Method can be summarized as using a series of iterative linear analyses to model the nonlinear material response, and represent the history of stress and inelastic strain. Therefore, calculating the linear elastic solutions of electrode particle under electrochemical load and mechanical load works as the first step before performing the subsequent cyclic plasticity assessment.

With using the developed ABAQUS subroutines, it is accessible to study the concurrent diffusion and stress generation process for spherical electrode particle under intercalation-deintercalation condition. Fig. 4.1 gives the history of cyclic diffusion-induced stress for 3um diameter electrode particle under 0.3 A/m² current density within one cycle. The DoD and SoC on X-axis respectively denote the depth of discharge and the state of charge, which are used to describe the status of electrode particle in the lithiation-delithiation cycle. Due to the change of

concentration gradient caused by Li-ion flow, the diffusion-induced stress presents the initial decreasing and subsequent increasing trends in both lithiation and delithiation phases. The LMM applies finite representative loading instants to describe the entire loading history and the rest instants with smaller loads are assumed to be encompassed. According to Fig. 4.1, four instants representing extreme situations are used to reflect the cyclic diffusion-induced stress history. The contours of stress and concentration fields at these four instants are presented in Fig. 4.2 (a) and (b) respectively. Instant 1 is the time point at the start of lithiation process (discharge phase, DoD 0%), when the residual concentration gradient from the last working cycle results in the residual stress field. Due to the influx of Li-ions, the concentration gradient is rapidly reduced leading to the decrease of diffusion-induced stress, and the instant with the minimum stress is defined as instant 2 at lithiation phase (discharge phase, DoD 0.84%). Hereafter, the continuing lithiation makes the concentration gradient reversely magnified, leading to the rise of diffusion-induced stress to instant 3 (discharge phase, DoD 100%), which experiences the maximum stress in lithiation process. For the delithiation process, it also experiences the initial decrease phase and the subsequent increase phase of concentration gradient and stress field due to the outflow of Li-ions. The inflection point in this process is presented as instant 4 (charge phase, SoC 0.84%) with the minimum stress. Hence, the instants with the maximum and minimum stresses in both lithiation and delithiation phases are applied to construct the loading cycle.

Besides, the lithiation caused swelling will result in the extrusion force between neighbouring particles as illustrated in Fig. 4.2 (c), which will further influence the carrying capacity of the electrode particle. Fig. 4.1 also gives the change of a mechanical reference stress on electrode particle within lithiation-delithiation cycle, where the extremum of the mechanical stress emerges at the end moment of intercalation process when the configuration is assumed to experience the maximum expansion and is defined as instant 3 (discharge phase, DoD 100%). The contour of mechanical reference stress at instant 3 is given as Fig. 4.2 (d). This varying mechanical reference stress is applied as the reference load for the LMM and is scaled to represent the cyclic plasticity limit of the electrode particle.

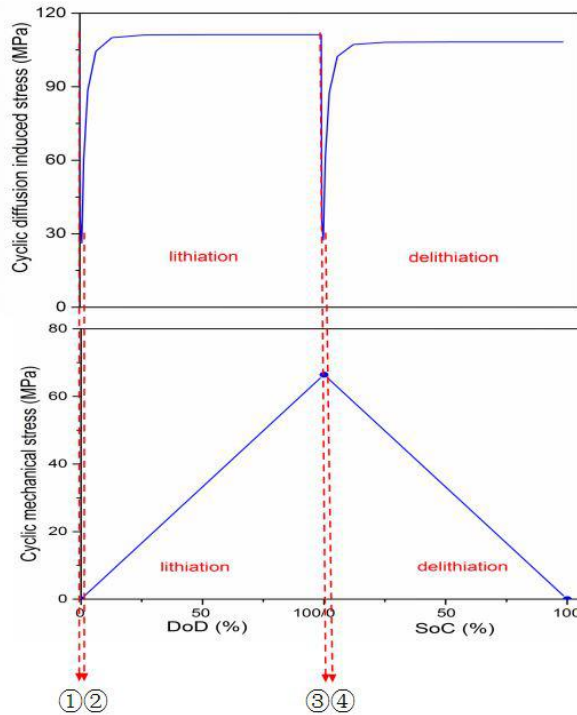
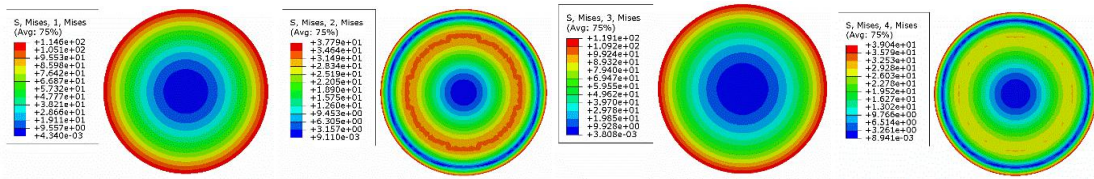
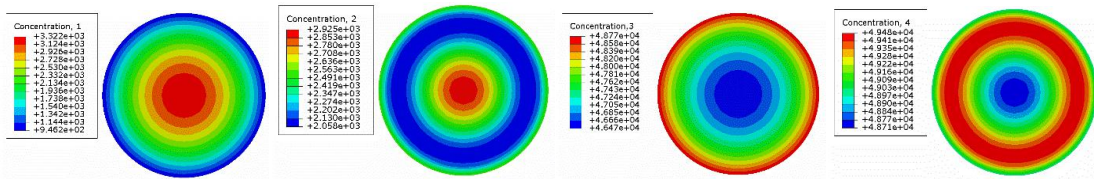


Fig 4. 1 The history of diffusion-induced stress under 0.3 A/m^2 and mechanical reference stress for $3\mu\text{m}$ diameter electrode particle within one cycle (DOD - depth of discharge, SOC - state of charge)



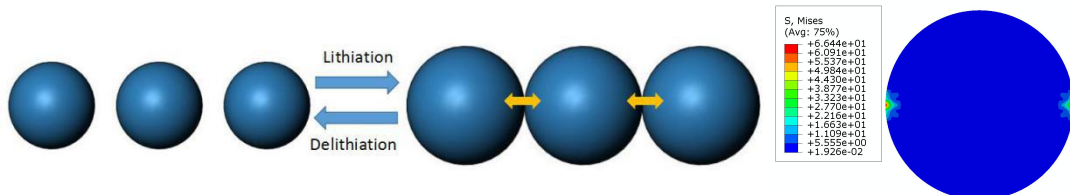
lithiation DoD 0% (instant 1) lithiation DoD 0.84% (instant 2) lithiation DoD 100% (instant 3) delithiation SoC 0.84% (instant 4)

(a)



lithiation DoD 0% (instant 1) lithiation DoD 0.84% (instant 2) lithiation DoD 100% (instant 3) delithiation SoC 0.84% (instant 4)

(b)



(c)

(d)

Fig 4. 2 (a) The contours of elastic von Mises effective stress of four selected instants, (b) the contours of concentration fields of four selected instants, (c) the schematic diagram of lithiation caused extrusion between adjacent particles, (d) the contour of mechanical reference stress at instant 3

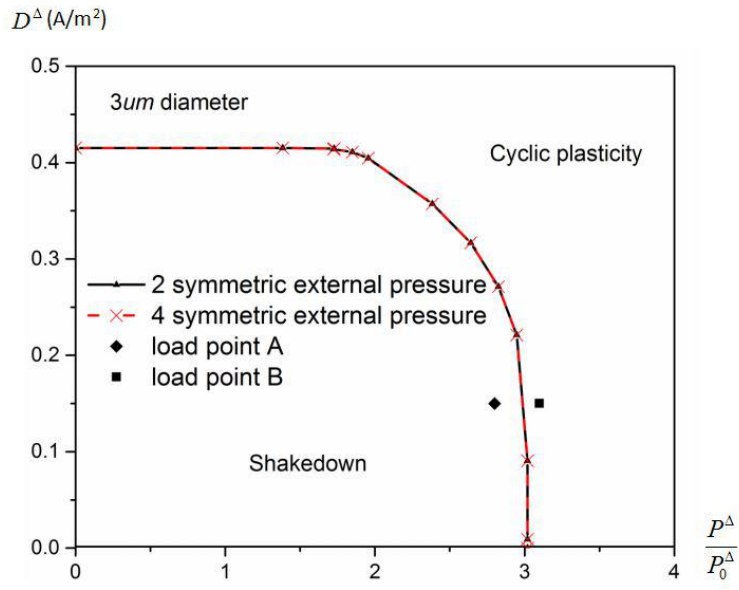
4.4 Shakedown Assessment

It has been demonstrated that the lithiation-delithiation behaviours of electrode material always accompany with plastic flow [4-22, 4-23]. Considering the successive operation condition of battery electrode, a series of cyclic plasticity behaviours, such as shakedown, reverse plasticity and ratcheting, are thought to contribute to capacity fading [2-63]. This section conducts shakedown assessment of electrode particle and the shakedown limit here is defined as the capacity to withstand cyclic current density leading to the generation of diffusion-induced stress and cyclic mechanical load. The LMM is used to perform shakedown analysis and ABAQUS step-by-step inelastic assessment is also conducted so as to testify the accuracy of the acquired shakedown boundary from LMM.

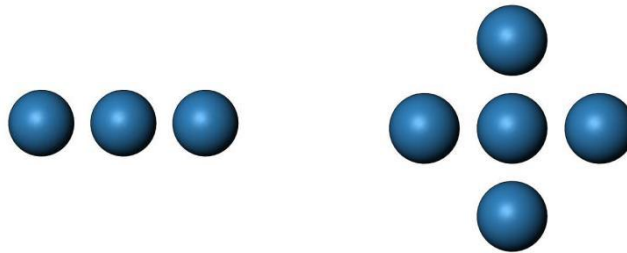
4.4.1 Shakedown limits of electrode particle

By calculating different combinations of cyclic current density and cyclic mechanical load, it is available to obtain the shakedown limit curves for electrode particle under cyclic lithiaion-delithiation condition. Fig 4.3 (a) presents the shakedown boundaries for a primary electrode particle with 3 μ m diameter under cyclic current density and symmetrically isometrical external pressures caused by neighbouring electrode particles. It is observable that the loading range is separated by shakedown boundary to two parts, as shakedown zone and cyclic plasticity zone. The Y-coordinate in Fig 4.3 (a) denotes the strength of current density which leads to the generation of cyclic diffusion-induced stress, and X-coordinate in Fig 4.3 (a) represents the ratio between the applied mechanical load and mechanical reference load. Additionally, the loading conditions on Y-axis in Fig 4.3 (a) represent the shakedown limits of primary particle subjected to only cyclic diffusion-induced stress, where the particle is presumed to have no contact with neighbouring particles when swelling happens.

It should be highlighted that the different particle arrangements, such as schematic diagrams shown in Fig 4.3 (b) and (c), may also affect the cyclic plasticity limit of primary electrode particle. In Fig 4.3 (b), the central particle will be under two symmetric external pressures during swelling process, and the central particle in Fig 4.3 (c) will experience four symmetric external pressures accompanying with lithiation behaviour. The cyclic plasticity boundaries of these two scenarios are presented in Fig 4.3 (a), and it is noteworthy that the shakedown boundary under two symmetric external pressures is identical with that under four symmetric external pressures. Fig 4.4 (a) and (b) provide the elastic von Mises stress solutions for primary particle under two and four mechanical reference loads. It can be seen that two extra mechanical loads have no impact on the maximum von Mises stress which always emerges at where the mechanical load acts. In addition, it is known that the shakedown limit is decided by the maximum elastic stress range. Hence, the shakedown limits for primary particle under two or four isometrical external pressures are identical.



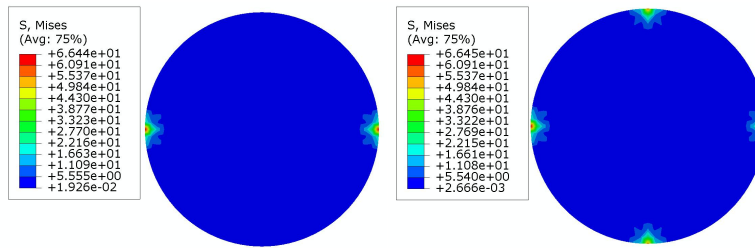
(a)



(b)

(c)

Fig 4. 3 (a) Shakedown boundaries of 3 μ m diameter particle under cyclic current density and mechanical load considering different particle arrangements, the schematic diagrams of different particle arrangements, (b) one central particle with two neighbouring particles, (c) one central particle with four neighbouring particles.



(a)

(b)

Fig 4. 4 The distribution of von Mises stress for 3 μ m diameter particle under (a) two, and (b) four mechanical reference loads

4.4.2 ABAQUS step-by-step analysis

For validating the accuracy of the obtained shakedown limits from the LMM, loading conditions in and out of the shakedown boundary are chosen for conducting the ABAQUS step-by-step analyses. Fig 4.5 (a) and (b) give the plastic strain history (PEMAG) for the most dangerous position of the primary particle under load points A and B shown in Fig 4.3 (a). The evolution of plastic strain in Fig 4.5 (a) presents that there will be no more new plastic strain generated after early cycles, which indicates the primary particle will be in shakedown status subjected to load point A. It is observed from Fig 4.5 (b) that, the produced positive plastic strain is equal to the negative plastic strain for the electrode particle under the load point B at the steady state, which shows the electrode particle experiencing the reverse plasticity behaviour. Therefore, the applicability of employing LMM to perform the cyclic plasticity evaluation for electrode particle has been verified via ABAQUS step-by-step analysis.

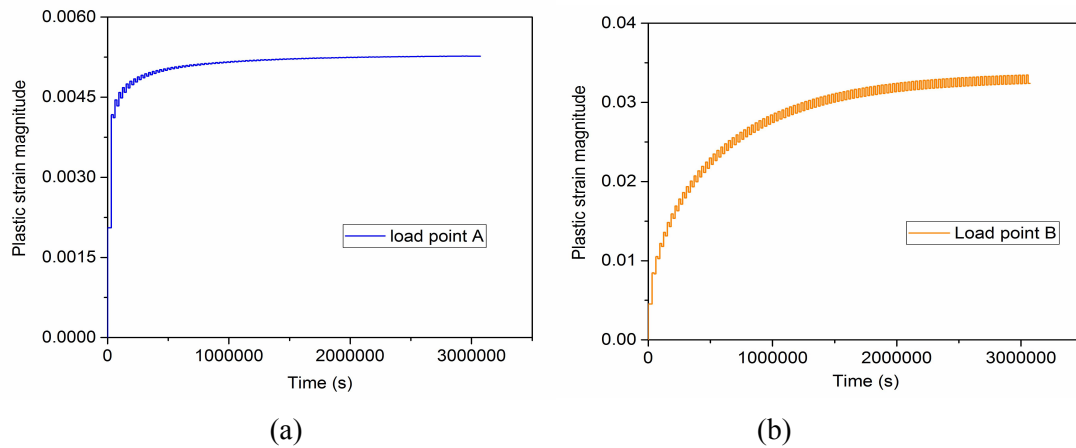


Fig 4. 5 Plastic strain history (PEMAG) obtained from ABAQUS step-by-step analyses for cyclic loading (a) load point A, (b) load point B

4.4.3 Shakedown boundaries with the changing of particle diameter

Due to the non-uniform size distribution of active electrode particles in micrometer scale, it is significant to investigate how the change in size affects the shakedown boundary of the electrode particle. According to the size distribution of NCM primary particles from experimental samples in Fig 3.18, five representative sizes (diameter 1 μ m, 2 μ m, 3 μ m, 4 μ m and 5 μ m) are selected to study the effects of size change on cyclic plasticity limit, with the thought that these five sizes cover the majority of size cases of NCM primary particles. Fig 4.6 gives the shakedown boundaries for electrode particle with varying dimensions subjected to cyclic current density and mechanical load. The shakedown limits on Y-axis present the permissible current density for individual electrode particle losing contact with neighbouring particles during swelling process. It is observed as general trend that this permissible current density decreases with an increase of particle dimension. In the last

section, the research work has also concluded the similar phenomenon that, with just considering the effect from current density, the electrode particle with larger size is more prone to crack initiation and crack propagation. Fig 4.7 (a) and (b) show the maximum von Mises stress during the lithiation-delithiation process for electrode particles with diameter 2 μ m and 4 μ m only under 0.15A/m². It can be seen that the stress generated of 2 μ m diameter particle is less than that of the particle with 4 μ m diameter under the same electrochemical load. Hence, the smaller particle is capable of withstanding greater current density.

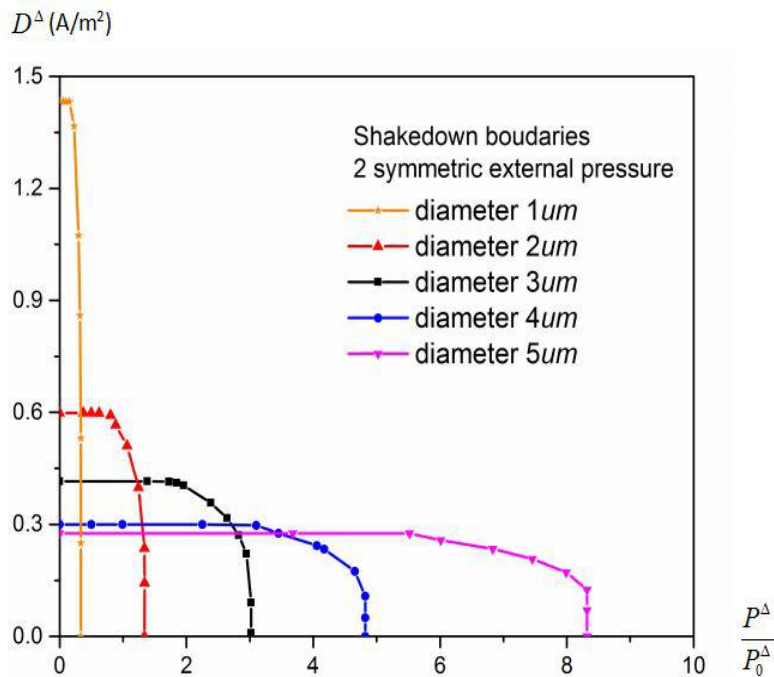


Fig 4. 6 The shakedown limit curves of the electrode particle with various dimensions subjected to cyclic current density and mechanical load

Another notable point is that, under the same current density, the capacity for electrode particle to withstand mechanical load is in positive correlation with the increasing of particle dimension. Fig 4.7 (c) and (d) illustrate the maximum von Mises stress for electrode particles with 2 μ m diameter and 4 μ m diameter only under mechanical reference load. In contrast to the electrochemical load, the particle with smaller size will experience relatively greater stress than that of the larger particle under the same mechanical load, which indicates the larger particle can withstand more mechanical load. The aforementioned mechanisms decide the changing trend of shakedown boundaries for electrode particles with varying dimensions, and the change of particle size makes considerable impact on the carrying capacity of electrode particle under electrochemical load and mechanical load.

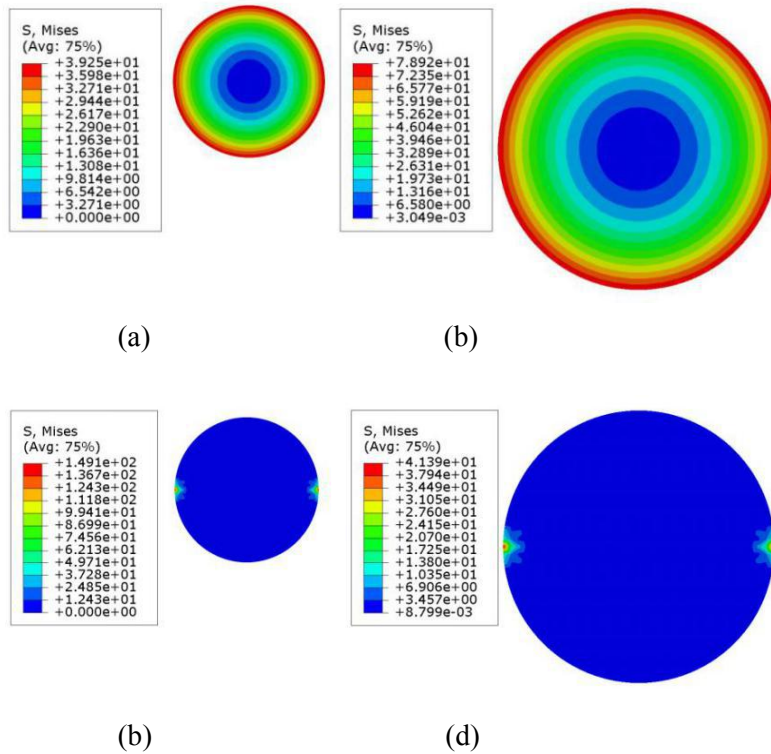


Fig 4. 7 The maximum von Mises stress under $0.15A/m^2$ (a) particle with diameter $2\mu m$, (b) particle with diameter $4\mu m$, the maximum von Mises stress under mechanical reference load (c) particle with diameter $2\mu m$, (d) particle diameter $4\mu m$

4.5 Steady state cycle and ratchet limit analysis

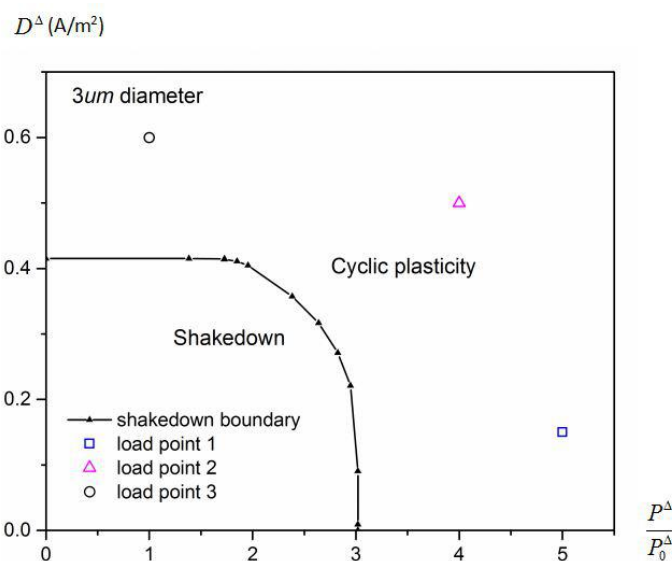
Two categories of failure mechanisms will occur when the configuration subjects to the loading condition out of shakedown boundary. In a loading cycle at steady state, when the produced plastic strain forms a closed cycle, the structure is assumed to be in reverse plasticity status. Associating the generated plastic strain range with material fatigue parameters, it is available to assess the low-cycle fatigue damage for the structure. Alternatively, if the plastic strain settles into an open cycle, the ratcheting behaviour is considered to happen where the strain accumulation will lead to the incremental plastic collapse of the structure.

4.5.1 Steady state cycle analysis

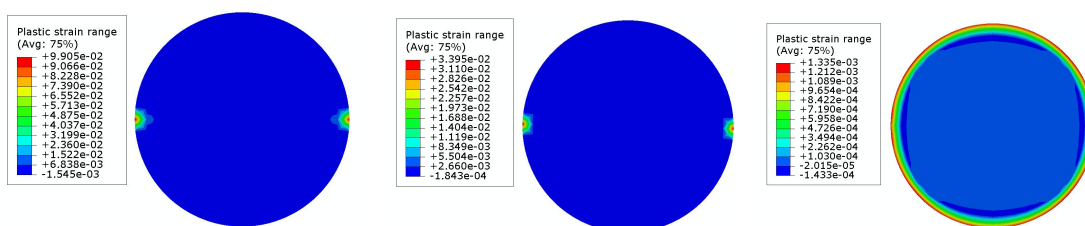
By employing the direct steady cycle analysis in the LMM, it is accessible to efficiently obtain the plastic strain range of the structure under certain loading condition and further evaluate the corresponding low-cycle fatigue damage. Fig 4.8 (a) gives the shakedown boundary of $3\mu m$ electrode particle with three loading conditions out of shakedown boundary. The locations of these three loading points are relatively far from the shakedown boundary so as to present more obvious plastic

strain range and low-cycle fatigue damage. Fig 4.8 (b), (c) and (d) illustrate the corresponding contours of plastic strain range for 3 μ m electrode particle under these loading histories, where the maximum values of plastic strain range reach 0.09905, 0.03395 and 0.001335 respectively. For loading point 1 and 2, the plastic strain range is mainly dominated by the cyclic mechanical load, where the significant plastic strain range appears to occur at the area applied with mechanical load. Whereas for loading point 3, the cyclic diffusion-induced stress works as the primary effective load. The maximum plastic strain range locates at the outermost layer of the particle where the maximum diffusion-induced stress happens.

Additionally, the ratcheting strain can also be given by using the direct steady cycle analysis, as shown in Fig 4.8, where the ratcheting strain is defined as the net accumulation of the plastic strain per cycle. It is available to see that, there is a relatively small ratcheting strain generated under loading point 3. While for the loading points 1 and 2, the obvious ratcheting strain will accumulate at the mechanical load acting area and the ratcheting failure assessment is required to conduct. According to these important output parameters, it is available to plot the hysteresis loops of the most dangerous position of electrode particle under three loading conditions, as shown in Fig 4.9. Due to the application of loading conditions far exceeding shakedown boundary, the plastic strain range and ratcheting strain are relatively large for electrode particle under load point 1 and 2.



(a)



(b) loading point 1

(c) loading point 2

(d) loading point 3

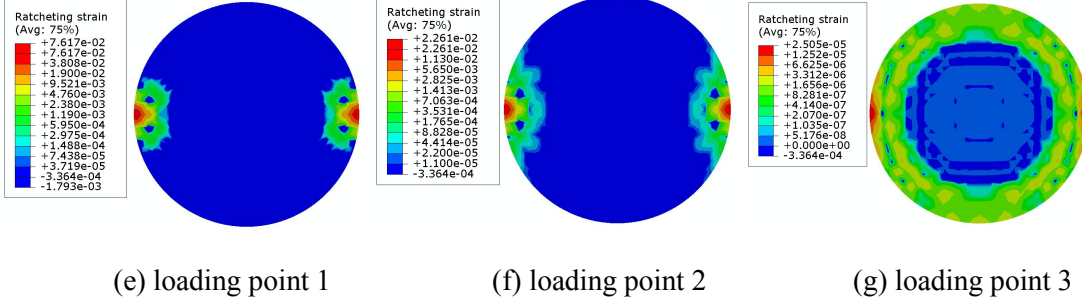


Fig 4. 8 (a) shakedown boundary of 3um particle with selected loading points, the contours of plastic strain range of 3um particle under (b) loading point 1, (c) loading point 2, (d) loading point 3, the contours of ratcheting strain of 3um particle under (e) loading point 1, (f) loading point 2, (g) loading point 3

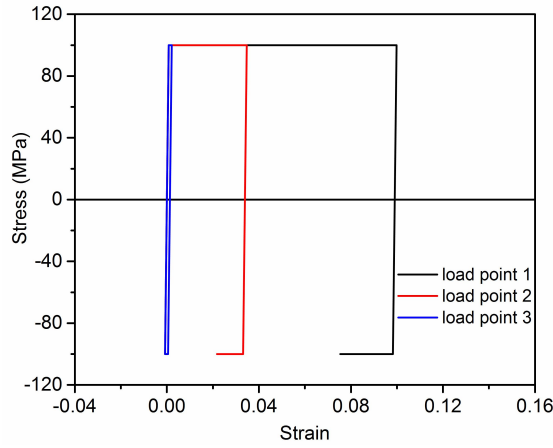


Fig 4. 9 Hysteresis loops at the most dangerous location of electrode particle under three loading conditions

According to the Manson-coffin equation shown below, the plastic strain range can be used as the input parameter to predict the fatigue life.

$$\frac{\Delta \varepsilon_p}{2} = \varepsilon'_f (2N)^{c'} \quad (4.12)$$

where $\Delta \varepsilon_p$ is the plastic strain range, $2N$ denotes the number of reversals to failure. ε'_f and c' represent two empirical constants known as the fatigue ductility coefficient and the fatigue ductility exponent respectively. By formula transformation, it is available to obtain the caused fatigue damage per cycle at steady state.

$$dD_{mi} = 2 \left(\frac{2\varepsilon'_f}{\Delta \varepsilon_p} \right)^{\frac{1}{c'}} = \frac{1}{N_i} \quad (4.13)$$

Table 4.2 presents the fatigue ductility coefficient and fatigue ductility exponent for NCM ternary material, and the details of obtaining these parameters are shown in chapter 5. According to the generated plastic strain range, it is thereby available to assess the corresponding low-cycle fatigue damage per cycle of electrode particle at steady state. Table 4.3 shows the fatigue damage per cycle of the most dangerous position on electrode particle and the corresponding number of cycles to low-cycle fatigue failure under three loading histories. It is worth noting that, the fatigue damage per cycle here is constant. Under cyclic loading condition, the material stress-strain response will come to a stable cyclic state after initial oscillation stage, and the fatigue damage here represents the fixed damage caused by each cycle in stable state. It is obvious that, under different loading conditions, the generated fatigue damage varies greatly. For loading points 1 and 2, the generated low-cycle fatigue damage makes a relatively great contribution to the structural failure. While for the loading point 3, the low-cycle fatigue caused damage is not significant.

Table 4.2 Fitted parameters in the fatigue damage model

$\dot{\epsilon}_f$	c'
3.184	-0.688

Table 4.3 Fatigue damage and number of cycles to fatigue failure

	Maximum damage per cycle	Number of cycles to failure
Load point 1	4.7E-3	212
Load point 2	9.9E-4	1010
Load point 3	9.0E-6	111111

4.5.2 Ratcheting assessment

A body experiencing ratcheting behaviour which eventually results in the incremental plastic collapse, should be rigorously avoided. The ratchet limit in this work is defined as the capacity for configuration under a predefined cyclic load to accommodate an extra constant load without representing ratcheting failure.

With the calculation of different combinations of cyclic current density and constant mechanical load, it is accessible to plot the ratcheting boundaries for 3 μ m electrode particle shown in Fig 4.10, where the shakedown boundaries are also given. In this case, the ratchet limit can be expressed as the capacity for structure experiencing cyclic current density to withstand extra constant mechanical load. For the Y-axis, the arbitrary applied cyclic current density is normalized with respect to a reference current density set as 0.3A/m². The entire loading range is divided by boundaries to three zones known as shakedown zone, reverse plasticity zone and ratcheting zone. This makes it easily accessible

to quickly understand the structural status once the loading condition is given. The contour plot in Fig 4.10 shows the ratcheting behaviour caused failure state of electrode particle, which indicates that the strain accumulations are mainly centered on the mechanical loading acting area.

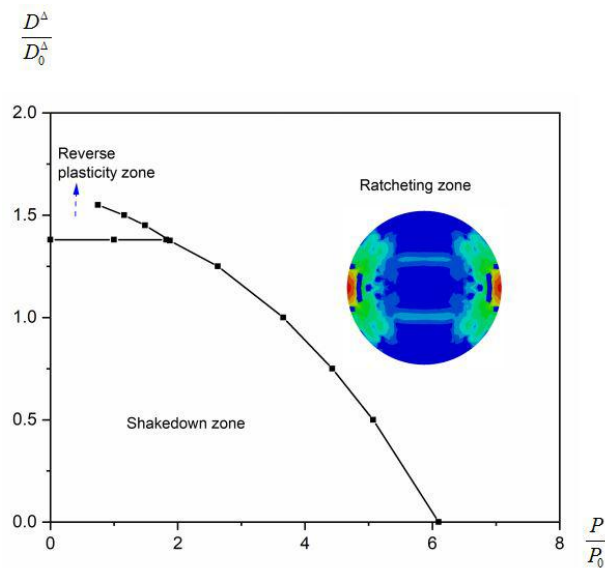


Fig 4. 10 Ratcheting and shakedown boundaries for 3μm particle subjected to cyclic current density and constant mechanical load

Considering the change of particle diameter, Fig 4.11 presents the ratcheting boundaries of electrode particle with various dimensions under cyclic current density and constant mechanical load. As explained in shakedown analysis, it is concluded that the capacity for electrode particle to withstand electrochemical load decreases with an increase in the particle size. On the contrary, larger particle is able to bear greater mechanical load. Hence, the ratcheting boundaries of electrode particle with various dimensions show in this way.

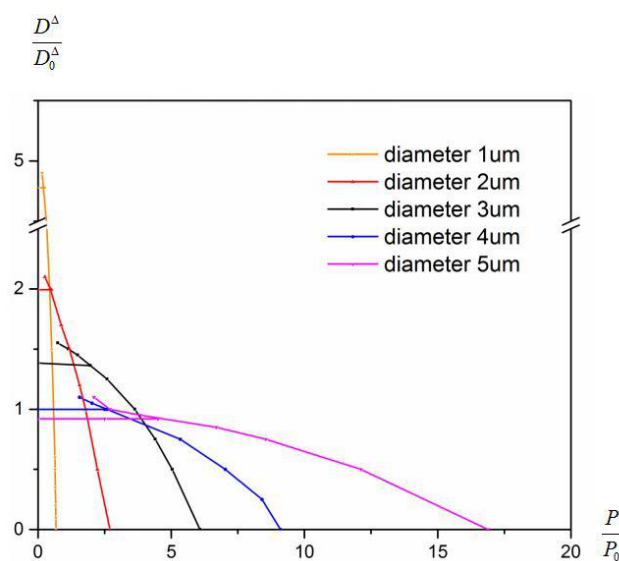


Fig 4. 11 Ratcheting and shakedown limit curves for electrode particle with various dimensions under cyclic current density and constant mechanical load

For comprehensively investigating the carrying capacity of electrode particle under electrochemical load and mechanical load, Fig 4.12 gives the ratchet and shakedown limit curves in another way, where the cyclic plasticity limit is expressed as the electrode particle subjected to a coupled cyclic current density - mechanical load PD^Δ to withstand an additional constant mechanical load P . The values on Y-axis represent the ratio between the applied coupled current density - mechanical load and the coupled reference current density - mechanical load. As the cyclic plasticity limit of small particle is sensitive to mechanical load, both the shakedown and ratchet limits of 1um and 2um electrode particles are greatly reduced with the adding of cyclic mechanical load to the predefined loading conditions. On the contrary, the cyclic plasticity limit of bulky particle (diameter 4um and 5um) is rarely modified due to the better carrying capacity to mechanical load, but it is greatly restricted by the cyclic current density. From the view of general performance under electrochemical-mechanical load, electrode particle with 3um diameter shows better mechanical stability under a large range of electrochemical-mechanical loads and this particle size is recommended in NCM electrode material preparation.

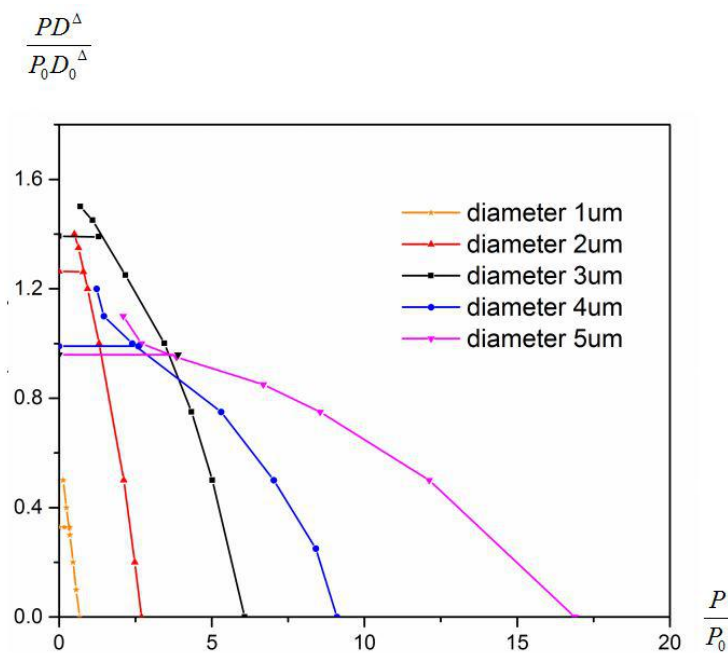


Fig 4. 12 Ratcheting and shakedown limit curves for electrode particle with various dimensions under coupled cyclic mechanical load - current density and constant mechanical load

4.6 Conclusions

This chapter has comprehensively analyzed the cyclic plasticity behaviors of electrode particle under electrochemical load and mechanical load by using the shakedown analysis, direct steady cycle analysis and ratchet analysis within the Linear Matching Method framework. The key conclusions are:

1. The shakedown boundaries of electrode particle considering the change of particle sizes are established, with the calculation of different combinations of cyclic current density and mechanical load. It is observed as general trends that, the endurance of electrode particle against current density, which leads to the generation of cyclic diffusion-induced stress, will decrease with an increase of particle dimension. On the contrary, larger particle is proved to be able to withstand greater mechanical load.

2. By using the direct steady cycle analysis in the LMM, it is accessible to efficiently assess the plastic strain range and identify the most dangerous location for electrode particle under different loading conditions at steady state. Associating with the presented low-cycle fatigue model, it is accessible to evaluate the low-cycle fatigue damage of electrode particle under representative loading cycles.

3. Two different forms of ratcheting boundaries of electrode particle are established to clarify the influence from cyclic current density as well as mechanical load on cyclic plasticity limits, and avoid the plastic collapse of electrode particle. It is concluded that, the particle with 3 μ m diameter presents relatively better mechanical stability under a large range of electrochemical-mechanical loads and is recommended in the preparation of NCM cathode material.

4.7 References

[4-1] J.P. Maranchi, A.F. Hepp, A.G. Evans, N.T. Nuhfer, P.N. Kumta. Interfacial Properties of the a-Si/Cu: Active-Inactive Thin-Film Anode System for Lithium-Ion Batteries. *Journal of The Electrochemical Society*, 2006, 153: A1246

[4-2] R. Kumar, A. Tokranov, B.W. Sheldon, X.C. Xiao, Z.Q. Huang, C.Z. Li, T. Mueller. In Situ and Operando Investigations of Failure Mechanisms of the Solid Electrolyte Interphase on Silicon Electrodes. *Acs Energy Lett*, 2016, 1: 689–697.

[4-3] Y. Shi, L. Weng, Y. Zhang, C. Xu, Q. Chen, B. Chen, J. Zhou, R. Cai. Chemo-mechanical analysis of ratcheting deformation in silicon particle electrode under cyclic charging and discharging. *Mechanics of Materials*, 2021, 162: 104062.

[4-4] Z.S. Ma, Z.C. Xie, Y. Wang, P.P. Zhang, Y. Pan, Y.C. Zhou, C. Lu. Failure modes of hollow core–shell structural active materials during the lithiation–delithiation process. *Journal of Power Sources*, 2015, 290: 114-122.

[4-5] Y.H. Liu, V. Carvelli, G. Maier. Integrity assessment of defective pressurized pipelines by direct simplified methods. *International Journal of Pressure Vessels and Piping*, 1997, 74: 49-57.

- [4-6] D.K. Vu, A.M. Yan, H. Nguyen-Dang. A primal–dual algorithm for shakedown analysis of structures. *Computer Method in Applied Mechanics and Engineering*, 2004, 193: 4663-4674.
- [4-7] M. Staat, M. Heitzer. LISA a European project for FEM-based limit and shakedown analysis. *Nuclear Engineering and Design*, 2001, 206: 151-166.
- [4-8] J. Abou-Hanna, T.E. McGreevy. A simplified ratchetting limit method based on limit analysis using modified yield surface. *International Journal of Pressure Vessels and Piping*, 2011, 88: 11-18.
- [4-9] R. Seshadri. Inelastic evaluation of mechanical and structural components using the generalized local stress strain method of analysis. *Nuclear Engineering and Design*, 1995, 153 (2–3): 287-303.
- [4-10] D. Mackenzie, J.T. Boyle, R. Hamilton. The elastic compensation method for limit and shakedown analysis: a review. *Journal of Strain Analysis*, 2000, 35 (3): 171-188
- [4-11] H.F. Chen, A.R.S. Ponter, R.A. Ainsworth. The linear matching method applied to the high temperature life integrity of structures, Part 1: assessments involving constant residual stress fields. *International Journal of Pressure Vessels and Piping*, 2006, 83 (2): 123-135
- [4-12] H.F. Chen, A.R.S. Ponter, R.A. Ainsworth. The linear matching method applied to the high temperature life integrity of structures, Part 2: assessments beyond shakedown involving changing residual stress fields. *International Journal of Pressure Vessels and Piping*, 2006, 83 (2): 136-147
- [4-13] Koiter, W.T. General theorems for elastic plastic solids. *Progress in Solid Mechanics*, 1960, pp. 167-221.
- [4-14] Melan, E. Theorie statisch unbestimmter Systeme aus ideal-plastischem Baustoff. *Sitzungsber. 1936. D. Akad. D. Wiss., Wien 2A (145)*, 195-218.
- [4-15] X.C. Zhu, H.F. Chen, F.Z. Xuan, X.H. Chen. Cyclic plasticity behaviors of steam turbine rotor subjected to cyclic thermal and mechanical loads. *European Journal of Mechanics - A/Solids*, 2017, 66: 243-255.
- [4-16] N.K. Cho, H.F. Chen. Shakedown, ratchet, and limit analyses of 90° back-to-back pipe bends under cyclic in-plane opening bending and steady internal pressure. *European Journal of Mechanics - A/Solids*, 2018, 67: 231-242.
- [4-17] J. Ure, H.F. Chen, D.J. Tipping. Verification of the linear matching method for limit and shakedown analysis by comparison with experiments. *Journal of Pressure Vessel Technology*, 2015, 137 (3): 031003–1-031003-6.
- [4-18] D.J. Tipping. *The Linear Matching Method: a Guide to the ABAQUS User Subroutines. E/REP/BBGB/0017/GEN/07*, British Energy Generation, 2007.
- [4-19] R.A. Ainsworth (Ed.), *R5: Assessment Procedure for the High Temperature Response of Structures*, vol 3, British Energy Generation Ltd, 2003.

- [4-20] H. Chen, A. Ponter. A direct method on the evaluation of ratchet limit. *Journal of Pressure Vessel Technology*, 2010, 132(4): 041202.
- [4-21] J.C.M. Li. Physical chemistry of some microstructural phenomena. *Metallurgical Materials Transactions A*, 1978, 9:1353
- [4-22] V.A. Sethuraman, M.J. Chon, M. Shimshak, V. Srinivasan, P.R. Guduru. In situ measurements of stress evolution in silicon thin films during electrochemical lithiation and delithiation. *Journal of Power Sources*, 2010, 195: 5062-5066
- [4-23] V.A. Sethuraman, V. Srinivasan, A.F. Bower, P.R. Guduru. In situ measurements of stress-potential coupling in lithiated silicon. *Journal of the Electrochemical Society*, 2010, 157: A1253-A1261

Chapter 5

Progressive fatigue damage assessment of battery electrode using strain based fatigue damage model

5.1 Introduction

Regarding the degradation of electrode as a fatigue damage process is gradually thought to be more according with the practical battery operation, as discussed in chapter 2. Nevertheless, how to quantitatively evaluate the fatigue induced degradation under electrochemical condition still remains to be clarified. In this chapter, the continuum damage mechanics founded by Kachanov [5-1] is applied to quantify the fatigue caused damage of Li-ion battery electrode upon electrochemical cycling. Building on the continuum mechanics and thermodynamics, the damage mechanics theory aims to derive the continuous evolution equation of damaged material by defining the applicable damage variable, so as to describe the dynamic stress-strain-damage fields of the target solid [5-2]. The continuum damage mechanics has been adopted in the assessment of damage phenomenon like elasticity, plasticity, viscoplasticity, creep, fatigue, etc., and is available to describe the damage for metallic material, composite material, concrete material and so on [5-3, 5-4, 5-5, 5-6]. Using the continuum damage mechanics in studying the mechanical failure behaviour of electrode is accessible to accurately track the overall degradation process of electrode during circulating operation.

This work takes the lead to model the continuous mechanical degradation of battery electrode under diffusion-induced stress as a fatigue damage process. The proposed fatigue evaluation approach for battery electrode is built on the continuum damage mechanics, and takes into consideration the coupling effect between diffusion behaviour, diffusion induced stress formation, and accumulated fatigue damage affected stress-strain response. Relevance assumption is made to connect the electrochemistry represented damage with mechanical fatigue damage. Circulating charging-discharging test cycled at the C-rate of 1C condition is performed as a benchmark to fit the fatigue parameters in the proposed cumulative damage model. The established assessment approach is then applied under other multi-electrochemical conditions, and further studied by comparing these numerical simulations with conducted experimental tests. This research work presents that it is accessible to quantify the fatigue degradation of Li-ion battery electrode based on the continuum damage mechanics, and provides understanding for mechanical failure of Li-ion battery electrode.

5.2 Mechanics and experiment represented damage models

In practical operation, the continuous mechanical degradation of electrode accompanies with the capacity fading of battery. One can make the assumption that, the mechanical damage over cycles is in proportion to the capacity fading represented damage. Based on the continuum damage mechanics (CDM), a cumulative damage model can be proposed to describe the deterioration of electrode in mechanical way. In addition, through performing charge-discharge tests, an experimental index of damage can also be defined so as to correlate with the mechanical damage.

5.2.1. Continuum damage mechanics

The research objective of continuum damage mechanics is the deformed solid containing multifarious categories of microdefects, which are regarded to continuously distribute in the target solid [5-7]. Under the action of external factors, the continuous nucleation, propagation and aggregation of microdefects will lead to the degradation of material and structure. This type of continuous distributed microdefects can be depicted by a field variable known as damage field. If the distribution of damage and its effect on material performance have no directional difference, the damage state can be regarded as isotropic and expressed by using a scalar damage variable D ($0 \leq D \leq 1$). In the present work, the symbol D makes a general reference to various types of damage fields including the calculated mechanical damage and the experiment indicated damage.

The evolution of microdefects or the growth of damage can reduce the load-carrying area, which will further magnify the stress. It is then available to obtain the following relation

$$\tilde{\sigma} = \sigma \frac{A}{A - A_D} \quad (5.1)$$

where A denotes the area before damage, and A_D is the detracted area caused by damage. $\tilde{\sigma}$ is defined as effective stress. Based on the definition of damage, one obtains [5-7]

$$\tilde{\sigma} = \frac{\sigma}{1 - D} \quad (5.2)$$

According to the strain equivalence principle, the strain caused by the effective stress $\tilde{\sigma}$ in the fictitious undamaged material is in equivalence to the strain of damaged material under nominal stress σ . The constitutive relation of the damaged material can thereby be derived from that of the undamaged material by using the effective stress of damaged material to replace the nominal stress in the constitutive relation of undamaged material.

$$\varepsilon = \frac{\tilde{\sigma}}{E_0} = \frac{\sigma}{E(D)} \quad (5.3)$$

where E_0 and $E(D)$ represent the Young's modulus of the fictitious undamaged material and that of the damaged material. Combining Eq. (5.2) and (5.3), one obtains

$$(1 - D)E_0 = E(D) \quad (5.4)$$

It is worth reminding that, the $E(D)$ is the factitiously revised Young's modulus for reflecting the effect of damage on material stress-strain response.

5.2.2. Fatigue damage model

In this work, the mechanical deterioration of electrode is regarded as a fatigue damage course. Under cyclic condition, the lithiation-delithiation behaviour of electrode material will lead to inhomogeneous concentration gradient inside electrode configuration, and the electrode deformation caused by ion insertion/extraction is constrained by physical constraints. These factors result in cyclic stress and plastic strain will be produced if cyclic stress is large enough. A cycle time is composed of charging duration and discharging duration, which depends on the setup of charging-discharging test. The cycling number of charging-discharging test indicates that it is a strain-controlled fatigue failure, where the number is normally less than 10^5 . Manson and Coffin [5-8] postulated that the fatigue life can be predicted by using plastic strain amplitude as the input parameter.

$$\frac{\Delta \varepsilon_p}{2} = \varepsilon'_f (2N)^{c'} \quad (5.5)$$

where $\frac{\Delta \varepsilon_p}{2}$ is the plastic strain amplitude, $2N$ is the number of reversals to failure. ε'_f and c' are two empirical constants known as fatigue ductility coefficient and fatigue ductility exponent respectively. By formula derivation, it is accessible to obtain the following expression, which can be applied to predict the mechanical damage per cycle dD_{mi} with specific plastic strain range.

$$dD_{mi} = 2 \left(\frac{2\varepsilon'_f}{\Delta \varepsilon_p} \right)^{\frac{1}{c'}} = \frac{1}{N_i} \quad (5.6)$$

The accumulated mechanical damage D_m over cycles is given by

$$D_m = \sum_{i=1}^n dD_{mi} \quad (5.7)$$

This accumulated fatigue damage varies at each material point which can be regarded as integration point in finite element analysis. Additionally, the damage also affects the yielding stress of the damaged material [5-9]. It is worth emphasizing that, the revised physical properties, such as Young's modulus and yield strength, are factitiously equivalent conversions in the continuum damage

mechanics for representing the degradation behaviour of the damaged material. The following expression is proposed to consider the effect of damage on yield strength.

$$\sigma_y(D) = \sigma_{y0}(1-D)^{n_r} \quad (5.8)$$

where σ_{y0} and $\sigma_y(D)$ denote the yield strength of initial undamaged material and damaged material, respectively. n_r is a nonlinearity index which determines the damage accumulation trend. The value of n_r allows to reflect the different effect degrees of damage on Young's modulus and yield stress. From a physical point of view, this index is set to be greater than or equal to 0 ($n_r \geq 0$), as the damage is considered to reduce the yield strength or have no impact on it under special circumstances.

5.2.3. Subroutine development

UMAT subroutine is developed to simulate the stress-strain response of battery electrode with the consideration of damage effect, shown in Appendix 3. Fig 5.1 shows the schematic flowchart of the compiled UMAT, which is called in each iterative computation. The calculated results such as stress, strain and damage will affect the iteration computation in the following cycle. Fig 5.1 also gives the schematic diagram of the communications between UMAT and ABAQUS for leaving a whole idea of performing FE analysis based on ABAQUS platform.

In the UMAT, the accumulated damage from previous cycles is first applied to factitiously revise the Young's modulus and yield strength of the material. The elastic stiffness is then defined, and stress as well as diffusion caused strain are calculated. Based on the von Mises stress, it is able to determine whether yielding occurs in this iteration. If the yielding condition is not satisfied, this iteration step follows the linear elastic calculation. Once plastic yielding is triggered, the plastic flow direction will be calculated following with updating stress/strain and redefining Jacobian. For the last iteration step in one lithiation-delithiation cycle, the fatigue damage generated from this cycle will be calculated based on the employed fatigue damage model and stored for updating material Young's modulus and yielding strength in the next cycle.

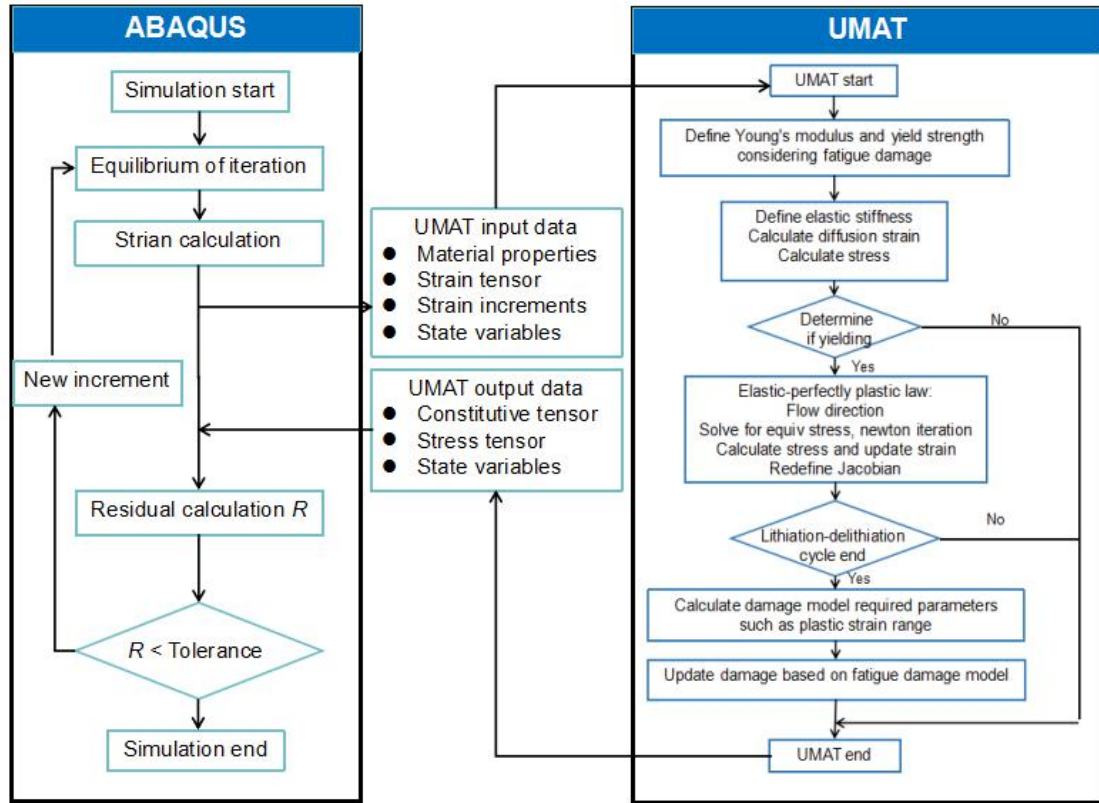


Fig 5. 1 Schematic flowchart showing the finite element implementation of the UMAT and the communications between UMAT and ABAQUS

5.2.4. The effect of nonlinearity index n_r on damage evolution

With the developed UMAT subroutine and UMATHT subroutine presented in section 3.2.1, it is available to conduct the coupled diffusion-stress analysis considering fatigue damage. Here, it exhibits the effect of nonlinearity index n_r on damage evolution with calling the developed UMAT subroutine. Fig 5.2 shows three categories of damage evolution trends with respect to three representative values of n_r , where the rest material properties are set as constant in these three scenarios. The damage produced from one cycle will be less than that of the subsequent cycle when $n_r > 1$ (15 as example) is satisfied. The damage then accumulates in a progressive way and changes the yield stress greatly than the Young's modulus. The damage accumulation will continue in a linear way when $n_r = 1$, where the damage produced from two neighbouring cycles are equivalent, and affects the yield stress and Young's modulus to the same degree. In the third scenario, $0 \leq n_r < 1$ (0.001 as example), the damage generated from one cycle is slightly greater than that of the subsequent cycle leading to the slight degressive accumulation of damage. In this case, the damage effect on yield stress is less than that of Young's modulus. Notably, the proposed damage model is capable of simulating multifarious types of damage accumulation rules. Corresponding to experimental results and relevance assumption, one can fit n_r so as to correlate the modeled damage with experimental damage.

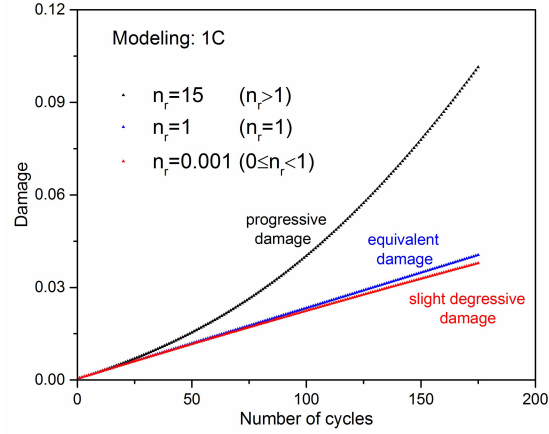


Fig 5. 2 The modeled three categories of damage evolution trends with respect to different values of n_r

5.2.5. Capacity fading represented damage rule

In a broad sense, one measurable state variable which monotonically changes with the proceeding of cyclic process, can be used as the measurement of fatigue damage. For battery electrode, the continuous mechanical fatigue degradation is simultaneous with the capacity fading process of battery [1-7, 5-10]. Therefore, the capacity can be selected as an experimental index to compare with the successive mechanical fatigue damage. Considering the following expression

$$C_e = C_{e0}(1 - D_e) \quad (5.9)$$

where C_{e0} represents the battery capacity before cycling and D_e is the cyclic charging-discharging experiment indicated damage. C_e is battery capacity corresponding to damage D_e after a certain number of lithiation-delithiation cycles. It can also be transferred to show the experiment indicated damage based on the change of battery capacity.

$$D_e = 1 - \frac{C_e}{C_{e0}} \quad (5.10)$$

Through cyclic charging-discharging tests, one can quantitatively obtain the capacity determined damage.

5.3 Finite element model

In this work, the finite element model is applied to evaluate the mechanical fatigue deterioration of NCM523 layered electrode with developing a set of UMAT-UMATHHT subroutines, which comprehensively take damage accumulation, interaction between stress and diffusion, damage affected stress-strain response into consideration. In the performed experiments, the cathode active

layer is a thin film with 12mm diameter and 20um thickness as shown in Fig 5.3 (a). For studying the evolution of fatigue damage along the direction of thickness, the finite element model of cathode active layer is built as a disk with 300um diameter and 20um thickness as presented in Fig 5.3 (b), where the diameter size is set as 15 times bigger than thickness size so as to reflect the structural character of thin film and make it available to present the fatigue damage distribution along the thickness. According to the analogy assumption, the coupled temperature-displacement element is selected and associated with the developed UMATHT subroutine to perform the coupled diffusion-stress analysis by employing the coupled temperature-displacement modulus in ABAQUS. Considering the computational task load for simulating more than 150 lithiation-delithiation cycles, the 20 nodes reduced integration element type is picked to ensure the accuracy and efficiency of the calculation. Hence, C3D20RT element (20 nodes thermal cubic elements with reduced integration) is adopted for conducting coupled diffusion-stress-damage analysis of electrode layer. The top surface of active layer adheres to electrolyte, and serves as the access for lithiation and delithiation. According to battery C-rate condition, the ion diffusion flux J flowing through the electrode surface can be obtained as following

$$i_n = mc_r \quad (5.11-1)$$

$$J = \frac{i_n}{F_a} \quad (5.11-2)$$

where m denotes C-rate. c_r is the rated capacity of the battery, which is 0.395 mAh for the tested experiment samples. i_n and F_a are current density and Faraday constant.

The bottom surface of active layer is bonded to a rigid substrate made of Al with 12mm diameter and 80um thickness. The thickness ratio between current collect and active layer is 4:1. Fig 5.3 (c) presents a finite element model including active layer and current collector. The thicknesses of active layer and current collect are set as 80um and 20um (4:1) respectively. The Young's modulus of active layer and current collector are 6.5GPa and 70GPa [5-11]. Fig 5.4 (a) and (b) exhibit the diffusion induced stress within active layer considering and without considering the effect of current collector under 1C. It is observed that, the stress distributions along the thickness direction are almost the same for these two scenarios. This is due to the fact that the Young's modulus of current collector is 10 times more than that of the active layer. Hence, employing a rigid surface to represent the current collector is acceptable in our case.

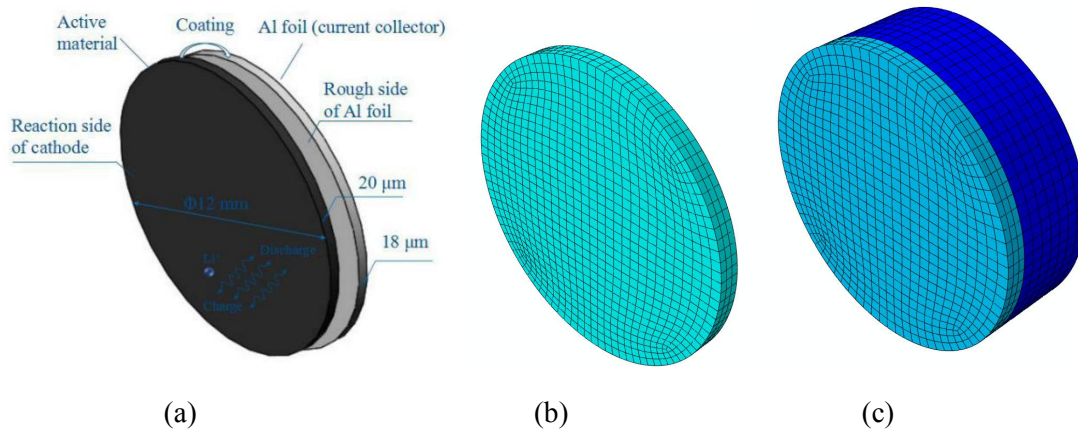


Fig 5. 3 (a) Schematic diagram of the experimentally tested layered electrode and current collector, (b) mesh of the cathode active layer, (c) mesh of cathode active layer and current collector

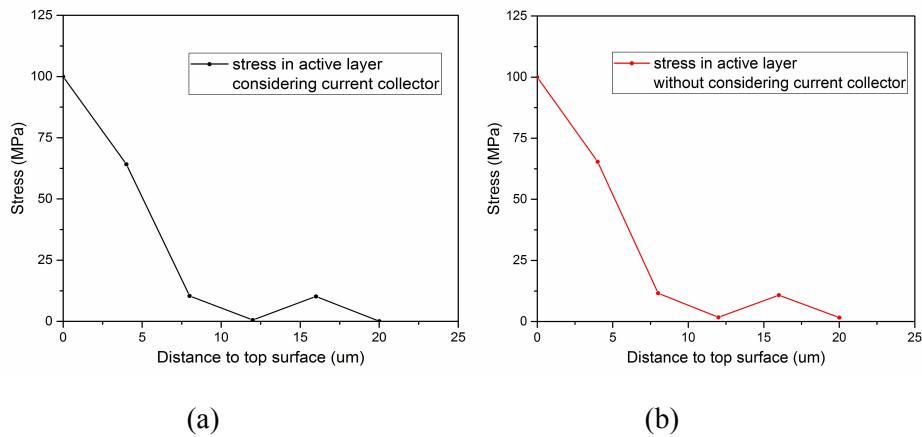


Fig 5. 4 The stress distribution within active layer along the thickness direction (a) considering current collector, (b) considering current collector as a rigid surface

The material properties adopted in this numerical work are listed in Table 5.1. The NCM cathode is assumed as an elastic-perfectly plastic material, which experiences no work-hardening during plastic deformation. The elastic-perfectly plastic model is widely used in the simulation of mechanical behaviour for electrode material [5-12, 5-13], as the hardening behaviour is not significant for such a material and it is available to model the stress-strain response of the material in the lack of hardening material properties. The yield strength of NCM electrode material is in a range, and is decided by material preparation, material composition, etc. It cannot be measured accurately by the experiment due to the preparation technology of oxide electrode material, and there is no accurate value of yield strength for NCM material in the literature. The commonly used yield strength of oxide electrode material having similar lattice structure with NCM is applied in this work, and is assumed as 100MPa. The Young's modulus adopted here is for electrode plate, which is different with the Young's modulus for electrode particle in micrometer scale. The adopted material parameters are collected from different reliable references. As the simulation requires different electrochemical and mechanical material properties, the measurement work needs to be conducted by different research

teams with different professional directions. Therefore, it is necessary to find relevant parameters from different references. Besides, there is no reliable experimental data on the fatigue ductility coefficient and the fatigue ductility exponent for NCM electrode material, which are only available for the common structural materials. Therefore, based on the relevance assumption that the fatigue damage is in proportion to the experiment represented damage, the capacity variation from the electrochemical performance test at 1C can be used as the benchmark to fit the fatigue parameters. After the parameterization, the proposed model is then available to simulate mechanical degradation of electrode under other electrochemical conditions. The capacity performance tests under the same electrochemical conditions are further conducted so as to verify the obtained parameterized fatigue damage model and relevance assumption via comparing the mechanical fatigue damage with electrochemistry indicated damage.

Table 5.1 Material properties of NCM electrode layer

Property	Value
Young's modulus at undamaged status (GPa)	6.5 [5-11]
Poisson's ratio	0.3 [3-10]
Diffusivity (m ² /s)	1E-15 [3-11]
Partial molar volume (m ³ /mol)	2.1E-6 [3-12]
Yield strength (MPa)	100

5.4 Experimental test

5.4.1 Electrode preparation

The preparation process of NCM523 cathode consists of the following steps: the NCM523 powder (commercial supplied) and acetylene are added in a mortar with a mass ratio of 8:1, and then ground to form a homogeneous mixture. The adopted mass ratio is an empirical ratio which is commonly used in the preparation of electrode [5-14, 5-15], and the performance of electrode with this ratio is relatively stable. NMP-based suspension is prepared by dispersing polyvinylidene fluoride binder (PVDF) in N-methyl-2-pyrrolidone, and the weight of PVDF is the same as acetylene in the obtained mixture. Whereafter, the NCM523 slurry is produced by dispersing the obtained powder mixture in the prepared suspension for 6 h at 800 RPM. Subsequently, the slurry is coated on the current collector, Al foil, with a density of 3.7 mg/cm², then the obtained slice is dried at 120°C in electric vacuum drying oven for 12 h to remove the solvent. The prepared cathode is trimmed in round slice with a diameter of 12 mm as working electrode. The areal weight of the NCM523 material is about 2.7 mg/cm² and the composition of active layer is shown in Table 5.2. All working electrodes

are then dried at 60°C in electric vacuum drying oven for 6 h to remove moisture before they are transferred into a glovebox.

Table 5.2 The composition of active layer

Ingredient	Mass percent
NCM523 powder	80%
Acetylene	10%
Polyvinylidene fluoride	10%

5.4.2 Cell assembling

The electrochemical performance of the cathode is assessed with assembling CR2025-type coin cells. The prepared working electrode is used as the cathode. A 1 M solution of LiPF₆ dissolved in EC: DEC (volume ratio=1:1) is used as the electrolyte, and lithium metal is employed as the anode. The separator of cell is polypropylene membrane (Celgard 2500). The CR2025-type coin cells are assembled in a glove box under a dry argon atmosphere (moisture and oxygen less than 0.1 ppm). To ensure a good contact between components of cells, all cells are placed for 12 h before test.

5.4.3 Electrochemical performance measurement

The electrochemical performance is investigated by using Land Cell System (CT2001A, Wuhan Jinnuo Electronic Co. Ltd, Wuhan China). The cells are cycled between 2.8 and 4.3V vs Li/Li⁺ via VSP potentiostats at different rates under galvanostatic condition. As an activation process, all cells operate for one cycle at the C-rates of 0.1C, 0.2C and 0.5C in turn. Subsequently, cells are cycled at the targeted C-rate of 0.5C / 1C / 2C until the capacity decreases to 80 percent. Where 80 percent of the initial capacity is the typical criteria for electric vehicle applications [5-16, 5-17]. Hereafter, the discharge capacity and the performance of capacitor can not meet the needs of use very well. Four samples are tested under each C-rate condition and the average capacity fading is used to define the experiment indicated damage. Fig 5.5 exhibits the schematic diagram of electrochemical performance measurement and the electrochemical performance of coin cell at cycling window of 2.8-4.3 V under 1C.

After electrochemical performance test, the change of battery capacity against the number of cycles can be obtained. Based on section 5.2.5, the battery capacity fading trend can be transferred to the accumulation trend of the experiment indicated damage. With the proposed relevance assumption, this experimental damage can compare with the numerical simulated fatigue damage, and further investigate detailed material response.

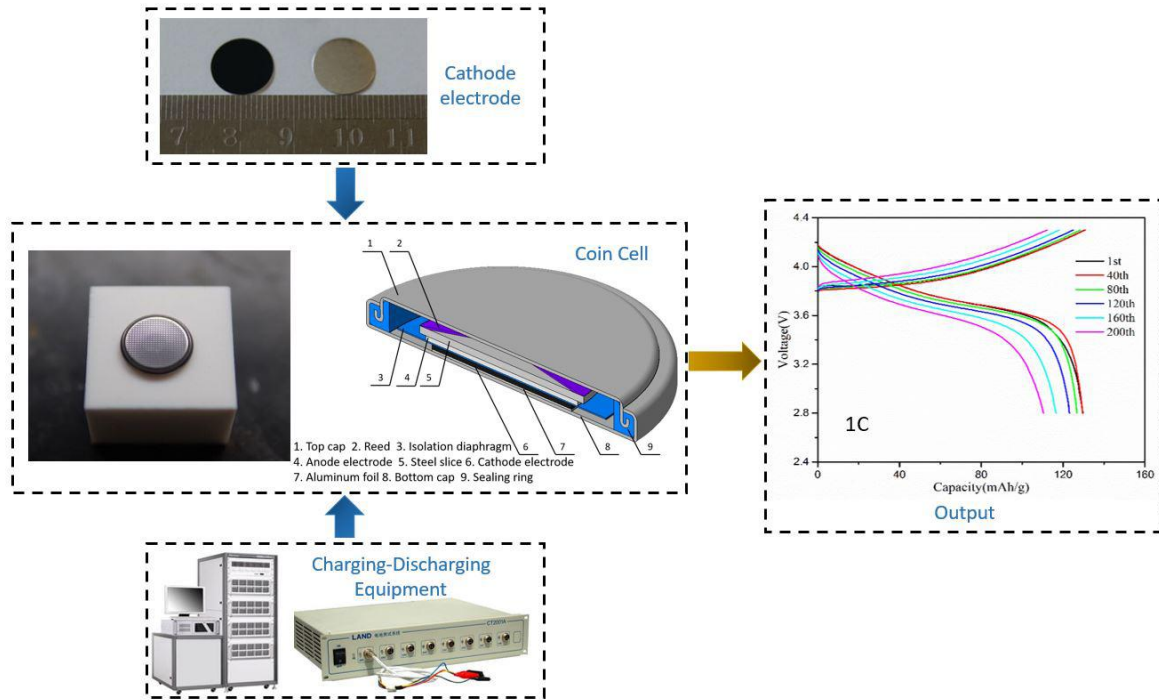


Fig 5. 5 Schematic diagram of electrochemical performance measurement and experimental output

5.5 Model establishment and validation under various C-rate

From electrochemical performance tests, it is accessible to acquire the degradation trend of discharge capacity with respect to the number of cycles for coin cell under 1C, and plot it in Fig 5.6. The irregularity of polarization voltage inside the battery and test accuracy range of the equipment result in the slight rebound of capacity in a few neighbouring cycles. It is common and inevitable in the charging-discharging test [5-18, 5-19, 5-20], but will not influence the overall variation trend of the capacity. It is available to quantify this degradation by defining a capacity fading represented damage via the aforementioned expression in Eq. (5.10). The evolution trend of this capacity data decided damage is also given in Fig 5.6. The result indicates that the capacity presents a fluctuated downtrend with the proceeding of cyclic process. The corresponding damage thereby follows an uptrend and almost obeys a linear dependence with the number of cycles. Hence the effect index n_r in cumulative damage model can be set as 1 for this case. What can also be observed is that it takes around 82 cycles and 157 cycles for experiment defined damage to accumulate to 0.1 and 0.2 at 1C. The cell is cycled until failure when the capacity of the cell falls to 80% of its initial capacity, which is the typical standard for the cell. Hence, the corresponding damage limit is around 0.2.

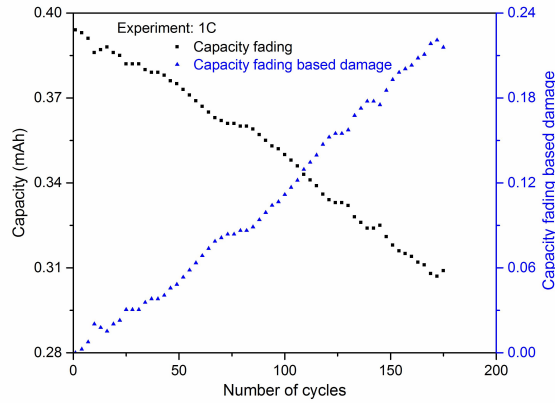


Fig 5. 6 The variation of capacity and capacity fading represented damage with respect to the number of cycles for coin cell under 1C

For the layered electrode model shown in Fig 5.3, one can make the assumption that the fatigue damage of top surface next to electrolyte is in equivalence to the tested capacity fading represented damage. As the mechanical collapse caused by fatigue damage on the top surface will interfere the channel for Li-ion transportation and interdict the electrochemical process. The fatigue damage on the top surface thereby dominates the overall mechanical damage status of the active layer. In this work, we first calculate the history of plastic strain range for NCM523 electrode plate cycled at 1C without considering fatigue damage effect, and the obtained plastic strain range at steady state is 0.04. According to the aforementioned analogous assumption, it is accessible to fit the initial fatigue parameters in computational equation (5.6) on mechanical damage from this plastic strain range by comparing with the capacity fading represented damage in Fig 5.6. With employing the fitted initial fatigue parameters, one can calculate the history of plastic strain range of electrode plate at 1C for the second time and the fatigue damage can also be given. The newly obtained plastic strain range is 0.0392 and the calculated fatigue damage is relatively less than the experimental damage via using the proposed relevance assumption. Hence, we fit the fatigue parameters based on the current plastic strain range again and the newly obtained fatigue parameters are employed to conduct the next calculation. Working as an iterative process, the correlation coefficient between the calculated fatigue damage and experiment indicated damage reaches 0.9956 in the fourth calculation, and the current fatigue properties are regarded as the final values for NCM523 active material. Subsequently, the parameterized fatigue damage model is applied to predict the mechanical degradation of electrode under other C-rates (0.5C, 2C) and compare with the experiment indicated damage to study the rationality of the fatigue damage model and relevance assumption. The fitted material properties are summarized in Table 5.3, where ϵ'_f and c' denote the fatigue ductile coefficient and fatigue ductile exponent respectively.

Table 5.3 Fitted parameters in the fatigue damage model

ϵ'_f	c'
3.184	-0.688

Fig 5.7 (a) shows the fatigue damage contour of electrode plate under 1C, and it is suggested that the produced mechanical damage is layered along the direction of Li-ion flow. Fig 5.7 (b) depicts the fatigue damage distribution along the direction of thickness after 50, 100 and 150 cycles. It is observed as a general trend that the fatigue damage of top surface next to electrolyte far exceeds that of the rest region, which indicates the top surface of electrode is more prone to fracture. Fig 5.8 presents the evolution trends of calculated fatigue damage and experiment represented damage cycle by cycle under 1C, where integration point 1 is on the top surface next to electrolyte and integration point 2 is on the bottom surface bonded to the rigid substrate.

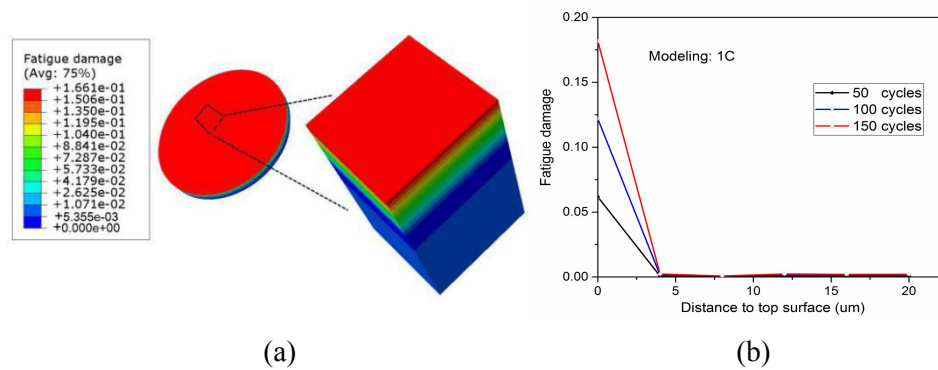


Fig 5. 7 (a) Contour plot of damage distribution on the layered electrode at 1C, (b) fatigue damage distribution along the direction of thickness

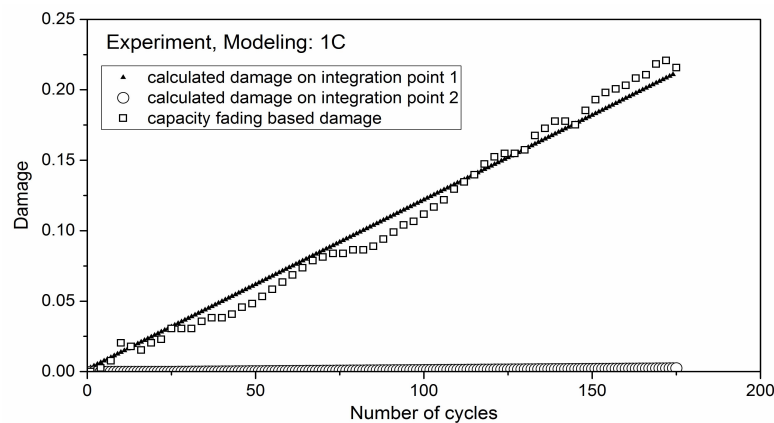


Fig 5. 8 Capacity fading represented damage, calculated fatigue damage on integration point 1 and 2 against the number of cycles under 1C

By performing further electrochemical performance tests, it is available to obtain the degradation trends of capacity and determine the evolution of capacity fading represented damage under other C-rate conditions (0.5C and 2C). The mechanical damages of electrode are simulated under the same electrochemical loads with the conducted charging-discharging tests. According to the presented relevance assumption, the parameterized fatigue damage model is validated herein by comparing the calculated damage results with the experiment indicated damage.

The experimental results of electrochemical performance tests cycled at 0.5C and 2C are given in Fig 5.9 (a) and (b). Based on the definition in Eq. (5.10), the capacity data is extracted to decide the experimental damage also given in Fig 5.9 (a) and (b), where the damage shows a linearly fluctuated uptrend over cycles in both scenarios. It takes around 98 cycles and 85 cycles at 0.5C and 2C to reach 0.1 of damage respectively. It can be found that, the capacity fading under low C-rate (0.5C) is relatively slower than the degradation under higher C-rates (1C, 2C).

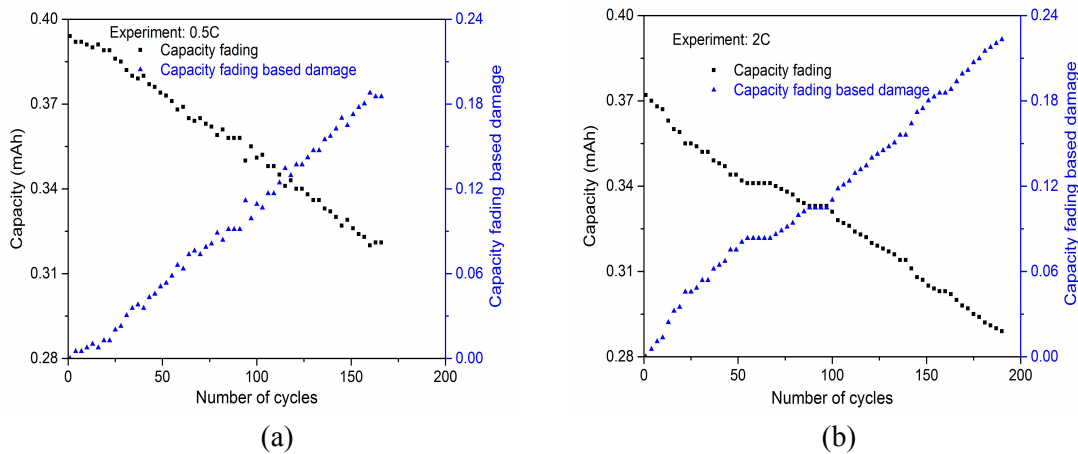
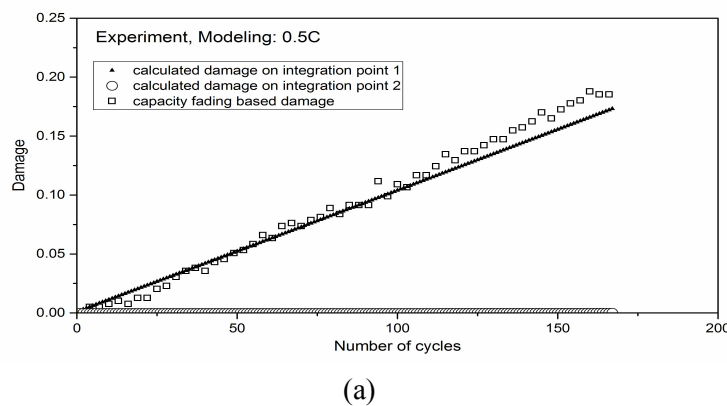
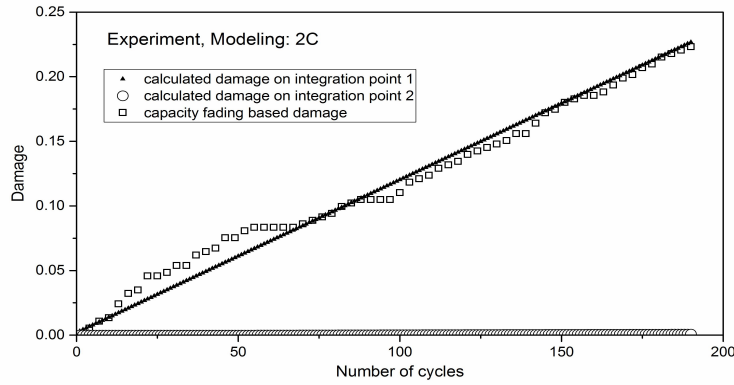


Fig 5. 9 The variation of capacity and capacity fading represented damage with respect to the number of cycles for coin cell under (a) 0.5C, (b) 2C

The parameterized fatigue damage model is adopted to track the mechanical damage evolution of lithium battery electrode cycled at 0.5C and 2C. Fig 5.10 (a) and (b) give the evolution trends of the capacity fading represented damage and calculated fatigue damage on integration point 1, 2 at 0.5C and 2C respectively. It is found that the calculated damages under these two scenarios both follow an approximately linear dependence with the number of cycles. The comparison between the damage on integration point 1 and the experiment indicated damage suggests that, under the researched electrochemical conditions, it is accessible to use the continuum damage approach to track the mechanical degradation of lithium-ion battery electrode.





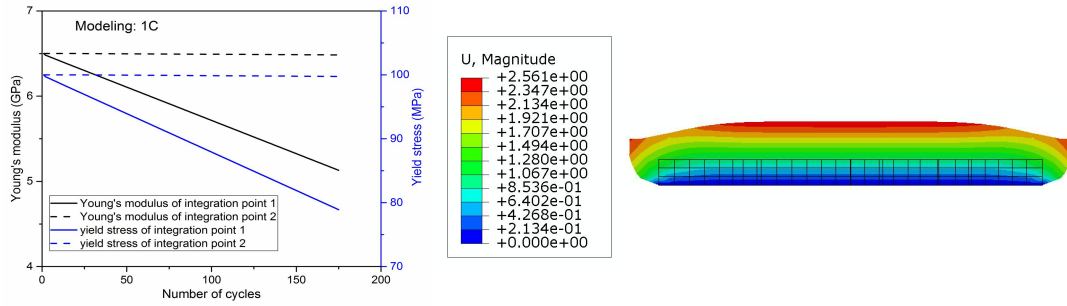
(b)

Fig 5. 10 Capacity fading based damage, calculated damage on integration point 1 and 2 against the number of cycles under (a) 0.5C, (b) 2C

5.6 Damage affected stress-strain response

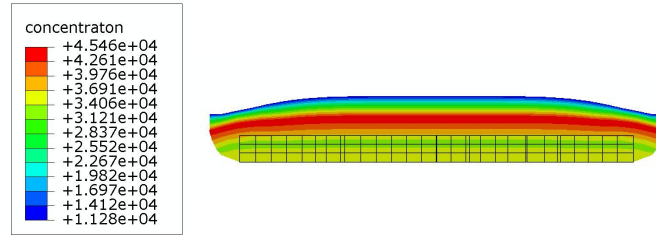
According to the description in section 5.2, the fatigue damage generated from one cycle can be incorporated in factitiously modifying the Young's modulus and yield strength of the material, which makes the material more prone to deform. Fig 5.11 (a) shows the monotonic reduction of the revised Young's modulus and yield strength of NCM523 cathode with the proceeding of cycles on two integration points at 1C. As the fatigue damage accumulation rate of integration point 1 next to electrolyte is considerably faster than integration 2 bonded to current collector, the descent rate of Young's modulus and yield strength of top surface of electrode is more rapid than that of the opposite. Besides, Fig 5.11 (b) shows the cross-sectional view of the deformed active layer after 150 cycles, where the meshes represent the undeformed active layer. It can be seen that, after 150 cycles, the lithiation behaviour changes the structure shape. The corresponding concentration distribution within active layer is given in Fig 5.11 (c) and the residual concentration gradient caused by Li-ion trapping mechanism results in the expansion phenomenon of the active layer.

Fig 5.12 (a) and (b) show the distribution of in-plane stress component and von Mises stress on electrode thickness section at the end of lithiation phase of 50th and 150th cycle under 1C. The structure character of electrode plate decides the fact that two in-plane stress components are equivalent and much larger than the stress component along the thickness direction. The distribution of in-plane stress component presents that the electrode plate is in compressive status at the end of lithiation phase. By comparing the von Mises stress with damage modified yield strength, it is observed that the upper layer next to electrolyte and the lower layer closing to current collector are in a state of plastic yielding at this moment. Due to the rapid rise of fatigue damage, the stress field of upper layer is significantly influenced, while the stress of lower layer is hardly changed as little fatigue damage is generated here.



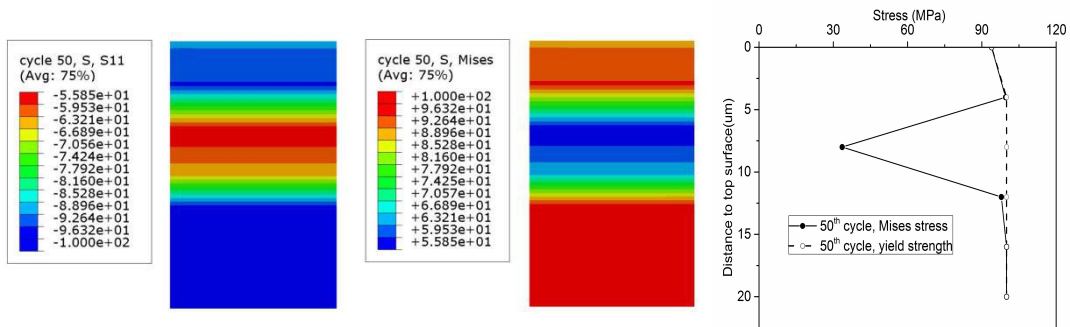
(a)

(b)

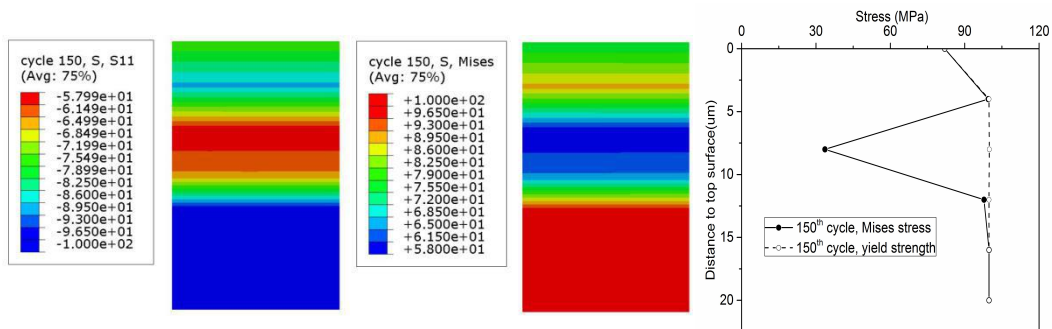


(c)

Fig 5. 11 (a) The corresponding damage affected Young's modulus and yield strength on two integration points versus the number of cycles, (b) the cross-sectional view of deformed active layer after 150 cycles, (c) the cross-sectional view of concentration distribution within active layer after 150 cycles.



(a)



(b)

Fig 5. 12 (a) The distribution of in-plane stress component and von Mises stress on the thickness section at the end of lithiation phase of 50th cycle, (b) the distribution of in-plane stress component and von Mises stress on the thickness section at the end of lithiation phase of 150th cycle

For the presented fatigue damage model shown in Eq. (5.6), with certain material properties including fatigue ductile coefficient and fatigue ductile exponent, the produced damage is determined by plastic strain range of each cycle. Fig 5.13 (a) and (b) give the stress-strain hysteresis loops of 50th, 100th and 150th cycle on integration point 1 as well as integration point 2 at 1C. The values of strain on horizontal axis are shown as relative values so as to compare the change of strain at these three cycles (50th, 100th and 150th cycle). Due to the fact that the elastic-perfectly plastic constitutive equation is used in modelling the post-yielding behaviour, the stress in plastic strain generation phase remains constant and equal to the current yield strength. At the initial phase of lithiation, the top surface of electrode experiences a tensile stress. With the proceeding of Li-ion insertion, the stress on top surface gradually converts to a compressive stress which results in the compressive strain generated in lithiation phase. While for the delithiation process, the extraction of Li-ion shifts the compressive stress to tensile stress for top surface and leads to the generation of tensile strain during the de-intercalation phase. On the contrary, the bottom surface bonded to current collector is subjected to compressive stress during the entire lithiation-delithiation process and compressive strain is generated at the end stage of intercalation phase.

For integration point 1, it can be seen that the yield strength of the material is gradually reduced with the proceeding of cycles due to the accumulated damage effect and the slope represented Young's modulus is also decreased. According to the Hooke's law, this synchronous decrease will lead to the generation of the same elastic strain range for these three cycles as 0.03076. For integration point 2, the generated elastic strain ranges of three cycles are approximately equal and the tiny difference of stress ranges results in the very little difference of elastic strain ranges.

It is also observed that the plastic strain range $\Delta\epsilon_p$ of these three cycles are identical to 0.03875 for integration point 1 and 0.00202 for integration point 2. In Fig 5.13 (c), the plastic strain range of two integration points versus the number of cycles are given. After a few initial cycles, the calculated plastic strain range per cycle is almost constant. It is because of that, according to the relevance assumption and linear accumulated damage obtained by experimental test, the Young's modulus and yield strength are synchronously revised by the accumulated damage in the numerical procedure. Hence, with certain fatigue parameters, the fatigue damage model will produce identical damage value per cycle after the initial oscillation phase, which makes the mechanical damage of electrode almost accumulate in a linear way. Besides, as shown in the previous section, the presented cumulative damage model with different n_r ($n_r \neq 1$) is capable of simulating the non-linear fatigue damage accumulation process based on the stress-strain response per cycle. In this circumstance, the Young's modulus and yield strength are asynchronously changed by damage. Additionally, the stress-strain hysteresis loops present the cyclic softening characteristic for surface next to electrolyte. With the proceeding of cycles, the fatigue damage effect is equivalently converted to the decrease of

yield strength of electrode material, which makes the resistance to deformation decrease as cycle proceeds. Due to the slower fatigue damage accumulation rate, the bottom surface of electrode plate presents the weak cyclic softening characteristic contrary to the rapid cyclic softening of top surface.

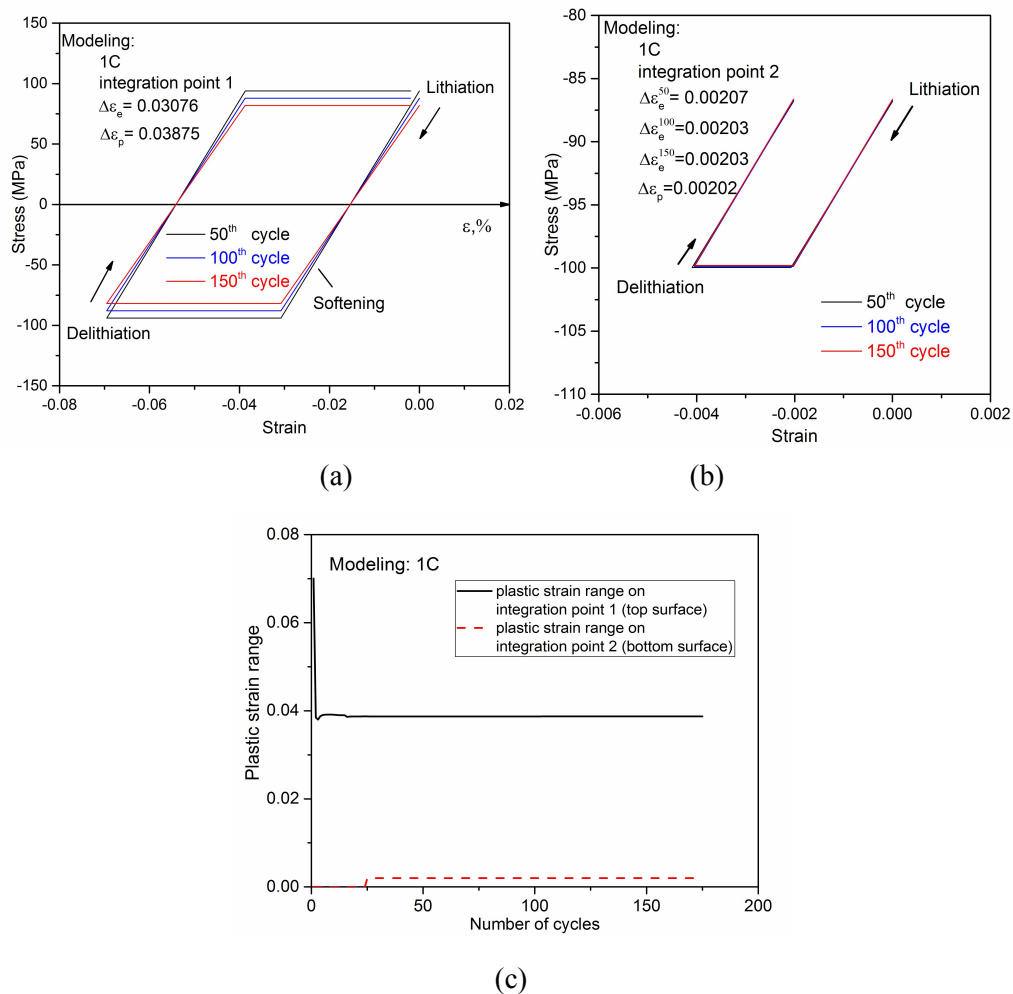


Fig 5. 13 The stress-strain hysteresis loops for 50th, 100th, 150th cycle at 1C on (a) integration point 1, (b) integration point 2, (c) the calculated plastic strain range on two integration points versus the number of cycles under 1C.

Fig 5.14 (a) and (b) show the stress-strain hysteresis loops of three continuous cycles at steady state under 1C for integration point 1 (top surface of electrode plate) and integration point 2 (bottom surface of electrode plate). The relative values of strain are shown on horizontal axis. It is accessible to see a shift of stress-strain curves along the negative direction of strain axis of both two integration points. For integration point 1, this is due to the fact that the plastic strain generated from tensile process is less than the reverse plastic strain in compressive phase. While for integration point 2, it is because of there is only compressive strain produced in the lithiation-delithiation process. These will cause the accumulation of plastic strain as well as the potential ratcheting collapse. The increments of plastic strain ϵ_{pi} are roughly equal of two integration points per cycle, as -0.00199 for integration point 1 and -0.00202 for integration point 2.

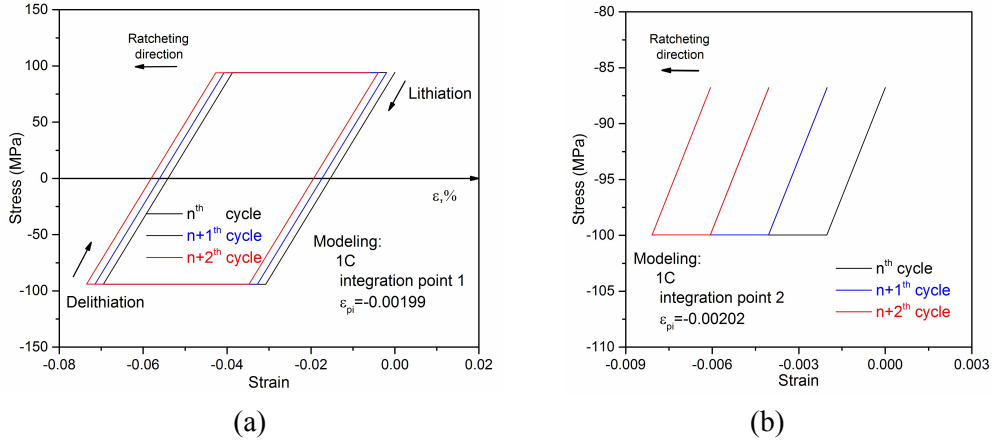


Fig 5. 14 Three continuous stress-strain hysteresis loops at 1C for (a) integration point 1, (b) integration point 2

In addition, the interaction between the formation of diffusion-induced stress and diffusion behaviour is also taken into consideration in the established approach. Fig 5.15 (a) shows the variation of hydrostatic stress of two integration points within three continuous cycles under 1C, and Fig 5.15 (b) presents the transient changed diffusivity, which is affected by hydrostatic stress based on Eq. (3.5). It can be seen that the variation of diffusivity follows the same trend with the changing of hydrostatic stress. For integration point 1 on the top surface of active layer, the influence of hydrostatic stress reduces the diffusivity from the intermediate stage of intercalation process to the intermediate stage of de-intercalation phase, and magnifies it at other moments. Contrary to top surface, the hydrostatic stress always hinders the diffusion behaviour in the lithiation-delithiation course for bottom surface. The maximum effects from hydrostatic stress on diffusivity reach 4.7% and 5.5% for integration point 1 and integration point 2 respectively.

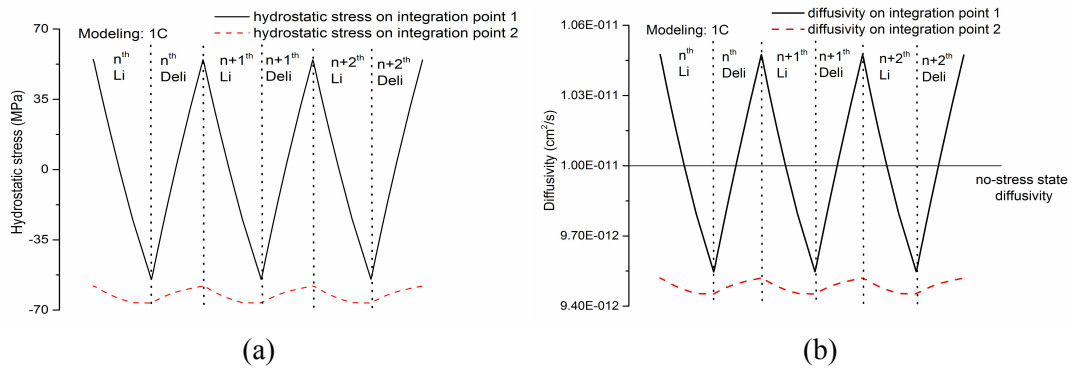


Fig 5. 15 (a) The variation of hydrostatic stress for two integration points within three continuous cycles, (b) the transient changed diffusivity affected by diffusion induced stress within three continuous cycles

Fig 5.16 (a) and (b) show the variation of plastic strain of the top surface and bottom surface of electrode within one cycle at 0.5C, 1C and 2C respectively. The solid lines and dot lines here represent the lithiation phase and delithiation phase. Under various electrochemical conditions, for top surface, both the lithiation and delithiation processes comprise an initial elastic phase and a

subsequent plastic phase. For the bottom surface, the intercalation phase will present yielding behaviour and de-intercalation phase is always in elastic status. The produced plastic strain range under three operation scenarios are far less than that of the top surface, which means the corresponding fatigue damage of top surface greatly exceeds the fatigue damage on bottom surface and dominates the mechanical degradation of electrode under the researched electrochemical loads.

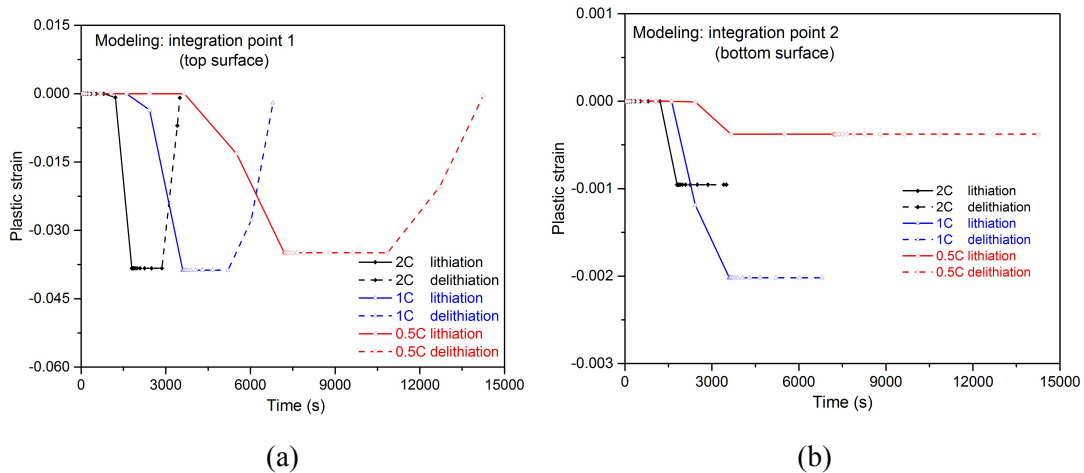


Fig 5. 16 The variation of plastic strain within one cycle under different electrochemical loads (0.5C, 1C, 2C) for (a) integration point 1(top surface), (b) integration point 2(bottom surface)

In Fig 5.17 (a) and (b), the stress-strain hysteresis loops for two locations (top surface and bottom surface) under different C-rates are shown, and the results are taken from 100th cycle for three operation strategies. As the elastic-perfectly plastic constitutive equation is used in the numerical simulations, the corresponding stress state when plastic deformation happens, denotes the yield strength of the material which is modified by the accumulated fatigue damage cycle by cycle. The comparison of yield stress between top surface and bottom surface shows that the top surface with lower yield stress subjects to greater fatigue damage and is more prone to fracture under all operation strategies.

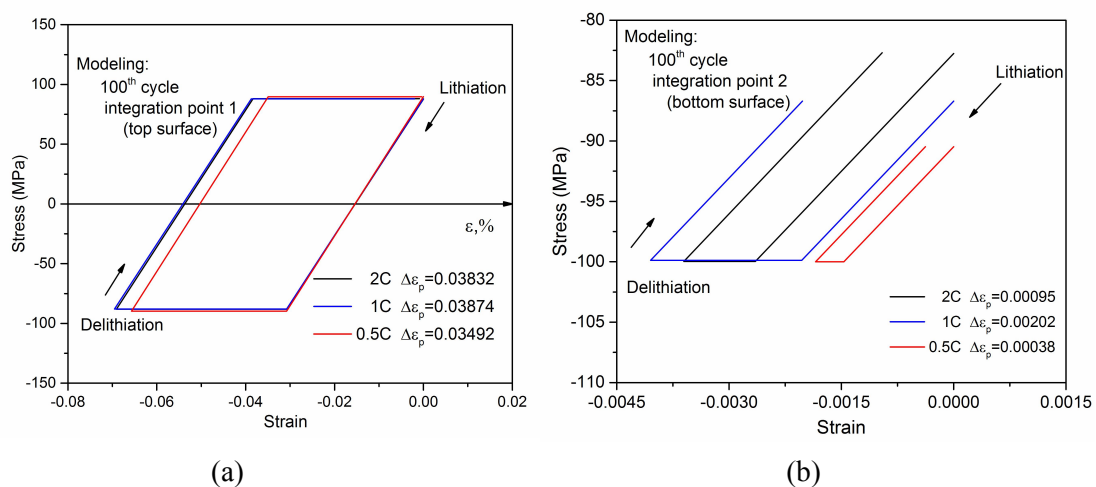


Fig 5. 17 The stress-strain hysteresis loops at 100th cycle under 0.5C, 1C and 2C for (a) integration point 1(top surface), (b) integration point 2(bottom surface).

5.7 Conclusions

A fatigue damage evaluation approach to track the continuous mechanical degradation of battery electrode is presented in this chapter. The fatigue damage and material responses of electrode plate under different C-rate conditions are investigated. The key conclusions are:

- (1) The fatigue damage assessment method of electrode is established, which includes three pieces of work. Firstly, based on the theory of continuum damage mechanics, the numerical procedure considering strain based fatigue damage model, damage effects on material properties and the coupling effect between diffusion behaviour and stress formation, is presented. By developing UMAT subroutine, this method is implemented in ABAQUS platform. Secondly, cyclic charging-discharging tests with respect to different electrochemical conditions are carried out to provide experiment indicated damage. Thirdly, the relevance assumption, that electrochemical damage is identical to the mechanical damage on the top surface of layered electrode, is proposed to associate electrochemistry degradation with mechanical deterioration
- (2) The numerical fatigue damage of electrode and capacity fading indicated damage are studied under different C-rate conditions. The fatigue damage of electrode is layered along the direction of Li-ion flow, and the electrode surface next to electrolyte is more prone to fracture. The effects of damage on material properties with the proceeding of cycles are also given.

5.8 References

- [5-1] L.M. Kachanov. On time to rupture in creep conditions. *Izvestia Akademii Nauk SSSR, Otdelenie Tekhnicheskikh Nauk*, 1958, 8: 26-31.
- [5-2] S. Murakami. *Continuum damage mechanics: a continuum mechanics approach to the analysis of damage and fracture*. Springer, Dordrecht, Heidelberg, London, New York (2012)
- [5-3] J.L. Chaboche. Continuum damage mechanics: Part I—general concepts. *Journal of Applied Mechanics*, 1988, 55(1), 59-64.
- [5-4] J.L. Chaboche. Continuum damage mechanics: Part II—damage growth, crack initiation, and crack growth. *Journal of Applied Mechanics*, 1988, 55(1), 65-72.
- [5-5] N. Liu, X. Cui, J. Xiao, J. Lua, N. Phan. A simplified continuum damage mechanics based modeling strategy for cumulative fatigue damage assessment of metallic bolted joints. *International Journal of Fatigue*, 2020, 131: 105302.
- [5-6] Z. Zhan, Q. Meng, W. Hu, Y. Sun, F. Shen, Y. Zhang. Continuum damage mechanics based approach to study the effects of the scarf angle, surface friction and clamping force over the fatigue life of scarf bolted joints. *International Journal of Fatigue*, 2017, 102: 59-78.

- [5-7] S. Murakami. Continuum damage mechanics: a continuum mechanics approach to the analysis of damage and fracture. Springer, Dordrecht, Heidelberg, London, New York (2012)
- [5-8] S.S. Manson. Fatigue: A complex subject some simple approximations. *Journal of Experiment Mechanics*, 1965, 5(7):193-226.
- [5-9] S. Baltic, J. Magnien, H. Gänser, T. Antretter, R.Hammer. Coupled damage variable based on fracture locus: Modelling and calibration. *International Journal of Plasticity*, 2020, 126: 102623
- [5-10] R. Xu, K. Zhao. Electrochemomechanics of Electrodes in Li-Ion Batteries: A Review. *Journal of Electrochemical Energy Conversion and Storage*, 2016, 13(3): 030803
- [5-11] J. Zhu, X. Zhang, H. Luo, E. Sahraei. Investigation of the deformation mechanisms of lithium-ion battery components using in-situ micro tests. *Applied Energy*, 2018, 224: 251-266.
- [5-12] A. Sarkar, P. Shrotriya, A. Chandra. Simulation-driven selection of electrode materials based on mechanical performance for Lithium-Ion battery. *Materials*, 2019, 12, 831.
- [5-13] R. Xu, L. Vasconcelos, K. Zhao. Computational analysis of chemomechanical behaviors of composite electrodes in Li-ion batteries. *Journal of Materials Research*, 2016, 31(18), 2715-2727.
- [5-14] Y. Shi, M. Zhang, C. Fang, Y. S. Meng, Urea-based hydrothermal synthesis of $\text{LiNi}_{0.5}\text{Co}_{0.2}\text{Mn}_{0.3}\text{O}_2$ cathode material for Li-ion battery. *Journal of Power Sources*, 2018, 394: 14-121.
- [5-15] X. Jia, M. Yan, Z. Zhou, X. Chen, C. Yao, D. Li, D. Chen, Y. Chen. Nd-doped $\text{LiNi}_{0.5}\text{Co}_{0.2}\text{Mn}_{0.3}\text{O}_2$ as a cathode material for better rate capability in high voltage cycling of Li-ion batteries. *Electrochimica Acta*, 2017, 254 :50–58.
- [5-16] Q. Liu, Y. Liu, F. Yang, H. He, X. Xiao, Y. Ren, W. Lu, E. Stach, J. Xie. Capacity fading mechanism of the commercial 18650 LiFePO_4 -based Lithium-ion batteries: an in situ time-resolved high-energy synchrotron XRD study. *Applied Materials & Interfaces*, 2018, 10: 4622-4629.
- [5-17] G. Zheng, Q. Zhang, J. Cha, Y. Yang, W. Li, Z. Seh, Y. Cui. Amphiphilic surface modification of hollow carbon nanofibers for improved cycle life of lithium sulfur batteries. *Nano Letters*, 2013, 13: 1265-1270.
- [5-18] A. Yasmin, M. Shehzad, X. Ding, J. Wang, R. Yu, M. Deng, Z. Tang, C. Chen. A first report on ex-situ synthesis and utilization of pure $\text{La}_4\text{NiLiO}_8$ in emerging highperformance safe batteries. *Journal of Alloys and Compounds*, 2020, 821: 153208
- [5-19] X. Jia, M. Yan, Z. Zhou, X. Chen, C. Yao, D. Li, D. Chen, Y. Chen. Nd-doped $\text{LiNi}_{0.5}\text{Co}_{0.2}\text{Mn}_{0.3}\text{O}_2$ as a cathode material for better rate capability in high voltage cycling of Li-ion batteries. *Electrochimica Acta*, 2017, 254: 50-58.
- [5-20] J. Gilbert, I. Shkrob, D. Abraham. Transition metal dissolution, Ion migration, electrocatalytic reduction and capacity loss in Lithium-Ion full cells. *Journal of The Electrochemical Society*, 2017, 164: A389-A399

Chapter 6

Progressive fatigue damage assessment of battery electrode using energy based fatigue damage model under different material scales

6.1 Introduction

For lithium ion battery, different material prescriptions, processing technics and packaging techniques all have considerable impacts on its electrochemical performance. Hence, the capacity fading and mechanical degradation are always in diverse evolution trends. A flexible and robust fatigue damage evaluation approach is thereby required to predict various damage evolution trends. In addition, under different material scales, the otherness of structural feature makes the elucidation of failure mechanism challengeable.

To shed light on these questions, this chapter presents an energy based fatigue damage model for battery electrode. Three primary fatigue damage evolution trends of battery electrode, known as moderative accumulation, accelerated accumulation and quasi-linear accumulation, can be expediently simulated. Considering the assumptions proposed in last chapter and C-rate variations, the fatigue damage of layered NCM electrode plate with non-linear capacity fading performance is investigated. Besides, the presented model is also applied to simulate the damage evolution of micro multigranular configuration using the representative volume element method. The effects of particle shape and relative configuration position are taken into consideration. The understanding of non-linear fatigue damage evolution of battery electrode under different scales would be conducive to the design of high performance lithium ion batteries.

6.2 Fatigue damage model

By simulating the development process of fatigue damage, the fatigue life prediction model not only makes it available to reduce the cost of fatigue test, but also provides the theoretical foundation for fatigue analysis [6-1]. Generally, the fatigue life prediction models fall into three categories, as stress based model, strain based model and energy based model. This section gives an introduction to various prediction models and describes the energy based model used in this chapter for electrode fatigue assessment.

6.2.1 Stress based fatigue life model

For stress based fatigue life model, the stress-fatigue life curve or $S-N$ curve, as shown in Fig 6.1, gives the relation between fatigue life and nominal stress applied on material or structure [6-1]. When the fatigue life N goes to infinity, the corresponding stress limit σ_0 is defined as fatigue limit, which represents the bearing capacity of material to cyclic stress. The $S-N$ curve is commonly used to evaluate the high-cycle fatigue behaviour, where the lower limit of fatigue life is around $10^4 \sim 10^5$ cycles and the upper limit of fatigue life is determined by fatigue limit. For the structure experiencing low cyclic stress, it has a relatively long fatigue life and the $S-N$ curve is able to give a more accurate prediction.

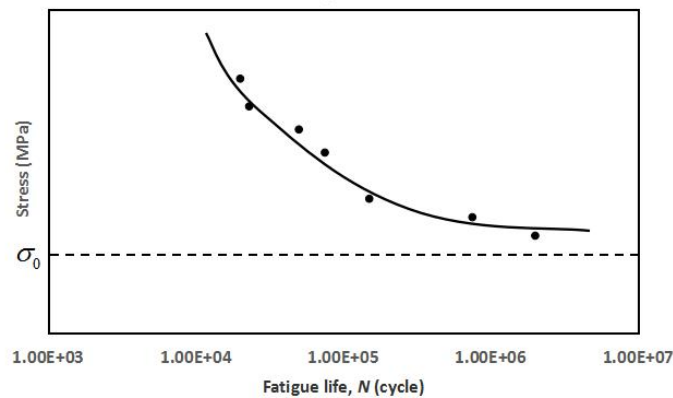


Fig 6. 1 Stress-fatigue life curve

There are various mathematical expressions describing the $S-N$ curve, and Table 6.1 presents the common formula forms. According to the parameter characteristics of the loading stress and the distribution law of material fatigue test data, it is accessible to select different mathematical models to analyze the change rule of fatigue life associating with stress parameters.

Table 6.1 Expressions of $S-N$ curve [6-1]

Name	Formula form	Note
Power function form	$\sigma^a N = C$	1. a and C are material parameters related to loading mode
Exponential form	$e^{a\sigma} N = C$	
Three-parameter form	$(\sigma - \sigma_0)^a N = C$	2. σ'_f and b' are fatigue strength coefficient and fatigue strength exponent
Basquin form	$\sigma_a = \sigma'_f (2N)^{b'}$	

6.2.2 Strain based fatigue life model

Considering a structure experiencing high cyclic stress, plastic deformation occurs inside the material when the stress amplitude exceeds the yielding strength. The cyclic hardening/softening behaviours may happen under the loading of cyclic stress with high amplitude. Therefore, the

generated strain may change irregularly with constant stress amplitude input. In such a case, the fatigue life is relatively low ($10^3 \sim 10^5$) and the fatigue life test is always conducted with strain control [6-1].

The Manson-coffin equation, described in Chapter 5, suggests the calculation of fatigue life based on plastic strain range, and establishes the relation between fatigue life and plastic strain range in logarithmic coordinates. This model, working as a classic strain fatigue life model, is widely used for conducting low-cycle fatigue analysis. Besides, for asymmetrical cyclic strain loading, it is required to consider the effect of mean stress σ_m or mean strain ε_m . Hence, a series of Manson-coffin modified models are proposed. In Table 6.2, various formula forms and basic features of modified Manson-coffin models are given.

Table 6.2 Expressions of strain-life models [6-1]

Name	Formula form	Note
Manson-coffin	$\varepsilon_{pa} = \varepsilon'_f (2N)^{c'}$ or $\varepsilon_a = \frac{\sigma'_f}{E} (2N)^{b'} + \varepsilon'_f (2N)^{c'}$	
Morrow elastic stress modified-model	$\varepsilon_a = \frac{\sigma'_f - \sigma_m}{E} (2N)^{b'} + \varepsilon'_f (2N)^{c'}$	1. Considering the effect of mean stress in elasticity phase 2. Regarding the relation between symmetric cyclic fatigue limit and static strength limit as a linear one
Gerber elastic stress modified-model	$\varepsilon_a = \frac{\sigma_f'^2 - \sigma_m^2}{E\sigma_f'} (2N)^{b'} + \varepsilon'_f (2N)^{c'}$	1. Considering the effect of mean stress in elasticity phase 2. Regarding the relation between symmetric cyclic fatigue limit and static strength limit as a nonlinear quadratic parabola
Morrow total strain modified model	$\varepsilon_a = \frac{\sigma'_f - \sigma_m}{\sigma'_f} \left[\frac{\sigma'_f}{E} (2N)^{b'} + \varepsilon'_f (2N)^{c'} \right]$	1. Considering the effect of mean stress in elasticity phase and plasticity phase
SWT mean stress modified model	$\sigma_{\max} \varepsilon_a = \frac{\sigma_f'^2}{E} (2N)^{2b'} + \sigma'_f \varepsilon'_f (2N)^{b'+c'}$	1. Considering the effect of mean stress hysteresis energy

6.2.3 Energy based fatigue life model

It is well known that, both cyclic plastic strain and stress have an important impact on the fatigue

behaviour. Comparing with the stress or strain based fatigue life model, the energy based fatigue life model is able to consider both plastic strain and stress state, and is generally more applicable to cope with complicated unstable conditions [6-2]. The energy based fatigue life model takes energy as the starting point and establishes the relation between strain energy and fatigue life. Besides, the energy model has material parameters with clear physical meaning and illustrates the nature of the material fatigue damage development process. Hence, an energy based fatigue life model is employed in this chapter to evaluate the nonlinear fatigue degradation of battery electrode.

The hysteresis energy considering stress and strain amplitudes exhibits better cyclic stability than stress or strain solely [6-2]. According to Ref [6-3, 6-4], a hysteresis energy model can be used to evaluate the fatigue behaviour and the energy damage form can be given as the following equations. In the model, fatigue degradation is regarded as a cumulative damage process of energy.

$$dD_{mi} = \left(\frac{W_p}{W_s}\right)^\beta \quad (6.1)$$

$$D_m = \sum_{i=1}^n dD_{mi} \quad (6.2)$$

In the equations, dD_{mi} and D_m respectively denote mechanical-damage per cycle and accumulated mechanical-damage. W_s and β in the equation represent fatigue toughness and fatigue damage exponent, which are both intrinsic material properties. W_p is plastic hysteresis energy and its unit is kJ/m^3 . The plastic hysteresis energy can be calculated by [6-5, 6-6]

$$W_p = 4 \left(\frac{1-n'}{1+n'} \right) \sigma_a \varepsilon_{pa} \quad (6.3)$$

σ_a and ε_{pa} here denote stress amplitude and plastic strain amplitude. n' is the strain hardening exponent. For elastic-perfectly plastic material, n' is assumed to be 0.

Besides, the plastic hysteresis energy has a clear physical meaning. When the material goes through certain loading cycles, the cyclic hardening/softening behaviour of the material tends to be stable and the dislocation competition tends to be balanced. The closed curve encircled by stress-strain at steady state cycle is called a hysteresis loop. Fig 6.2 gives the schematic diagram of a hysteresis loop, which is represented by the red line. In schematic diagram, $\Delta\sigma$ denotes stress range. $\Delta\varepsilon_e$, $\Delta\varepsilon_p$, $\Delta\varepsilon_t$ respectively represent elastic strain range, plastic strain range and total strain range. The plastic hysteresis energy can be clearly exhibited as the area enclosed by the hysteresis loop. Hence, the calculations of plastic hysteresis energy and damage have a visual representation.

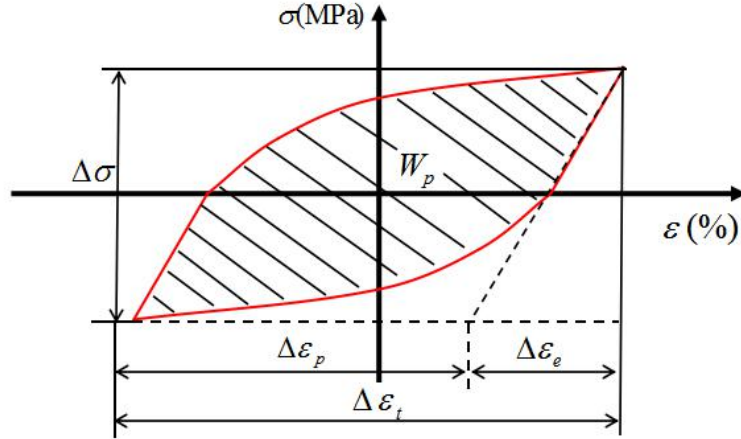


Fig 6. 2 Schematic diagram of hysteresis loop

Based on its mathematical form, the above energy based damage model is able to simulate various damage accumulation trends of battery electrode. It is noteworthy that, unlike the previous chapter, the damage is set to affect the Young's modulus and yield strength of the material to the same extent in this chapter. According to the last chapter, for the research object - thin film electrode plate, the calculated plastic strain amplitude and plastic strain range per cycle at the most dangerous position hold constant with the proceeding of cyclic lithiation-delithiation process. Besides, the stress amplitude of a loading cycle is equal to the yield strength when yielding happens. In our evaluation approach, the yield strength is revised by accumulated damage cycle by cycle and obeys a monotonic decrease. Accordingly, the calculated plastic hysteresis energy W_p maintains a monotonic descent as the cycle goes on. Considering the exponential form, if $0 < \frac{W_p}{W_s} < 1$ and $\beta > 0$, the calculated damage per cycle decreases cycle by cycle and damage accumulation follows a moderative way. On the contrary, if $\frac{W_p}{W_s} > 1$ and $\beta < 0$, the mechanical damage per cycle increases as the cycle goes on and damage accumulation shows a trend of accelerated growth. Hence, the formula form of energy damage model provides the foundation for simulating various damage accumulation trends.

Chapter 5 presents the description of fatigue damage evaluation approach of battery electrode based on continuum damage mechanics and the corresponding subroutine development. Using the energy based fatigue damage model to replace the strain based damage model, it is available to conduct the fatigue damage analysis of battery electrode considering energy evolution.

6.3 Various damage accumulation trends of battery electrode

With using the energy based fatigue damage model, it is accessible to exhibit different fatigue damage evolution trends of electrode plate. The finite element model of electrode plate is as same as the model in Chapter 5 under 1C condition. Three typical damage accumulation trends, as moderative

accumulation, accelerated accumulation and quasi-linear accumulation, are detailedly presented in this section.

6.3.1 Moderative damage accumulation

Fig 6.3 (a) gives the moderative damage accumulation trend of the top surface of electrode plate. The top surface of electrode plate adhering to electrolyte accumulates the most significant fatigue damage with the proceeding of lithiation-delithiation cycles, and the fatigue damage is uniform at top surface as shown in damage distribution contour of electrode plate in Fig 5.7. Here, in fatigue damage model, $\frac{W_p}{W_s}$ is always calculated to be less than 1 as shown in Fig 6.3 (b) and β is greater than 0. It is apparent that the damage generated from one cycle is less than that of the previous cycle.

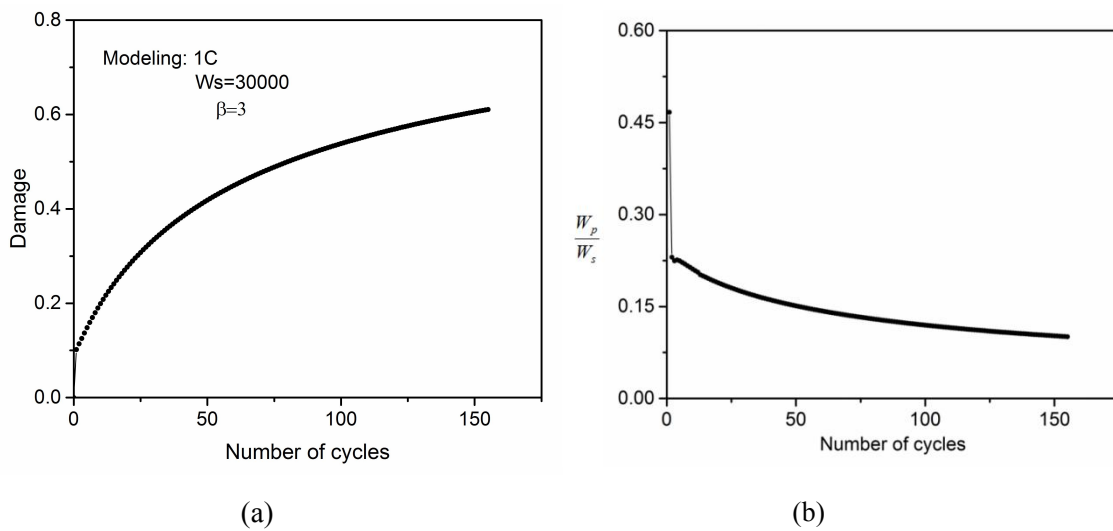


Fig 6. 3 (a) Moderative damage accumulation trend of the top surface of thin film electrode plate, (b) the evolution of the ratio between plastic hysteresis energy and fatigue toughness for moderative accumulation

Fig 6.4 (a) and (b) respectively illustrate the variations of stress amplitude and plastic strain amplitude as the cycle goes on. It can be observed that the produced stress amplitude per cycle gradually decreases. Considering the fact that the stress amplitude equals to the yield strength when yielding occurs, the generated damage per cycle declines with the proceeding of cycles and the damage decreases less yield strength and stress amplitude as the cycle goes on.

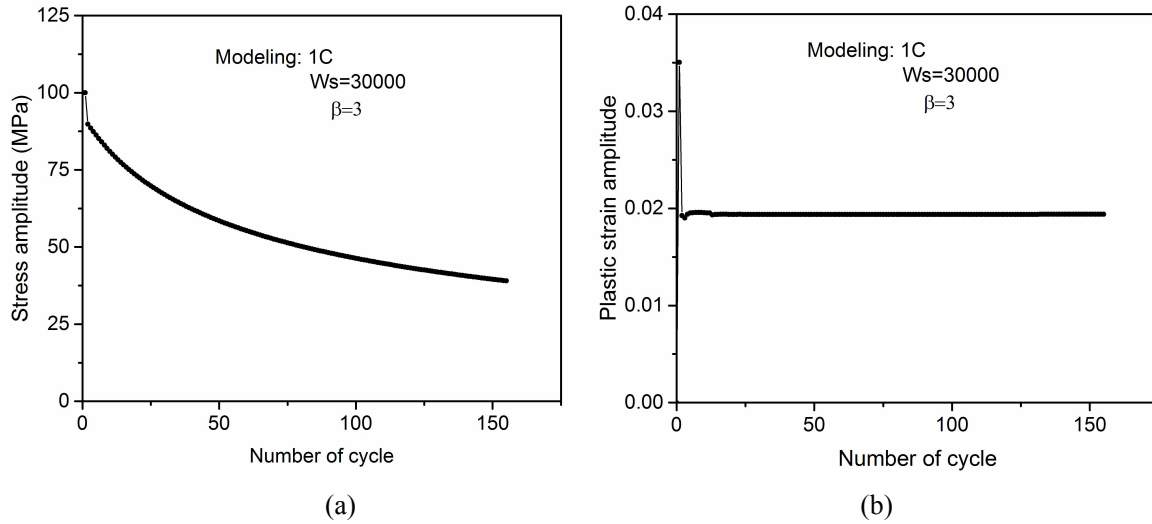


Fig 6. 4 The evolution of (a) stress amplitude, (b) plastic strain amplitude with moderate damage accumulation trend

Besides, it can also be seen that, after the initial cycles, the calculated plastic strain amplitude per cycle is relatively stable with the proceeding of cycles. In the numerical procedure, the calculated fatigue damage is set to synchronously revise the Young's modulus and yield strength of the material. As shown in Fig 6.5, the evolution of Young's modulus and yield stress follow the same trend, and both reflect the non-linear damage effect. With the elastic-perfectly plastic material model, the constant electrochemical loading leads to the relatively stable response.

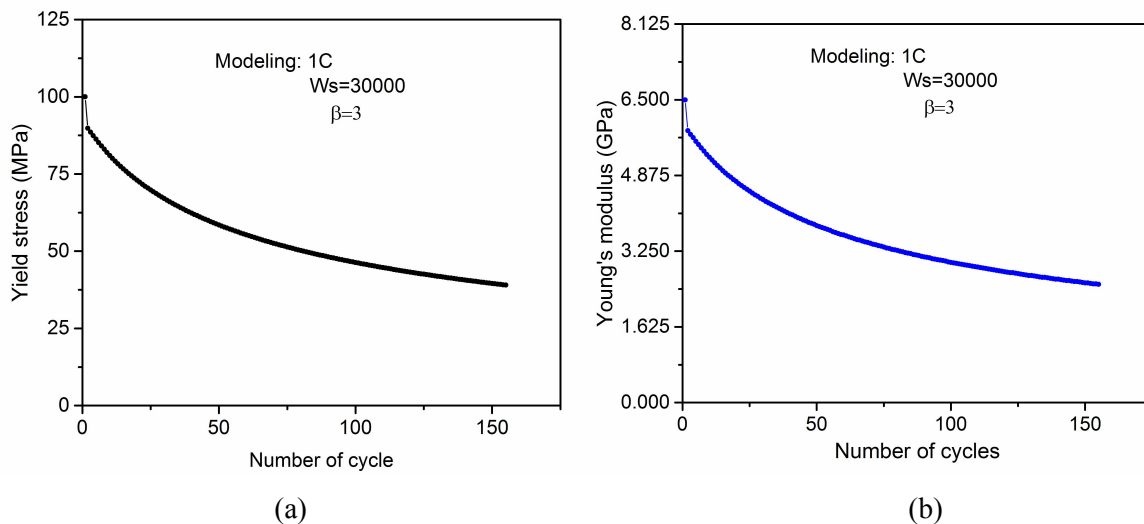


Fig 6. 5 The variation of (a) yield stress, (b) Young's modulus of the top surface of electrode plate affected by moderate fatigue damage accumulation

Considering the change of stress amplitude, plastic strain amplitude and fatigue damage comprehensively, the generated damage from n th cycle reduces the yield strength and stress amplitude of $n+1$ th cycle. Comparing with n th cycle, the decreased stress amplitude and stable plastic strain amplitude produce less plastic hysteresis energy in $n+1$ th cycle. For energy based

damage model with $0 < \frac{W_p}{W_s} < 1$ and $\beta > 0$, the damage generated from $n + 1$ th cycle is less than that of n th cycle. Working as a cycling process, the development trend of damage shows in a moderative way.

Fig 6.6 illustrates the stress-strain hysteresis loops of the top surface of electrode plate at 30th, 65th, 100th, 135th cycle with moderative damage accumulation trend. For electrode material, it is believed that the hardening behaviour is not significant and the elastic-perfectly plastic material model is commonly used in the simulation work [5-12, 5-13]. In addition, due to the characteristics of oxide electrode material, the traditional mechanical performance test is not easily accessible and there is a lack of hardening related material properties of the researched material via literature review. Hence, the hardening behaviour is temporarily not considered in this work. With using the elastic-perfectly plastic constitutive model, the yield strength affected by fatigue damage is the stress at the time of plastic yielding. It can be intuitively seen that the decrements of yield strength between these cycles are different. As the damage accumulation slows down, the damage affected yield strength also decreases slowly. From 30th cycle to 65th cycle, the yielding strength is reduced by around 13.1 MPa. While, it only falls by 5 MPa from 100th cycle to 135th cycle. Besides, it can also be observed that, for electrode top surface, the plastic strain range generated from lithiation process is a little bigger than that of delithiation phase and a slight plastic strain increment is accumulated after one cycle. The increment of plastic strain is around -0.002, which may cause the potential ratcheting behaviour.

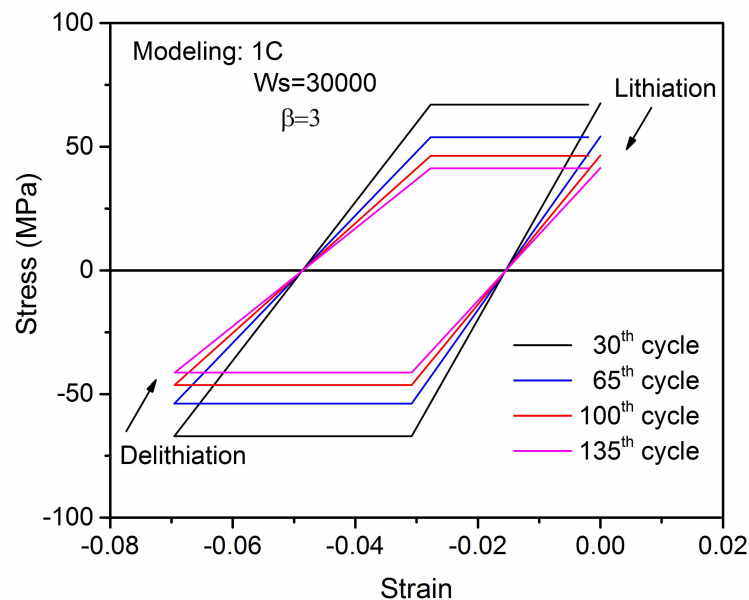


Fig 6. 6 The stress-strain hysteresis loops of the top surface of electrode plate at 30th, 65th, 100th, 135th cycle with moderative damage accumulation trend

6.3.2 Accelerated damage accumulation

Fig 6.7 (a) shows the accelerated damage evolution trend of electrode top surface, where the produced damage of one cycle is greater than that of the previous cycle. For energy based fatigue damage model, the calculated $\frac{W_p}{W_s}$ is always greater than 1 as shown in Fig 6.7 (b) and β is less than 0.

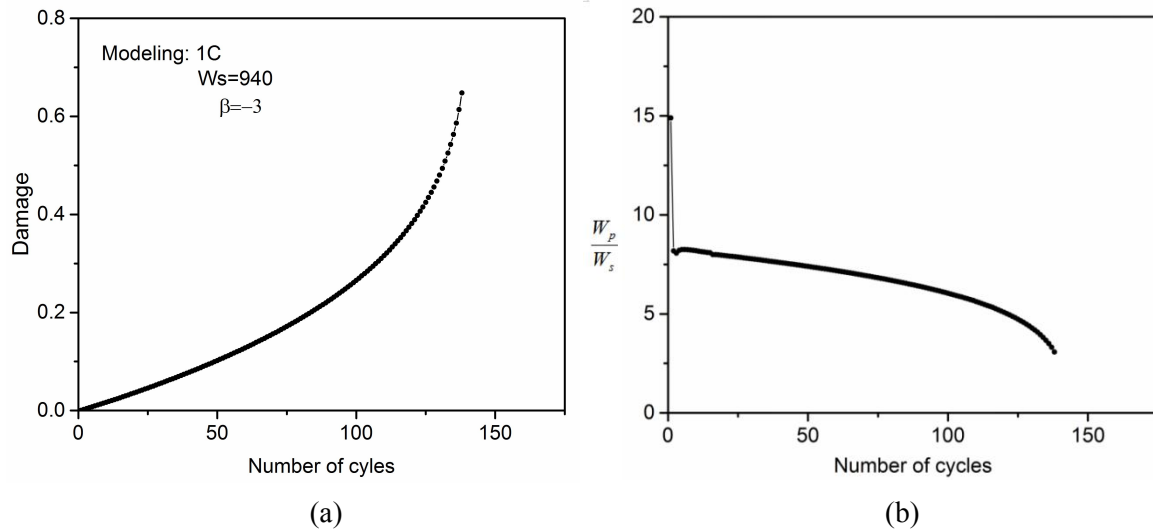


Fig 6. 7 (a) Accelerated damage accumulation trend of the top surface of thin film electrode plate, (b) the evolution of the ratio between plastic hysteresis energy and fatigue toughness for accelerated accumulation

Fig 6.8 (a) and (b) illustrate the corresponding changes of stress amplitude and plastic strain amplitude of electrode top surface. It can be seen that the stress amplitude shows the accelerated decrease with the proceeding of cycles. As damage modifies the yield strength and stress amplitude when yielding happens, the accelerated damage development results in an accelerated decline of yield strength and stress amplitude. The plastic strain amplitude also maintains relatively stable with similar to moderate damage accumulation. Comparing with moderate damage accumulation, only the parameters to calculate fatigue damage is changed. The finite element model and material model keep the same. The calculated fatigue damage is also used to synchronously revise the Young's modulus and yield strength of the material, as shown in Fig 6.9. Hence, the plastic strain amplitude remains essentially constant.

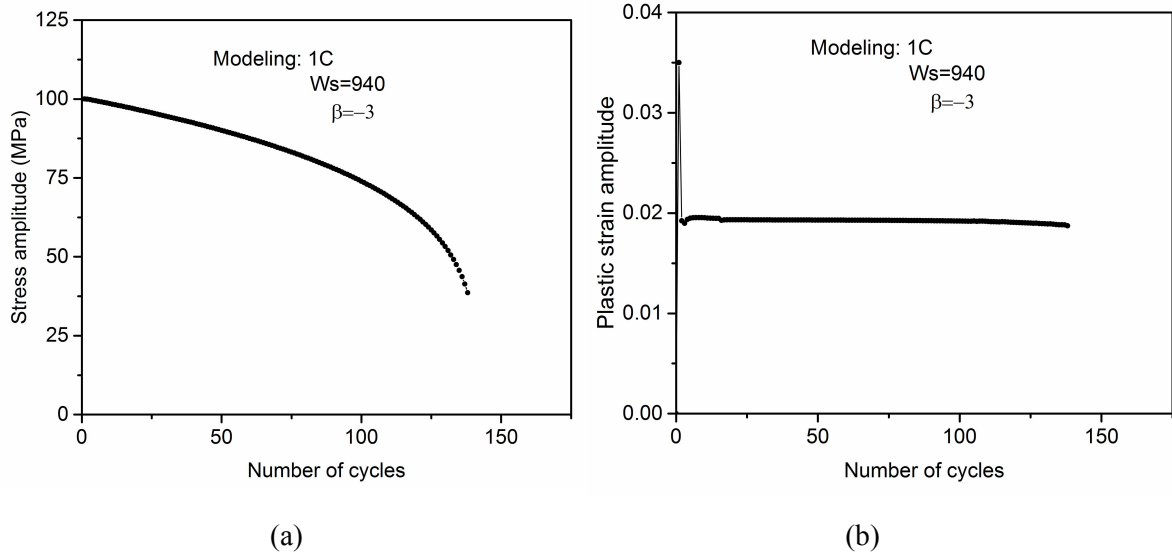


Fig 6. 8 The evolution of (a) stress amplitude, (b) plastic strain amplitude with accelerated damage accumulation trend

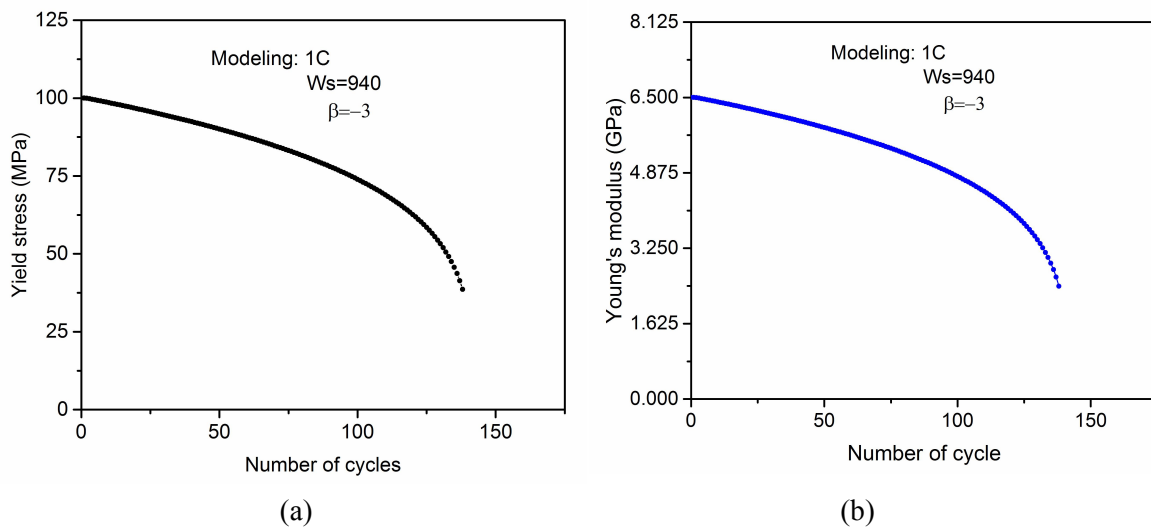


Fig 6. 9 The variation of (a) yield stress, (b) Young's modulus of the top surface of electrode plate affected by accelerated fatigue damage accumulation

For energy damage model with $\frac{W_p}{W_s} > 1$ and $\beta < 0$, the produced fatigue damage in n^{th} cycle also decreases the yield strength and stress amplitude of $n+1^{\text{th}}$ cycle. The generated plastic hysteresis energy W_p and energy ratio $\frac{W_p}{W_s}$ of $n+1^{\text{th}}$ cycle are reduced due to the decreased stress amplitude and stable plastic strain amplitude. While, the formula form with $\frac{W_p}{W_s} > 1$ and $\beta < 0$ leads to the generation of greater damage in $n+1^{\text{th}}$ cycle than that of n^{th} cycle. The damage accumulation therefore presents in an accelerated form.

The stress-strain hysteresis loops of electrode top surface at 30th, 65th, 100th, 135th cycle with

accelerated fatigue damage model are given in Fig 6.10. It is apparent that the decay rate of yield strength gradually increases with the proceeding of cycles. It is lessened by 8.5 MPa between 30th cycle and 65th cycle. From 100th cycle to 135th cycle, it turns out to present a sharp fall by 28.8 MPa. On the whole, the material response shows the cyclic softening characteristic. It has been demonstrated that, under cyclic operation conditions, the nucleation, growth and aggregation of microcracks inside electrode structure will produce voids and reduce loading area [1-9]. This phenomenon will weaken the stiffness of the material with the proceeding of cycles and lead to the cyclic softening characteristic. It can also be seen that there is a slight plastic strain increment after one cycle, which remains around -0.002 . It has to do with the finite element model, boundary condition and loading condition, rather than the applied fatigue damage model. Hence, with similar to moderate damage accumulation situation, the top surface of electrode plate accumulates a slight plastic strain after one lithiation-delithiation cycle and may suffer from ratcheting behaviour.

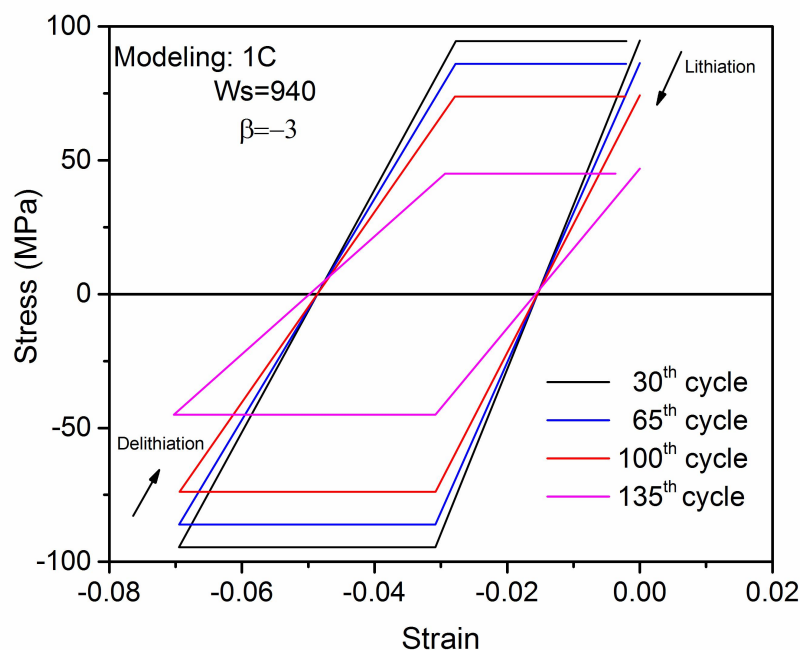


Fig 6. 10 The stress-strain hysteresis loops of the top surface of electrode plate at 30th, 65th, 100th, 135th cycle with accelerated damage accumulation trend

6.3.3 Quasi-linear damage accumulation

The linear/quasi-linear damage accumulation can also be simulated as a particular case. Fig 6.11 (a) illustrates a quasi-linear damage evolution trend of electrode top surface under 1C, where the damage generated from neighbouring cycles are approximately equal. In the energy damage model, the fatigue damage exponent β is set to be 1. In this way, the amplification/reduction effect of exponent is not considered. Fig 6.11 (b) gives the evolution of the calculated $\frac{W_p}{W_s}$ of electrode top

surface with the proceeding of cycles. Although, the calculated $\frac{W_p}{W_s}$ is not equal of different cycles. Without the exponent effect, the damage accumulation also presents a quasi-linear way due to the slow change of plastic hysteresis energy.

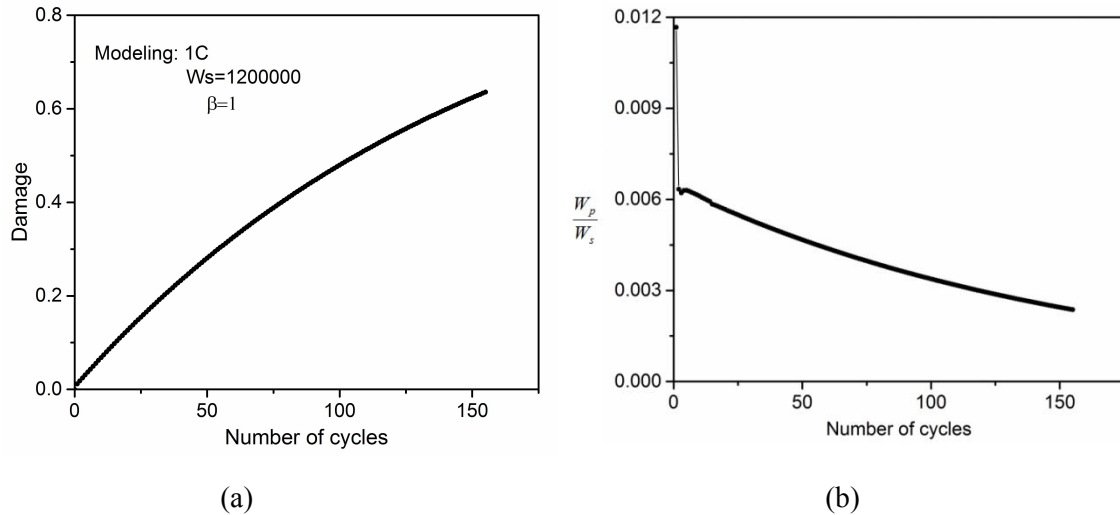


Fig 6. 11 (a) Quasi-linear damage accumulation trend of the top surface of thin film electrode plate, (b) the evolution of the ratio between plastic hysteresis energy and fatigue toughness for quasi-linear accumulation

Fig 6.12 (a) and (b) present the variations of stress amplitude and plastic strain amplitude of the top surface of electrode plate with quasi-linear damage accumulation. It can be seen that the stress amplitude almost follows the linear decrease and the plastic strain amplitude keeps constant after initial unstable-phase as explained in last two sections. Fig 6.13 shows the corresponding stress-strain hysteresis loops of electrode top surface at 50th, 100th, 150th cycle. In this case, the declining quantities of yield stress between these three cycles are nearly equal, which also reflects the effect of quasi-linear damage accumulation.

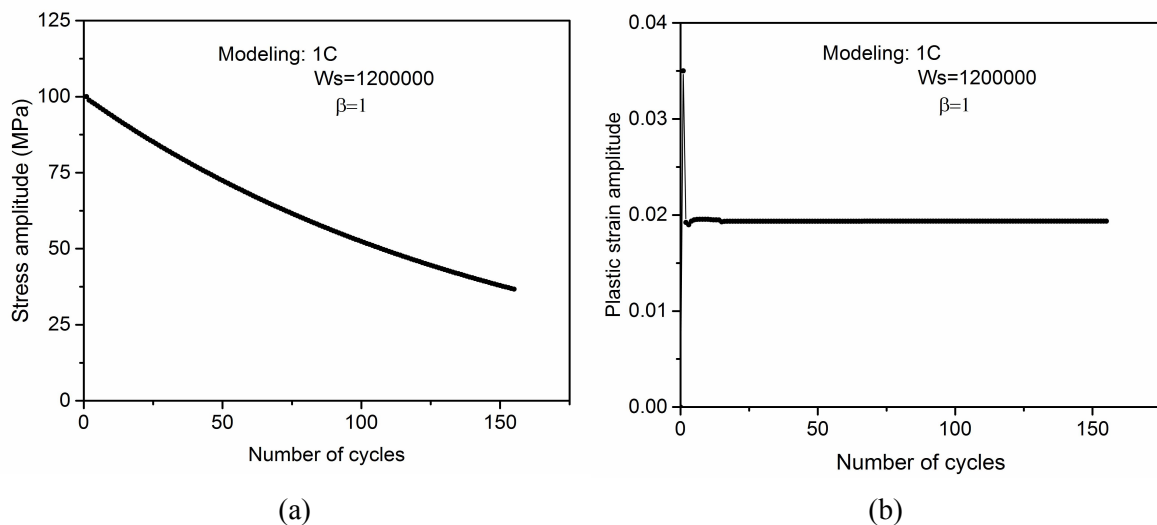


Fig 6. 12 The evolution of (a) stress amplitude, (b) plastic strain amplitude with quasi-linear damage accumulation trend

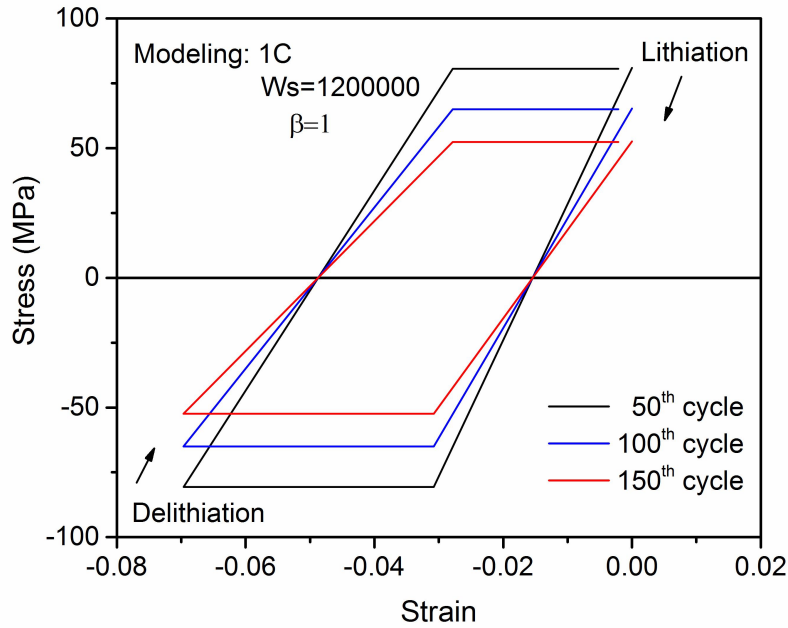


Fig 6. 13 The stress-strain hysteresis loops of electrode top surface at 50th, 100th, 150th cycle with quasi-linear damage accumulation trend

The simulations here present that the applied energy damage equation is capable of modeling different non-linear fatigue damage evolution trends of battery electrode according to its formula form. The energy based fatigue damage model is then employed to study the cyclic degradation behaviour of battery electrode at different material levels.

6.4 Non-linear fatigue damage simulation of layered electrode

It is known that, for cells fabricated from different manufactures, the capacity degradation rate may differ and sometimes the difference could be threefold in cycle counted to 80% capacity [6-7]. Tiny changes in materials, such as active material composition or electrolyte composition, can substantially influence the electrochemical performance of battery. The capacity fading and the corresponding mechanical degradation could therefore show different trends. In this section, the presented energy based fatigue damage model is applied to trace the non-linear degradation of layered electrode plate, where the finite element model of electrode plate keeps in line with chapter 5.

An investigation has been conducted for electrode plate under a benchmark condition corresponding to 1C, so as to fit the material parameters in energy based damage model. Fig 6.14 plots a degradation trend of discharging capacity with respect to the number of cycles under 1C [6-7]. In this case, the capacity falling gradually slows down. According to the aforementioned expression in Eq. 5.10, it is accessible to quantify this degradation by defining a capacity fading represented damage. Fig 6.14 also shows the corresponding capacity based damage of NCM battery under 1C. It

is suggested that the capacity fading represented damage of NCM battery could obey a moderate accumulation trend, where the damage generated in one cycle is less than the previous one.

In this part of the work, the finite element model of electrode plate described in section 5.3 is used. Additionally, in the last chapter, the assumption is proposed that the fatigue damage of the top surface of electrode plate adhering to electrolyte is in equivalence to the capacity fading represented damage. It is because of that the mechanical destruction caused by fatigue damage on the top surface will interfere the channel for Li-ion transportation and interdict the electrochemical process. Using this assumption, it is available to iteratively calculate the fatigue damage of the top surface of electrode plate based on energy damage model, and compare it to experiment damage for approaching fatigue toughness W_s and fatigue damage exponent β . The fitted values of energy based damage model are summarized in Table 6.3. Fig 6.15 presents the comparison between the capacity fading indicated damage and the calculated fatigue damage on the top surface of NCM electrode plate against the number of cycles under 1C. It can be seen that the calculated fatigue damage matches the capacity fading represented damage in a high degree, which also demonstrates the applicability of using the energy based model to describe the non-linear fatigue damage of electrode plate.

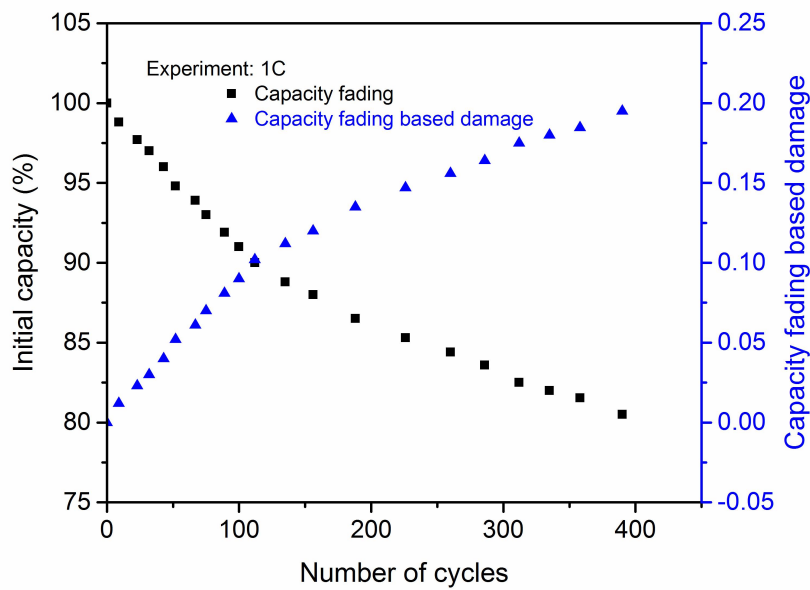


Fig 6. 14 The variation of capacity and capacity fading represented damage with respect to the number of cycles under 1C [6-7]

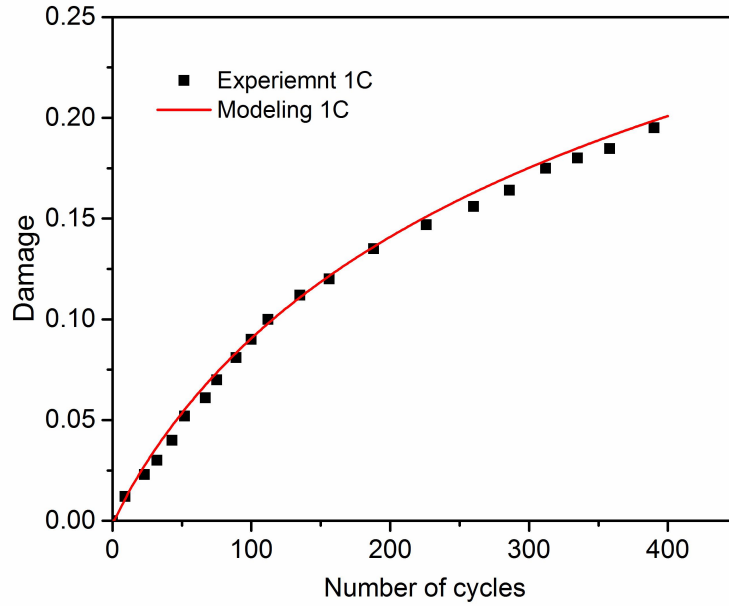
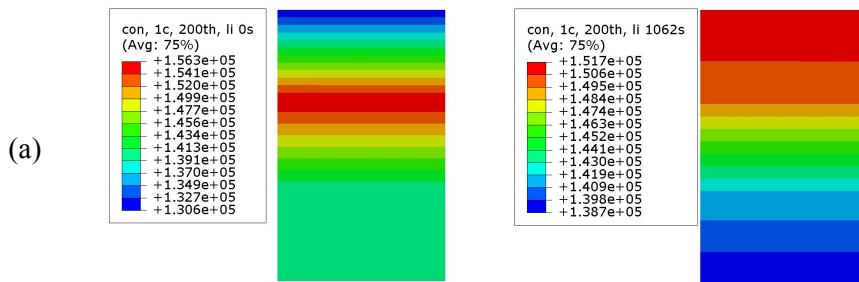


Fig 6. 15 Experiment indicated damage and calculated fatigue damage on plate top surface under 1C

Table 6.3 Fitted parameters in the energy based fatigue damage model

W_s	β
17700	8

Fig 6.16 (a) and (b) respectively show the distribution of Li-ion concentration on the thickness section at 200th cycle and 400th cycle under 1C. It is available to see that, at the beginning of lithiation phase, the residual Li ions mainly gather around the interlayer of the electrode plate. With the proceeding of intercalation, the concentration at the top surface accepting diffusion flux rapidly rises and would be significantly higher than other positions at the end of the intercalation phase. Hereafter, Li ions take out through the top surface and the interlayer remains at the maximum concentration at the end of the deintercalation phase as a cycle. Comparing the illustrated two cycles, the changes of concentration within one cycle are similar. While the residual Li ions would continue to accumulate and prompt the rising of the overall concentration field in electrode plate.



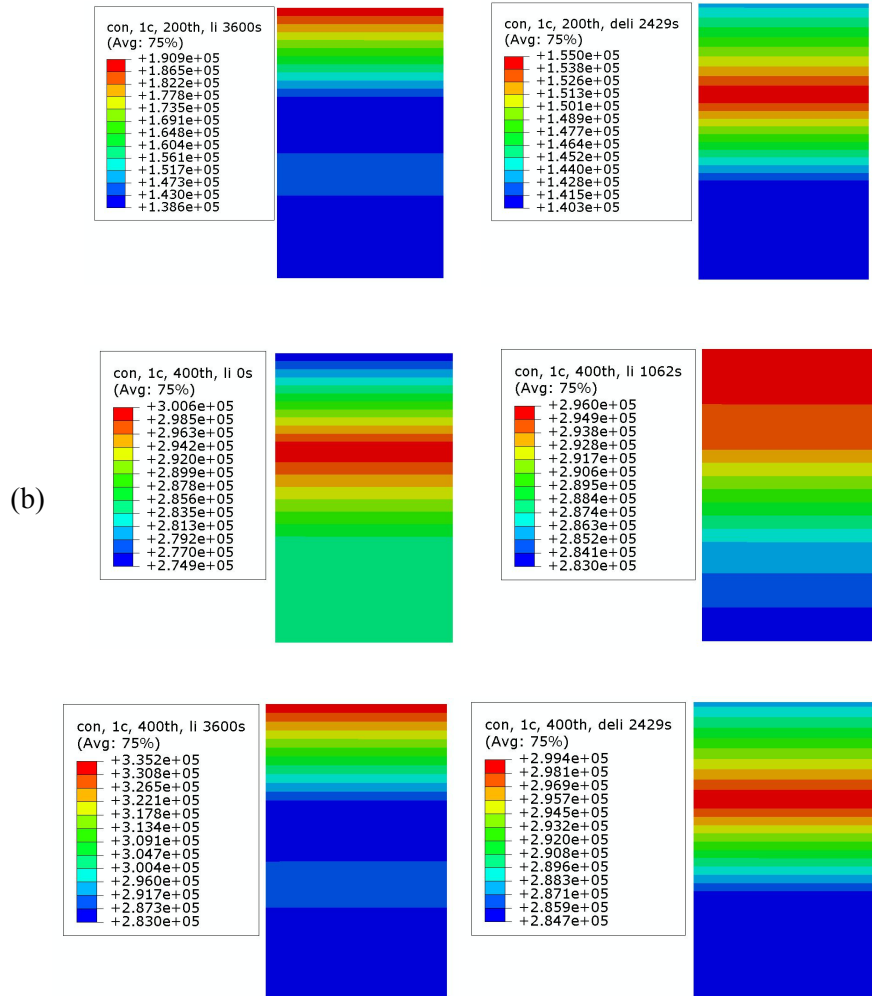


Fig 6. 16 The variation of Li-ion concentration on the thickness of the section at (a) 200th cycle, (b) 400th cycle

With using the parameterized energy damage model, it is available to simulate the damage evolution trends of electrode plate under different charging conditions. Fig 6.17 illustrates the simulated damage evolution of the top surface of electrode plate under 0.5C, 1C and 2C in the range of 200 cycles. It can be observed that the cumulative rate of damage increases with the rising of C-rate. Under higher C-rate conditions (1C, 2C), the moderate character of damage accumulation is relatively significant. On the contrary, the damage accumulation is almost in a linear way under low charging condition 0.5C. It is due to the fact that the calculated damage of one cycle under high C-rates is more pronounced, which significantly affects the stress amplitude and corresponding hysteresis energy. Hence, according to the energy damage model, the damage of subsequent cycles changes greater compared with this cycle. While, the hysteresis energies of two neighbouring cycles are numerically similar under low C-rate, which leads to the generation of similar damage and the linear damage accumulation trend at 0.5C.

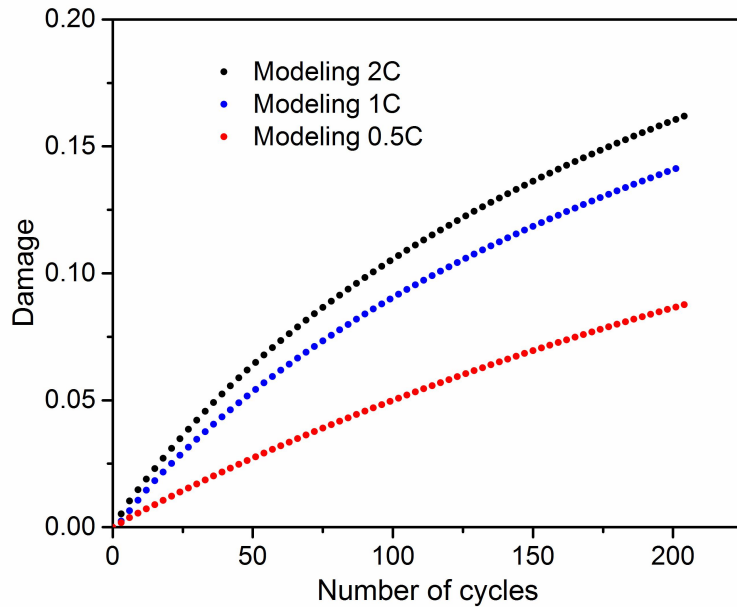


Fig 6. 17 The damage evolution trends of electrode plate under different C-rate conditions (0.5C, 1C and 2C)

Fig 6.18 shows the damage affected yield stress and Young's modulus of the top surface at the given charging conditions. It is clear that the yield stress and the Young's modulus decline with following the same trend, due to the fatigue damage is set to modify these two variables to the same extent. As expected, the mechanical properties of electrode material are revised more significant with higher C-rate and fast charging will bring the irreversible harm to mechanical integrity of battery electrode. Fig 6.19 shows the variations of stress amplitude and plastic strain amplitude of top surface under three electrochemical conditions. These two key parameters are applied to construct the energy model in this work. As plastic yielding happens in each cycle under all three C-rate conditions, the stress amplitude is equal to yield stress in quantity. After a few initial cycles, the calculated plastic strain amplitude per cycle is almost constant for each C-rate. The underlying mechanism is detailedly explained in section 5.6 and section 6.3. Considering the fact that plastic strain amplitude almost holds constant, with certain fatigue toughness and fatigue damage exponent, the calculated hysteresis energy per cycle is ascertained by the variation of stress amplitude. The yield stress is reduced by damage from one cycle and the corresponding stress amplitude is also decreased. It makes the calculated hysteresis energy less than the last cycle. According to equation 6.1, the generated damage is also less than that of the previous cycle, which leads to the moderative damage evolution trend over cyclic process.

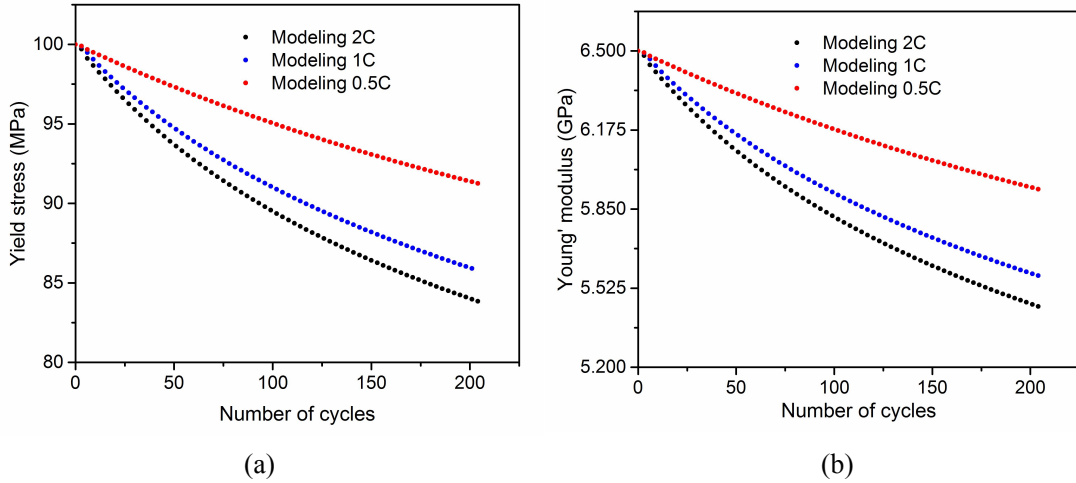


Fig 6. 18 The variation of (a) yield stress, (b) Young's modulus of electrode plate under under different C-rate conditions (0.5C, 1C and 2C)

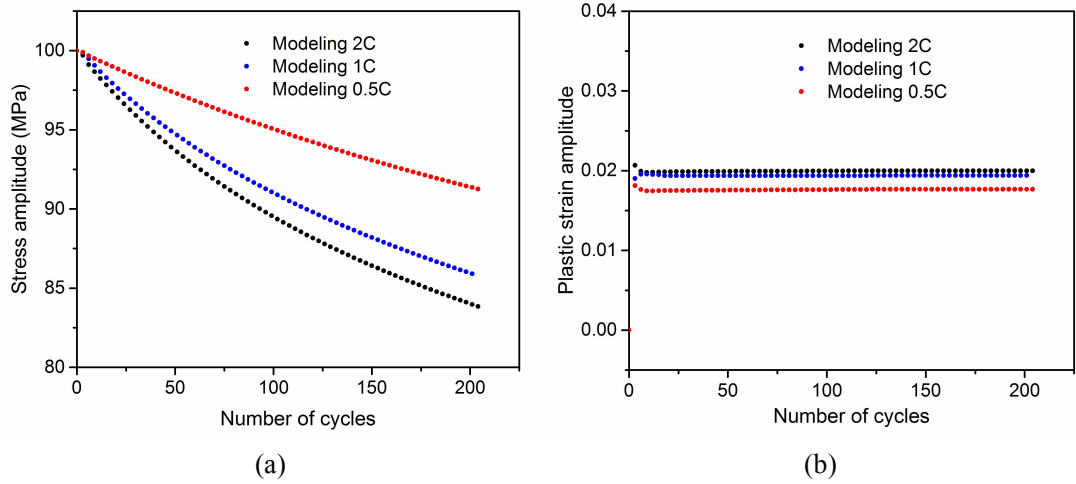
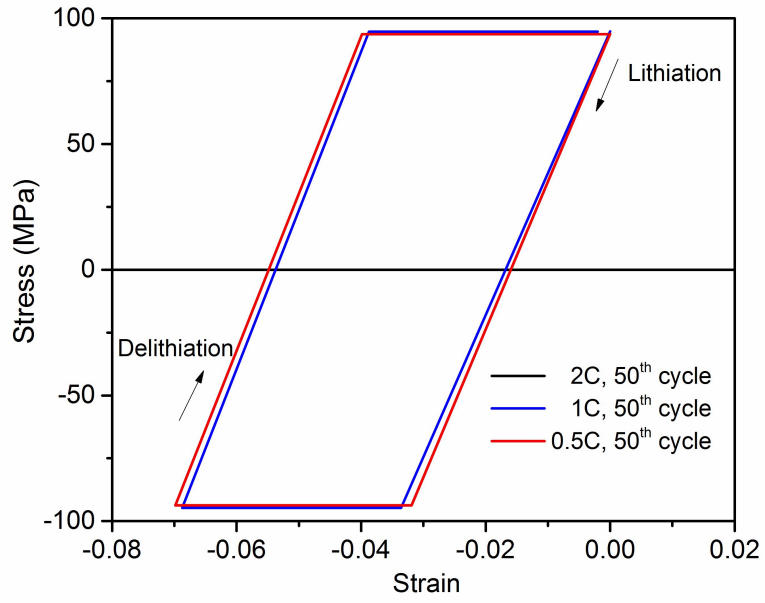
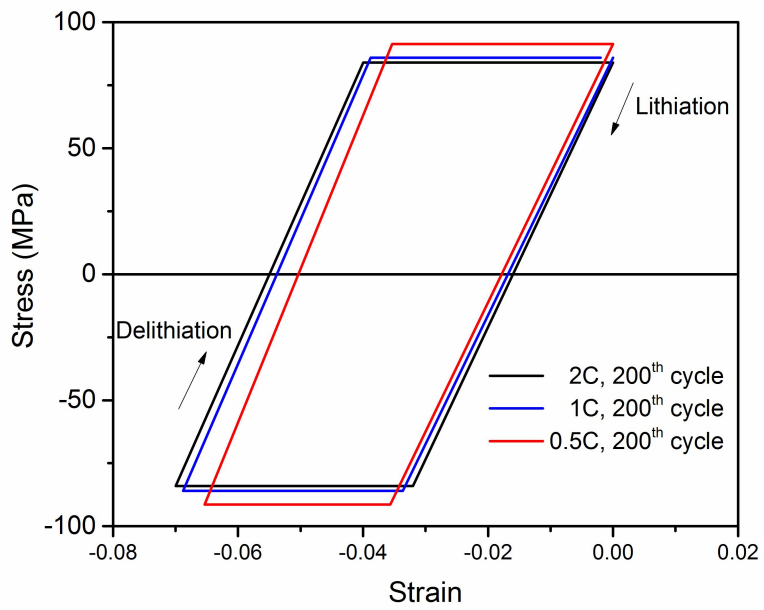


Fig 6. 19 The variation of (a) stress amplitude, (b) plastic strain amplitude of electrode plate under under different C-rate conditions (0.5C, 1C and 2C)

Hysteresis loops of 50th and 200th cycle under the researched C-rate conditions are generated and presented in Fig 6.20. It is clear that the plastic yielding happens at these two cycles and it is also accessible to reflect the damage accumulation state by observing the damage affected yield stress. At 50th cycle, the stress states under three loading conditions are similar and the accumulated damages are relatively small, which pose an inapparent influence to yield stress. At 200th cycle, the difference of stress states shows up with experiencing different charging conditions. Due to the rapid fatigue damage accumulation, the yield stress is significantly reduced under high C-rate conditions 1C and 2C, compared with that of 0.5C. It can be concluded that, fast charging more seriously affects the mechanical stability of electrode and poses a negative influence on electrochemical performance.



(a)



(b)

Fig 6. 20 Hysteresis loops of top surface of electrode plate under 0.5C, 1C and 2C at (a) 50th cycle, (b) 200th cycle

6.5 Fatigue damage simulation of microscopic multi-particle electrode

6.5.1 Model description

Under micro/meco scale, it is valuable and challengeable to study the fatigue damage evolution of multi-particle electrode considering the effects of different particle shapes as well as relative particle positions. In this section, the presented energy damage assessment approach is applied to investigate the fatigue failure behaviour of the micro multi-particle electrode model using the representative volume element (RVE) method.

Fig 6.21 (a) shows the researched representative volume element, in which the particles indicate NCM active material and the rest area encompassing active particles is occupied by electrolyte. The particles are modeled as two-dimensional cylinders, which are used to reflect the characteristic of wire electrode [2-23]. It has been thought that this electrode configuration is able to endure large strain without pulverization and better at electronic conduction. The high reversible capacity and satisfactory electrochemical performance make this configuration promising as the future electrode structure [2-24, 2-46, 6-8]. For studying the different scenarios in micro scale, particles with different shapes and located with different relative positions are constructed. Particle P1 and P2 respectively represent two cylinder particles with both circular 3 μ m-diameter cross section. Particle P3 and P4 are two cylinder particles with ellipsoid cross section. The semimajor axes of P3 and P4 are both 1.5 μ m and the corresponding aspect ratios of the two ellipsoid cross sections are respectively set as 1.25 and 1.5. Besides, for investigating the effect of relative particle position on fatigue damage development, different particle spacings are set in RVE model. Particle 2 appears to have 0.1 μ m and 0.3 μ m distance from particle 1 and 3. While, Particle 1 is in contact with particle 4. Different relative particle positions influence the interaction between particles. As the particle spacing affects the electrolyte content between the neighbouring particles, which further influence the ion diffusion and stress generation of the related particle surfaces. Fig 6.21 (b) gives the mesh distribution of the representative volume element. The performed coupled-diffusion-stress-damage analysis takes tremendous computing efforts as it includes multiple analysis steps for modeling multiple lithiation-delithiation cycles. Considering the calculation accuracy and calculation efficiency comprehensively, 8632 CPE8RT elements are applied for the coupled diffusion-stress-damage analysis.

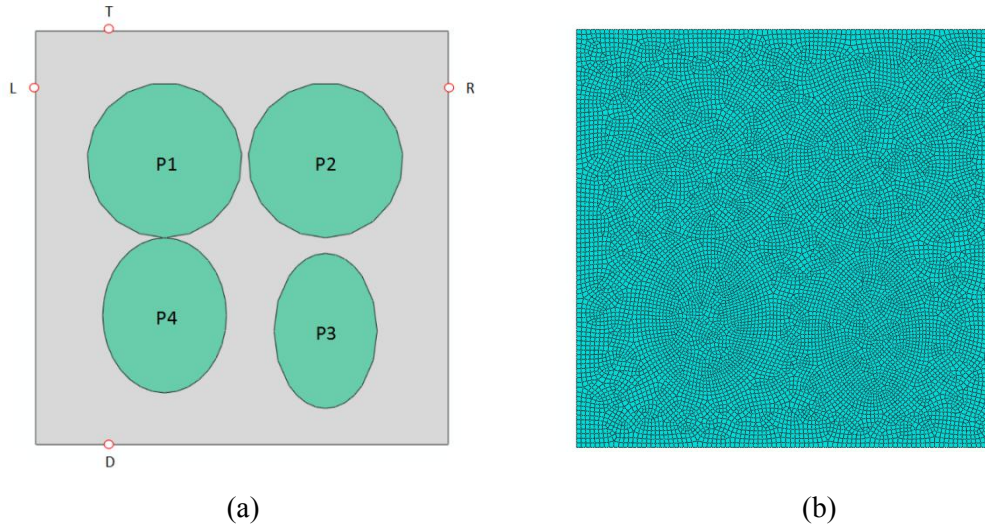


Fig 6. 21 (a) A representative volume element of micro multi-particle electrode model, in which the particles represent active material and the rest area is occupied by electrolyte, (b) mesh distribution of the representative volume element

The material properties of NCM active particle and electrolyte used in this section are given in Table 6.4. According to the equivalent conversion principle provided in section 3.2, a coupled thermal-stress analysis can be performed as the coupled diffusion-stress analysis based on ABAQUS platform with the developed UMATHT subroutine. The equivalent thermal properties are also listed in Table 6.4. It is worth noting that, there is no fixed system of units in ABAQUS software and user is required to unify the units according to the characteristics of the analysis model. The researched RVE model is at micrometer(μm) scale and the material properties are therefore given in μm unit. The units of Young's modulus, yield strength and the calculated stress field are 10^{12}Pa , and for the sake of presentation, the numerical values of these variables time 10^6 can be converted to be in MPa unit. Besides, the electrochemical properties of active particle are not applicable for the electrolyte material. The mechanical response of electrolyte is regarded to be elastic, as plasticity and fatigue damage behaviour are not considered for the electrolyte.

Table 6.4 Material properties of RVE model [3-10, 3-11, 3-12]

NCM active particle

Electrochemical property		Equivalent thermal property	
Diffusivity (um ² /s)	1E-3	Conductivity (J/(um*k*s))	1E-3
Partial molar volume(um ³ /mol)	2.1E12	Thermal expansivity (1/k)	7E11
Mechanical property		Specific heat (J/(kg*k))	
Young's modulus (N/um ² or 10 ¹² Pa)	0.125	Density (kg/um ³)	1
Poisson's ratio	0.3		
Yield strength (N/um ² or 10 ¹² Pa)	1E-4		
Electrolyte			
Electrochemical property		Equivalent thermal property	
Diffusivity (um ² /s)	-	Conductivity (J/(um*k*s))	0
Partial molar volume(um ³ /mol)	-	Thermal expansivity (1/k)	1
Mechanical property		Specific heat (J/(kg*k))	
Young's modulus (N/um ² or 10 ¹² Pa)	6E-5	Density (kg/um ³)	1
Poisson's ratio	0.3		
Yield strength (N/um ² or 10 ¹² Pa)	-		

According to the fact that, the diffusion velocity of Li-ion in electrolyte greatly exceeds that of the solid particle, the area occupied with electrolyte is assumed to inject or receive lithium ions from active particles during lithiation/delithiation process with a constant diffusion flux. A current density i_n as 0.8A/m² (8E-13A/um²) is applied in this simulation, which is within the range of commonly used current density for electrode particle analysis [2-13, 3-3]. Based on the relation between current density and diffusion flux as $J = \frac{i_n}{F_a}$, it is available to obtain the Li-ion diffusion flux J as 8.28E-6 mol/m²s (8.28E-18mol/um²s). Fig 6.22 (a) gives the loading condition of diffusion flux in one lithiation-delithiation cycle, and Fig 6.22 (b) presents the area of loading where the diffusion flux flows through the area occupied with electrolyte (grey area in Fig 6.22 (b)). In the equivalent coupled thermal-stress analysis, the thermal heat flux appears to be the substitute of diffusion flux. The magnitude and variation rule of thermal heat flux are consistent with diffusion flux as shown in Fig 6.22 (a). The applying area of thermal heat flux is also as same as that of diffusion flux as shown in Fig 6.22 (b).

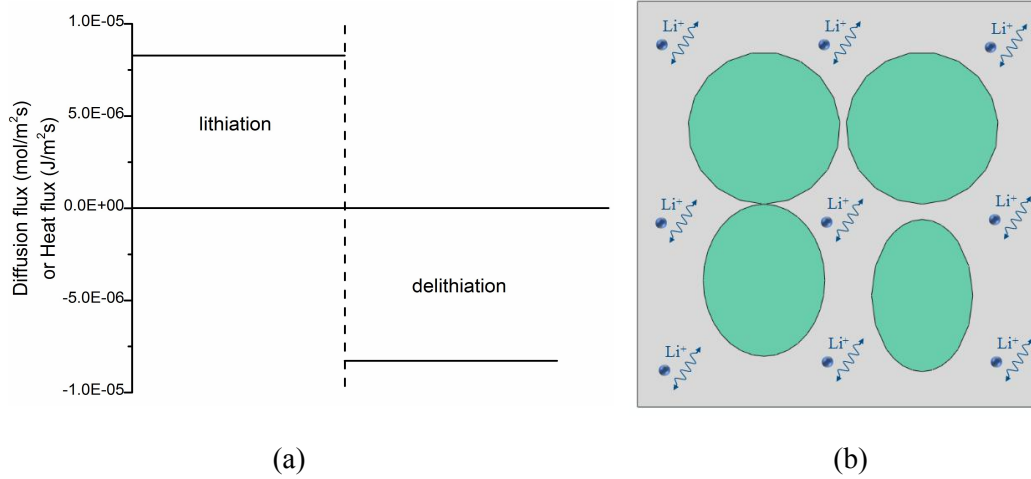


Fig 6. 22 (a) Loading condition in a lithiation-delithiation cycle, (b) schematic diagram showing the area of loading

Periodic boundary condition can be applied for approximating the mechanical response of a large electrode system by using the local material model. In Fig 6.21, mark L and R represent an arbitrary pair of nearest points on the left and right sides, while mark T and D indicate an arbitrary pair of nearest points on the top and down sides. In this case, each point on the boundary has three degrees of freedom, as two displacement degrees of freedom (U_1 and U_2) and one concentration degree of freedom (c), and the periodic boundary condition can be presented as the following three groups of equations, which give the displacement and concentration relationships of all boundary points. Taking the first equation as an example, the displacement of one point on the top side in the process of deformation is constrained to be equal to the displacement of the nearest point on the down side. In other words, if a point above moves up by a certain distance, the corresponding point below also moves up by the same distance. A set of Python scripts are developed to implement the constraints of node points on the boundaries of RVE model. Firstly, using a Python script to output the numbers of all points on the edges and their coordinates. Whereafter, by calling functions, it is available to calculate each pair of nearest points on two opposite edges. Then, it is accessible to respectively impose the following equation constraints for nodes on top-down sides and left-right sides.

$$\left\{ \begin{array}{l} U_{1T} = U_{1D} \\ U_{1R} = U_{1L} \end{array} \right. \quad (6.4-1)$$

$$\left\{ \begin{array}{l} U_{2T} = U_{2D} \\ U_{2R} = U_{2L} \end{array} \right. \quad (6.4-2)$$

$$\left\{ \begin{array}{l} c_T = c_D \\ c_R = c_L \end{array} \right. \quad (6.4-3)$$

6.5.2 Results and discussions

Fig 6.23 presents the contour plots of displacement of the deformed RVE model. Due to the non-uniform distribution of electrode particles and diffusion-induced stress inside RVE model, the displacement is characterized by unbalance. It can be seen that the top side shows the same displacement deformation comparing with the down side. The left side and the right side also move the same distance. It is thought that the four neighbouring representative volume elements (top/down/left/right) experiencing the same deformation can piece together with this representative volume element.

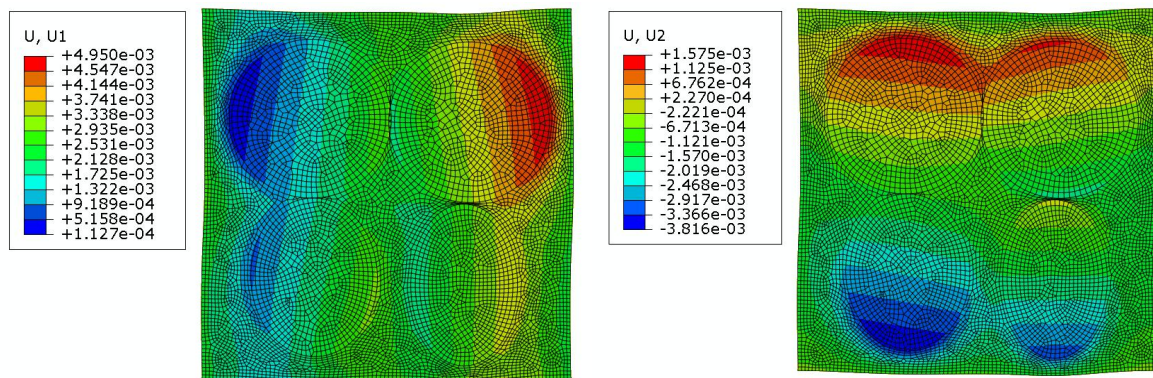


Fig 6. 23 The contour plots of displacement of the deformed RVE model

Fig 6.24 (a) gives the Li-ion concentration distribution of active particles inside RVE model after lithiation and Fig 6.24 (b) presents the corresponding von Mises stress distribution of the active particles. It is particularly interesting to note that, the Li-ion concentration of completed-contact particle surface between P1 and P4 is lower than free surface, and the generated stress at this area is also less than that of free surface. The reason for this phenomenon is that the complete contact separates the active material from electrolyte and hampers the transportation of Li-ion at surfaces. Therefore, it leads to the less concentration, concentration gradient and stress at this area. It is also apparent that the Li-ion concentration at the clipper seam between P1 and P2 is far less than other electrolyte areas. The quasi-contact surfaces of P1 and P2 gather a relatively higher concentration field and experience greater diffusion induced stress. The complex structure feature in this area makes the exchange of Li-ions blocked during lithiation/delithiation process, which could lead to the accumulation of more Li-ions and the generation of greater stress. While, for sufficient space as 0.3um between P2 and P3, there presents no more ion concentration and stress generation. And this space is suitable for ion transportation of cylinder particle with 3um-diameter cross section. In addition, it is available to see that, due to the greater specific surface area, the long-axis tip area of particle P3 also accumulates a relatively higher Li concentration comparing with other areas. Fig 6.24 (c) gives the von Mises stress distribution of electrolyte. It can be seen that the stress generated inside electrolyte is far less than that of the active particles, and its plasticity behaviour as well as fatigue

damage are not considered in this section.

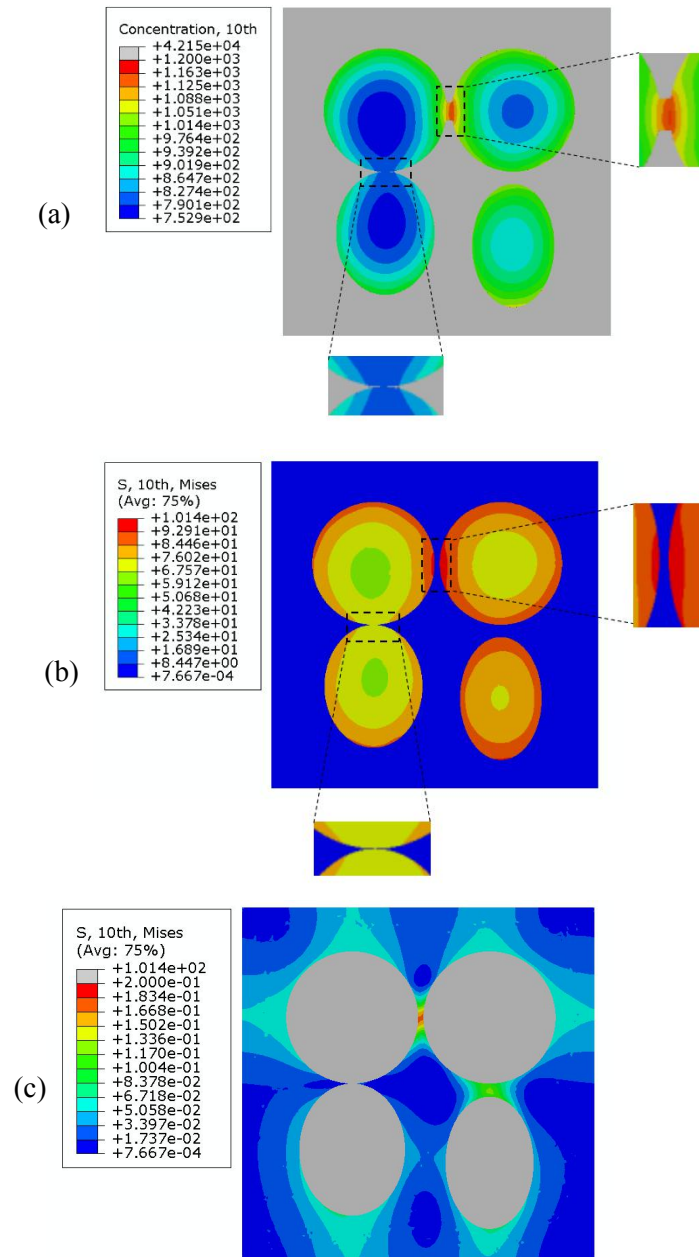


Fig 6. 24 (a) The Li-ion concentration distribution of active particles inside RVE model after 10th lithiation, the contour plots of the corresponding von Mises stress of (b) active particles, (c) electrolyte

Fig 6.25 presents the accumulated fatigue damage of the researched model after 25 and 50 cycles. The results provided show that the surface areas with a small distance to other particles amass the most significant damage. While, completed-contact particle surfaces are in a state of relative safety. In order to display the damage of different positions more clearly, several representative positions are selected as shown in Fig 6.26 and damages of these representative positions are given in Table 6.5.

Position 1, 2 and 3 respectively represent the quasi-contact area, the completed-contact area and the free area. It is observed that the quasi-contact area accumulates the most fatigue damage, and the completed-contact area has the minimal fatigue damage. As the given Li-ion concentration distribution in Fig 6.24 (a), higher Li-ion concentration field and steeper concentration gradient at position 1 will lead to the generation of greater diffusion-induced stress shown in Fig 6.24 (b) and more significant fatigue damage. For the same reason, the completed-contact position 2 with lower Li-ion concentration and smooth concentration gradient is less exposed to diffusion-induced stress and fatigue damage, comparing with that of the free position 3.

By comparing the damage generated at position 3 and 4, it is accessible to see the effect of particle shape on fatigue damage accumulation. Position 3 denotes the free surface of cylinder particle with circular cross section, and position 4 is at the long-axis tip of ellipsoid cross section of cylinder particle. Due to the greater specific surface area and additional ion concentration accumulation, position 4 experiences greater diffusion induced stress as well as fatigue damage. Hence, in the synthesis process of electrode material, it is better to prepare the cylinder particle with the circular cross section rather than the ellipsoid cross section, so as to avoid additional damage generation.

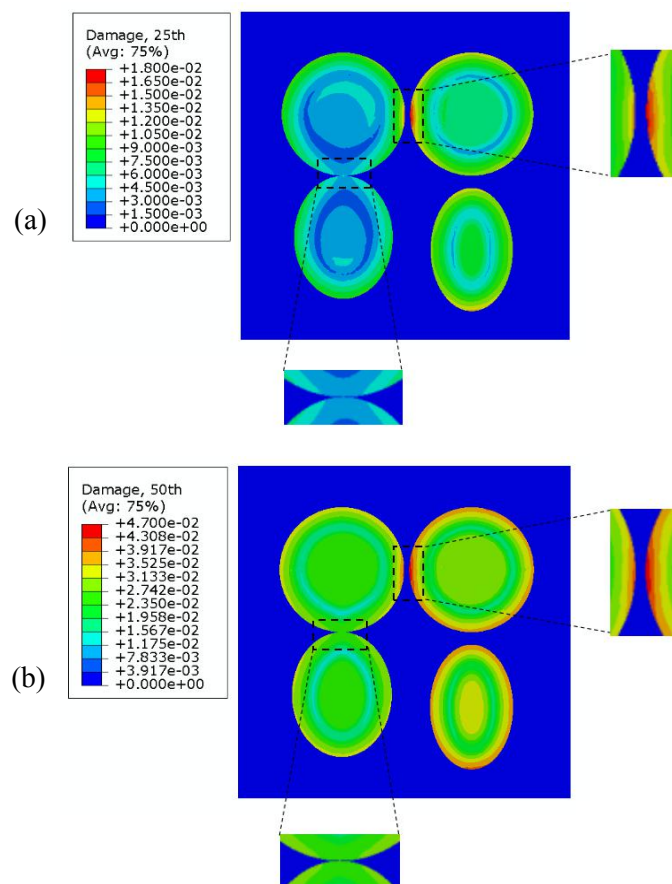


Fig 6. 25 The accumulated fatigue damage of RVE model after (a) 25, (b) 50 lithiation-delithiation cycles

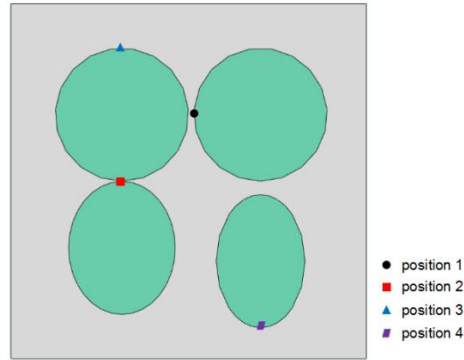


Fig 6. 26 Schematic diagram showing the representative positions on the RVE model

Table 6.5 The damage of the representative positions on the RVE model

	25 th cycle	50 th cycle
Position 1	0.01669	0.04425
Position 2	0.00437	0.02647
Position 3	0.00929	0.03265
Position 4	0.01298	0.03892

According to the energy damage model, the stress amplitude and the plastic strain amplitude are two key parameters applied for calculating fatigue damage. Fig 6.27 (a) and (b) respectively give the stress amplitude and the plastic strain amplitude of the representative positions against the number of cycles. It can be seen that, at the initial cycles, the representative positions are all in elastic state and no plastic-yielding happens. As the cycle goes on, the Li-ion trapping mechanism will lead to the rising of ion concentration field shown in Fig 6.27 (c), which presents the ion concentration of the representative positions at the end of lithiation phase against the number of cycles. After one lithiation-delithiation cycle, the Li-ions embedded in the electrode structure will not completely escape and a resident ion concentration field is thereby formed. This phenomenon results in the rising of ion concentration as well as diffusion induced stress. With the proceeding of cycles, the diffusion induced stress of each representative positions increases and the yielding behaviour will gradually occur at each positions when the generated stress exceeds the yield strength of the material. The plastic strain amplitude is then produced and the corresponding fatigue damage also starts accumulating.

The fatigue damage generated from one cycle is applied to reduce the yield strength and the Young's modulus of the material. The stress amplitude is equal to the yield strength when yielding occurs, and is gradually decreased due to the damage effect. The ion trapping mechanism, the damage affected yield strength and Young's modulus have a combined effect on the stress-strain response, the plastic strain amplitude and the generated fatigue damage of the next cycle. It can be seen that the generated plastic strain amplitude fluctuates within a certain range due to the joint action of multiple

factors, and position 1 presents the relatively significant amplitude of change because of the complex structure characteristics here. Fig 6.28 (a) and (b) respectively present the stress-strain loops of the representative positions at 25th cycle and 50th cycle. For different positions at different cycles, the yield stress and the Young's modulus which is the slop in elastic phase, show differences due to the differentiated effect of fatigue damage.

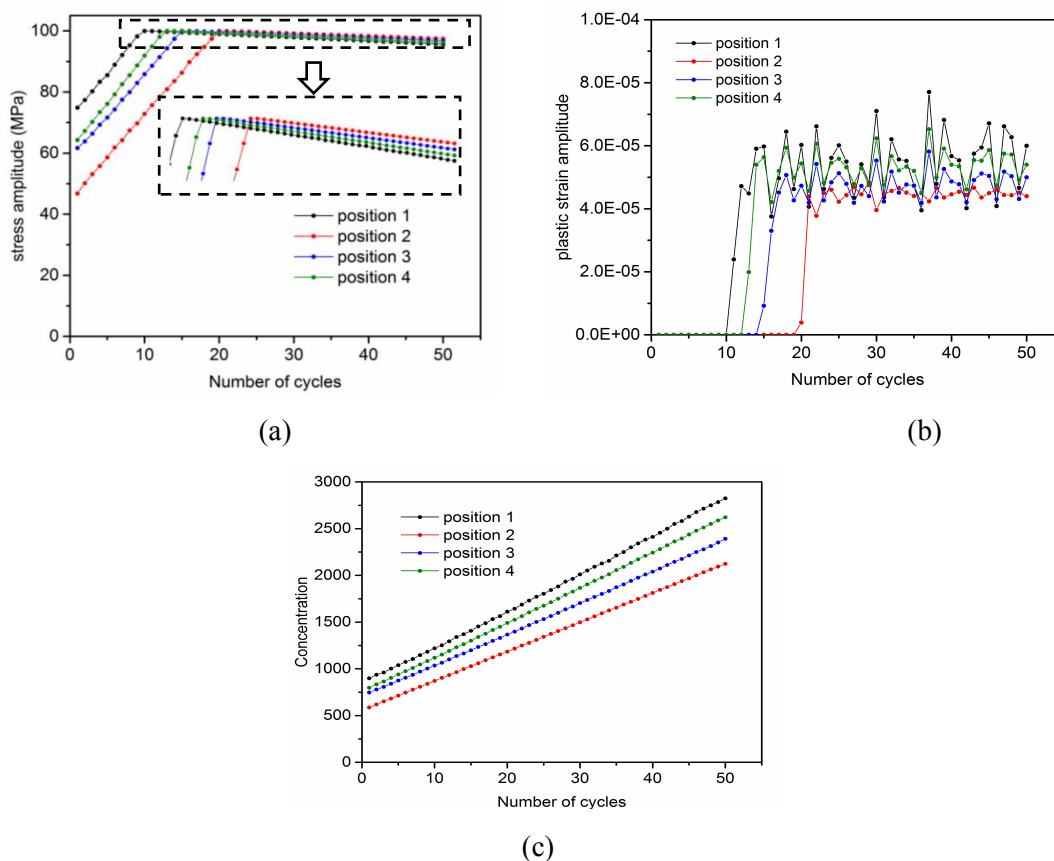


Fig 6. 27 The stress amplitude, (b) the plastic strain amplitude of the representative positions against the number of cycles, (c) the Li-ion concentration of the representative positions at the end of lithiation phase against the number of cycles

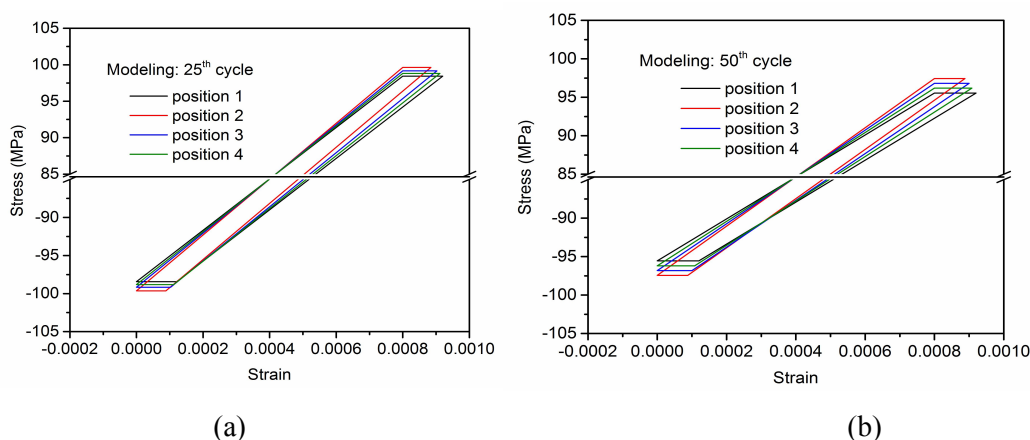


Fig 6. 28 The stress-strain loops of the representative positions at (a) 25th, (b) 50th lithiation-delithiation cycle

Fig 6.29 and Fig 6.30 respectively give the contour plots of the damage affected yield strength and Young's modulus of the representative volume element after 25 and 50 lithiation-delithiation cycles. Table 6.6 and Table 6.7 present the magnitudes of yield strength and Young's modulus of the representative positions on RVE model. It is apparent that, for different positions, the changes of yield strength and Young's modulus vary, and these two material properties are reduced the most at where the accumulation of fatigue damage is most significant. It is also available to observe that, the declines of yield strength and Young's modulus follow the same trend as the fatigue damage is applied to synchronously revise these two parameters.

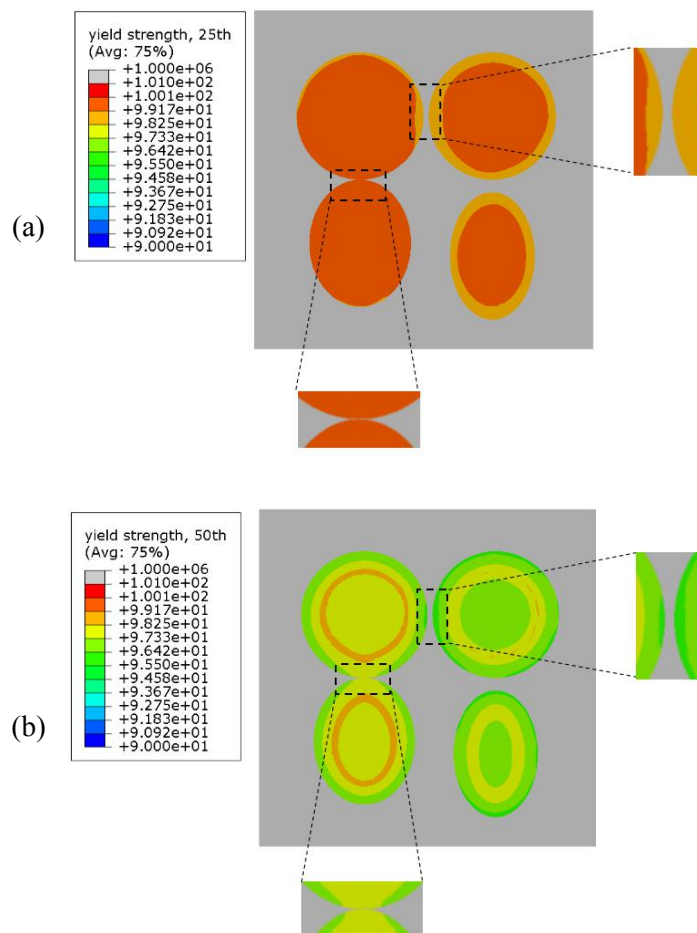


Fig 6. 29 The yield strength of RVE model after (a) 25, (b) 50 lithiation-delithiation cycles

Table 6.6 The yield strength of the representative positions on the RVE model

	yield strength before cycle (MPa)	yield strength after 25 th cycle (MPa)	yield strength after 50 th cycle (MPa)
Position 1	100	98.331	95.575
Position 2	100	99.563	97.353
Position 3	100	99.071	96.735
Position 4	100	98.702	96.108

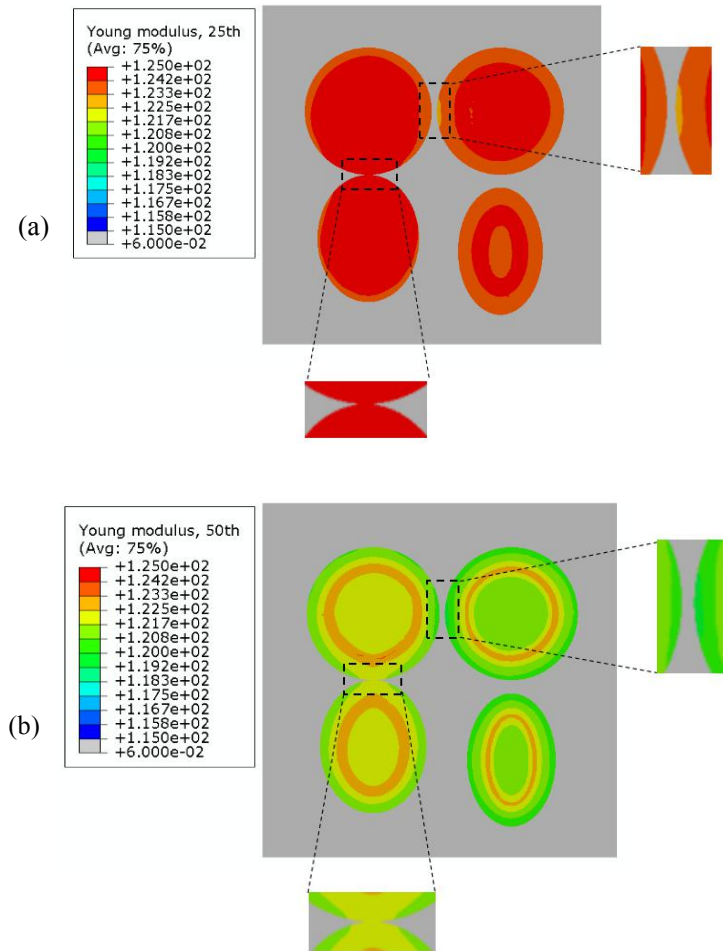


Fig 6. 30 The Young's modulus of RVE model after (a) 25, (b) 50 lithiation-delithiation cycles

Table 6.7 The Young's modulus of the representative positions on the RVE model

	Young's modulus before cycle (GPa)	Young's modulus after 25 th cycle (GPa)	Young's modulus after 50 th cycle (GPa)
Position 1	125	122.913	119.468
Position 2	125	124.453	121.691
Position 3	125	123.838	120.918
Position 4	125	123.377	120.135

It is well known that, dense particle arrangement of electrode material is able to improve the energy density of battery electrode. Although, the completed-contact surfaces in this simulation show less damage generation. While, the dense arrangement caused contacting constraints from multiple directions will lead to the generation of extrusion force between particles, which will weaken the stability of electrode material. Besides, insufficient particle spacing also leads to the accumulation of more ion concentration and fatigue damage. Hence, a proper distance should be left between electrode particles in the preparing process of electrode material. The simulation of RVE model in this section presents that, for the cylinder particle with circular 3 μ m-diameter cross section, 0.3 μ m space is

sufficient for smooth Li-ion transportation between particles. Besides, the simulation also presents that the cylinder particle with circular cross section is able to avoid additional damage caused by greater specific surface area comparing with the particle with ellipsoid cross section. The simulation in this section provides the theoretical support of the mechanical analysis of battery electrode and the instruction information on electrode material preparation.

6.6 Conclusions

In this chapter, an energy-based damage model is presented and implanted in the fatigue damage approach for assessing the mechanical degradation of lithium battery electrode. The newly established approach is available to model the different fatigue damage evolution trends of electrode under electrochemical conditions. It is used to evaluate the fatigue damage accumulation of NCM thin film electrode plate and micro multi-particle electrode configuration by using the representative volume element method. The key conclusion are:

- (1) An energy-based fatigue damage model is implemented in the fatigue assessment method of battery electrode by developing UMAT subroutine. The energy-based model has the advantages of considering both plastic strain and stress state, so as to incorporate more details of material response for generating the fatigue damage.
- (2) Three primary damage accumulation trends, known as moderative accumulation, accelerated accumulation and linear/quasi-linear accumulation, can be expediently modeled with energy-based model. In all scenarios, the damage equally modifies the yield strength and Young's modulus of the material, and the damage nonlinearity comes from the stress/strain change at different cycles.
- (3) The presented energy-based damage evaluation approach is applied to model the non-linear damage evolution of a thin film electrode plate and further compare with capacity fading indicated damage. The rising of C-rate promotes the damage accumulation rate. Under higher C-rate conditions (1C, 2C), the damage accumulation presents a significantly moderative feature. While, under lower C-rate (0.5C), the damage almost increases in a linear way. Besides, the fatigue damage is also modeled of a representative volume element including multi particles. It is founded that the sufficient particle spacing should be saved in order to avoid additional fatigue damage caused by the barrier of ion transportation. And the particle with circular cross section is less vulnerable to fatigue damage comparing with the particle with ellipsoid cross section.

6.7 References

- [6-1] X. Fu. Research on fatigue damage model under multi-load effect and life prediction of compressor blade. University of Tianjin, 2018, PhD thesis.
- [6-2] M. Wang, J.C. Pang, H.Q. Liu, C.L. Zou, S.X. Li, Z.F. Zhang. Deformation mechanism and fatigue life of an Al-12Si alloy at different temperatures and strain rates. *International Journal of Fatigue*, 2019, 127: 268-274.
- [6-3] R. Liu, Z.J. Zhang, P. Zhang, Z.F. Zhang. Extremely-low-cycle fatigue behaviors of Cu and Cu–Al alloys: Damage mechanisms and life prediction. *Acta Materialia*, 2015, 83: 341-356
- [6-4] C.W. Shao, P. Zhang, R. Liu, Z.J. Zhang, J.C. Pang, Z.F. Zhang. Low-cycle and extremely-low-cycle fatigue behaviors of high-Mn austenitic TRIP/TWIP alloys: Property evaluation, damage mechanisms and life prediction. *Acta Materialia*, 2016, 103: 781-795
- [6-5] C. S. Chang, W. T. Pimbley, H. D. Conway. An analysis of metal fatigue based on hysteresis energy. *Experimental Mechanics*, 1968, 8: 133–137
- [6-6] S.K. Koh. Fatigue damage evaluation of a high pressure tube steel using cyclic strain energy density. *International Journal of Pressure Vessels and Piping*, 2002, 79: 791-798
- [6-7] Y. Preger, H. M. Barkholtz, A. Fresquez, D. L. Campbell, B. W. Juba, J. Romàn-Kustas, S. R. Ferreira, B. Chalamala. Degradation of Commercial Lithium-Ion Cells as a Function of Chemistry and Cycling Conditions. *Journal of The Electrochemical Society*, 2020, 167, 120532.
- [6-8] S.J. Harris, R.D. Deshpande, Y. Qi. Mesopores inside electrode particles can change the Li-ion transport mechanism and diffusion-induced stress. *Journal of Materials Research*, 2010, 25, 1433–1440.

Chapter 7

Conclusions and Future Work

7.1 Conclusions

The work presented in this dissertation deals with the mechanical failure investigation of lithium ion battery electrode under electrochemical condition and provides the introduction of a new perspective of evaluation approach. The major outcomes of this thesis are summarised as following:

1. A diffusion driven method and a chemical potential driven method are developed and implemented for conducting coupled diffusion-stress analysis.
2. Studies on crack initiation, growth and fracture of primary electrode particle have been performed.
3. Extending the knowledge on shakedown, reverse plasticity and ratcheting behaviours of electrode configuration.
4. A fatigue damage evaluation method is established to simulate different degradation trends of battery electrode.
5. Extending the knowledge on continuous fatigue damage of electrode configurations at different material scales.

The implementation of diffusion driven method and chemical potential driven method by writing UMATHT subroutines in chapter 3 makes it available to use ABAQUS platform to perform coupled diffusion-stress analysis for battery electrode. The diffusion-induced stress calculation of primary electrode particle has been discussed. Based on the stress analysis, a more comprehensive cracking analysis has been conducted, where the complete crack initiation, growth and fracture process is investigated rather than studying the electrode configuration with pre-existing crack. The more comprehensive critical cracking failure boundaries considering both crack initiation and fracture are established.

Considering the cyclic operation condition, a lot must be done to further understand the cyclic plasticity failure behaviours of battery electrode. Efforts have been done with using the LMM to investigate the shakedown, reverse plasticity and ratcheting of primary electrode particle in chapter 4. The shakedown and ratcheting boundaries have been established for electrode particle considering the change of electrochemical load, mechanical load and particle size. It has been found that the

endurance of electrode particle against current density, which leads to the generation of cyclic diffusion-induced stress, will decrease with a rising in particle dimension. Contrarily, the larger particle is demonstrated to have better affordability of mechanical load. The calculation can also give the detailed material response such as plastic strain range, which is able to associate with the low-cycle fatigue damage model for evaluating the low-cycle fatigue damage.

A fatigue damage assessment method is proposed for understanding the continuous mechanical degradation of oxide battery electrode, and this has been discussed in depth in chapter 5. UMAT subroutine is developed for implementing the numerical part of the method and cyclic charging-discharging tests are performed for deciding the capacity fading indicated damage. The strategy to correlate the electrochemistry represented damage with mechanical fatigue damage is proposed. The fatigue damage accumulation of typical electrode plate under different C-rate conditions has been discussed. The work in this chapter makes it available to use the fatigue damage method to evaluate the mechanical degradation of oxide battery electrode under cyclic electrochemical loads.

For modeling the different degradation trends of battery electrode, an energy based damage model considering both stress and strain is implanted in the fatigue evaluation approach in Chapter 6. It is now available to model the primary fatigue degradation trends, such as moderate, accelerated and linear/quasi-linear degradation. The fatigue degradation of macroscopic electrode plate with non-linear capacity fading is simulated considering C-rate variations. Additionally, with using the representative volume element method, fatigue degradation of microscopic multiple-cylinder-particle configuration is modeled considering the difference of particle shape and relative location. The research work in this chapter gives the approach for non-linear fatigue damage evaluation of battery electrode and suggestions on avoiding fatigue degradation of battery electrode at different material levels.

7.2 Future work

To make mechanical integrity assessment of battery electrode more reliable, the following areas have been identified as future work with scope for improvements.

In simulating the post yielding behaviour of the battery electrode, the elastic-perfectly plastic model is employed in this work. The researched electrode material is Nickel Manganese Cobalt Oxide. Unlike traditional metallic material, the mechanical property test is not easily accessible to be conducted for this oxide material and the plasticity related parameters are not easily available in the literature. However, it is commonly regarded that the mechanical integrity of electrode appears to be one of the crucial factors affecting the performance of lithium battery, and it is important to accurately assess the stress-strain response. For further promotion, it is significant to develop improved

physically-based constitutive models, which are specific for battery electrode materials. A lot more should be done to reflect accurate mechanical response of electrode material, such as plasticity hardening/softening, visco-plasticity. Besides, it is interesting to study the effects of loading conditions on material response, such as the effects of abnormal electrochemical condition, flexible loading as well as cyclic loading rate. Also, it is required to design new method and experimental facilities to determine the material properties for improving the constitutive models.

Battery is a complex electrochemical-mechanical system. It is important to develop more in-depth physical insights on electrochemical reaction mechanism, material electrochemical degradation and mechanical failure mechanism. Also, it is challengeable to understand the interaction between these mechanisms, including reciprocal relationship, promoting or inhibiting effects and so on. These works will form a basis for developing more advanced and practical modeling analysis.

Under different scales, the material models are interrelated and influence each other. Since macro description may fail in local areas, it could be replaced by micro modelling. The micro characteristics of the model are not only subjected to macro factors, but also significantly affect the macro performance. The fatigue failure of macroscopic electrode plate is a kind of representation of micro fatigue damage of multiple particle configuration. It is valuable to establish the interconnection between the two, and figure out the impact of the interaction.

Appendix 1

Diffusion driven USDFLD-UMATHHT

Update DZ (diffusivity without considering stress effect, 1E-3), PMV (partial molar volume, 2.1E12), RT (gas constant times absolute temperature, 2.479E9), SPECHT (specific heat, 1), DENS (density, 1) (Note: The inputted material properties in this code are for reference only)

```
      SUBROUTINE USDFLD(FIELD,STATEV,PNEWDT,DIRECT,T,CELENT,
1  TIME,DTIME,CMNAME,ORNAME,NFIELD,NSTATV,NOEL,NPT,LAYER,
2  KSPT,KSTEP,KINC,NDI,NSHR,COORD,JMAC,JMATYP,MATLAYO,
3  LACCFLA)
C
C   INCLUDE 'ABA_PARAM.INC'
C
C   CHARACTER*80 CMNAME,ORNAME
C   CHARACTER*3  FLGRAY(15)
C   DIMENSION FIELD(NFIELD),STATEV(NSTATV),DIRECT(3,3),
1  T(3,3),TIME(2)
C   DIMENSION ARRAY(15),JARRAY(15),JMAC(*),JMATYP(*),
1  COORD(*)
C
C   Access to stress tensor
C   CALL GETVRM('S',ARRAY,JARRAY,FLGRAY,JRCD,JMAC,JMATYP,
1  MATLAYO,LACCFLA)
C
C   Store 3 primary stress components into STATEV
C   DO I=1,3
C     STATEV(I)=ARRAY(I)
C   END DO
C   RETURN
C   END
C
C
C   SUBROUTINE UMATHHT(U,DUDT,DUDG,FLUX,DFDT,DFDG,
1  STATEV,TEMP,DTEMP,DTEMDX,TIME,DTIME,PREDEF,DPRED,
2  CMNAME,NTGRD,NSTATV,PROPS,NPROPS,COORDS,PNEWDT,
3  NOEL,NPT,LAYER,KSPT,KSTEP,KINC)
C
C   INCLUDE 'ABA_PARAM.INC'
C
C   CHARACTER*80 CMNAME
C   DIMENSION DUDG(NTGRD),FLUX(NTGRD),DFDT(NTGRD),
```

```
1 DFDG(NTGRD,NTGRD),STATEV(NSTATV),DTEMDC(NTGRD),
2 TIME(2),PREDEF(1),DPRED(1),PROPS(NPROPS),COORDS(3)
```

C Input diffusivity at stress free condition, partial molar volume, RT, specific heat, density
DOUBLE PRECISION DZ, PMV, RT, COE1, COE2, COE3

```
DZ=
```

```
PMV=
```

```
RT=
```

```
SPECHT=
```

```
DENS=
```

```
DESP=DENS*SPECHT
```

C Calculate hydrostatic stress

```
VHPC=(STATEV(1)+STATEV(2)+STATEV(3))/3.0
```

```
STATEV(4)=VHPC
```

C Redefine DUDT, FLUX, CONDUCTIVITY

```
DUDT=SPECHT
```

```
DU=DUDT*DTEMP
```

```
STATEV(17)=DTEMP
```

```
U=U+DU
```

```
STATEV(5)=U
```

```
COE1=VHPC*PMV/RT
```

```
STATEV(6)=COE1
```

```
COE2=EXP(COE1)
```

```
STATEV(7)=COE2
```

```
COE3=DZ*COE2*DESP
```

```
STATEV(8)=COE3
```

```
DO i=1, NTGRD
```

```
    FLUX(i) = -COE3*DTEMDC(i)
```

```
END DO
```

```
STATEV(18)=DTEMDC(1)
```

```
DO i=1, NTGRD
```

```
    DFDG(i,i) = -COE3
```

```
END DO
```

RETURN
END

Appendix 2

Chemical potential driven USDFLD-UMATHT

Update DZ (diffusivity without considering stress effect, 1E-3), PMV (partial molar volume, 2.1E12), RT (gas constant times absolute temperature, 2.479E9), SPECHT (specific heat, 1), DENS (density, 1) (Note: The inputted material properties in this code are for reference only)

```
      SUBROUTINE USDFLD(FIELD,STATEV,PNEWDT,DIRECT,T,CELENT,
1 TIME,DTIME,CMNAME,ORNAME,NFIELD,NSTATV,NOEL,NPT,LAYER,
2 KSPT,KSTEP,KINC,NDI,NSHR,COORD,JMAC,JMATYP,MATLAYO,
3 LACCFLA)
C
C   INCLUDE 'ABA_PARAM.INC'
C
C   CHARACTER*80 CMNAME,ORNAME
C   CHARACTER*3  FLGRAY(15)
C   DIMENSION FIELD(NFIELD),STATEV(NSTATV),DIRECT(3,3),
1 T(3,3),TIME(2)
C   DIMENSION ARRAY(15),JARRAY(15),JMAC(*),JMATYP(*),
1 COORD(*)
C
C   INTEGER NEL,NUPT,NCO,NCOOR
C   PARAMETER(NEL=, NUPT=, NCO=, NCOOR=)
C   DIMENSION EICDS(NEL,NUPT,NCO,NCOOR)
C   COMMON /MATRIX/EICDS
C
C   Access to stress tensor
C   CALL GETVRM('S',ARRAY,JARRAY,FLGRAY,JRCD,JMAC,JMATYP,
1  MATLAYO,LACCFLA)
C
C   Store 3 primary stress components into STATEV
C   DO I=1,3
C     STATEV(I)=ARRAY(I)
C   END DO
C
C   DO G=1,3
C     EICDS(NOEL,NPT,1,G)=COORD(G)
C     EICDS(NOEL,NPT,2,G)=ARRAY(G)
C   END DO
C
C   RETURN
C   END
```

C
C

```
      SUBROUTINE UMATHT(U,DUDT,DUDG,FLUX,DFDT,DFDG,  
1 STATEV,TEMP,DTEMP,DTEMPDX,TIME,DTIME,PREDEF,DPRED,  
2 CMNAME,NTGRD,NSTATV,PROPS,NPROPS,COORDS,PNEWDT,  
3 NOEL,NPT,LAYER,KSPT,KSTEP,KINC)
```

C

```
      INCLUDE 'ABA_PARAM.INC'
```

C

```
      CHARACTER*80 CMNAME  
      DIMENSION DUDG(NTGRD),FLUX(NTGRD),DFDT(NTGRD),  
1 DFDG(NTGRD,NTGRD),STATEV(NSTATV),DTEMPDX(NTGRD),  
2 TIME(2),PREDEF(1),DPRED(1),PROPS(NPROPS),COORDS(3)
```

```
      INTEGER NEL,NUPT,NCO,NCOOR  
      PARAMETER(NEL=, NUPT=, NCO=, NCOOR=)  
      DIMENSION EICDS(NEL,NUPT,NCO,NCOOR)  
      COMMON /MATRIX/EICDS
```

C Input diffusivity at stress free condition, partial molar volume, RT, specific heat, density

```
      DOUBLE PRECISION DZ, PMV, RT, COE1, COE2, COE3, COE4, a1, a2, a3,  
1 b1, b2, b3  
      DZ=  
      PMV=  
      RT=  
      SPECHT=  
      DENS=
```

```
      DESP=DENS*SPECHT
```

C Redefine DUDT, FLUX

```
      DUDT=SPECHT  
      DU=DUDT*DTEMP
```

```
      STATEV(17)=DTEMP
```

```
      U=U+DU  
      STATEV(4)=U
```

```
      COE1=DZ*DESP  
      COE2=-COE1  
      STATEV(5)=COE2
```

```
      COE3=PMV*TEMP/RT
```

STATEV(6)=COE3

b1=COORDS(1)

b2=COORDS(2)

b3=COORDS(3)

C Calculate partial derivative

DO I=1,NEL

DO J=1,NUPT

JUDGE2=EICDS(I,J,1,1)**2+

1 EICDS(I,J,1,2)**2+

2 EICDS(I,J,1,3)**2

IF (JUDGE2.NE.0) THEN

JUDGE=(EICDS(I,J,1,1)-b1)**2+

1 (EICDS(I,J,1,2)-b2)**2+

2 (EICDS(I,J,1,3)-b3)**2

JUDGE1=SQRT(JUDGE)

IF (JUDGE1.LE.2) THEN

COUNT=COUNT+1

STATEV(18)=COUNT

VHP=(EICDS(I,J,2,1)+EICDS(I,J,2,2)+EICDS(I,J,2,3))/3.0

YI=VHP

X1I=EICDS(I,J,1,1)

X2I=EICDS(I,J,1,2)

X3I=EICDS(I,J,1,3)

X1IYI=X1I*YI

X2IYI=X2I*YI

X3IYI=X3I*YI

X1I2=X1I*X1I

X1IX2I=X1I*X2I

X1IX3I=X1I*X3I

X2I2= X2I* X2I

X2IX3I=X2I*X3I

X3I2=X3I*X3I

```

depni=COUNT
depX1i=depX1i+X1I
depX2i=depX2i+X2I
depX3i=depX3i+X3I
depyi=depyi+YI
depX1i2=depX1i2+X1I2
depX1ix2i=depX1ix2i+X1IX2I
depX1ix3i=depX1ix3i+X1IX3I
depX1iyi=depX1iyi+X1IYI
depX2i2=depX2i2+X2I2
depX2ix3i=depX2ix3i+X2IX3I
depX2iyi=depX2iyi+X2IYI
depX3i2=depX3i2+X3I2
depX3iyi=depX3iyi+X3IYI

```

END IF

END IF

END DO

END DO

$$a111 = \text{depX1iyi} * (\text{depX3i2} * \text{depX2i}^{**2} - 2 * \text{depX2i} * \text{depX3i} * \text{depX2ix3i} + 1 \text{ depX2i2} * \text{depX3i}^{**2} + \text{depni} * \text{depX2ix3i}^{**2} - \text{depni} * \text{depX2i2} * \text{depX3i2})$$

$$a1121 = -\text{depX1i}^{**2} * \text{depX2ix3i}^{**2} + \text{depX2i2} * \text{depX3i2} * \text{depX1i}^{**2} - 1 \text{ 2} * \text{depX3i2} * \text{depX1i} * \text{depX2i} * \text{depX1ix2i} + 2 \text{ 2} * \text{depX1i} * \text{depX2i} * \text{depX1ix3i} * \text{depX2ix3i} + 3 \text{ 2} * \text{depX1i} * \text{depX3i} * \text{depX1ix2i} * \text{depX2ix3i} - 4 \text{ 2} * \text{depX2i2} * \text{depX1i} * \text{depX3i} * \text{depX1ix3i} - \text{depX2i}^{**2} * \text{depX1ix3i}^{**2}$$

$$a1122 = \text{depX1i2} * \text{depX3i2} * \text{depX2i}^{**2} + 1 \text{ 2} * \text{depX2i} * \text{depX3i} * \text{depX1ix2i} * \text{depX1ix3i} - 2 \text{ 2} * \text{depX1i2} * \text{depX2i} * \text{depX3i} * \text{depX2ix3i} - \text{depX3i}^{**2} * \text{depX1ix2i}^{**2} + 3 \text{ depX1i2} * \text{depX2i2} * \text{depX3i}^{**2} + \text{depni} * \text{depX3i2} * \text{depX1ix2i}^{**2} - 4 \text{ 2} * \text{depni} * \text{depX1ix2i} * \text{depX1ix3i} * \text{depX2ix3i} + 5 \text{ depni} * \text{depX2i2} * \text{depX1ix3i}^{**2} + \text{depni} * \text{depX1i2} * \text{depX2ix3i}^{**2} - 6 \text{ depni} * \text{depX1i2} * \text{depX2i2} * \text{depX3i2}$$

$$a112 = a1121 + a1122$$

$$a11 = a111 / a112$$

$$a121 = \text{depX3iyi} * (\text{depX2i}^{**2} * \text{depX1ix3i} +$$

$$\begin{aligned}
& 1 \text{ depx1i*depx3i*depx2i2} - \text{depx2i*depx3i*depx1ix2i} - \\
& 2 \text{ depni*depx2i2*depx1ix3i} - \text{depx1i*depx2i*depx2ix3i} + \\
& 3 \text{ depni*depx1ix2i*depx2ix3i}
\end{aligned}$$

$$\begin{aligned}
& a1221 = -\text{depx1i**2*depx2ix3i**2} + \\
& 1 \text{ depx2i2*depx3i2*depx1i**2} - 2 \text{ depx3i2*depx1i*depx2i*depx1ix2i} + \\
& 2 \text{ 2*depx1i*depx2i*depx1ix3i*depx2ix3i} + \\
& 3 \text{ 2*depx1i*depx3i*depx1ix2i*depx2ix3i} - \\
& 4 \text{ 2*depx2i2*depx1i*depx3i*depx1ix3i} - \text{depx2i**2*depx1ix3i**2}
\end{aligned}$$

$$\begin{aligned}
& a1222 = \text{depx1i2*depx3i2*depx2i**2} + \\
& 1 \text{ 2*depx2i*depx3i*depx1ix2i*depx1ix3i} - \\
& 2 \text{ 2*depx1i2*depx2i*depx3i*depx2ix3i} - \text{depx3i**2*depx1ix2i**2} + \\
& 3 \text{ depx1i2*depx2i2*depx3i**2} + \text{depni*depx3i2*depx1ix2i**2} - \\
& 4 \text{ 2*depni*depx1ix2i*depx1ix3i*depx2ix3i} + \\
& 5 \text{ depni*depx2i2*depx1ix3i**2} + \text{depni*depx1i2*depx2ix3i**2} - \\
& 6 \text{ depni*depx1i2*depx2i2*depx3i2}
\end{aligned}$$

$$a122 = a1221 + a1222$$

$$a12 = a121 / a122$$

$$\begin{aligned}
& a131 = \text{depx2iyi*(depx3i**2*depx1ix2i} + \text{depx1i*depx2i*depx3i2} - \\
& 1 \text{ depx2i*depx3i*depx1ix3i} - \text{depx1i*depx3i*depx2ix3i} - \\
& 2 \text{ depni*depx3i2*depx1ix2i} + \text{depni*depx1ix3i*depx2ix3i})
\end{aligned}$$

$$\begin{aligned}
& a1321 = -\text{depx1i**2*depx2ix3i**2} + \text{depx2i2*depx3i2*depx1i**2} - \\
& 1 \text{ 2*depx3i2*depx1i*depx2i*depx1ix2i} + \\
& 2 \text{ 2*depx1i*depx2i*depx1ix3i*depx2ix3i} + \\
& 3 \text{ 2*depx1i*depx3i*depx1ix2i*depx2ix3i} - \\
& 4 \text{ 2*depx2i2*depx1i*depx3i*depx1ix3i} - \text{depx2i**2*depx1ix3i**2}
\end{aligned}$$

$$\begin{aligned}
& a1322 = \text{depx1i2*depx3i2*depx2i**2} + \\
& 1 \text{ 2*depx2i*depx3i*depx1ix2i*depx1ix3i} - \\
& 2 \text{ 2*depx1i2*depx2i*depx3i*depx2ix3i} - \text{depx3i**2*depx1ix2i**2} + \\
& 3 \text{ depx1i2*depx2i2*depx3i**2} + \text{depni*depx3i2*depx1ix2i**2} - \\
& 4 \text{ 2*depni*depx1ix2i*depx1ix3i*depx2ix3i} + \\
& 5 \text{ depni*depx2i2*depx1ix3i**2} + \text{depni*depx1i2*depx2ix3i**2} - \\
& 6 \text{ depni*depx1i2*depx2i2*depx3i2}
\end{aligned}$$

$$a132 = a1321 + a1322$$

$$a13 = a131 / a132$$

$$\begin{aligned}
a141 = & \text{depyi} * (\text{dep}x1i * \text{dep}x2ix3i^{**2} - \\
& 1 \text{ dep}x1i * \text{dep}x2i2 * \text{dep}x3i2 + \text{dep}x3i * \text{dep}x2i2 * \text{dep}x1ix3i + \\
& 2 \text{ dep}x2i * \text{dep}x3i2 * \text{dep}x1ix2i - \text{dep}x2i * \text{dep}x1ix3i * \text{dep}x2ix3i - \\
& 3 \text{ dep}x3i * \text{dep}x1ix2i * \text{dep}x2ix3i)
\end{aligned}$$

$$\begin{aligned}
a1421 = & -\text{dep}x1i^{**2} * \text{dep}x2ix3i^{**2} + \\
& 1 \text{ dep}x2i2 * \text{dep}x3i2 * \text{dep}x1i^{**2} - 2 * \text{dep}x3i2 * \text{dep}x1i * \text{dep}x2i * \text{dep}x1ix2i + \\
& 2 * \text{dep}x1i * \text{dep}x2i * \text{dep}x1ix3i * \text{dep}x2ix3i + \\
& 3 * \text{dep}x1i * \text{dep}x3i * \text{dep}x1ix2i * \text{dep}x2ix3i - \\
& 4 * \text{dep}x2i2 * \text{dep}x1i * \text{dep}x3i * \text{dep}x1ix3i - \text{dep}x2i^{**2} * \text{dep}x1ix3i^{**2}
\end{aligned}$$

$$\begin{aligned}
a1422 = & \text{dep}x1i2 * \text{dep}x3i2 * \text{dep}x2i^{**2} + \\
& 1 * \text{dep}x2i * \text{dep}x3i * \text{dep}x1ix2i * \text{dep}x1ix3i - \\
& 2 * \text{dep}x1i2 * \text{dep}x2i * \text{dep}x3i * \text{dep}x2ix3i - \text{dep}x3i^{**2} * \text{dep}x1ix2i^{**2} + \\
& 3 \text{ dep}x1i2 * \text{dep}x2i2 * \text{dep}x3i^{**2} + \text{dep}ni * \text{dep}x3i2 * \text{dep}x1ix2i^{**2} - \\
& 4 * \text{dep}ni * \text{dep}x1ix2i * \text{dep}x1ix3i * \text{dep}x2ix3i + \\
& 5 \text{ dep}ni * \text{dep}x2i2 * \text{dep}x1ix3i^{**2} + \text{dep}ni * \text{dep}x1i2 * \text{dep}x2ix3i^{**2} - \\
& 6 \text{ dep}ni * \text{dep}x1i2 * \text{dep}x2i2 * \text{dep}x3i2
\end{aligned}$$

$$a142 = a1421 + a1422$$

$$a14 = a141 / a142$$

$$a1 = a11 - a12 - a13 - a14$$

$$\begin{aligned}
a211 = & \text{dep}x2iyi * (\text{dep}x3i2 * \text{dep}x1i^{**2} - 2 * \text{dep}x1i * \text{dep}x3i * \text{dep}x1ix3i + \\
& 1 \text{ dep}x1i2 * \text{dep}x3i^{**2} + \text{dep}ni * \text{dep}x1ix3i^{**2} - \text{dep}ni * \text{dep}x1i2 * \text{dep}x3i2)
\end{aligned}$$

$$\begin{aligned}
a2121 = & -\text{dep}x1i^{**2} * \text{dep}x2ix3i^{**2} + \text{dep}x2i2 * \text{dep}x3i2 * \text{dep}x1i^{**2} - \\
& 1 * \text{dep}x3i2 * \text{dep}x1i * \text{dep}x2i * \text{dep}x1ix2i + \\
& 2 * \text{dep}x1i * \text{dep}x2i * \text{dep}x1ix3i * \text{dep}x2ix3i + \\
& 3 * \text{dep}x1i * \text{dep}x3i * \text{dep}x1ix2i * \text{dep}x2ix3i - \\
& 4 * \text{dep}x2i2 * \text{dep}x1i * \text{dep}x3i * \text{dep}x1ix3i - \text{dep}x2i^{**2} * \text{dep}x1ix3i^{**2}
\end{aligned}$$

$$\begin{aligned}
a2122 = & \text{dep}x1i2 * \text{dep}x3i2 * \text{dep}x2i^{**2} + \\
& 1 * \text{dep}x2i * \text{dep}x3i * \text{dep}x1ix2i * \text{dep}x1ix3i - \\
& 2 * \text{dep}x1i2 * \text{dep}x2i * \text{dep}x3i * \text{dep}x2ix3i - \text{dep}x3i^{**2} * \text{dep}x1ix2i^{**2} + \\
& 3 \text{ dep}x1i2 * \text{dep}x2i2 * \text{dep}x3i^{**2} + \text{dep}ni * \text{dep}x3i2 * \text{dep}x1ix2i^{**2} - \\
& 4 * \text{dep}ni * \text{dep}x1ix2i * \text{dep}x1ix3i * \text{dep}x2ix3i + \\
& 5 \text{ dep}ni * \text{dep}x2i2 * \text{dep}x1ix3i^{**2} + \text{dep}ni * \text{dep}x1i2 * \text{dep}x2ix3i^{**2} - \\
& 6 \text{ dep}ni * \text{dep}x1i2 * \text{dep}x2i2 * \text{dep}x3i2
\end{aligned}$$

$$a212 = a2121 + a2122$$

$$a_{21} = a_{211}/a_{212}$$

$$a_{221} = \text{depx}_{3i} y_i (\text{depx}_{1i}^{**2} \text{depx}_{2i} \text{ix}_{3i} +$$

- 1 $\text{depx}_{2i} \text{depx}_{3i} \text{depx}_{1i}^2 - \text{depx}_{1i} \text{depx}_{2i} \text{depx}_{1i} \text{ix}_{3i} -$
- 2 $\text{depx}_{1i} \text{depx}_{3i} \text{depx}_{1i} \text{ix}_{2i} - \text{dep}_{ni} \text{depx}_{1i}^2 \text{depx}_{2i} \text{ix}_{3i} +$
- 3 $\text{dep}_{ni} \text{depx}_{1i} \text{ix}_{2i} \text{depx}_{1i} \text{ix}_{3i})$

$$a_{2221} = -\text{depx}_{1i}^{**2} \text{depx}_{2i} \text{ix}_{3i}^{**2} +$$

- 1 $\text{depx}_{2i}^2 \text{depx}_{3i}^2 \text{depx}_{1i}^{**2} - 2 \text{depx}_{3i}^2 \text{depx}_{1i} \text{depx}_{2i} \text{depx}_{1i} \text{ix}_{2i} +$
- 2 $2 \text{depx}_{1i} \text{depx}_{2i} \text{depx}_{1i} \text{ix}_{3i} \text{depx}_{2i} \text{ix}_{3i} +$
- 3 $2 \text{depx}_{1i} \text{depx}_{3i} \text{depx}_{1i} \text{ix}_{2i} \text{depx}_{2i} \text{ix}_{3i} -$
- 4 $2 \text{depx}_{2i}^2 \text{depx}_{1i} \text{depx}_{3i} \text{depx}_{1i} \text{ix}_{3i} - \text{depx}_{2i}^{**2} \text{depx}_{1i} \text{ix}_{3i}^{**2}$

$$a_{2222} = \text{depx}_{1i}^2 \text{depx}_{3i}^2 \text{depx}_{2i}^{**2} +$$

- 1 $2 \text{depx}_{2i} \text{depx}_{3i} \text{depx}_{1i} \text{ix}_{2i} \text{depx}_{1i} \text{ix}_{3i} -$
- 2 $2 \text{depx}_{1i}^2 \text{depx}_{2i} \text{depx}_{3i} \text{depx}_{2i} \text{ix}_{3i} - \text{depx}_{3i}^{**2} \text{depx}_{1i} \text{ix}_{2i}^{**2} +$
- 3 $\text{depx}_{1i}^2 \text{depx}_{2i}^2 \text{depx}_{3i}^{**2} + \text{dep}_{ni} \text{depx}_{3i}^2 \text{depx}_{1i} \text{ix}_{2i}^{**2} -$
- 4 $2 \text{dep}_{ni} \text{depx}_{1i} \text{ix}_{2i} \text{depx}_{1i} \text{ix}_{3i} \text{depx}_{2i} \text{ix}_{3i} +$
- 5 $\text{dep}_{ni} \text{depx}_{2i}^2 \text{depx}_{1i} \text{ix}_{3i}^{**2} + \text{dep}_{ni} \text{depx}_{1i}^2 \text{depx}_{2i} \text{ix}_{3i}^{**2} -$
- 6 $\text{dep}_{ni} \text{depx}_{1i}^2 \text{depx}_{2i}^2 \text{depx}_{3i}^2$

$$a_{222} = a_{2221} + a_{2222}$$

$$a_{22} = a_{221}/a_{222}$$

$$a_{231} = \text{depx}_{1i} y_i (\text{depx}_{3i}^{**2} \text{depx}_{1i} \text{ix}_{2i} + \text{depx}_{1i} \text{depx}_{2i} \text{depx}_{3i}^2 -$$

- 1 $\text{depx}_{2i} \text{depx}_{3i} \text{depx}_{1i} \text{ix}_{3i} - \text{depx}_{1i} \text{depx}_{3i} \text{depx}_{2i} \text{ix}_{3i} -$
- 2 $\text{dep}_{ni} \text{depx}_{3i}^2 \text{depx}_{1i} \text{ix}_{2i} + \text{dep}_{ni} \text{depx}_{1i} \text{ix}_{3i} \text{depx}_{2i} \text{ix}_{3i})$

$$a_{2321} = -\text{depx}_{1i}^{**2} \text{depx}_{2i} \text{ix}_{3i}^{**2} + \text{depx}_{2i}^2 \text{depx}_{3i}^2 \text{depx}_{1i}^{**2} -$$

- 1 $2 \text{depx}_{3i}^2 \text{depx}_{1i} \text{depx}_{2i} \text{depx}_{1i} \text{ix}_{2i} +$
- 2 $2 \text{depx}_{1i} \text{depx}_{2i} \text{depx}_{1i} \text{ix}_{3i} \text{depx}_{2i} \text{ix}_{3i} +$
- 3 $2 \text{depx}_{1i} \text{depx}_{3i} \text{depx}_{1i} \text{ix}_{2i} \text{depx}_{2i} \text{ix}_{3i} -$
- 4 $2 \text{depx}_{2i}^2 \text{depx}_{1i} \text{depx}_{3i} \text{depx}_{1i} \text{ix}_{3i} - \text{depx}_{2i}^{**2} \text{depx}_{1i} \text{ix}_{3i}^{**2}$

$$a_{2322} = \text{depx}_{1i}^2 \text{depx}_{3i}^2 \text{depx}_{2i}^{**2} +$$

- 1 $2 \text{depx}_{2i} \text{depx}_{3i} \text{depx}_{1i} \text{ix}_{2i} \text{depx}_{1i} \text{ix}_{3i} -$
- 2 $2 \text{depx}_{1i}^2 \text{depx}_{2i} \text{depx}_{3i} \text{depx}_{2i} \text{ix}_{3i} - \text{depx}_{3i}^{**2} \text{depx}_{1i} \text{ix}_{2i}^{**2} +$
- 3 $\text{depx}_{1i}^2 \text{depx}_{2i}^2 \text{depx}_{3i}^{**2} + \text{dep}_{ni} \text{depx}_{3i}^2 \text{depx}_{1i} \text{ix}_{2i}^{**2} -$
- 4 $2 \text{dep}_{ni} \text{depx}_{1i} \text{ix}_{2i} \text{depx}_{1i} \text{ix}_{3i} \text{depx}_{2i} \text{ix}_{3i} +$
- 5 $\text{dep}_{ni} \text{depx}_{2i}^2 \text{depx}_{1i} \text{ix}_{3i}^{**2} + \text{dep}_{ni} \text{depx}_{1i}^2 \text{depx}_{2i} \text{ix}_{3i}^{**2} -$
- 6 $\text{dep}_{ni} \text{depx}_{1i}^2 \text{depx}_{2i}^2 \text{depx}_{3i}^2$

$$a_{232} = a_{2321} + a_{2322}$$

$$a_{23} = a_{231} / a_{232}$$

$$a_{241} = \text{depyi} * (\text{dep}x_{2i} * \text{dep}x_{1ix3i}^{**2} - \\ 1 \text{ dep}x_{2i} * \text{dep}x_{1i2} * \text{dep}x_{3i2} + \text{dep}x_{3i} * \text{dep}x_{1i2} * \text{dep}x_{2ix3i} + \\ 2 \text{ dep}x_{1i} * \text{dep}x_{3i2} * \text{dep}x_{1ix2i} - \text{dep}x_{3i} * \text{dep}x_{1ix2i} * \text{dep}x_{1ix3i} - \\ 3 \text{ dep}x_{1i} * \text{dep}x_{1ix3i} * \text{dep}x_{2ix3i})$$

$$a_{2421} = -\text{dep}x_{1i}^{**2} * \text{dep}x_{2ix3i}^{**2} + \\ 1 \text{ dep}x_{2i2} * \text{dep}x_{3i2} * \text{dep}x_{1i}^{**2} - 2 * \text{dep}x_{3i2} * \text{dep}x_{1i} * \text{dep}x_{2i} * \text{dep}x_{1ix2i} + \\ 2 * 2 * \text{dep}x_{1i} * \text{dep}x_{2i} * \text{dep}x_{1ix3i} * \text{dep}x_{2ix3i} + \\ 3 * 2 * \text{dep}x_{1i} * \text{dep}x_{3i} * \text{dep}x_{1ix2i} * \text{dep}x_{2ix3i} - \\ 4 * 2 * \text{dep}x_{2i2} * \text{dep}x_{1i} * \text{dep}x_{3i} * \text{dep}x_{1ix3i} - \text{dep}x_{2i}^{**2} * \text{dep}x_{1ix3i}^{**2}$$

$$a_{2422} = \text{dep}x_{1i2} * \text{dep}x_{3i2} * \text{dep}x_{2i}^{**2} + \\ 1 * 2 * \text{dep}x_{2i} * \text{dep}x_{3i} * \text{dep}x_{1ix2i} * \text{dep}x_{1ix3i} - \\ 2 * 2 * \text{dep}x_{1i2} * \text{dep}x_{2i} * \text{dep}x_{3i} * \text{dep}x_{2ix3i} - \text{dep}x_{3i}^{**2} * \text{dep}x_{1ix2i}^{**2} + \\ 3 \text{ dep}x_{1i2} * \text{dep}x_{2i2} * \text{dep}x_{3i}^{**2} + \text{dep}ni * \text{dep}x_{3i2} * \text{dep}x_{1ix2i}^{**2} - \\ 4 * 2 * \text{dep}ni * \text{dep}x_{1ix2i} * \text{dep}x_{1ix3i} * \text{dep}x_{2ix3i} + \\ 5 \text{ dep}ni * \text{dep}x_{2i2} * \text{dep}x_{1ix3i}^{**2} + \text{dep}ni * \text{dep}x_{1i2} * \text{dep}x_{2ix3i}^{**2} - \\ 6 \text{ dep}ni * \text{dep}x_{1i2} * \text{dep}x_{2i2} * \text{dep}x_{3i2}$$

$$a_{242} = a_{2421} + a_{2422}$$

$$a_{24} = a_{241} / a_{242}$$

$$a_2 = a_{21} - a_{22} - a_{23} - a_{24}$$

$$a_{311} = \text{dep}x_{3iyi} * (\text{dep}x_{2i2} * \text{dep}x_{1i}^{**2} - 2 * \text{dep}x_{1i} * \text{dep}x_{2i} * \text{dep}x_{1ix2i} + \\ 1 \text{ dep}x_{1i2} * \text{dep}x_{2i}^{**2} + \text{dep}ni * \text{dep}x_{1ix2i}^{**2} - \text{dep}ni * \text{dep}x_{1i2} * \text{dep}x_{2i2})$$

$$a_{3121} = -\text{dep}x_{1i}^{**2} * \text{dep}x_{2ix3i}^{**2} + \text{dep}x_{2i2} * \text{dep}x_{3i2} * \text{dep}x_{1i}^{**2} - \\ 1 * 2 * \text{dep}x_{3i2} * \text{dep}x_{1i} * \text{dep}x_{2i} * \text{dep}x_{1ix2i} + \\ 2 * 2 * \text{dep}x_{1i} * \text{dep}x_{2i} * \text{dep}x_{1ix3i} * \text{dep}x_{2ix3i} + \\ 3 * 2 * \text{dep}x_{1i} * \text{dep}x_{3i} * \text{dep}x_{1ix2i} * \text{dep}x_{2ix3i} - \\ 4 * 2 * \text{dep}x_{2i2} * \text{dep}x_{1i} * \text{dep}x_{3i} * \text{dep}x_{1ix3i} - \text{dep}x_{2i}^{**2} * \text{dep}x_{1ix3i}^{**2}$$

$$a_{3122} = \text{dep}x_{1i2} * \text{dep}x_{3i2} * \text{dep}x_{2i}^{**2} + \\ 1 * 2 * \text{dep}x_{2i} * \text{dep}x_{3i} * \text{dep}x_{1ix2i} * \text{dep}x_{1ix3i} - \\ 2 * 2 * \text{dep}x_{1i2} * \text{dep}x_{2i} * \text{dep}x_{3i} * \text{dep}x_{2ix3i} - \text{dep}x_{3i}^{**2} * \text{dep}x_{1ix2i}^{**2} + \\ 3 \text{ dep}x_{1i2} * \text{dep}x_{2i2} * \text{dep}x_{3i}^{**2} + \text{dep}ni * \text{dep}x_{3i2} * \text{dep}x_{1ix2i}^{**2} - \\ 4 * 2 * \text{dep}ni * \text{dep}x_{1ix2i} * \text{dep}x_{1ix3i} * \text{dep}x_{2ix3i} + \\ 5 \text{ dep}ni * \text{dep}x_{2i2} * \text{dep}x_{1ix3i}^{**2} + \text{dep}ni * \text{dep}x_{1i2} * \text{dep}x_{2ix3i}^{**2} - \\ 6 \text{ dep}ni * \text{dep}x_{1i2} * \text{dep}x_{2i2} * \text{dep}x_{3i2}$$

$$a_{312} = a_{3121} + a_{3122}$$

$$a_{31} = a_{311} / a_{312}$$

$$a_{321} = \text{dep}x_{2iy} * (\text{dep}x_{1i}^{**2} * \text{dep}x_{2ix3i} + \\ 1 \text{ dep}x_{2i} * \text{dep}x_{3i} * \text{dep}x_{1i2} - \text{dep}x_{1i} * \text{dep}x_{2i} * \text{dep}x_{1ix3i} - \\ 2 \text{ dep}x_{1i} * \text{dep}x_{3i} * \text{dep}x_{1ix2i} - \text{dep}ni * \text{dep}x_{1i2} * \text{dep}x_{2ix3i} + \\ 3 \text{ dep}ni * \text{dep}x_{1ix2i} * \text{dep}x_{1ix3i})$$

$$a_{3221} = -\text{dep}x_{1i}^{**2} * \text{dep}x_{2ix3i}^{**2} + \\ 1 \text{ dep}x_{2i2} * \text{dep}x_{3i2} * \text{dep}x_{1i}^{**2} - 2 * \text{dep}x_{3i2} * \text{dep}x_{1i} * \text{dep}x_{2i} * \text{dep}x_{1ix2i} + \\ 2 * 2 * \text{dep}x_{1i} * \text{dep}x_{2i} * \text{dep}x_{1ix3i} * \text{dep}x_{2ix3i} + \\ 3 * 2 * \text{dep}x_{1i} * \text{dep}x_{3i} * \text{dep}x_{1ix2i} * \text{dep}x_{2ix3i} - \\ 4 * 2 * \text{dep}x_{2i2} * \text{dep}x_{1i} * \text{dep}x_{3i} * \text{dep}x_{1ix3i} - \text{dep}x_{2i}^{**2} * \text{dep}x_{1ix3i}^{**2}$$

$$a_{3222} = \text{dep}x_{1i2} * \text{dep}x_{3i2} * \text{dep}x_{2i}^{**2} + \\ 1 * 2 * \text{dep}x_{2i} * \text{dep}x_{3i} * \text{dep}x_{1ix2i} * \text{dep}x_{1ix3i} - \\ 2 * 2 * \text{dep}x_{1i2} * \text{dep}x_{2i} * \text{dep}x_{3i} * \text{dep}x_{2ix3i} - \text{dep}x_{3i}^{**2} * \text{dep}x_{1ix2i}^{**2} + \\ 3 \text{ dep}x_{1i2} * \text{dep}x_{2i2} * \text{dep}x_{3i}^{**2} + \text{dep}ni * \text{dep}x_{3i2} * \text{dep}x_{1ix2i}^{**2} - \\ 4 * 2 * \text{dep}ni * \text{dep}x_{1ix2i} * \text{dep}x_{1ix3i} * \text{dep}x_{2ix3i} + \\ 5 \text{ dep}ni * \text{dep}x_{2i2} * \text{dep}x_{1ix3i}^{**2} + \text{dep}ni * \text{dep}x_{1i2} * \text{dep}x_{2ix3i}^{**2} - \\ 6 \text{ dep}ni * \text{dep}x_{1i2} * \text{dep}x_{2i2} * \text{dep}x_{3i2}$$

$$a_{322} = a_{3221} + a_{3222}$$

$$a_{32} = a_{321} / a_{322}$$

$$a_{331} = \text{dep}x_{1iy} * (\text{dep}x_{2i}^{**2} * \text{dep}x_{1ix3i} + \text{dep}x_{1i} * \text{dep}x_{3i} * \text{dep}x_{2i2} - \\ 1 \text{ dep}x_{2i} * \text{dep}x_{3i} * \text{dep}x_{1ix2i} - \text{dep}ni * \text{dep}x_{2i2} * \text{dep}x_{1ix3i} - \\ 2 \text{ dep}x_{1i} * \text{dep}x_{2i} * \text{dep}x_{2ix3i} + \text{dep}ni * \text{dep}x_{1ix2i} * \text{dep}x_{2ix3i})$$

$$a_{3321} = -\text{dep}x_{1i}^{**2} * \text{dep}x_{2ix3i}^{**2} + \text{dep}x_{2i2} * \text{dep}x_{3i2} * \text{dep}x_{1i}^{**2} - \\ 1 * 2 * \text{dep}x_{3i2} * \text{dep}x_{1i} * \text{dep}x_{2i} * \text{dep}x_{1ix2i} + \\ 2 * 2 * \text{dep}x_{1i} * \text{dep}x_{2i} * \text{dep}x_{1ix3i} * \text{dep}x_{2ix3i} + \\ 3 * 2 * \text{dep}x_{1i} * \text{dep}x_{3i} * \text{dep}x_{1ix2i} * \text{dep}x_{2ix3i} - \\ 4 * 2 * \text{dep}x_{2i2} * \text{dep}x_{1i} * \text{dep}x_{3i} * \text{dep}x_{1ix3i} - \text{dep}x_{2i}^{**2} * \text{dep}x_{1ix3i}^{**2}$$

$$a_{3322} = \text{dep}x_{1i2} * \text{dep}x_{3i2} * \text{dep}x_{2i}^{**2} + \\ 1 * 2 * \text{dep}x_{2i} * \text{dep}x_{3i} * \text{dep}x_{1ix2i} * \text{dep}x_{1ix3i} - \\ 2 * 2 * \text{dep}x_{1i2} * \text{dep}x_{2i} * \text{dep}x_{3i} * \text{dep}x_{2ix3i} - \text{dep}x_{3i}^{**2} * \text{dep}x_{1ix2i}^{**2} + \\ 3 \text{ dep}x_{1i2} * \text{dep}x_{2i2} * \text{dep}x_{3i}^{**2} + \text{dep}ni * \text{dep}x_{3i2} * \text{dep}x_{1ix2i}^{**2} - \\ 4 * 2 * \text{dep}ni * \text{dep}x_{1ix2i} * \text{dep}x_{1ix3i} * \text{dep}x_{2ix3i} + \\ 5 \text{ dep}ni * \text{dep}x_{2i2} * \text{dep}x_{1ix3i}^{**2} + \text{dep}ni * \text{dep}x_{1i2} * \text{dep}x_{2ix3i}^{**2} -$$

6 depni*dep1i2*dep2i2*dep3i2

a332=a3321+a3322

a33=a331/a332

a341= depyi*(dep3i*dep1ix2i**2 -
1 depx3i*dep1i2*dep2i2 + dep1i*dep2i2*dep1ix3i +
2 dep2i*dep1i2*dep2ix3i - dep2i*dep1ix2i*dep1ix3i -
3 dep1i*dep1ix2i*dep2ix3i)

a3421= -dep1i**2*dep2ix3i**2 +
1 dep2i2*dep3i2*dep1i**2 - 2*dep3i2*dep1i*dep2i*dep1ix2i +
2 2*dep1i*dep2i*dep1ix3i*dep2ix3i +
3 2*dep1i*dep3i*dep1ix2i*dep2ix3i -
4 2*dep2i2*dep1i*dep3i*dep1ix3i - dep2i**2*dep1ix3i**2

a3422= dep1i2*dep3i2*dep2i**2 +
1 2*dep2i*dep3i*dep1ix2i*dep1ix3i-
2 2*dep1i2*dep2i*dep3i*dep2ix3i - dep3i**2*dep1ix2i**2 +
3 dep1i2*dep2i2*dep3i**2 + depni*dep3i2*dep1ix2i**2 -
4 2*depni*dep1ix2i*dep1ix3i*dep2ix3i +
5 depni*dep2i2*dep1ix3i**2 + depni*dep1i2*dep2ix3i**2 -
6 depni*dep1i2*dep2i2*dep3i2

a342=a3421+a3422

a34=a341/a342

a3=a31-a32-a33-a34

COUNT=0

depni=0

dep1i=0

dep2i=0

dep3i=0

depyi=0

dep1i2=0

dep1ix2i=0

dep1ix3i=0

dep1iyi=0

dep2i2=0

dep2ix3i=0

dep2iyi=0

```
depx3i2=0  
depx3iyi=0
```

```
STATEV(7)=a1  
STATEV(8)=a2  
STATEV(9)=a3
```

```
FLUX(1) = COE2*(DTEM DX(1)-COE3*a1)  
FLUX(2) = COE2*(DTEM DX(2)-COE3*a2)  
FLUX(3) = COE2*(DTEM DX(3)-COE3*a3)
```

C Redefine DFDT, Conductivity

```
COE4=PMV/RT  
DFDT(1)=COE1*COE4*a1  
DFDT(2)=COE1*COE4*a2  
DFDT(3)=COE1*COE4*a3
```

```
DO i=1, NTGRD  
  DFDG(i,i) = COE2  
END DO
```

```
RETURN  
END
```

Appendix 3

Elastic-perfectly plastic model and damage UMAT for 3D, plain strain and axisymmetric problem

Update ALFA (thermal expansion coefficient, 7E11), EMOD (Young's modulus, 1.25E-1), SYIEL0 (yield strength, 1E-4), ENU (Poisson's ratio, 3E-1), FDC (fatigue ductile coefficient, 3.184), FDE (fatigue ductile exponent, -6.88E-1) (Note: The inputted material properties in this code are for reference only)

```
      SUBROUTINE UMAT(STRESS,STATEV,DDSDDE,SSE,SPD,SCD,
1 RPL,DDSDDT,DRPLDE,DRPLDT,STRAN,DSTRAN,
2 TIME,DTIME,TEMP,DTEMP,PREDEF,DPRED,MATERL,NDI,NSHR,NTENS,
3 NSTATV,PROPS,NPROPS,COORDS,DROT,PNEWDT,CELENT,
4 DFGRD0,DFGRD1,NOEL,NPT,KSLAY,KSPT,KSTEP,KINC)
C
      INCLUDE 'ABA_PARAM.INC'
C
      CHARACTER*80 MATERL
      DIMENSION STRESS(NTENS),STATEV(NSTATV),
1 DDSDE(NTENS,NTENS),DDSDDT(NTENS),DRPLDE(NTENS),
2 STRAN(NTENS),DSTRAN(NTENS),TIME(2),PREDEF(1),DPRED(1),
3 PROPS(NPROPS),COORDS(3),DROT(3,3),
4 DFGRD0(3,3),DFGRD1(3,3)

      DIMENSION EELAS(6),EPLAS(6),FLOW(6),ETHERM(6),DTHERM(6)
      PARAMETER (ONE=1.0D0,TWO=2.0D0,THREE=3.0D0,SIX=6.0D0)
      DATA NEWTON,TOLER/10,1.D-6/

      DOUBLE PRECISION SSE

      COMMON/VIDAMA/VDAMAGE,TEST
      DOUBLE PRECISION VDAMAGE,TEST

C   Input partial molar volume replaced thermal expansivity, Young's modulus, Poisson's ratio
      ALFA=
      EMOD=
      EMOD=EMOD*(1-STATEV(112))
      STATEV(113)=VDAMAGE
      STATEV(114)=EMOD
      ENU=

C   Elastic stiffness
      EBULK3=EMOD/(ONE-TWO*ENU)
```

```
EG2=EMOD/(ONE+ENU)
EG=EG2/TWO
EG3=THREE*EG
ELAM=(EBULK3-EG2)/THREE
```

```
DO 20 K1=1,NTENS
  DO 10 K2=1,NTENS
    DDSDDE(K2,K1)=0.0
10  CONTINUE
20  CONTINUE
```

```
DO I=1,NDI
  DDSDDE(I,I)=EG2+ELAM
END DO
```

```
DO I=2,NDI
  K=I-1
  DO J=1,K
    DDSDDE(J,I) = ELAM
    DDSDDE(I,J) = ELAM
  END DO
END DO
```

```
DO I=NDI+1,NTENS
  DDSDDE(I,I)=EG
END DO
```

C Calculate thermal expansion

```
DO K1=1,NDI
  ETHERM(K1)=ALFA*TEMP
  DTHERM(K1)=ALFA*DTEMP
END DO
```

```
DO K1=NDI+1,NTENS
  ETHERM(K1)=0
  DTHERM(K1)=0
END DO
```

```
DO K1=1,NTENS
```

```
  DO K2=1,NTENS
    STRESS(K1)=STRESS(K1)+DDSDDE(K1,K2)*(DSTRAN(K2)-DTHERM(K2))
  END DO
```

END DO

C Recover elastic and plastic strain

DO 80 K1=1,NTENS

EELAS(K1)=STRAN(K1)+DSTRAN(K1)-ETHERM(K1)

EPLAS(K1)=STATEV(K1+NTENS)

ETHERM(K1)=ETHERM(K1)+DTHERM(K1)

80 CONTINUE

EQPLAS=STATEV(1+2*NTENS)

IF(NPROPS.GT.2) THEN

SMISES=(STRESS(1)-STRESS(2))*(STRESS(1)-STRESS(2)) +

1 (STRESS(2)-STRESS(3))*(STRESS(2)-STRESS(3)) +

1 (STRESS(3)-STRESS(1))*(STRESS(3)-STRESS(1))

DO 90 K1=NDI+1,NTENS

SMISES=SMISES+SIX*STRESS(K1)*STRESS(K1)

90 CONTINUE

SMISES=SQRT(SMISES/TWO)

NVALUE=NPROPS/2-1

C For considering the plasticity behaviour, define SYIELD0 (material yield strength) here and consider the effect of damage on material yield strength

SYIELD0=

SYIELD0=SYIELD0*(1-STATEV(112))

STATEV(41)=SYIELD0

C Determine if actively yielding

IF (SMISES.GT.(1.0+TOLER)*SYIELD0) THEN

SHYDRO=(STRESS(1)+STRESS(2)+STRESS(3))/THREE

ONESY=ONE/SMISES

DO 110 K1=1,NDI

FLOW(K1)=ONESY*(STRESS(K1)-SHYDRO)

110 CONTINUE

DO 120 K1=NDI+1,NTENS

FLOW(K1)=STRESS(K1)*ONESY

120 CONTINUE

SYIELD=SYIELD0

DEQPL=0.0

```

DO 130 KEWTON=1,NEWTON
  RHS=SMISES-EG3*DEQPL-SYIELD
  DEQPL=DEQPL+RHS/(EG3+HARD)
  IF(ABS(RHS).LT.TOLER*SYIEL0) GOTO 140
130  CONTINUE
  WRITE(6,2) NEWTON
2    FORMAT(/,30X,'***WARNING - PLASTICITY ALGORITHM DID NOT ',
1      'CONVERGE AFTER ',I3,' ITERATIONS')
140  CONTINUE
  EFFHRD=EG3*HARD/(EG3+HARD)

```

C Calculate stress and update strain

```

DO 150 K1=1,NDI
  STRESS(K1)=FLOW(K1)*SYIELD+SHYDRO
  EPLAS(K1)=EPLAS(K1)+THREE*FLOW(K1)*DEQPL/TWO
  EELAS(K1)=EELAS(K1)-THREE*FLOW(K1)*DEQPL/TWO
150  CONTINUE
DO 160 K1=NDI+1,NTENS
  STRESS(K1)=FLOW(K1)*SYIELD
  EPLAS(K1)=EPLAS(K1)+THREE*FLOW(K1)*DEQPL
  EELAS(K1)=EELAS(K1)-THREE*FLOW(K1)*DEQPL
160  CONTINUE
  EQPLAS=EQPLAS+DEQPL
  SPD=DEQPL*(SYIEL0+SYIELD)/TWO

  EFFG=EG*SYIELD/SMISES
  EFFG2=TWO*EFFG
  EFFG3=THREE*EFFG2/TWO
  EFFLAM=(EBULK3-EFFG2)/THREE

DO I=1,NDI
  DDSDDDE(I,I)=EFFG2+EFFLAM
END DO

DO I=2,NDI
  K=I-1
  DO J=1,K
    DDSDDDE(J,I) = EFFLAM
    DDSDDDE(I,J) = EFFLAM
  END DO
END DO

DO I=NDI+1,NTENS
  DDSDDDE(I,I)=EFFG

```

```

        END DO

        DO 250 K1=1,NTENS
            DO 240 K2=1,NTENS
                DDSDE(K2,K1)=DDSDE(K2,K1)+FLOW(K2)*FLOW(K1)
1                *(EFFHRD-EFFG3)
240            CONTINUE
250        CONTINUE
            ENDIF
        ENDIF

```

C Store strains in state variable array

```

        DO 310 K1=1,NTENS
            STATEV(K1)=EELAS(K1)
            STATEV(K1+NTENS)=EPLAS(K1)
310    CONTINUE
        STATEV(1+2*NTENS)=EQPLAS

```

C Calculate fatigue damage

```

        STATEV(101)=MOD(KSTEP,2)

        IF (STATEV(101).EQ.1) THEN

            IF (KINC.EQ.1) THEN
                STATEV(102)=EQPLAS

            ELSE IF (KINC.EQ.2) THEN
                STATEV(103)=EQPLAS
                STATEV(104)=STATEV(103)-STATEV(102)

            ELSE
                STATEV(105)=EQPLAS-STATEV(102)
                IF (STATEV(105).GT.STATEV(104)) THEN
                    STATEV(104)=STATEV(105)
                END IF
            END IF

        END IF

        ELSE

            IF (KINC.EQ.1) THEN
                STATEV(106)=EQPLAS

            ELSE IF (KINC.EQ.2) THEN

```

```

STATEV(107)=EQPLAS
STATEV(108)=STATEV(107)-STATEV(106)

Else
STATEV(109)=EQPLAS-STATEV(106)
IF (STATEV(109).GT.STATEV(108)) THEN
STATEV(108)=STATEV(109)
END IF

IF (STATEV(108).GT.STATEV(104)) THEN
STATEV(110)=STATEV(108)
ELSE
STATEV(110)=STATEV(104)
END IF

END IF

STATEV(115)=TIME(1)+DTIME

IF(STATEV(115).EQ.) THEN

FDC=
FDE=
DFDE=1/FDE
DDAMAGE=2*(2*FDC/STATEV(110)**DFDE
STATEV(111)=DDAMAGE

STATEV(112)=STATEV(112)+STATEV(111)
SSE=STATEV(112)

END IF

END IF

RETURN
END

C
C
SUBROUTINE URDFIL(LSTOP,LOVRWRT,KSTEP,KINC,DTIME,TIME)

INCLUDE 'ABA_PARAM.INC'

DIMENSION ARRAY(513),JRRAY(NPRECD,513),TIME(2)
EQUIVALENCE (ARRAY(1),JRRAY(1,1))

```

```
COMMON/VIDAMA/VDAMAGE,TEST
DOUBLE PRECISION VDAMAGE,TEST

CALL POSFIL(KSTEP,KINC,ARRAY,JRCD)

DO K1=1,999999
  CALL DBFILE(0,ARRAY,JRCD)
  IF (JRCD.NE.0) GO TO 110
  KEY=JRRAY(1,2)

  IF(KEY.EQ.1999) THEN
    VDAMAGE=ARRAY(4)

    TEST=KINC

  END IF

END DO
110 CONTINUE

RETURN
END
```